Drag Production of Filamentous Biofilm

by

Joel Hartenberger

A dissertation submitted in partial fulfillment
of the requirements for the degree of
Doctor of Philosophy
(Naval Architecture and Marine Engineering)
in the University of Michigan
2019

Doctoral Committee:

Professor Steven L. Ceccio, Co-Chair
Professor Marc Perlin, Co-Chair
Professor Luis Bernal
Dr. Peter Chang, NSWCCD
Dr. James Gose
Professor Michael Schultz, United States Naval Academy

Joel Hartenberger
jdharte@umich.edu
ORCID iD: 0000-0002-1429-6522

Learn why the world wags and what wags it.

For my family.

ACKNOWLEDGEMENTS

This work was funded as part of the Naval Engineering Education Consortium (NEEC) by NAVSEA through the Naval Surface Warfare Center Carderock Division (contract N00174-16-C-0027). Additional support was provided to me personally through the U.S. DoD Science, Mathematics And Research for Transformation (SMART) Scholarship program for which I am most grateful.

I have been the beneficiary of support from a multitude of people, without whom this work could never have happened. Thanks go to:

—my advisors, Professors Steven Ceccio and Marc Perlin who made this project a reality. Steve, you are the reason I came to the University of Michigan and I am grateful to have had the opportunity to learn firsthand from your example. Marc, whether you were down the hall or halfway across the world, you always made time for me–even in the eleventh hour. I am immensely grateful to have had guidance from you both and I know that I will return to the lessons you taught me throughout my career

—the members of my committee: Dr. James Gose whose experience and knowledge of the lab helped me overcome obstacles and sidestep potential stumbling blocks; Prof. Mike Schultz whose early input informed this effort and who helped me navigate the world of biofilm hydrodynamics; Prof. Luis Bernal in whose classes I learned the basics of boundary layer theory and turbulence; and Dr. Peter Chang whose technical guidance helped direct this project

—the many students with whom I have had the pleasure to work. First and foremost, I would like to acknowledge the help of Elizabeth Callison whose endurance and work ethic were invaluable to this effort. Ellie, I am fortunate to have shared the lab with someone as cheerful and laid back as you, and I enjoyed swapping stories about camping, climbing, biking, and running. I would also like to thank the many masters and undergraduate students whom I have met through the NEEC project. Although your names and contributions are too great to list here, I will not forget your support

—Dr. Timothy O'Hern who introduced the world of fluid mechanics to me and Dr. Craig Merrill who sparked my interest in working for the Navy

—Dr. Eric Holm for keeping me in touch with biofilm efforts around the world

—Dr. Harish Ganesh who is equally equipped to talk about problems in the lab or the vagaries of life

—The many NAME and MHL staff members who have helped me with everything from part fabrication to project finances

I'd also like to acknowledge the support of friends and family who were there to share my happiness in joyful times and sustain me through the lows and frustrations of my time as a graduate student. I will miss the many wonderful people with whom I have gotten to share the years in Ann Arbor. Alyx, your love and support have nurtured me during these final months of my Ph.D. Mom, Dad, Erich, Deasy, Ilana, Jessica, Leif, Casper, and Liam—words cannot describe the love I have received from you and what I feel in return.

TABLE OF CONTENTS

DEDICATION ii

ACKNOWLEDGEMENTS iii

LIST OF FIGURES viii

LIST OF TABLES xix

ABSTRACT xx

CHAPTER

I. Introduction 1

1.1 Motivation 1
1.2 Background 3
1.2.1 Wall-bounded Turbulent Flows 4
1.2.2 Resistance of Biofilms 15
1.3 Contributions 22

II. Methodology 24

2.1 Overview 24
2.2 Growing Biofilm 25
2.3 Biofilm Characterization 31
2.3.1 Areal Coverage 31
2.3.2 Surface Topography 32
2.4 Developing Rigid Replicas of Live Biofilm 38
2.5 Measuring Resistance 41
2.6 Measuring the Flow Field 43
2.7 Measurement Challenges and Uncertainty Estimation 48
2.8 Validation of Methodology for Smooth and Rough Surfaces . 51
2.8.1 Mean Velocity Profiles Over Smooth Baseline and Sand Grain Roughness 53

III. Resistance of Biofilm Layers 58

3.1 Overview 58
3.2 Resistance of Biofilm Covered Surfaces 60
3.2.1 Three Week Biofilm Layers 60
3.2.2 Five Week Biofilm Layers 70
3.2.3 Ten Week Biofilm Layers 76
3.3 Scaling the Roughness Function for Biofilm Layers 88
3.4 Relating Added Drag to Biofilm Characteristics 92
3.5 Chapter Summary 93

IV. Resistance of Rigid Replicas 97

4.1 Overview 97
4.2 Comparing the Resistance of Biofilms to Their Rigid Replicas 101
4.2.1 Five Week Biofilms and Rigid Replicas 101
4.2.2 Ten Week Biofilms and Rigid Replicas 110
4.3 Scaling the Roughness Function for Rigid Replicas 118
4.4 Characterizing the Added Drag of Rigid Replicas 120
4.5 Roughness and Compliance Contributions to Added Drag . . 122
4.6 Chapter Summary 124

V. Flow over Biofilms and Their Rigid Replicas 126

5.1 Overview 126
5.2 Mean Velocity Profiles 127
5.2.1 Five Week Biofilms and Rigid Replicas 127
5.2.2 Ten Week Biofilms and Rigid Replicas 136
5.3 Comparing Results from Flow and Friction 142
5.4 Chapter Summary 145

VI. Conclusions and Recommendations 147

6.1 Conclusions 147
6.1.1 Frictional Performance of Biofilm Layers 147
6.1.2 Scaling and Predicting Biofilm Resistance 148
6.1.3 Frictional Performance of Rigid Replicas 148
6.1.4 Scaling and Predicting Rigid Replica Resistance . . 149
6.1.5 Roughness and Compliance Contributions to Added Drag 149
6.1.6 Mean Flow Structure Over Biofilm Layers and Their Rigid Replicas 150
6.1.7 Contributions 150
6.2 Limitations and Recommendations for Future Research . . . 151
6.3 Concluding Remarks 152

BIBLIOGRAPHY 153

LIST OF FIGURES

Figure

1.1 Schematic showing important parameters and features of plane channel flow. . . . 5
1.2 Resistance curves for smooth wall, turbulent plane channel flow as determined by [47] show good agreement with the correlation proposed by [58]. . . . 6
1.3 Fully developed plane channel flow over smooth walls at $Re_\tau = 2000$ is shown using outer layer scaling [47]. . . . 7
1.4 Fully developed plane channel flow scaled using inner layer variables [47]. Note that the data points marked by the hollow triangle are the same as those shown in Figure 1.3. . . . 8
1.5 Structure of the mean velocity profile of an external turbulent boundary layer at high Reynolds number (figure from [25]; data from [38]). 9
1.6 Root-mean-square velocity fluctuations (Reynolds normal stresses) are non-dimensionalized by the friction velocity (a) show where turbulent motions peak in the flow over a smooth channel wall. Reynolds shear stress (b) characterizes the momentum transport after the viscous sublayer (reproduced from [22]; experimental data from [24]). . . . 10
1.7 Profiles of viscous shear stress and Reynolds shear stress for smooth wall, fully developed channel flow (reproduced from [40]; data from [22]). Note that the dashed lines correspond to lower Reynolds number flow than the solid lines. . . . 11
1.8 The roughness function, ΔU^+, captures the offset in the mean velocity profile that is experienced by rough surfaces in the log layer of the flow (reproduced from [10]). . . . 12
1.9 Scaling the roughness function, ΔU^+, with the equivalent sand grain roughness Reynolds number, k_s^+ collapses data from a wide variety of roughness types [10]. . . . 13
2.1 A microscope image of the biofilm mix grown at the University of Michigan for this study shows a range of organisms are present. . . 26
2.2 Chains of filamentous green algae ($\sim$1 μm thick) appeared to comprise a majority of the biomass. . . . 26

2.3 Solidworks® rendering of the biofilm growth loop. Soft biofilm was grown on acrylic test surfaces housed in canisters inside the growth sections. Flow control was provided by a large industrial pump, a chiller maintained the loop at 25° C and fluorescent lights surrounding the growth sections (not shown) provided illumination. The length of each growth section is a little over a meter. 27
2.4 Overhead photos of biofilm grown on acrylic test surfaces are recorded before, during, and after experimental trials in the SF3. Varying the incubation time for the panels resulted in biofilm coverage ranging from slight (a) to moderate (b) to significant (c). Sloughing did sometimes occur during growth as is evidenced by loss of the thick biofilm layer near the end of the panel shown in (c). In the images, flow moved from left to right during growth and trials and the panels are ∼1.14 meters in length. 29
2.5 A series of images taken during biofilm Trial 5W2 shows the evolution of biofilm coverage due to bulk sloughing. For each trial, images were collected just before changing the flow rate using a GoPro Hero 5 black mounted above the SF3. Subsequent analysis of these images provides several parameters quantifying areal coverage. 33
2.6 Pictures captured from an overhead camera (a) were cropped and binarized into black and white images (b). Binary images were then used to determine several areal characterization parameters and the average channel gap height, H_{AVG}, across the SF3 measurement region. The measurement region of the SF3 test section is roughly 50 cm in length (shown boxed in red). 34
2.7 A laser line scanner was mounted to a two-axis traverse system as pictured above. A thin laser line illuminates the profile of sandpaper mounted in a setup similar to the final installation below the SF3. . 35
2.8 MATLAB rendering of laser scan data (25.4 mm by 25.4 mm) recorded during trials of a test surface covered in 80 grit sandpaper. A very slight 'tilt' can be seen in the data which may be indicative of a small misalignment between the laser scanner and the SF3 test section. . 36
2.9 MATLAB rendering of surface topography as recorded by the laser scanner. Streamer heights have been magnified 4x to better show variations in elevation. the rendering is roughly 100 mm from top to bottom (although it is shown at a slight angle to better visualize the surface). 37
2.10 Binary image shows streamers with elevations above k_{rms} as black regions. Centroids (green dots) and bounding boxes (red squares) identify streamer location and dimensions. Note that the smallest regions have been excluded from the analysis. This binary image spans roughly 25 mm from top to bottom. 37

2.11 Pictured above is a portion of one 3D printed tile generated from laser scan data recorded during trials of a panel covered in live biofilm grown for ten weeks. Point cloud data from the scanner were meshed then printed using a Stratasys J750. As observed visually in the lab, the rigid replica geometry seen above appears to match the time-averaged, spatially filtered profile for the live biofilm (not shown) well. 39
2.12 Overhead photos show (a) the extent of biofilm coverage on an acrylic test panel covered in biofilm grown for ten weeks after experimental trials as well as (b) a 3D printed copy of the surface in (a) generated from laser scan data. 39
2.13 MATLAB renderings of laser scans collected for (a) a layer of ten week biofilm growth (Trial 10W6) and (b) its rigid replica (Trial 10W6RR). Note that scanner data were collected under similar flow conditions for both surfaces. Slight longitudinal and span shifts are observed in the renderings and are the result of an adjustment made to the laser scanning system location between trials. 40
2.14 The Skin Friction Flow Facility (SF3) is a closed channel water tunnel with a high-aspect ratio that has been previously used to evaluate superhydrophobic surfaces (SHS) and was modified for evaluation of surfaces covered in soft, filamentous biofilm. The test section is roughly 1.14 meters long, spans just over 100 mm, and has a nominal gap height of 7 mm. 41
2.15 Two-dimensional, two component (2D2C), planar PIV measurements were collected using a dual-pulsed Nd:YAG laser, CCD camera, and computer running DaVis 8.4. Images were recorded at five locations in span but only those from the centerline are presented in this work. 43
2.16 Images of the particle-laden flow field were recorded during experimental trials. The surface of a five week biofilm layer (and the strong reflections off it) is clearly visible in the above image. Pictures were collected at five spanwise locations and would later be used to perform planar, two component (2D2C) PIV. The image shown above is roughly 8.25 mm tall and 6.5 mm wide. 45
2.17 Vector fields were produced from frame pairs in 2D2C PIV. Both (a) instantaneous and (b) time-averaged vector fields were calculated. Spurious vectors are seen near the top boundary of the flow which result from reflections off biofilm streamers. The particle reflections off the bottom smooth wall are captured allowing precise determination of its location. Vectors in (a) are shown relative to the mean flow field to visualize flow features such as vortical structures. Figure dimensions are the same as in Figure 2.16. 46

2.18 The mean velocity profile across the channel (red data points) was used to determine an initial guess for the location where $y = 0$. The origin was chosen either where the value of the velocity was zero, or where data began (if a null velocity was not measured). In the case shown, the offset between the PIV FOV origin and initial $y = 0$ is $\sim$2.1 mm. 47
2.19 The effect of the wall offset, ϵ, on the velocity profile is seen in the figure above. A MATLAB routine found the line of best fit for inner-scaled velocity profile data in the log layer (the bounds are shown in purple and were assumed to be $y^+ = 30$ and $y/\delta = 0.3$ for this data set). 48
2.20 The schematic above shows the asymmetric boundaries in the SF3 and their affect on flow development. PIV data were used to determine the wall shear stress on the bottom (smooth) window via the Clauser chart method [53] which can then be used along with measurements of pressure drop and average channel gap height to determine the shear stress on the biofilm layer via Equation 2.5. . . 50
2.21 Measurements of a baseline smooth acrylic panel validate the method used to quantify frictional resistance of test surfaces and serve as a point of comparison for biofilm layers and rigid replicas. The correlation proposed by Zanoun *et al.* [58] (dashed line) is shown along with data calculated assuming symmetric walls (black squares) and corrected using PIV measurements (purple diamonds). 52
2.22 A panel covered in sand grain roughness shows a substantial ($\sim$110–185%) increase in drag compared to the smooth baseline. Data corrected for the asymmetric channel walls (orange diamonds) show a significant increase in added drag ($\Delta C_f \approx 160\%$) as compared to results reported which assume symmetric boundaries (light orange squares, $\Delta C_f \approx 90\%$). 53
2.23 The mean velocity profile of flow through the SF3 test section is shown using (a) outer layer and (b) inner layer non-dimensionalizations. The results from PIV match those of DNS at a similar value of Re_τ [33]. 54
2.24 Turbulent flow over roughened surfaces (in this case 80 grit sandpaper, orange diamonds) experiences a drag increase which can be seen in (b) by a shift in the location of the log-layer data. This shift is the roughness function, ΔU^+. The asymmetric surface conditions of the top ($(y + \epsilon)/\delta = 0$) and bottom ($(y + \epsilon)/\delta = 2$) walls in the SF3 is evident by the shift in maximum velocity toward the smoother wall (shown in (a)). 56

3.1 Trial 3W1 exhibited a very slight amount of sloughing. Resistance data in (a) show a drag increase of $\Delta C_f \approx 85$–110% and only a moderate amount of hysteresis. Overhead pictures in (b) show the extent of fouling coverage. The top image in the series corresponds to the data at the beginning of the trial and the bottom images shows the fouling at the trial's end. The fifth image from the top was recorded at the maximum flow speed at the conclusion of the evolving leg of the trial (just before the stable portion began). . . . 64
3.2 Trial 3W2 experienced severe sloughing. In (a) the drag increase begins at $\Delta C_f \approx 150\%$ but quickly drops to $\Delta C_f \approx 20\%$ then follows the trend seen for the smooth baseline. The maximum flow speed corresponds to the ninth image from the top in (b). 65
3.3 The panel with the least amount of fouling was evaluated in Trial 3W3. The added drag was roughly $\Delta C_f \approx 40\%$ as shown in (a). The panel experienced only a slight amount of sloughing as shown in (b). The peak flow speed was experienced in the sixth image from the top. Part of a clamp can be seen in the first two images which was later moved. Clamping is a precautionary measure used to keep the SF3 test section from expanding at elevated flow speeds. 66
3.4 Resistance data for Trial 3W4 (a) show $\Delta C_f \approx 120\%$ initially which decreased to $\Delta C_f \approx 60\%$ after sloughing. The seventh image from the top in (b) was recorded at the maximum flow speed. 67
3.5 Resistance data for Trial 3W5 resemble those seen in Figure 3.4 with $\Delta C_f \approx 130\%$ initially and $\Delta C_f \approx 65\%$ after sloughing. The seventh image from the top in (b) was recorded at the maximum flow speed. Note that the reflection of overhead fluorescent lighting seen near the leading edge of the panel did not affect calculation of the fouled area. 68
3.6 Severe sloughing occurred in the evolving leg of Trial 5W1 as seen in the resistance data (a) and overhead images (b). The fifth image from the top in (b) was recorded during the maximum flow speed. Note that the heterogeneity in surface condition during the stable portion of the trial may violate the assumption that flow is two-dimensional through the SF3 test section. 73
3.7 Only moderate sloughing occurred in Trial 5W2 which is reflected in a smaller hysteresis offset in the resistance data (a) between the evolving (right-pointing, light green triangles) and stable (left-pointing, dark green triangles) biofilm layers. The fourth images from the top in (b) was recorded during the maximum flow speed. Some sloughing continued after this as seen in the fifth image down (and also in the stable resistance data). Note that growth shown in (b) appears to be less uniform as compared to the other five week biofilm trials. . . . 74

3.8 Very little sloughing was observed in Trial 5W1 and the resistance data (a) for the evolving and stable biofilm layers lie on top of one another. The picture series in (b) has been compressed for display purposes but the limit of sloughing can still be observed. The ninth image from the top shows the biofilm layer after the maximum flow speed was achieved. 75
3.9 Resistance data (a) collected for Trial 10W1 do not show the hysteresis common in most other trials which also exhibited sloughing. Although the cause behind the lack of hysteresis is unknown it may related to the elevated values of k_{rms} and k_t seen in the stable portion of Trial 10W1. Overhead images in (b) show that the surface experiences a moderate amount of sloughing after the maximum flow speed was achieved (seen in the fourth image from the top in (b)). 79
3.10 The biofilm layer was thickest in Trial 10W2 which also shows the greatest drag penalty, ΔC_f, as seen in (a). Overhead photos (b) show that sloughing was limited to the downstream half of the panel. The eighth panel from the top in (b) corresponds to the maximum achieved flow speed. 80
3.11 The biofilm layer investigated in Trial 10W3 appears significantly different from most examined in this work as can be seen visually in (b). Despite the apparent differences in layer formation, the frictional behavior (a) appears quite similar to what was observed in other trials. Note that the eighth image from the top was captured while the panel was exposed to the maximum achieved flow speed. 82
3.12 A modest Reynolds number range and relatively significant Reynolds number dependence were displayed in Trial 10W4 resistance data (a). Sloughing was relatively subdued as evidenced by the photo series in (b). Sloughing appeared to occur even after the maximum flow speed was recorded in the fifth image down as the seventh image down in (b) shows loss of the biofilm layer. Despite this, the stable resistance data appear unaffected. 83
3.13 Nearly the entire biofilm layer was lost in Trial 10W5 as shown by the resistance data (a) and overhead photos (b). The rapid loss of biofilm results in a substantial increase in Re_H. The eighth photo from the top in (b) was recorded at the maximum flow rate. The portion of a support clamp which is visible (top, left) did not affect estimation of the fouled area since it was upstream of the measurement volume. 86
3.14 A very slight amount of bulk sloughing was observed in Trial 10W6 (similarly to Trial 5W1). The result is relatively steady, Reynolds number independent resistance data in (a). Trial 10W6 was performed prior to installation of an overhead camera in the SF3, but before and after photos (b) were taken which show the extent of sloughing (or lack thereof). 87

3.15 Several previously proposed correlations between roughness parameters and the roughness function, ΔU^+, were explored using the data collected in this dissertation. While it does not appear to completely collapse the data, the correlation proposed by Schultz *et al.* [49] provides reasonably good collapse. 89
3.16 After a slight adjustment to the constant in k_{eff}, stable biofilm data appear to collapse relatively well and show Colebrook-type behavior. This is in contrast to many types of roughness which align better with the formula set forth by Nikuradse. 90
3.17 A least squares regression derived the optimal fit of stable biofilm data with a Π grouping (Equation 3.3) which contains the fouled area, A_b and non-dimensional mean biofilm thickness, k_b. Data for nearly all the stable biofilm layers fall within the 95% confidence interval for the suggested linear fit Equation 3.4. Note that H_o was used to non-dimensionalize k_b because the mean biofilm layer thickness is used to calculate the average channel gap height, H_{AVG}. 92
4.1 Resistance data for the evolving biofilm in Trial 5W1 (right-pointing triangles; overhead picture shown in (b)) are compared with data for a rigid replica (upward-pointing blue triangles; shown in (c)) of the surface scanned at $Re_H \approx 6500$ (shown in solid red). The data show substantial differences in the magnitude of C_f indicating that both roughness and compliance effects are important in drag production. 103
4.2 A closeup shows the texture of the rigid replica evaluated in Trial 5W1RR. A dense patchwork of small streamers can be observed. Note that the image shown here was taken at an angle to show better contrast between streamers which was not accounted for by the shown scale bar. 104
4.3 The frictional behavior of Trials 5W2 and 5W2RR shows similar offsets between biofilm and rigid replica data with $\Delta C_{f,\,soft} = 43.2\%$. The large uncertainty bounds make it difficult to determine if the slight decrease in added drag due to compliance is the result of differences in the biofilm layer. The biofilm shown in (b) and rigid replica in (c) had good agreement in surface coverage which is difficult to visualize from the yellow coloring of the rigid replica. 105
4.4 A closeup shows the texture of the rigid replica evaluated in Trial 5W2RR. A flash camera was used to better illuminate surface texture since the yellow color causes 'flat' lighting conditions. Note that the image shown here was taken at an angle to show better contrast between streamers which was not accounted for by the shown scale bar. 106

4.5 Two rigid replicas were produced from data collected in Trial 5W3. As shown here, biofilm resistance data (left-, right-pointing triangles) and data from corresponding rigid replicas (upward-, downward-pointing blue triangles) show consistent behavior in $\Delta C_{f,\,soft}$ and Reynolds number dependence. Although some deviation is seen at low Reynolds numbers between Trial 5W3RRe (upward-pointing blue triangles) and Trial 5W3RRs (downward-pointing dark blue triangles), the data agree well near the scanned flow speed ($Re_H \approx 13\,700$). Overhead images in (b)–(e) show the sloughing which occurred over Trial 5W3 and also demonstrate that the rigid replicas accurately capture areal coverage. 107

4.6 A close-up shows the texture of the rigid replica evaluated in Trial 5W3RRe. A dense patchwork of small streamers similar to those of Trial 5W1RR can be observed. Note that the image shown here was taken at an angle to show better contrast between streamers which was not accounted for by the shown scale bar. 108

4.7 A portion of the rigid replica evaluated in Trial 5W3RRs. Since the picture was taken near the same location as in Figure 4.6, specific streamers can be found which are duplicated between the two trials . Note that the image shown here was taken at an angle to show better contrast between streamers which was not accounted for by the shown scale bar. 109

4.8 Trials 10W2 and 10W2RR show a compliance drag penalty of $\Delta C_{f,\,soft} = 40.4\%$. Rigid replica data (shown as upward-pointing blue triangles) show little Reynolds number dependence which is contrary to data collected for the evolving biofilm layer (right-pointing green triangles). Comparison of $\Delta C_{f,\,soft}$ is made at the scanned condition (solid red right-pointing triangles). 112

4.9 A portion of the rigid replica evaluated in Trial 10W2RR. Streamers were particularly elongated for this thickest of the biofilm layers. Note that the image shown here was taken at an angle to show better contrast between streamers which was not accounted for by the shown scale bar. 113

4.10 Resistance data are shown for Trials 10W4 (right-pointing light green triangles) and 10W4RR (upward-pointing blue triangles). The compliance drag penalty at the scanned condition (right-pointing red triangles) was $\Delta C_{f,\,soft} = 46.9\%$ which was the highest of any ten week trials. 114

4.11 A portion of the rigid replica evaluated in Trial 10W4RR. The surface shows particularly sharp contrast between large streamers and the surrounding biofilm unlike what was observed for the rigid replica evaluated in Trial 10W2RR. Note that the image shown here was taken at an angle to show better contrast between streamers which was not accounted for by the shown scale bar. 115

4.12 Resistance data for a stable biofilm layer (left-pointing green triangles) and its rigid replica (downward-pointing dark blue triangles) are shown above. Despite the fact that the data correspond to a stable surface condition, and that different methods were used to find the bulk mean velocity, U_m, the compliance drag penalty was similar to what was measured for the other ten week trials ($\Delta C_{f,\,soft} = 36.4\%$). 116
4.13 A portion of the rigid replica evaluated in Trial 10W6RR. Sloughing shows the thickness of the biofilm layer and surface streamers are partiularly well visualized by this slightly darker green color. Note that the image shown here was taken at an angle to show better contrast between streamers which was not accounted for by the shown scale bar. 117
4.14 An equivalent roughness length scale, k_{RR}, provides a partial collapse of ΔU^+ for the rigid replica data. It is difficult to tell if the scatter remaining is due to uncertainty in the estimates of k_t and λ_x or if a key roughness parameter in drag production remains missing. . . . 119
4.15 The empirical relationship defined in Equation 4.4 consistently captures the drag penalty for rigid replicas, $\Delta C_{f,\,RR}$. Within uncertainty, all measured data correspond with the 95% confidence interval for Equation 4.3. 120
4.16 Applying the empirical formulas which characterize the rigid replica drag penalty shows that compliance effects are important in drag production of biofilm layers. 122
5.1 Mean velocity profiles for Trials 5W1 and 5W1RR show that the biofilm layer experiences a greater drag increase. The biofilm data (green circles) also appear to display 'near-viscous' behavior in the region of flow immediately adjacent to the wall while data for the rigid replica (blue triangles) exhibit fully rough behavior. Biofilm flow data also appear to show an increased 'wake' region in the outer layer flow. 128
5.2 Velocity defect profiles for Trials 5W1 and 5W1RR show that outer layer flow over the biofilm surface deviates somewhat from those measured for the smooth baseline and rigid replica. 129
5.3 Mean velocity profiles derived from PIV data collected during Trials 5W2 and 5W2RR show similar behavior with what can be observed in Figure 5.1. Note that one difference is the slight, wake region of flow observed in the rigid replica data shown in (a). The inner-scaled mean velocity profiles between rigid replica and soft biofilm exhibit strikingly similar behavior in the log-layer and beyond. 130
5.4 Outer layer similarity is observed for the flow the surfaces evaluated in Trials 5W2 and 5W2RR. This is in contrast to what was observed for Trials 5W1 and 5W1RR. The reason for the difference is not known but may be due to the specific features of the local topography above the PIV field of view. 131

5.5 Flow over the biofilm layer in Trial 5W3 shows somewhat different near-wall behavior than was observed for the other trials with a slow increase in ΔU^+ until the log-layer is reached. Rigid replica data for Trial 5W3RRe also have slightly different behavior but the reasons behind the difference are unknown. 132
5.6 Outer layer similarity appears to hold for the smooth baseline, rigid replica, and biofilm surfaces in Trials 5W3e and Trial 5W3RRe. The data begin to diverge around $(y + \epsilon)/\delta = 0.3$. 133
5.7 Mean velocity profiles captured during Trials 5W3 and 5W3RRs are shown above using outer (a) and inner (b) scaling. Flow over the rigid replica examined in Trial 5W3RRs appears to be somewhat different than that for Trial 5W3RRe (Figure 5.5) despite replicating the same panel (but for evolving and stable conditions). The asymmetry shown in (a) for the stable rigid replica appears to be slighter than was seen for the evolving replica and the stable replica also does not show a wake-like flow region although the evolving replica did. 134
5.8 In contrast to what was observed for the evolving data, the velocity defect profiles in Trials 5W3s and 5W3sRR do not appear to exhibit particularly similar outer layer flow. As the flow over the biofilm layers in Trials 5W3e and 5W3s appears to collapse tolerably well with the smooth baseline data, this is likely due to differences in the manufacturing process used between the Trials 5W3RRe and 5W3RRs. 135
5.9 Flow data collected during Trial 10W2 and 10W2RR show peculiar features in the near-wall region as an inflection point can be seen which is not generally observed for flow data from the other ten week trials. Significant differences in flow structure can be seen between the biofilm layer and its rigid replica in the outer layer of flow as well. These are likely due to differences in local topography and the relatively small separation in surface roughness and outer flow length scales. 137
5.10 Velocity profiles from Trials 10W2 and 10W2RR show significant differences with one another and the smooth baseline. This is likely due to differing local topography and the small separation in surface roughness and outer length scales. 138
5.11 The mean velocity profiles for Trials 5W4 and 5W4RR show similar behavior in both (a) and (b). A surprisingly similar level of asymmetry is seen in (a) while the behavior of the flow over the rigid replica closely mimics that for the biofilm layer, albeit at a lesser offset in ΔU^+. Note that the near-wall behavior between the two surfaces does not agree which is typical. 139

5.12 The relatively good collapse of velocity defect profile data in Trials 10W4 and 10W4RR stands in contrast to what was observed for Trials 10W2 and 10W2RR. It is difficult to know whether the difference is due to the scale separation between surface roughness and outer flow length scale or differences in manufacturing for the two rigid replicas. 140
5.13 Flow data for Trials 10W6 and 10W6RR show fairly strong differences as compared to the other trials. The lack of 'viscous sublayer-like' flow in the region just above the biofilm layer is likely due to the use of a geometric mask in PIV analysis which was not used for the other trials. Strong reflections off the rigid replica's surface are likely the cause of the peculiar flow in the near-wall region above it. 141
5.14 Collapse of the velocity data for Trials 10W6 and 10W6RR is relatively good considering the large separation in Re_τ values among the flow over the three surfaces. The departure seen between the biofilm and rigid replica flow data in the middle of the curves may be an artifact of the procedure used to find the wall offset, ϵ. 142

LIST OF TABLES

Table

1.1	Rough wall flow regimes and their bounds	14
1.2	A selection of recent biofilm studies	18
2.1	Comparison of 80 grit sandpaper roughness	55
3.1	Matrix of biofilm experiments	59
3.2	Results summary for three week biofilm trials	61
3.3	Results summary for five week biofilm trials	71
3.4	Results summary for ten week biofilm trials	77
3.5	Comparison of predicted and measured biofilm resistance (for cases with rigid replica data)	93
4.1	Results summary for rigid replicas and the biofilm layers to which they correspond	98
4.2	Differences between biofilm and rigid replica frictional behavior and surface features	99
4.3	Comparison of predicted and measured biofilm resistance (for cases with rigid replica data)	121
4.4	Measured and predicted added drag contributions due to softness and roughness	123
5.1	Results summary for rigid replicas and the biofilm layers to which they correspond	144

ABSTRACT

The presence of significant hard and soft biofouling on the hull of a marine vessel can produce increased resistance potentially limiting system performance and leading to added fuel consumption. It has been estimated that the presence of biofouling has led to roughly $2.9 billion in additional operating costs and the resulting excess fuel consumed each year is expected to introduce about 23 million tons of carbon dioxide into the atmosphere [1]. Therefore, it is important to understand how biofouling leads to increased friction drag for flows over marine surfaces with the ultimate aim of reducing their deleterious effects.

While a body of research exploring the consequences and means of drag production for hard fouling exists which informs the efforts of ship designers and operators, the effects and drag production mechanisms of soft fouling remain relatively unexplored. The few studies performed on soft biofilm layers show drag increases ranging from ∼10–300% in lab scale experiments [4, 35, 43, 49]; ship trials showed that after removal of a biofilm layer from its hull, a frigate required 18% less shaft power to maintain a cruising speed of 25 knots [17]. That such large drag penalties can be produced by low-form, 'slimy' surfaces is a surprising result which researchers suggest may be due to additional physical mechanisms different from those of hard biofouling.

The primary objective of this dissertation was to disassociate the added drag produced by filamentous biofilm layers into contributions from roughness and compliance effects. Biofilm layers comprised of diatoms and filamentous green algae were grown on smooth acrylic surfaces for nominal incubation times of three, five, and ten weeks in a specially built flow loop. During hydrodynamics trials, biofouled surfaces were installed in a high-aspect ratio, fully developed channel flow facility and exposed to flows ranging from $Re_H \approx 5\,000 - 30\,000$. Measurements of the pressure drop along each fouled panel revealed drag increases spanning $\Delta C_f \approx 14$–364%. The wide range in drag penalty was linked to variations in flow speed, average thickness of the biofilm layers, and the percentage of each surface covered by fouling. These results support a previously proposed scaling correlation which also relates frictional performance of biofilm layers to their thickness and coverage. Empirical formulations were produced that characterized the added drag of stable biofilm layers within ±10% of their

measured values.

Seven rigid surfaces replicating six biofilm layers were manufactured using highly resolved laser scans of the time-averaged, spatially filtered biofilm surface profiles. Drag penalties of $\Delta C_f \approx 57$–193% were measured for these rigid surfaces and shown to scale with the average trough-to-peak roughness height and downstream spacing between large streamers. An empirical formula characterized the added drag on rigid replicas to within $\pm 15\%$ of measurements.

Finally, a simple model was proposed which decomposes the added drag experienced by a biofilm layer into contributions from roughness and compliance effects. Once applied to this model, resistance data show that about half of the added drag experienced by the biofilm layers was due to rough effects.

Particle Image Velocimetry measurements captured the mean flow along the surfaces. Results reveal that flow above biofilm layers and rigid replicas largely resemble one another in the outer flow region suggesting that mechanisms underlying the drag increase are confined to a region of flow in the immediate vicinity of the biofilm layers.

CHAPTER I

Introduction

1.1 Motivation

Biofilms are ubiquitous and affect fields ranging from medicine and health care to energy production and shipping. As such, the consequences of biofouling affect our well-being; both directly—through the spread of infections and illness—and indirectly—by inhibiting the performance of engineered systems such as heat exchangers, offshore platforms, hydropower generators, and ships. One of the best known—and perhaps the first recognized examples of biofouling—is the accumulation of 'slime, weed and shell' on the hull of a ship [52]. The presence of hard, calcareous organisms such as mussels or barnacles and soft biofilm layers comprised of algae and bacteria below the waterline of a vessel increases the resistance it experiences [17, 29, 46, 52]. This drag penalty leads to additional fuel consumption and pollution, and decreases vessel top speed and range [17, 45, 52].

The full costs of biofouling are not exactly known, but attempts have been made to quantify the magnitude of the impact on shipping. [45] examined the expense of fuel, hull coatings, hull coating application and removal, and hull cleaning for an *Arleigh-Burke* class destroyer (DDG51) in a study which estimated the cost of biofouling for the U.S. Navy fleet. Assuming the direct cost of distillate fuel marine—DFM—to be \$104.16 per barrel and the indirect cost to be \$59.93 per barrel, the authors estimated the U.S. Navy fleet-wide annual cost due to hull fouling at between \$180M−\$260M for typically observed fouling ratings (FR-30) and \$400M−\$500M if the rating falls in the upper band for previously identified fouling (FR-60). Note that these projected expenses are driven primarily by the increased fuel consumption and will vary with the cost of fuel and according to powering characteristics (e.g. conventional or nuclear power).

Cost estimates of biofouling for the world fleet have not been performed recently, but an in-depth cost-benefit analysis of tributyltin self-polishing copolymer (TBT-SPC) paints was performed in 1989 and 1996 to show their efficacy before an upcoming world-wide ban of organotin biocides by the International Maritime Organization (IMO) [1]. The authors of the study considered annual savings derived from TBT coatings in four main areas: added fuel, fuel related overhead expenses, reduced dry-docking, and added shipping that would have otherwise been required to transport the added fuel. Assuming the cost of fuel to be $100 per ton and that TBT-SPC coatings provided 4% fuel savings (from decreased frictional resistance), the authors estimated that world-wide savings in these four categories amounted to $730M, $800M, $1080M, and $304M respectively, for a total annual savings of roughly $2.9B. While new fouling mitigation strategies have been pursued since the implementation of the IMO ban in 2003, it is reasonable to assume that—with the increase in the price of marine fuel oil—the yearly economic cost of biofouling on maritime shipping remains in the billions of dollars.

The environmental impacts of biofouling are also substantial. A complete ban of organotin biocides was instituted by the IMO in 2003 as a response to studies showing that the release of toxins from TBT coatings on ship hulls affects the development and reproductive processes of marine life, especially planktonic organisms and mollusks [1, 2]. While regulation has addressed this particular threat to marine species, ship emissions continue to pollute the environment. The study performed by [1] estimated that in the early 1990s, TBT-SPC coatings reduced emissions from the world fleet by roughly 23 million tons of carbon dioxide and around 750 thousand tons of sulfur dioxide annually. New biofouling mitigation strategies have been implemented since the IMO ban which provide fuel savings, but the environmental effects of biofouling remain significant.

Beside substantial economic and environmental consequences associated with the biofouling of a ship hull, the operational capabilities of the vessel may be diminished. Full scale ship trials of a *Knox* class frigate (*USS Brewton*) were performed which measured the shaft power required for the ship to cruise at a speed of 25 knots before and after cleaning of a light microbial fouling layer [17]. The authors observed that the *Brewton* required 18% less shaft horsepower to maintain a speed of 25 knots and that the maximum speed the frigate could reach increased by one knot after cleaning a moderate biofilm layer from its hull. The reduction in ship performance due to biofouling can also lead to delays in shipping, more frequent stops, or—in extreme cases—compromise the safety of the ship and crew.

Given the enormity of these consequences, it is not surprising that humans have endeavored throughout history to mitigate the problem of ship hull fouling [9]. Two types of coatings provide the means to passively limit biofouling: 1) biocidal 'antifouling' (AF) paints and 2) non-biocidal 'foul release' (FR) coatings. Prior to the 1990s, toxic AF coatings dominated the commercial shipping sector with TBT-SPC delivering unparalleled performance until a 2003 IMO ban on the application of these coatings. After 2003, increased focus was turned to silicone and fluoropolymer FR coatings which had become more economically practical. While current AF paints and FR coatings have proven largely effective against calcareous macrofouling, their efficacy in controlling soft microfouling (e.g. biofilms) remains relatively poor—particularly for slower vessels and those that spend more time in static conditions (e.g. pleasure craft).

Ultimately, only active cleaning of a vessel's hull can keep it free of soft biofilm layers. Hull husbandry practices must balance the cost in added fuel and increased transit time arising from marine biofouling with the need to maintain a high-activity ship schedule. Expenses relating to cleaning and reapplication of an antifouling coating are equivalent to roughly 1-2 months' operating profit not including the opportunity cost of the days out of service [1]. For ship operators like the United States Navy, time in service can be as—or more—important than economic considerations; however, the detriment of biofouling on ship capabilities still motivates a need for periodic cleaning. Whatever the driver, vessel operators need to balance the ship schedule with hydrodynamic performance which requires understanding the frictional performance of biofilm covered surfaces. In particular, common parameters characterizing a biofilm layer should be linked to its hydrodynamics and the means of biofilm drag production discovered. Armed with this knowledge, ship designers and operators can develop better hull husbandry practices and inform models which evaluate the hydrodynamic performance of a ship.

1.2 Background

Many of the consequences of biofouling mentioned in the previous section are due to an increase in frictional resistance that results from its presence. While those in the naval community have understood this for centuries, relatively few efforts have been undertaken to systematically study the fundamental physical processes which lead to increased friction and drag on fouled vessels. Of the studies that have examined the hydrodynamic consequences of biofouling, most evaluate the performance

of antifouling or foul release coatings; only a handful have sought to focus on the physical mechanisms by which fouling leads to increased drag. While the evaluation of mitigation strategies is a pressing issue, understanding the fundamental drag production processes for calcareous (i.e. 'hard') and compliant (i.e. 'soft' biofilm) fouling will better enable ship builders to predict the hydrodynamic impact of biofouling on ships and inform mitigation efforts.

1.2.1 Wall-bounded Turbulent Flows

As a ship pushes through water it generates turbulent shear flow over its hull producing frictional drag through the creation of a velocity gradient and the exchange of momentum by low and high speed fluid. This is just one example of the wall-bounded turbulent flows which are ubiquitous in flow applications. Fully developed pipe flow, fully developed plane channel flow, and the zero-pressure-gradient turbulent boundary layer (ZPG-TBL) are three canonical flows that have been the subject of a vast number of studies which have greatly informed current understanding of turbulent flow [47]. Fluid dynamicists now have an in-depth understanding of these canonical flows when the boundaries are smooth, and knowledge of rough-wall effects is rapidly growing for rigid roughness; but, characterization of the flow over and forces on soft, compliant surfaces (such as biofilm) remains lacking.

The challenges of measuring and simulating turbulent flow over compliant surfaces are significant and require the development of new tools and techniques for both experimentalists and numericists. In the following paragraphs, a brief summary of current understanding for wall-bounded turbulent flows over smooth and rough walls will be discussed before reviewing prior hydrodynamic studies of biofouling. This will familiarize the reader with basic concepts such as the determination of the coefficient of friction (C_f), inner and outer scaling, the law of the wall, the roughness function (ΔU^+), and effective sand grain roughness height (k_s) which are needed to understand theories of biofouling drag production.

1.2.1.1 Flow over Smooth Walls

The explanation of fundamentally important concepts describing turbulent flow over smooth walls provided below is necessarily brief. However, as the topic has a long and rich history, many resources exist for further study; primary references used here include books by Kundu, Cohen, and Dowling [25], Pope [40], and White [56, 55] as well as several articles [31, 38, 47, 50, 58].

Figure 1.1 is a schematic showing important parameters in plane channel flow. In this illustration, fluid of uniform velocity U_e enters a channel of height H beginning at $x = 0$. As flow progresses downstream, boundary layers develop along the channel walls having a thickness, δ, which grows as flow develops downstream. Eventually, the boundary layers reach a maximum thickness equal to the channel half-height, h, at a development length, L_h, and the flow is considered to be fully developed with a mean velocity profile, $u(y)$, that is only a function of the distance to the walls, y. While the form of the velocity profile does not change significantly once flow becomes fully developed, its shape will depend on whether the flow is laminar or turbulent. As the flows studied in this dissertation are turbulent, all remaining results and discussion will focus only on turbulent flows.

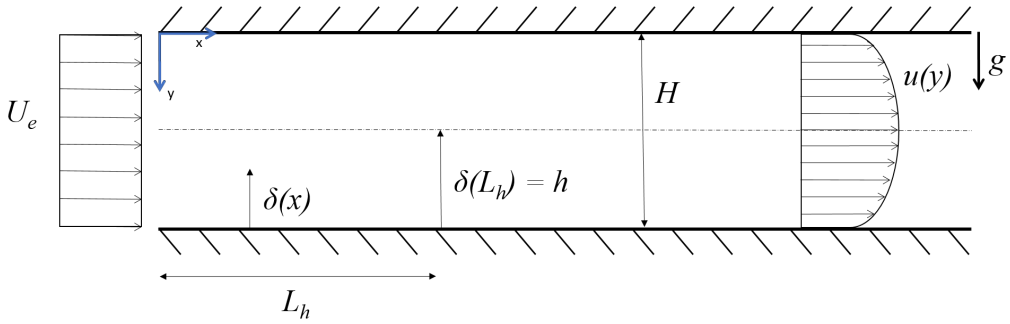

Figure 1.1: Schematic showing important parameters and features of plane channel flow.

Performing a control volume analysis for the fully developed portion of Figure 1.1 yields a simple equation relating shear stress experienced by the walls, τ_w, to the pressure drop along the channel length, $\frac{dp}{dx}$.

$$\tau_w = -\frac{H}{2}\frac{dp}{dx} \tag{1.1}$$

If the average velocity through the channel, U_m (the 'bulk mean velocity'), is known, a coefficient of friction, C_f, can be defined which characterizes the frictional resistance experienced by the channel walls.

$$C_f = \frac{\tau_w}{\frac{1}{2}\rho U_m^2} \tag{1.2}$$

The coefficient of friction for turbulent channel flow is a fundamental parameter used extensively by naval architects, engineers, and modelers to predict system performance and it is clear from Equations 1.1 and 1.2 that it can be determined for smooth wall, plane channel flow assuming only four simple parameters are known

[55]. Figure 1.2 displays the coefficient of friction as a function of Reynolds number, $Re_H = Re_m = \frac{U_m H}{\nu}$, where ν is the kinematic viscosity of the fluid.

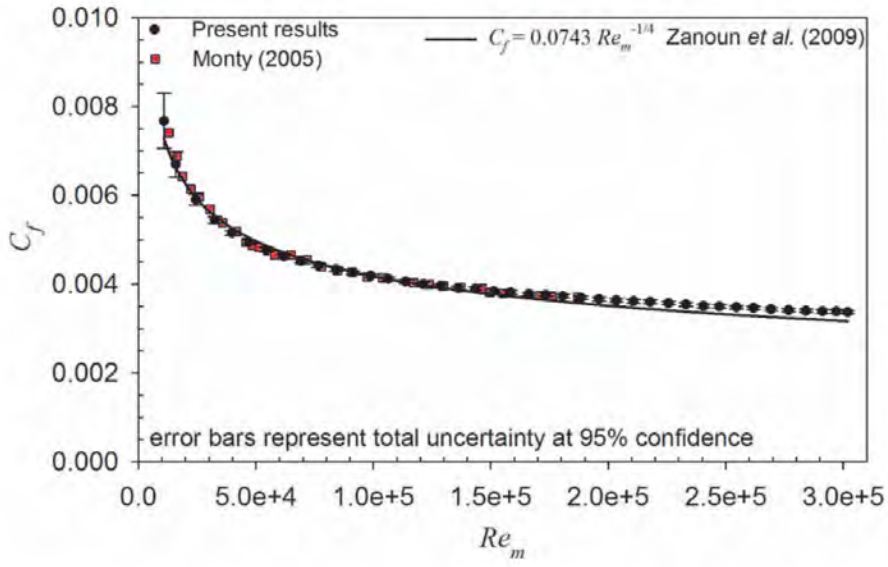

Figure 1.2: Resistance curves for smooth wall, turbulent plane channel flow as determined by [47] show good agreement with the correlation proposed by [58].

A deeper understanding of the fundamental physical processes responsible for drag production requires more than determining the frictional behavior of flow through a channel via a global parameter such as the coefficient of friction—flow field structure must also be known. Figure 1.3 shows the mean velocity profile of fully developed flow through a smooth plane channel [47]. In this figure, the axes are made dimensionless using the centerline velocity, U_{CL}, and channel half-height, h, which are the relevant outer scales. Note that while the velocity profile increases gradually in the core flow near the centerline of the channel (where $y = h$), a region of strong shear exists near the channel walls. In this high-shear region friction at the channel boundaries influences the flow heavily and the dynamics which characterize the flow shift. Rather than using outer layer scales which are representative of the largest flow features, new scales are needed which describe the smallest motions of the flow.

Figure 1.4 displays mean velocity profiles for the same fully developed channel flow using inner layer scaling to non-dimensionalize the data [47]. This detailed look into the high-shear region of the flow near the channel walls shows where frictional effects dominate and flow motions decay to small, inner layer scales defined using parameters such as the fluid viscosity, ν, and wall shear stress, τ_w. These inner layer scales are known as the friction velocity, $u_\tau \equiv \sqrt{\tau_w/\rho}$, and viscous length scale,

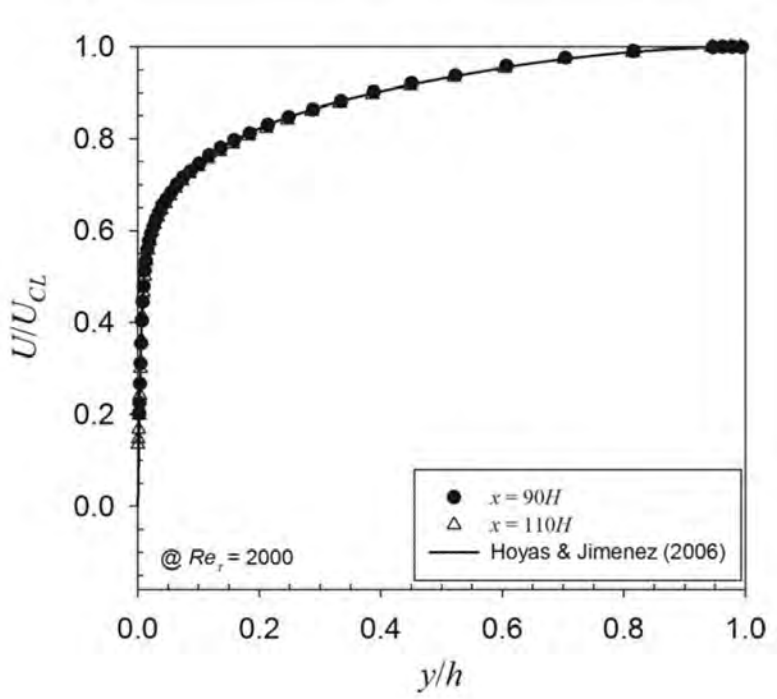

Figure 1.3: Fully developed plane channel flow over smooth walls at $Re_\tau = 2000$ is shown using outer layer scaling [47].

$l_\nu \equiv \nu/u_\tau$. Another important parameter is the friction Reynolds number, $Re_\tau = \frac{u_\tau \delta}{\nu}$. Also known as the von Kármán number, Re_τ compares the outer and inner scales of the flow (in this case, δ is the channel half-height). Note that in Figure 1.4, data corresponding to the case of $Re_\tau = 2000$ are the same data which are plotted in Figure 1.3.

This duality of scales is a defining feature of wall-bounded turbulent flows which puzzled early students of the field. However, in the 1930s Theodore von Kármán and Ludwig Prandtl provided key insights which led to the development of one of the most important concepts in boundary layer theory—the logarithmic law of the wall [25]. Using the simple power of dimensional reasoning, [21] and [41] observed that the velocity profile of turbulent flow over boundaries was comprised of an inner layer in which viscous shear dominates, an outer layer in which turbulent shear dominates, and an overlap region where both types of shear are important and the profile smoothly connects the inner and outer regions [56]. The result of this analysis is the logarithmic law of the wall (known commonly as the log-law) which is shown in Equation 1.3.

$$U^+ = \frac{1}{\kappa} \ln y^+ + B \tag{1.3}$$

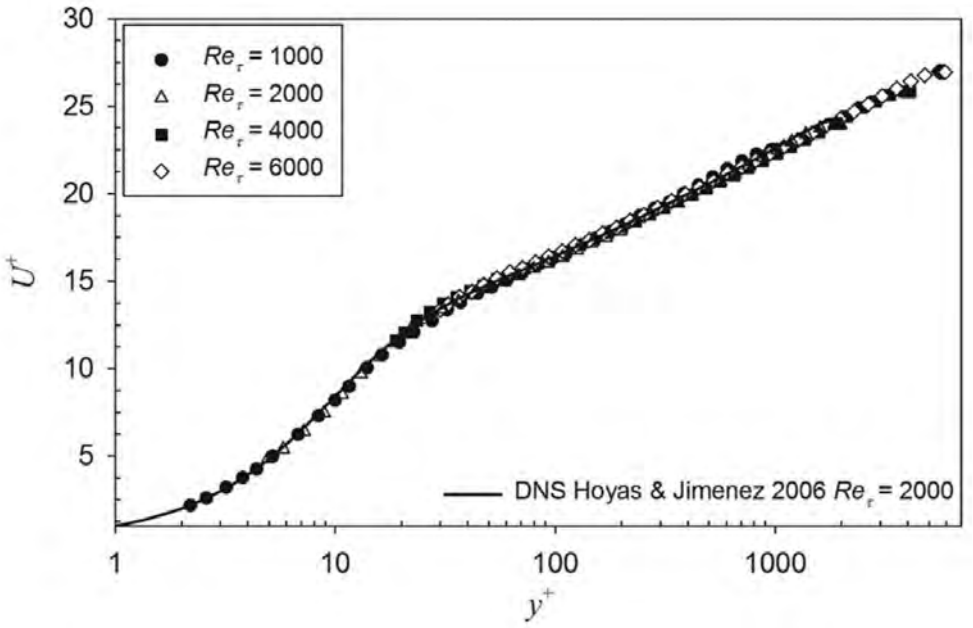

Figure 1.4: Fully developed plane channel flow scaled using inner layer variables [47]. Note that the data points marked by the hollow triangle are the same as those shown in Figure 1.3.

Here $U^+ = u/u_\tau$ and $y^+ = y/l_\nu$ represent the dimensionless average streamwise velocity and wall-normal distance from the wall scaled using inner layer variables (denoted by the '+' superscript). The log-law characterizes the mean velocity profile of flow over a smooth, flat boundary accurately using only two universal values—the von Kármán constant, κ, and the wall offset, B. Although some debate remains as to the exact value of these constants (typical values of κ range from 0.38 to 0.42 and B ranges from 4.5 to 5.5) and whether they are truly 'universal', the log-law remains an established result used extensively by ship designers and engineers throughout the field.

While the law of the wall is a useful approximation of flow near a smooth boundary, it does not fully describe the structure of a turbulent boundary layer. Figure 1.5 shows mean velocity profiles of high Reynolds number flow over an external boundary layer with several regions of the flow labeled [25].

In this figure, the flow is divided into the inner layer and outer layer mentioned in the preceding paragraph. These two layers are further subdivided into four regions: the viscous sublayer, the buffer layer, the logarithmic layer, and the wake [25]. The viscous sublayer is the region of flow where turbulent fluctuations are strongly dampened due to the close proximity of the wall and influence of viscosity. This region of

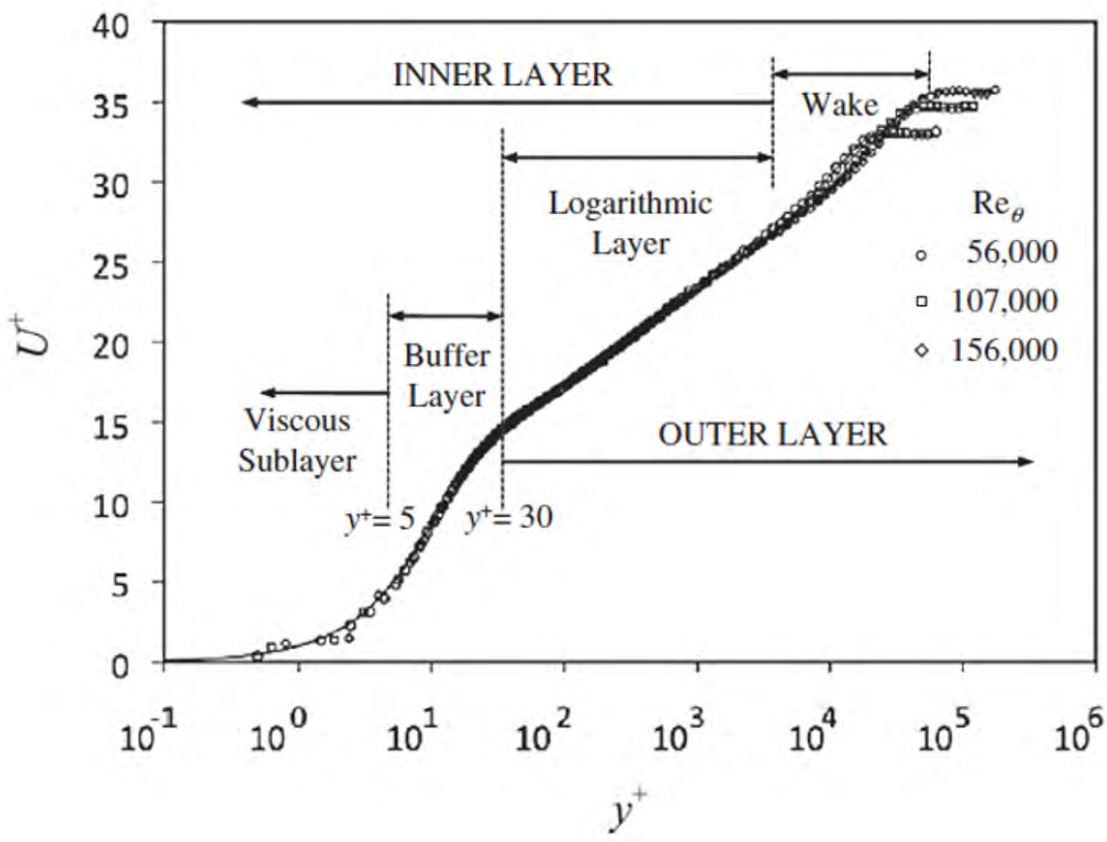

Figure 1.5: Structure of the mean velocity profile of an external turbulent boundary layer at high Reynolds number (figure from [25]; data from [38]).

the flow is typically very thin ($y^+ < 5$) and the mean velocity profile here is linear with $U^+ = y^+$. The viscous sublayer transitions to the buffer layer farther from the wall. The buffer layer spans a relatively small range of $y^+ = 5$ to $y^+ = 30$, yet it is in this region that turbulence production peaks and the flow is neither linear nor logarithmic. The inner layer of the flow ends—and the outer layer begins—with the logarithmic layer which has already been discussed. For smooth walls, the logarithmic layer typically begins at $y^+ = 30$ and extends to roughly $y/\delta = 0.3$.

The final region of the flow shown in Figure 1.5 is the wake. Development of the wake region depends on the pressure gradient of the flow as favorable pressure gradients ($\frac{dp_e}{dx} < 0$) suppress deviations from the logarithmic layer and adverse pressure gradients ($\frac{dp_e}{dx} > 0$) quickly cause significant departure from the log line. Note that as Figure 1.5 is scaled using inner variables, flow data no longer collapse in the wake region (which scales with y/δ) [25]. Figure 1.5 helps describe the structure of the mean flow in a turbulent boundary layer (TBL) but can be deceptive when consider-

ing the physical scales of the flow. Since the plot is shown in log-linear coordinates, the inner layer appears to occupy a significant portion of the flow; however, in reality it is confined to a relatively small section of the boundary layer making up ∼30% of the flow. Although the inner layer may constitute only a small portion of the flow, its effects on the development of turbulence and drag is significant.

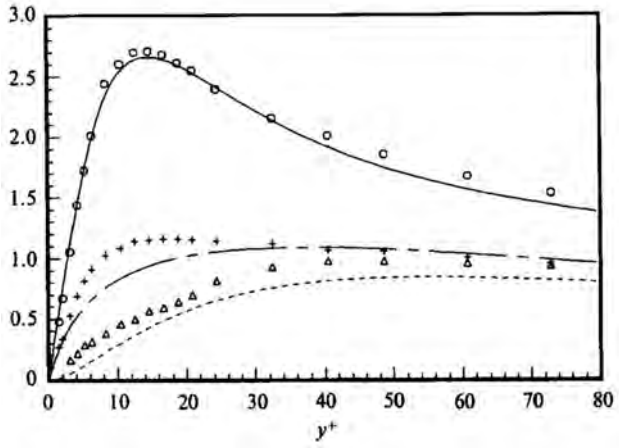

(a)

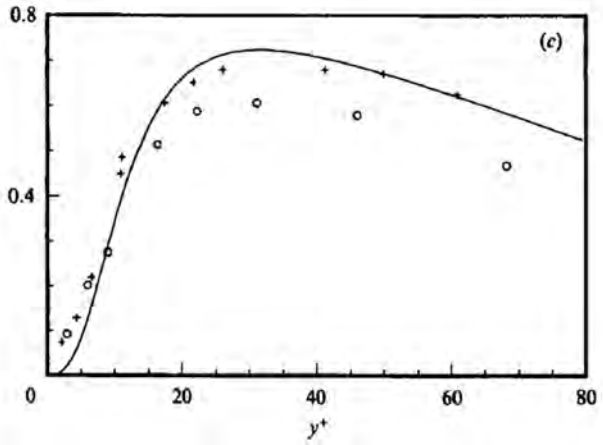

(b)

Figure 1.6: Root-mean-square velocity fluctuations (Reynolds normal stresses) are non-dimensionalized by the friction velocity (a) show where turbulent motions peak in the flow over a smooth channel wall. Reynolds shear stress (b) characterizes the momentum transport after the viscous sublayer (reproduced from [22]; experimental data from [24]).

The dynamical importance of inner layer flow results from turbulent motions in the buffer layer. Figure 1.6 shows the Reynolds stresses in the near-wall flow with $y^+ \leq 80$ (reproduced from [22]). Both the streamwise ($\sqrt{\overline{u'^2}}/u_\tau$, open circles; solid

line) and wall-normal ($\sqrt{\overline{v'^2}}/u_\tau$, plus symbols; long dashed line) Reynolds normal stresses peak at $y^+ \approx 15$ indicating that turbulence is greatest just after the viscous sublayer. It follows that the Reynolds shear stress ($-\overline{u'v'}/u_\tau^2$, solid line) also peaks at this location as shown in Figure 1.6b.

The relationship between flow behavior and drag production is clearly delineated in Figure 1.7 which displays the distribution of shear stress in fully developed, smooth wall channel flow [40]. In the region immediately above the wall, the no slip condition and influence of viscosity conspire to keep flow laminar and momentum transport occurs by viscous diffusion; however, the influence of viscosity diminishes rapidly and turbulent motions dominate momentum transport for the remainder of the flow.

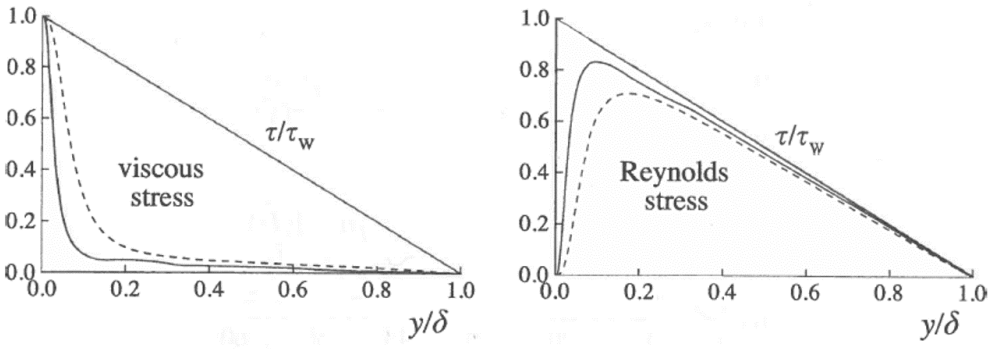

Figure 1.7: Profiles of viscous shear stress and Reynolds shear stress for smooth wall, fully developed channel flow (reproduced from [40]; data from [22]). Note that the dashed lines correspond to lower Reynolds number flow than the solid lines.

The drag experienced by walls bounding fully developed channel flow can be determined using just four key parameters—fluid density, ρ, channel gap height, H, bulk mean velocity, U_m, and the pressure drop along a length of the channel, $\frac{dp}{dx}$—to derive a coefficient of friction, C_f. While this characterizes the frictional performance of a given surface, such global measurements do not furnish detailed information about the fundamental physical processes underlying the drag production. These are determined by local, highly resolved measurements of the velocity field from the surface bounding flow to the outermost regions of the domain.

1.2.1.2 Flow over Rough Walls

Perhaps surprisingly, much of the theory presented above remains applicable to most rough wall flows and accurate representation of the mean velocity profile in the logarithmic layer requires only an additional offset term, ΔU^+, which is known as

the roughness function [11, 20, 51]. Thus, for most rough surfaces the law of the wall becomes:

$$U^+ = \frac{1}{\kappa} \ln y^+ + B - \Delta U^+ \tag{1.4}$$

This result is immediately evident in Figure 1.8 which shows how the mean flow over rough walls departs from smooth wall behavior [46]. It is also clear that the magnitude of the offset is determined by the degree of roughness—captured by the equivalent sand grain roughness Reynolds number, $k_s^+ \equiv k_s/l_\nu$. For those cases shown with $k_s^+ > 9.2$ the effect of the roughness is sufficiently significant to prevent the formation of the viscous sublayer and buffer layer.

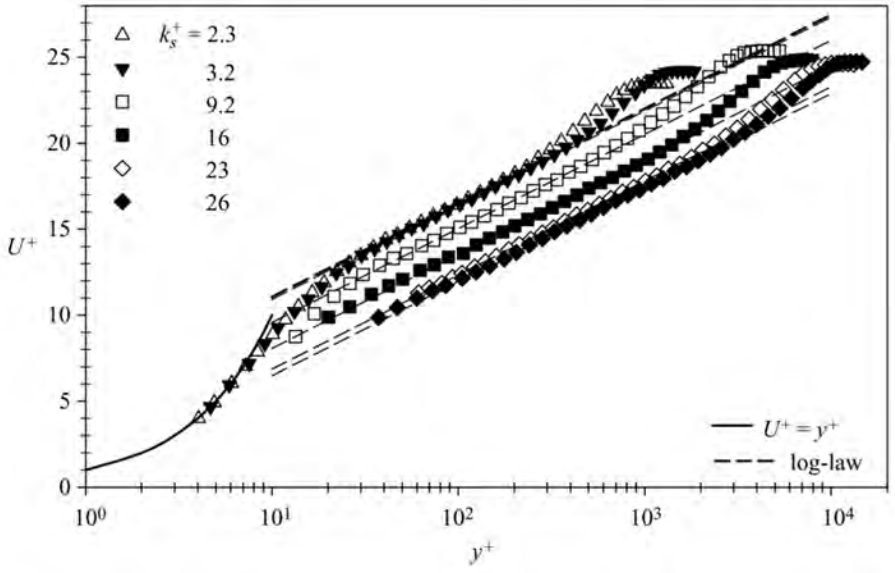

Figure 1.8: The roughness function, ΔU^+, captures the offset in the mean velocity profile that is experienced by rough surfaces in the log layer of the flow (reproduced from [10]).

The equivalent sand grain roughness Reynolds number, k_s^+, and its dimensional counterpart, the effective sand grain roughness height, k_s, are particularly useful in classifying the hydrodynamic performance of a large variety of rough walls. Figure 1.9 shows the relationship between the roughness function and k_s^+ for various roughness types. Three distinct regions of the plot can be identified: 1) a range where $k_s^+ > 70$ and good collapse is seen for all types of roughness, 2) a small range below $k_s^+ \approx 5$ where the roughness is small and smooth wall behavior is seen, and 3) a transition region between the two. These regions are known as the fully rough, hydraulically smooth, and transitionally rough regimes and are summarized in Table 1.1.

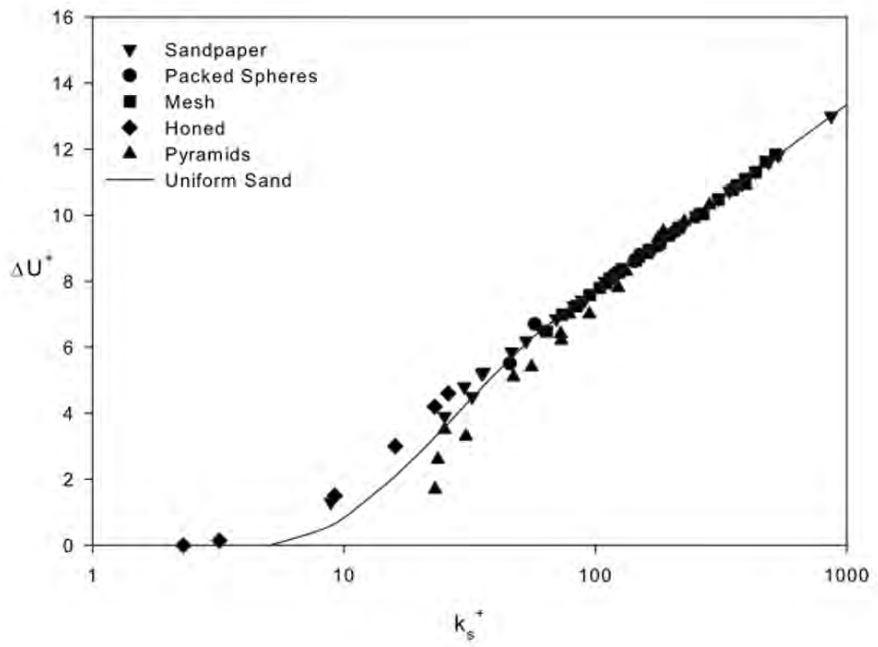

Figure 1.9: Scaling the roughness function, ΔU^+, with the equivalent sand grain roughness Reynolds number, k_s^+ collapses data from a wide variety of roughness types [10].

While some debate remains regarding the precise bounds of these roughness regimes, it is clear that roughness effects relate to both the physical length scales associated with the roughness features and the scales of the boundary layer over the wall [13]. Hydraulically smooth flow appears to occur when the equivalent roughness is at or below the height of the viscous sublayer leaving the buffer layer and logarithmic layer intact. In the transitionally rough regime, the roughness nears the scale of the buffer layer causing the viscous sublayer to deteriorate [39]. When this occurs the wall shear stress, τ_w, depends on both viscosity, ν, and the roughness scale, k. Finally, as the roughness protrudes above the buffer layer and into the log layer, pressure drag on surface features dominates drag production and the wall shear stress loses its dependence on ν. When flow over the rough wall reaches this final state a surface is considered to be fully rough.

As seen in Figure 1.9, a strong correlation exists between the roughness function and equivalent sand grain roughness Reynolds number in the fully rough regime. The relationship between ΔU^+ and k_s^+ is given by:

$$\Delta U^+ = \frac{1}{\kappa} \ln k_s^+ + B - B_N \tag{1.5}$$

Table 1.1: Rough wall flow regimes and their bounds

Flow Regime	**Roughness Range**
Hydraulically Smooth	$k_s^+ < 5$
Transitionally Rough	$5 < k_s^+ < 70$
Fully Rough	$70 < k_s^+$

where B_N is the Nikuradse roughness function ($\approx$8.5 for fully rough flow, see [30]). While Equation 1.5 provides a means to relate the hydrodynamic performance of a wide variety of roughness types, it does not allow the roughness function corresponding to a general surface to be determined directly from physical measures of the roughness. Instead, the hydrodynamic performance of a rough surface can only be known once evaluated under a set of flow conditions. Ideally, designers would be able to determine the frictional resistance and flow behavior of rough surfaces from one or two parameters describing the most relevant aspects of the roughness. Therefore, it is common for researchers to propose scaling correlations relating parameters such as roughness height, k, spacing, λ, density and shape, Λ, etc. with an effective sand grain roughness height, k_s (covered thoroughly in [10]).

Once a reasonably accurate value for k_s has been obtained for a given roughness, and the viscous length scale, l_ν, is known, ΔU^+ can be predicted. Then, the coefficient of friction for the rough surface may be determined indirectly from:

$$\Delta U^+_{Granville} = \sqrt{\frac{2}{C_{f,\,smooth}}} - \sqrt{\frac{2}{C_{f,\,rough}}} \tag{1.6}$$

where C_f is evaluated at the same relevant Reynolds number (i.e. $Re_\tau = \frac{u_\tau \delta}{\nu}$). Using Equation 1.6 to derive the roughness function from resistance data is sometimes called the Granville method and assumes that flow in the outer layer is similar between the smooth and rough surfaces (i.e. that they display outer layer similarity) [14].

1.2.1.3 Effects of Surface Compliance on Flow and Friction

Although this dissertation focuses on the effects of surface roughness, the biofilm layers studied are compliant and a brief summary of the effect compliant surfaces have on flow—and the friction thereby experienced—is provided. Further discussion of the general topic is provided in review articles by [7] and [16].

Investigations of drag on, and flow over, compliant surfaces typically focus on the

potential of flow-induced surface instabilities (FISI) to decrease drag. Working off the observation that dolphins are able to swim at speeds greater than expected when considering their muscular power output, [23] postulated that the compliant nature of dolphin skin produced drag reduction and performed experiments using a model towed behind an out-board motor boat, claiming that a dolphin skin-like layer of composite rubber achieved drag reductions of up to 50%. The promise of compliant surface drag reduction prompted several follow on studies which were unable to replicate Kramer's findings; however, continued investigations provided deeper insight revealing that flow is quite sensitive to the compliance of the coating and careful optimization is required when attempting to modulate flow using compliant layers [16].

Subsequent efforts have shown that drag reduction by compliant coatings can occur by either delaying the transition from laminar to turbulent flow, or, through favorable interactions between the deforming surface and turbulent flow above it. [7] reviews several studies and claims that it may be possible to maintain laminar flow to indefinitely high Reynolds numbers through the use of multiple panel compliant walls (which would require careful tuning of compliance parameters). [26] investigated the near-wall flow structure of a ZPG-TBL over a single-layer compliant surface and observed the appearance of intermittent 'laminarization-like' phenomena which thickened the viscous sublayer and buffer region providing a reduction in the streamwise turbulence intensity and reduction in the local C_f. Although an exact link between surface compliance and drag production (or reduction) has not been found, it is clear that compliant layers can interact with flow in ways that rigid surfaces cannot. Note that most compliance studies have focused on smooth compliant surfaces and that the extension of previous findings to biofilm layers with roughness is problematic.

1.2.2 Resistance of Biofilms

1.2.2.1 Calcareous Fouling

Both calcareous, hard biofouling and compliant, soft biofilms can lead to a substantial increase in the frictional resistance experienced by a ship [3, 29, 44, 45, 52]. However—perhaps due to the magnitude of the increase in resistance—drag production by calcareous fouling organisms has been more widely studied and is better understood [49, 52]. If basic fouling geometry is known, the added resistance due to the presence of mussels, barnacles, and other calcareous fouling organisms on a ship hull may be predicted [44]. According to Townsin, surfaces with rigid roughness having a trough-to-peak height less than 230 μm (in the transitionally rough regime

for most ships), the drag penalty (ΔC_f) can be calculated according to:

$$1000\Delta C_f = 44\left[\frac{AHR}{L}^{1/3} - 10Re_L^{-1/3}\right] + 0.125 \tag{1.7}$$

given a ship length, L, average hull roughness, AHR, and a ship Reynolds number, Re_L [52].

The drag penalty due to calcareous fouling may also be determined if a representative roughness length scale is known using a roughness function such as that given by Grigson [15]:

$$\Delta U^+_{Grigson} = \frac{1}{\kappa}\ln(1 + k^+) \tag{1.8}$$

$$k = 0.059R_t(\%\text{ barnacle fouling}) \tag{1.9}$$

where R_t is the height of the largest barnacles and k is the roughness length scale proposed by Schultz [44]. Here k is seen to be a function of the largest roughness elements and extent of fouling covering the ship hull. Schultz [44] showed that this proposed correlation provides an excellent collapse of his data demonstrating that knowledge of hard fouling geometry and fouled area alone can accurately predict the drag penalty for a surface covered in calcareous fouling. Both Equation 1.7 and 1.8 suggest calcareous fouling acts much like many types of rigid roughness in the fully rough regime where form drag provides the primary contribution to added resistance.

1.2.2.2 Soft Fouling

Studies of soft microfouling are less frequent than those concerning hard fouling and the drag production mechanisms of compliant biofilms remain poorly understood. This is likely due to the fact that 1) calcareous fouling typically results in a higher drag penalty so understanding it has been a more pressing practicality and 2) the compliant nature of soft biofilms complicates the determination of key parameters and boundary conditions making experiments and simulations difficult to perform. For instance, developing scaling relations which correlate the drag penalty experienced by a surface to its condition (e.g. roughness geometry) is difficult because the profile of the biofilm changes with the flow around it and researchers have not been able to measure the biofilm surface *in situ* but have had to take measurements of the wet surface in air before or after trials have been performed. These measurements are used to derive common roughness parameters such as the root-mean-squared and

trough-to-peak roughness height (k_{rms} and k_t, respectively) which may be significantly skewed. It is difficult to determine many parameters characterizing hydrodynamic performance due to biofilm compliance, its complex geometry, and the fact that it interacts with the nearby flow.

Despite these challenges, research examining the hydrodynamic performance of biofilms has steadily accumulated providing researchers with more data to develop and test theories of soft fouling drag production. Table 1.2 shows a summary of several recent investigations into soft fouling. While previous studies stretch across a wide variety of biofilms and research methods, many follow a similar approach.

Establishing consensus across studies of biofilm can be difficult given the vast range of living, highly adaptable biofilm species and morphologies available for study. However, common findings have been reported. Firstly, the vast majority of studies have found that the presence of biofilm on a surface exposed to flow leads to an increase in drag (see Table 1.2) with a few notable exceptions. Andrewartha and her co-authors mention that in trials of a very light, uniform cover of biofouling, a lower local skin friction coefficient was found than for the hydraulically smooth case suggesting that drag *reduction* was observed for an establishing freshwater biofilm [3]. In a 1995 study, Lewandowski and Stoodley caution the use of Nuclear Magnetic Resonance Imaging in small biofilm reactors to image flow, positing that for low flow rates biofilm formation appears to decrease drag by smoothing channel walls [27]. Note that these exceptions either examined low flow or very light fouling conditions which is not the case in most studies. While researchers agree that the presence of biofilm increases drag, findings suggest that the wide variation in the magnitude of added resistance appears to depend on flow speed, duration of growth, surface coverage, and base surface roughness. These confounding factors likely complicate efforts to link the roughness function or drag penalty to roughness parameters [49, 54].

Table 1.2: A selection of recent biofilm studies

Source	**Biofilm Type**	**Flow Environment**	**Added Drag (ΔC_f, ΔU^+, etc.)**
Haslbeck & Bohlander [17]	microbial biofilm	rotating disk, ship trials	ΔC_f = 0–30%(disks), 8-18% power decrease after hull cleaning
Lewandowski & Stoodley [27]	filamentous biofilm	channel, low Re_H	$\Delta C_f \sim 200\%$
Schultz & Swain [48]	marine biofilm	ZPG TBL	ΔC_f = 33–187%
Schultz [43]	filamentous algae	ZPG TBL	ΔC_f = 110–125%, $\Delta U^+ \approx$ 10–12
Andrewartha *et al.* [5]	artificial biofilm (array of evenly spaced wool threads)	ZPG TBL	$\Delta U^+ \approx 0$
Andrewartha *et al.* [3]	freshwater slime with filaments	ZPG TBL	ΔC_f = 8–68%
Ng & Walker [36]	single artificial filament (wool thread)	ZPG TBL	N/A
Walker *et al.* [54]	freshwater slime with filaments	ZPG TBL	$\Delta C_f = 160\%$
Schultz *et al.* [49]	diatomaceous slime with filaments	channel	ΔC_f = 14–70%
Hunsucker *et al.* [19]	biofilm and calcareous organisms	rotating disk	ΔC_f = 150–442%
Yeginbayeva *et al.* [57]	slime with filaments (grown in lab and on vessel at sea)	ZPG TBL	ΔC_f = 7–81%
Murphy *et al.* [35]	diatomaceous slime with filaments	ZPG TBL	$\Delta U^+ = 12.8$

Investigation into flow field statistics provides further insight into the mechanisms driving soft biofouling drag production. Description of the flow over and around biofilms is typically provided using either point-wise techniques such as Laser Doppler Anemometry (LDA) or whole-field methods such as Particle Image Velocimetry (PIV). From these measurements the average velocity profile and higher order turbulent statistics are calculated and compared to those obtained for smooth walls and rigid roughness. Researchers generally agree that the mean TBL structure over biofilms behaves similarly to that seen over rigid roughness. Murphy *et al.* performed detailed investigations of the flow field above a smooth surface covered uniformly in biofilm grown for ten weeks and observed that the mean velocity profile showed similar structure to what has been observed for rigid roughness [35]. Further evidence that the mean velocity profile above biofilm layers matches that for turbulent flow over rigid roughness is provided by several studies including those by Andrewartha & Sargison, Schultz, Schultz & Swain, and Walker *et al.* [4, 43, 48, 54].

While researchers have generally found the mean TBL flow structure over biofilm layers to resemble that seen for rigid roughness, deviations have been observed for artificial biofilm streamers [5, 28, 36]. Three investigations performed by a research team at the University of Tasmania (UTAS) examining flow over artificial biofilms which exhibited notable differences are of particular interest. A 2008 study examined the flow field around an array of artificial wool streamers roughly 80 mm in length that were spaced 100 mm apart on a regular grid. The authors found that the mean velocity profile and turbulence intensity showed no deviation from the hydraulically smooth case when the flow field was measured in the region between the evenly spaced streamers. However, when the measurement location was moved to be immediately behind a streamer, a stronger wake region was observed in the mean TBL structure and the turbulence intensity was higher in the region of flow corresponding to the maximum outward extent of streamer motion [5]. A follow-up study performed by researchers from the same group in 2012 confirmed that both the mean velocity profile and turbulence structure are significantly altered in the region of flow near a streamer [36]. However, a 2010 study only partially confirmed these findings when examining flow over a staggered array of wool streamers. In this work, the authors found that the mean velocity profiles measured downstream of the artificial streamers behaved similarly to that seen for a smooth wall—other than having the expected shift corresponding with roughness effects, ΔU^+—while the turbulence structure was significantly altered by the streamers [4].

Considering the proximity of a flow field measurement location to a streamer may

help to explain these apparently contradictory findings. It may be expected that wall-bounded flow in the immediate vicinity of a large surface-normal obstruction (relative to the smallest flow scales) will deviate from what has been observed for smooth surfaces. This appears to be the case for several instances in the University of Tasmania studies which show that when the flow measurement location is in the immediate vicinity of a wool streamer the mean velocity profiles and turbulence structure are disrupted. However, when measurements are collected farther from streamers the mean flow structure behaves similarly to the hydraulically smooth case while the higher-order turbulent statistics still exhibit sensitivity to disruptions in the flow.

Although these results pertain to a relatively sparse collection of artificial wool streamers, it is possible that the scenario explains flow features seen in the study by Murphy *et al.* [35] who observed that in the outer layer of the TBL over a biofilm layer, Reynolds stresses matched those for a smooth baseline surface. However, velocity measurements in the near-wall layer showed significant differences as compared to the smooth wall baseline. Firstly, the sharp peak in streamwise Reynolds normal stress seen for smooth wall flow was suppressed in the biofilm velocity profile. Additionally, the peak in wall-normal Reynolds stress and Reynolds shear stress were elevated, shifted away from the biofilm bed, and sharper in shape than what was observed for the smooth baseline case. Murphy and her fellow researchers theorized that small scale turbulent structures which correspond to local topography and are not seen for smooth walls or rigid roughness might be present in the near-wall region of flow. Considering this statement along with theory postulated to explain the UTAS findings, it is likely that turbulent motions in the outer layer flow are driven by shear phenomena while flow in the immediate vicinity of features such as streamers may be altered according to local interactions.

Knowing that measurements of the flow field over biofilm covered surfaces bear remarkable similarities to those observed for walls covered in rigid roughness and that scaling correlations have been employed with some success for different types of rigid roughness, researchers naturally search for correlations between the roughness function, ΔU^+, and measures of biofilm surface roughness. However, finding the appropriate parameters relating biofilm characterization to hydrodynamic performance is not straightforward as several studies have found the equivalent sand grain roughness height k_s for biofilms is greater than any physical measurement of the biofilm roughness [3, 34, 54]. It may be that the compliant nature of the biofilm provides additional sources of energy dissipation. In particular, Walker *et al.* [54] report that the outsize effective roughness may be due to the vibration of algae filaments present

in the biofilm and/or vibrations of the low form gelatinous 'mat' portion of the biofilm layer.

Despite these complications, efforts to relate biofilm coverage and hydrodynamic performance have been undertaken. A particularly relevant study by Schultz *et al.* [49] presents the scaling correlation:

$$k_s \approx k_{eff} \approx 0.055 k_b (\% \text{ biofilm coverage})^{\frac{1}{2}} \tag{1.10}$$

which relates mean biofilm thickness, k_b, and the extent of fouling coverage to the roughness function. This correlation bears a strong similarity to the one Schultz [44] proposed for calcareous fouling which showed excellent collapse (Equation 1.9 above). Schultz *et al.* [49] note that for surfaces exhibiting fully rough behavior (i.e. Reynolds number independence) this correlation appears to scale their data fairly well but that collapse is not observed for cases which do not demonstrate fully rough behavior. Furthermore, it is worth noting that the proposed correlation does not include any parameters characterizing compliance; yet, manages to predict the roughness function. This may suggest that—at least in some cases (i.e. for fully rough biofilm layers)—the role of compliance is diminished compared to roughness effects. It is possible—given the vast variety of biofilm morphologies—that prior findings cover both the transitionally rough and fully rough regimes resulting in confusion over the role played by compliance and rigid roughness resistance mechanisms such as form drag.

As the preceding paragraphs demonstrate, knowledge of drag on and flow over soft fouling has progressed over the past century. Researchers have shown that the presence of soft biofilm fouling on walls bounding turbulent shear flow often leads to significant increases in drag. Evaluation of the flow field over and around living biofilm and artificial substitutes suggests that while variation in the near wall region of flow may be unique to biofilm layers, the structure of turbulence for the outer layer of the flow closely resembles that seen for walls covered in rigid roughness. Yet practical differences from most types of rigid roughness remain as calculations of the effective sand grain height, k_s, suggest that compliance and motion in the biofilm layer may play an important role in the development of shear stress in the near wall flow region. Evidence from the studies mentioned above has led to compelling theories suggesting that biofilm drag production may be due to traditional rigid roughness mechanisms and/or as yet unknown compliance effects (including those arising from mat and streamer motions). Further research is needed to confirm and expand the understanding of biofilm drag production gained thus far. Scaling relations and em-

pirical formulas describing biofilm drag production will advance models and enable naval architects and engineers to better predict the effects of biofilm on system performance.

1.3 Contributions

Current understanding of biofilm drag production mechanisms is limited to theories suggested by flow field features and relatively little work has been performed to discover the relationship between biofilm structure and drag development. The primary goal of this work is to determine the contributions of 'rough' and 'compliant' drag production mechanisms by comparing the hydrodynamic performance of compliant biofilms with rigid replicas having the same time-averaged, spatially filtered surface profile. To meet this goal, new facilities and novel experimental techniques and analysis procedures were developed. A biofilm growth loop capable of producing relatively consistent biofilm layers on test panels was designed and constructed at the University of Michigan's Marine Hydrodynamics Lab, a scanning system was developed to capture the biofilm surface profile while subject to flow, and a procedure was developed to generate 3D printed rigid replicas from scans of the living biofilm. To the best of the author's knowledge, no prior study has measured the surface of a biofilm under flow or attempted to decouple the relative contributions of rough drag production mechanisms (i.e. from form drag and surface friction) from compliance effects (i.e. motion and vibration of the biofilm layer).

The work presented in the following chapters examines the role of roughness drag in the overall resistance of a surface covered in soft biofilm by evaluating the frictional performance of live biofilms grown in the lab and rigid counterparts of select biofilm trials. Chapter One has introduced basic concepts of wall-bounded turbulence and summarized the findings of prior biofouling studies which are needed to better understand the results of this work. Chapter Two provides a detailed description of the facilities and experimental methods used to grow biofilms on test surfaces and evaluate their hydrodynamic performance. In Chapter Three, the frictional resistance of biofilms and several parameters characterizing biofilm structure are quantified and compared before attempts to relate biofilm structure and flow conditions with the added drag a surface experiences are discussed. Frictional performance of rigid replicas and the contributions from roughness and the effects of compliance are presented in Chapter Four while Chapter Five explores the flow field measured for select biofilm layers and the rigid replicas which correspond to them. Finally, Chapter Six sum-

marizes the major findings of this work and suggests several avenues of study for future investigation. It is hoped that findings presented in this dissertation will help quantify the contributions of roughness and compliance in biofilm drag production, inform current drag-predictive models, and help researchers chart the path of future studies into soft biofouling.

CHAPTER II

Methodology

2.1 Overview

Investigating the hydrodynamic performance of biofilm fouling typically follows a procedure which consists of three key steps. Firstly, researchers must grow biofilm on test surfaces either in their native environment or—more commonly—in a growth tank/flow loop. Secondly, after a period of growth development, the hydrodynamic performance of the fouled surfaces is determined using either full scale or lab trials. Finally, a description of the biofilm studied is given which often includes the extent and thickness of the coverage as well as biofilm composition and other characterization parameters. The following sections of this chapter provide a detailed description of the methods used to investigate the mechanisms underlying drag production of surfaces covered in soft biofouling. In Section 2.2 the design and operation of a recirculating loop used to grow biofilm layers on smooth test panels will be described. Section 2.3 outlines the measurements and analysis used to characterize the biofilm layers before, during, and after hydrodynamic trials. Next the process used to develop rigid replicas of select biofilm trials via 3D printing will be detailed in Section 2.4. Section 2.5 covers the facility and measurements used to evaluate the hydrodynamic performance of panels covered in live fouling and rigid replicas corresponding to select biofilm trials. In Section 2.6 details of the planar (two-dimensional, two component—2D2C) particle image velocimetry (PIV) setup are discussed. Finally, several measurement challenges and their potential solutions are discussed in Section 2.7 before validation results for baseline smooth and rough surfaces are given in Section 2.8.

2.2 Growing Biofilm

A wide variety of organisms are present in the biofilms attached to marine vessels and investigating the full extent of morphologies and species is impossible. Researchers typically chose to either limit the scope of investigation to a single, reasonably well controlled biofilm consisting of a mixture of species or, rarely, perform full scale sea trials using whatever vessel is at their disposal. As most researchers do not have access to a ship (or flexible in-service time to schedule sea trials), it is encouraging that at least one study has demonstrated that the frictional performance of soft biofilms grown in the lab show no major differences in frictional behavior to those grown at sea [57].

Growing biofilms in a laboratory provides researchers with the ability to investigate phenomena that may otherwise be inaccessible and provides some modest means to control growth—a process which is already highly variable in nature. The biofilm layers grown in this study were cultivated from a diatomaceous sample provided by Prof. Michael Schultz of the United States Naval Academy (USNA). Originally collected from a rubber panel which had been exposed in the Indian River Lagoon near Sebastian Inlet, Florida, USA for about four and a half years, the sample contained diatoms from four genera: *Amphora, Achnanthes, Entomoneis* and *Navicula* [49]. Microscopic images taken of samples from the growth loop at the University of Michigan revealed that these diatoms are present along with an unidentified filamentous green algae and zoo plankton (example images shown in Figures 2.1 and 2.2). Although anecdotal and not systematically examined, it is worth noting that the number of diatoms seen in microscope images appeared to vary as this work progressed. The reasons for this variation are not known, but it is possible that the green algae thrive in the brighter conditions experienced at the start of a growth cycle while diatoms flourish beneath the layer of filamentous green algae where flow is slower and less light penetrates.

Cultivating a healthy biofilm mix comprised of diatoms and filamentous green algae requires lighting, nutrients, and sea water (or an appropriate seawater substitute). Temperature and flow control are also necessary to replicate conditions similar to those experienced by a marine vessel. Bearing in mind these considerations, biofilm was cultivated on smooth, acrylic test surfaces in a custom-built growth loop (shown in Figure 2.3).

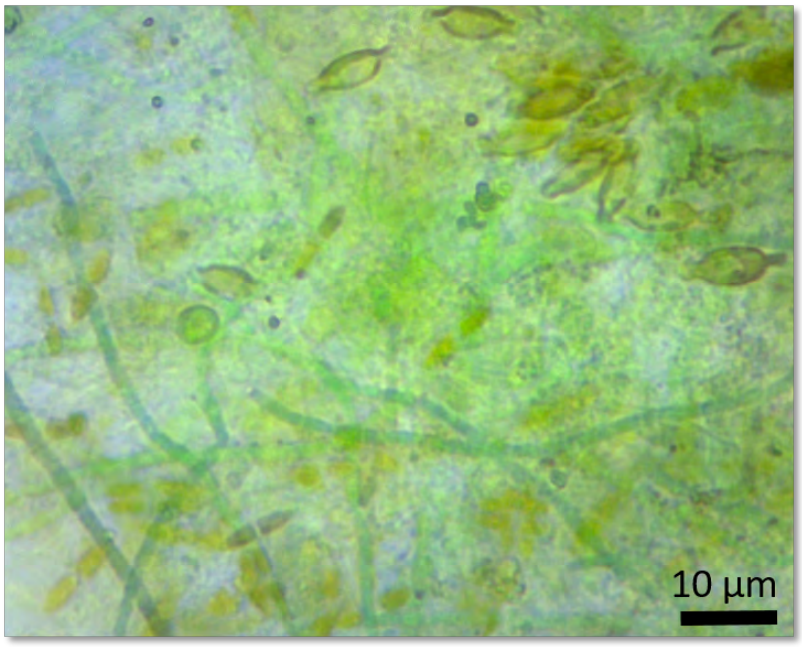

Figure 2.1: A microscope image of the biofilm mix grown at the University of Michigan for this study shows a range of organisms are present.

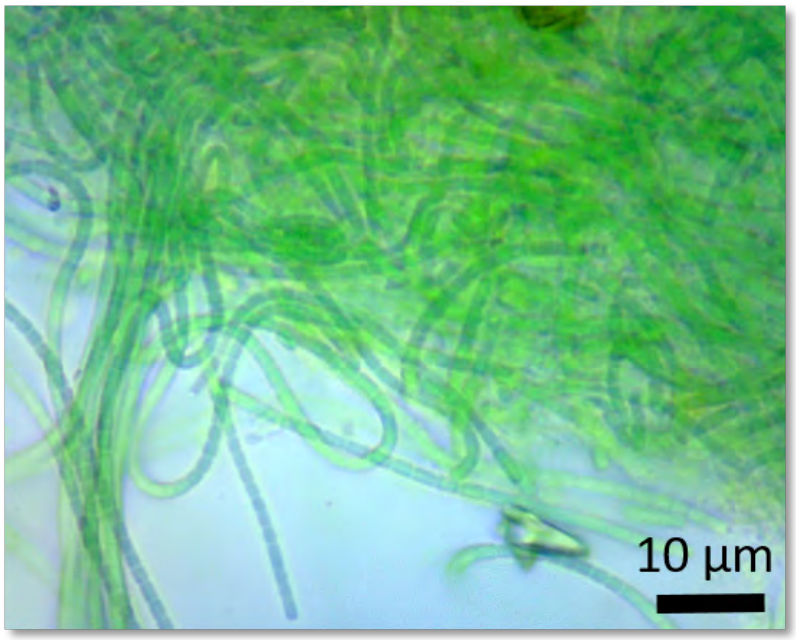

Figure 2.2: Chains of filamentous green algae ($\sim$1 μm thick) appeared to comprise a majority of the biomass.

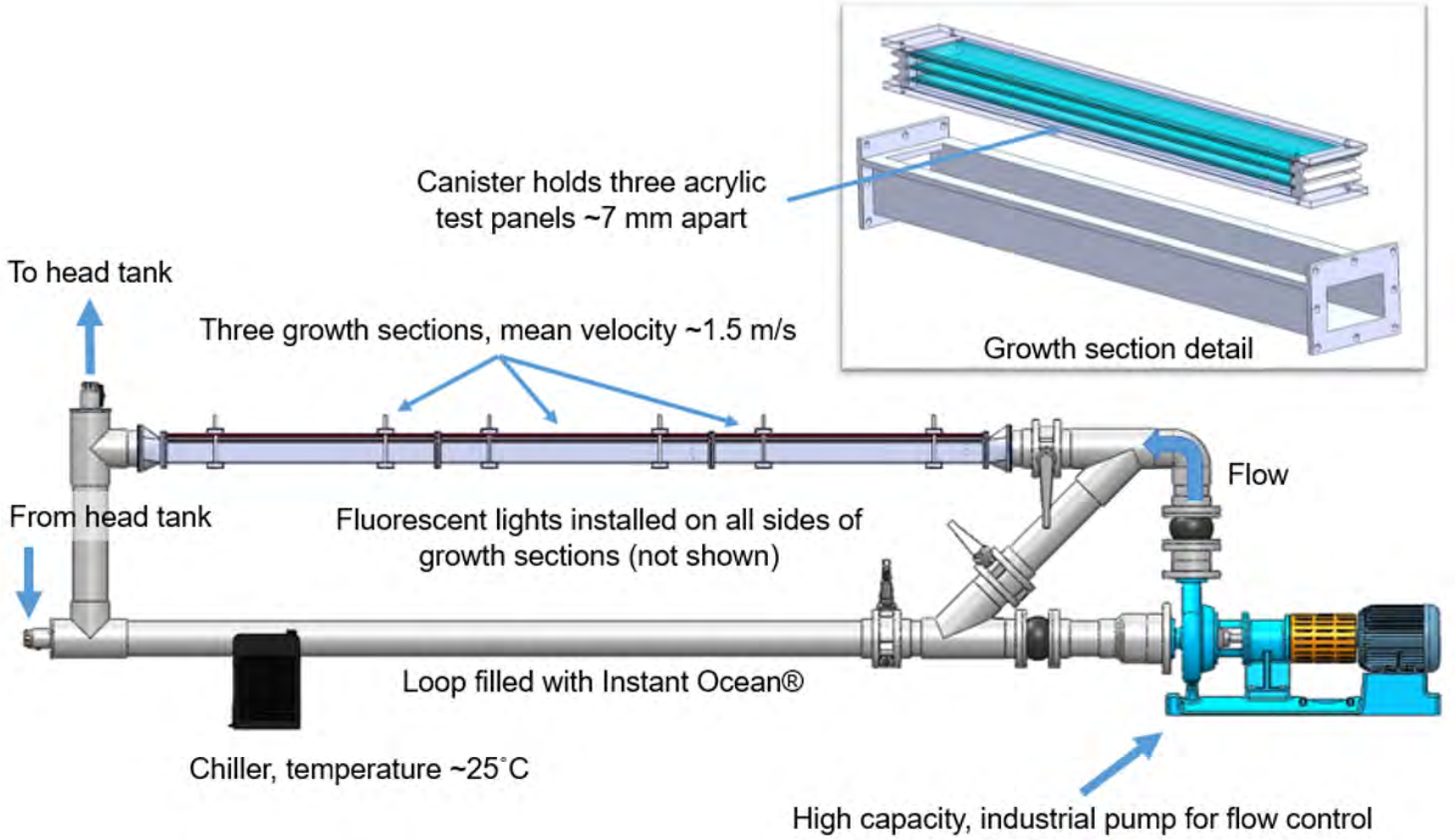

Figure 2.3: Solidworks® rendering of the biofilm growth loop. Soft biofilm was grown on acrylic test surfaces housed in canisters inside the growth sections. Flow control was provided by a large industrial pump, a chiller maintained the loop at 25° C and fluorescent lights surrounding the growth sections (not shown) provided illumination. The length of each growth section is a little over a meter.

The biofilm growth loop was constructed of polycarbonate and acrylic and has the capacity to hold nine test panels housed in three canisters. Each of these canisters is inserted in a corresponding growth section just downstream of a high-capacity, industrial pump (Goulds pump, 3196 XLT-X 6x8-13) which provides flow through the loop at a nominal bulk mean velocity of $\sim$1.5 m/s. This growth speed provides the reasonably high shear rates needed to develop robust biofilm layers on the test surfaces; yet, is gentle enough to allow the loop to remain in constant operation. Biofilm formation is particularly dependent on the surrounding flow conditions [18] and care was taken to insure that flow through the growth loop would resemble that experienced during hydrodynamic trials. Flow contractions and diffusers were installed at the fore and aft ends of each canister which holds three test surfaces stacked about 7 mm apart. This distance was chosen to match the nominal gap height of the Skin-Friction Flow Facility (SF3) test section so that both the bulk mean velocity and wall shear stress experienced during growth could be replicated in the experimental trials.

At the beginning of a growth cycle, the test panels were cleaned using ethanol, then rinsed with tap water prior to submergence in a static tank containing several liters of wet biomass. After a week—when a base layer of biofilm growth was observed on the test surfaces—the panels were gently transferred to the growth loop and exposed to flow. Panels were rotated 180° and installed with gravity acting to draw features of the biofilm away from the test surface (similar to what is observed on a flat-bottomed vessel). Once installed in the growth loop, panels were illuminated on all sides by fluorescent lighting (Philips F32T8, 4100K) and provided with 88 mL of Guillard's F/2 formula (with silica). A chiller (AquaEuro AC50H) maintained the loop temperature at $25 \pm 1^\circ$ C.

Weekly cleanings were preformed to clear biofilm from windows in order for the amount of light reaching the test surfaces to remain relatively constant. During these cleaning periods, growth on the panels was recorded using an overhead camera (GoPro Hero 5 Black) before reinstalling them in the slot below their previous location (the bottom window was moved to the top) in an attempt to further maintain consistent growth among the panels. Once biofilm growth reached a predetermined level of coverage and thickness (determined visually), a panel of interest was removed from the loop for characterization and experimental trials.

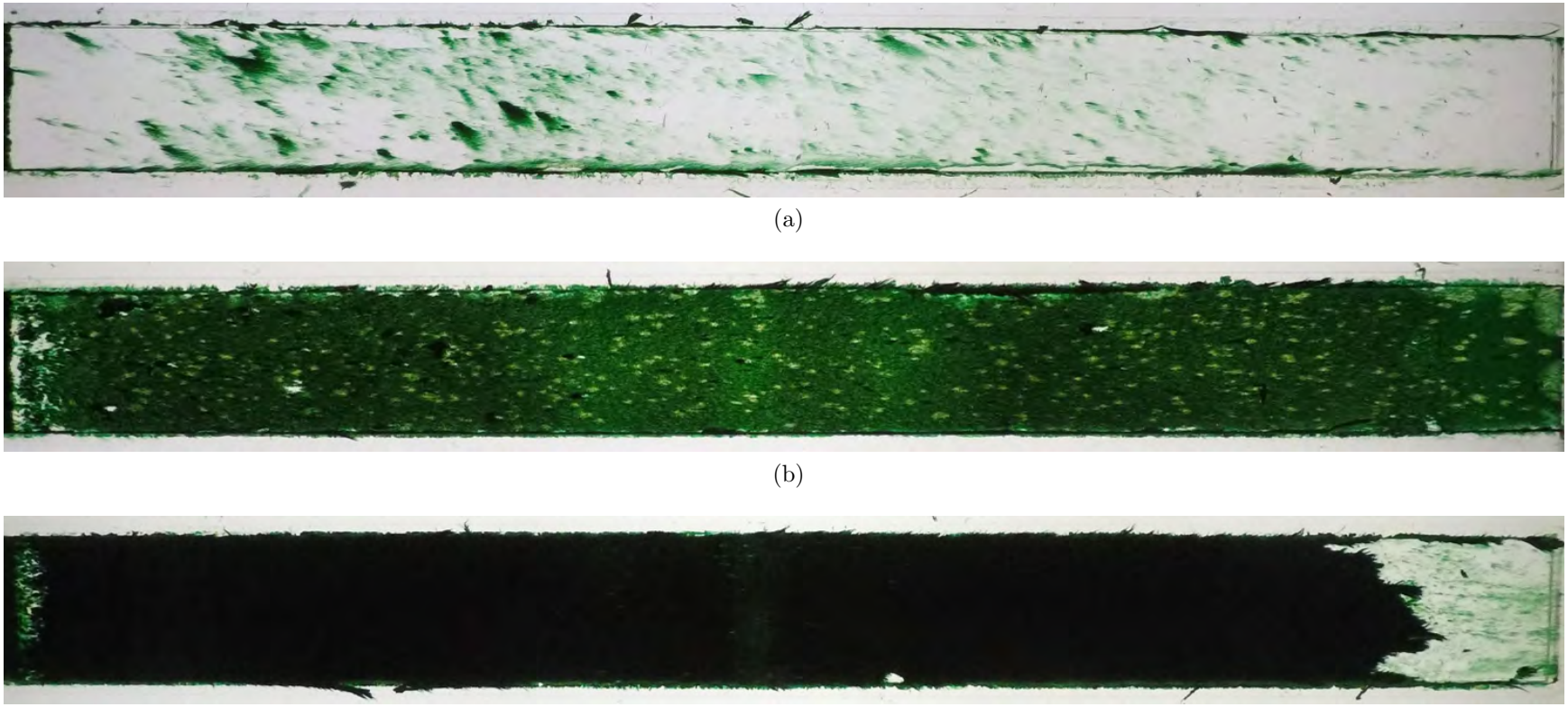

(a)

(b)

(c)

Figure 2.4: Overhead photos of biofilm grown on acrylic test surfaces are recorded before, during, and after experimental trials in the SF3. Varying the incubation time for the panels resulted in biofilm coverage ranging from slight (a) to moderate (b) to significant (c). Sloughing did sometimes occur during growth as is evidenced by loss of the thick biofilm layer near the end of the panel shown in (c). In the images, flow moved from left to right during growth and trials and the panels are ∼1.14 meters in length.

Three nominal growth duration times (also referred to as incubation times) were studied in this work (three, five, and ten week growth periods) and the resulting coverage ranged from slight to significant as can be seen in Figure 2.4. While visual inspection before trials showed that each panel tested was covered completely by a biofilm layer, the layer thickness could sometimes vary over the extent of a panel. For instance, the relatively short incubation time experienced for the three week growth led to patchy coverage with some areas of the panels covered in thicker, darker growth and other portions having only a very thin layer of streamers which appear almost unfouled (see Figure 2.4a). Sometimes sloughing occurred during growth—particularly as biofilm layers became thick (seen in Figure 2.4c).

Biofilm layers grown for five and ten week incubation times (IT) fully covered the panel surface except when sloughing occurred and panels with the least amount of sloughing were selected for experimental trials. Biofilm layers grown for five weeks appear to show some variation in thickness which corresponds to the growth loop lighting conditions. An area of lighter fouling is clearly seen near the middle of the panel displayed in Figure 2.4b which occurred where support structure for the growth loop was placed. Although undesirable, shading in this region was unavoidable and eliminating it would have required a complete redesign of the growth loop. The same pattern was observed for the three and ten week biofilm layers but to a lesser extent. Occasionally, five week biofilm layers showed small, infrequent patches of growth across the fouled area. These thinner patches of growth can be seen visually as lighter 'islands' in the biofilm layer. Biofilm layers grown for ten weeks did not display this behavior as thinner portions of the biofilm would naturally receive greater illumination in later stages of growth.

Loss of biofilm from the surface of a panel appeared to occur in a few ways. Firstly, large portions of the biofilm layer could become unattached at the surface of the acrylic panel and be swept away during growth or experimental trials. The bond between streamers in the thicker biofilm layers was apparently stronger than the attachment points in this type of sloughing which led to 'peeling' of the layer prior to complete removal. This is type of material loss is termed 'bulk sloughing' or simply 'sloughing' throughout this dissertation. The strong proclivity toward bulk sloughing of the acrylic panels used in this study likely results from the smoothness of their surface which was measured at $R_a = 0.02$ μm and $R_t = 0.43$ μm (although surface chemistry also plays an important role in biofilm adhesion). In-service vessels have rougher surfaces and therefore do not experience such a strong level of sloughing (indeed this is the major problem of soft biofouling!). A solution would be to grow

biofilm layer on rougher panels; this was considered but not pursued because rough substrates would provide additional drag not related to the biofilm layer. Such a scenario would confound the main objective of this work which is to determine the contributions of biofilm roughness and compliance to the overall drag increase.

Secondly—although not systematically cataloged—a shortening of the streamer filaments was also conjectured to occur during growth and experiments. Evidence of this is seen in the tables listed in Chapter Three which show biofilm thickness and roughness values. The magnitude of these values appears to decrease with increasing flow speed which may indicate a 'flattening' of the streamers when exposed to increased flow speeds. Comparison of measurements taken at the beginning and end of experimental trials also reveals that while some 'elasticity' is seen for average biofilm thickness, k_b, root-mean-squared roughness, k_{rms} and the trough-to-peak roughness, k_t, the values at the end of a trial were often measurably less than those at the trial's start. This behavior is indicative of trimming or shortening of the biofilm streamer filaments and is referred to as 'trimming'.

2.3 Biofilm Characterization

Despite the efforts made to maintain consistent conditions during the growth process, a variety of biofilm layers naturally developed. In order to compare hydrodynamic performance across this array of fouled panels, photos and laser scans were captured before, during, and after hydrodynamic trials and then analyzed to derive characterization parameters quantifying biofilm coverage and topography. Photos were captured using an overhead camera (GoPro Hero 5 black) mounted above the SF3 and profiles of the biofilm topography taken from below the SF3 using a laser line scanner (Micro-Epsilon scanCONTROL 2900-25, 25 mm line length, surface elevation resolved to four μm) and two axis traverse system. Analysis of the biofilm surface data was performed using Mathworks® MATLAB, ImageJ, and software supplied by the manufacturer of the laser line scanner (scanCONTROL Configuration Tools 5.1 and scanCONTROL 3D-View 3.0).

2.3.1 Areal Coverage

Figure 2.5 shows a series of pictures recorded by the overhead camera during the trial of a panel covered in five week biofilm growth. While the areal coverage of biofilm can vary from panel to panel, it is clear from this image series that coverage can also vary across a trial if bulk sloughing occurs. Each picture in the series was

captured immediately before a change in velocity through the SF3 test section. The first five images were recorded after flow through the SF3 was increased until reaching a maximum flow speed was achieved by the fifth image. The maximum flow speed was greater than the growth speed which explains why significant bulk sloughing is observed. This portion of the trial—in which flow is increased to a peak speed—is termed the 'evolving' leg since the areal coverage of the biofilm layer degrades with each change in speed. The bottom six pictures in the series were captured as the speed through the SF3 test section was decreased and show essentially no sloughing which is why this leg of the trial is referred to as 'stable'. Roughly half of the panels evaluated experienced significant bulk sloughing similar to what is seen in Figure 2.5 and a record of overhead images was captured for every trial (except one conducted before installation of the GoPro).

Overhead photos were analyzed to evaluate the extent and distribution of the biofilm layer covering a panel using the image processing toolbox in MATLAB. Firstly, pixels were sorted using color hue (green values typically spanned from about 60/360 to 160/360), then filtered using saturation and intensity thresholds (0.5, 0.9 out of 1, respectively). After this, the images were cropped to cover only the area where pressure drop measurements were collected (red box in Figure 2.6a). The cropped images where then binarized into black (biofouled) and white (clean) regions from which the percent coverage, areal porosity, average downstream run length (AHRL), average span run length (AVRL), average diffusion distance (ADD) and maximum diffusion distance (MDD) were calculated. All of these parameters are common in biofilm characterization literature and were chosen in part based on the findings of Renslow *et al.* [42]. Figure 2.6 shows an example of an original image (2.6a) and its corresponding binary image (2.6b).

2.3.2 Surface Topography

While overhead photos provided a global view of biofilm coverage, detailed, *in situ* measurements of the biofilm surface profile were obtained from the laser line scanner which was mounted below the SF3.

Figure 2.7 shows the scanner and a two-axis traverse system during an early evaluation of the scanner setup (short traverse: Ametek RGS04 linear rail, long traverse: Kollmorgen R2A-AKM23D). As the laser scanner can only image a thin line about 25 mm in length and the SF3 test section measures roughly 100 mm wide and about 1140 mm long, a two-axis traverse system was constructed to provide accurate motion control of the scanner. Using this motion control system, the scanner could be

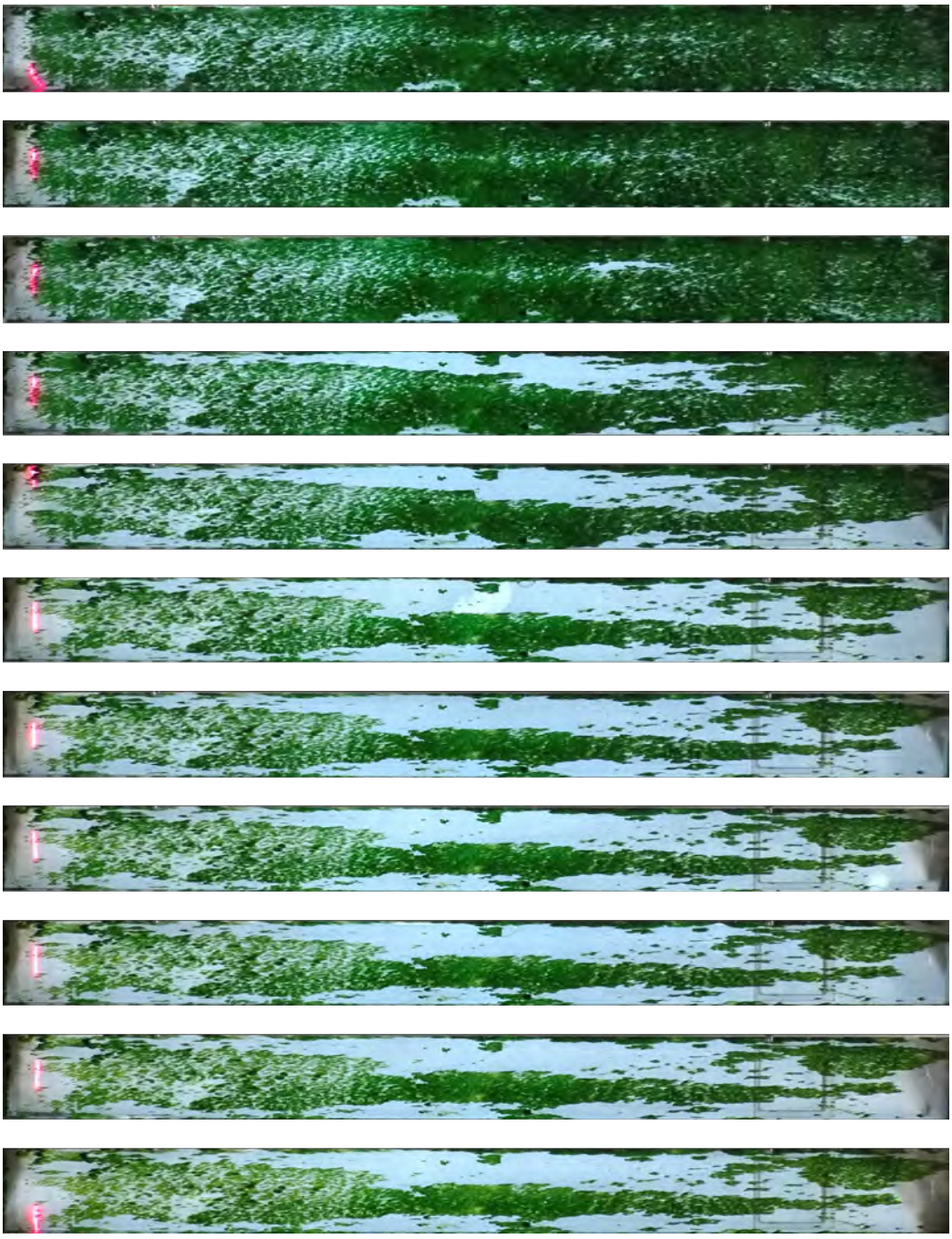

Figure 2.5: A series of images taken during biofilm Trial 5W2 shows the evolution of biofilm coverage due to bulk sloughing. For each trial, images were collected just before changing the flow rate using a GoPro Hero 5 black mounted above the SF3. Subsequent analysis of these images provides several parameters quantifying areal coverage.

traversed across nearly the full span and length of the SF3 test section (∼95% of each test surface could be captured with this system). The travel speed of the scanner was

(a)

(b)

Figure 2.6: Pictures captured from an overhead camera (a) were cropped and binarized into black and white images (b). Binary images were then used to determine several areal characterization parameters and the average channel gap height, H_{AVG}, across the SF3 measurement region. The measurement region of the SF3 test section is roughly 50 cm in length (shown boxed in red).

set at 2.54 mm/s and readings of each laser line profile recorded at a rate of 40 Hz which yielded a streamwise resolution of ∼64 μm—a value less than the manufacturer suggested thickness of the laser line (estimated to be at least 100 μm). Therefore, no gaps in data were expected for scanned profiles. Data from the scanner were passed through software provided by the manufacturer to derive Z (spanmwise) and Y (surface-normal) profiles and convert time series readings to the X (streamwise) coordinate. The resulting point clouds (such as that shown in Figure 2.8) represent the time-averaged, spatially filtered surface topography and were used to calculate channel gap height, H, average biofilm layer thickness, k_b, and roughness parameters (k_{rms}, k_t), and also to generate high-quality meshes capable of being 3D printed.

Three types of laser scans were performed for biofilm trials: 1) representative scans, 2) full panel scans, and 3) stationary time series scans. Representative scans were collected by first locating the laser scanner at its extreme upstream position (roughly 50 mm aft of the boundary layer trip) at the SF3 span centerline. Once positioned, profiles were recorded and the scanner moved to the downstream end of the SF3 while staying centered about the mid-span location of the SF3. This process measured the middle 25% of a biofilm surface, providing a reasonable representation of the biofilm thickness and roughness. Representative scans were performed for each flow speed during a trial and also before and after testing in quiescent flow. Scanner data from these scans were used to calculate the channel gap height and roughness statistics for every Reynolds number as shown in Equation 2.1 ($k_b^{'}$ is the height of the biofilm layer at a given X, Y, Z position). Note that measurements were recorded for every flow speed because slight changes in the biofilm layer geometry occurred when

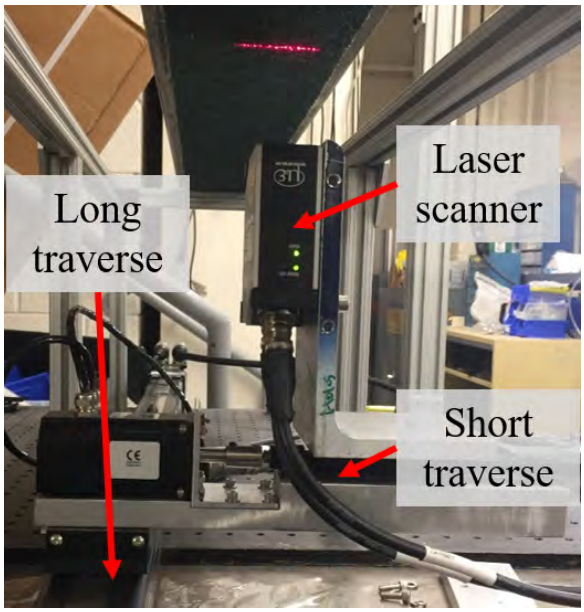

Figure 2.7: A laser line scanner was mounted to a two-axis traverse system as pictured above. A thin laser line illuminates the profile of sandpaper mounted in a setup similar to the final installation below the SF3.

it 'flattened' as flow was increased.

$$H = H_{nominal} - k_b \tag{2.1}$$

$$k_{rms} = \sqrt{\overline{k_b'^2}} \tag{2.2}$$

$$k_t = \max k_b' - \min k_b' \tag{2.3}$$

Each full panel scan typically required an hour to collect and so were performed for only a few select flow speeds. Generally, a full scan of the surface was taken for five different flow speeds. These spanned the Reynolds number range and were collected 1) at the minimum flow speed at the beginning of each trial, 2) when the bulk mean velocity roughly matched the nominal growth flow rate (e.g. ∼1.5 m/s) on the evolving leg of a trial, 3) at the maximum flow speed, 4) when the bulk mean velocity roughly matched the growth speed on the stable leg of a trial, and 5) at the minimum flow speed at the end of a trial. Full scans were used to generate rigid replicas and to characterize the largest streamers in the flow.

The biofilm layers examined in this study were comprised of diatoms and filamentous green algae which appeared to knot together and form streamers (resembling dreadlock-type formations). As the drag experienced by a surface is related to its

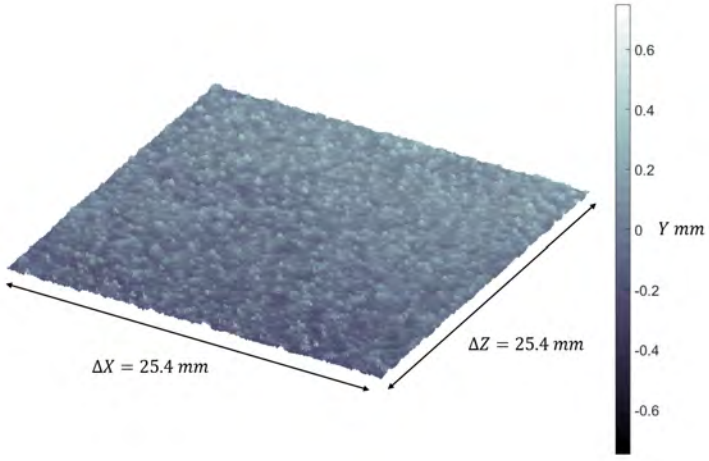

Figure 2.8: MATLAB rendering of laser scan data (25.4 mm by 25.4 mm) recorded during trials of a test surface covered in 80 grit sandpaper. A very slight 'tilt' can be seen in the data which may be indicative of a small misalignment between the laser scanner and the SF3 test section.

surface condition, and the biofilm and rigid replica surfaces appear to be covered in streamers, it is important to characterize their geometry. Figure 2.9 displays a MATLAB rendering of the surface topography for a five week rigid replica. As this figure shows, streamer geometry is relatively easy to describe qualitatively but a more rigorous process was required to quantify streamer dimensions and average spacing.

Firstly, laser scanner data were loaded into MATLAB and a 'cut' was taken at the value of k_{rms} which equally divided the elevation data. Then filtered elevation data were binarized as either white (below k_{rms}) or black (above k_{rms}) and identified using the MATLAB function 'regionprops'. Next, streamers having areas less than three square millimeters were excluded from the analysis as they appeared to represent portions of streamers just at the cutoff height. The centroid of each identified region was found and a bounding box captured the streamer length, L_s, and width, D_s. Average spacing between streamers (streamwise, λ_x, and spanwise, λ_z) was found by comparing the centroid locations to that of the nearest neighbor (within a projection of $2D_s$ in the streamwise direction and $0.5L_s$ in the spanwise direction). Figure 2.10 shows the filtered elevation data with accompanying centroid locations and bounding boxes.

Time series recordings of the biofilm motion were collected for each Reynolds number range by locating the scanner at a set position at the mid-span of the SF3 and roughly a quarter of the way downstream of the SF3 test section entrance. Scans

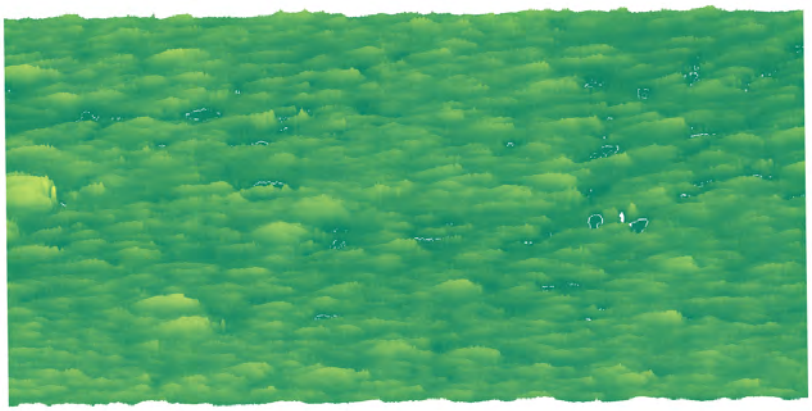

Figure 2.9: MATLAB rendering of surface topography as recorded by the laser scanner. Streamer heights have been magnified 4x to better show variations in elevation. the rendering is roughly 100 mm from top to bottom (although it is shown at a slight angle to better visualize the surface).

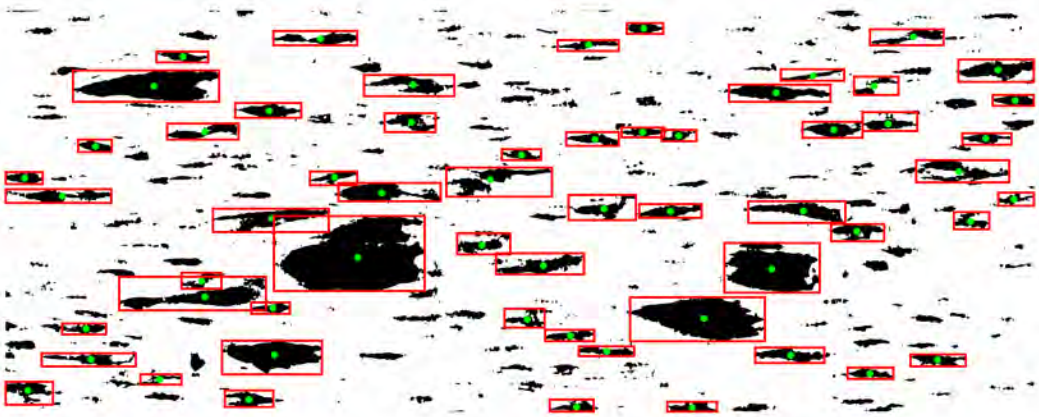

Figure 2.10: Binary image shows streamers with elevations above k_{rms} as black regions. Centroids (green dots) and bounding boxes (red squares) identify streamer location and dimensions. Note that the smallest regions have been excluded from the analysis. This binary image spans roughly 25 mm from top to bottom.

of this single profile were collected for a little over one minute at a rate of 40 Hz. Time series scans may be used in the future to characterize streamer motion (i.e. frequency of flutter, extent of streamer 'sweep' into and out of the flow).

2.4 Developing Rigid Replicas of Live Biofilm

The laser scanner system provided the means to accurately measure the biofilm surface while subject to flow, which not only provided greater certainty of roughness parameters, but also grants the opportunity to replicate nearly the entire biofilm surface for a given flow condition. However, before a rigid replica of soft biofilm could be 3D printed, point cloud data had to be meshed, analyzed, and made free of errors (e.g. spikes, holes, non-manifold polygons, etc.) that are non-physical and prohibitive to the 3D printing process. Initially, 3D Systems® Geomagic Wrap and later a custom MATLAB program were used to convert point cloud data from the scanner into a polygon mesh surface which was cut into four tiles (tiling was required due to limitations in the printer build area). When using Geomagic Wrap, the resulting .stl files consisted of roughly 10 million triangles each, which—for the sake of achieving a reasonable processing time—were decimated to about 2 million triangles. In the decimation process, the geometry was set to maintain deviations better than 100 μm which is similar to the accuracy of the scanner data and not much larger than the minimum print voxel of the Stratasys J750 printer used to manufacture the rigid copy (28 μm). A similar procedure was used when processing files in MATLAB but resolving the surface at a feature detail of 50 μm resulted in files about twice as large (20-25 million triangles per tile) which had to be decimated in Materialise® Magics (again maintaining feature accuracy to at least 100 μm). Tiles were printed of green, cyan, and yellow J750 PolyJet material at the University of Michigan's UM3D print lab using a Stratasys J750 printer.

Due to the limited length of the scanner laser line and capabilities of the manufacturer provided software, several separate meshes had to be stitched together to produce the four tiles that eventually formed the rigid replica. Each tile measured roughly 270 mm by 100 mm. Figure 2.11 shows part of one such tile in detail. Furthermore, while ∼95% of the biofilm surface was captured during the scanning process, portions of the test surface which were covered in biofilm (just downstream of the boundary layer trip) lay outside the measurement range of the scanning system. Rather than leaving these portions bare, or substituting them with a flat section with the same mean roughness height, scan data in the immediate area was extended and placed where overhead photos dictated. While the overall deviation from the true surface profile for these sections is unknown, the difference may not serve as a significant source of error in frictional analysis given the quasi-random, somewhat repeated nature of the biofilm morphology.

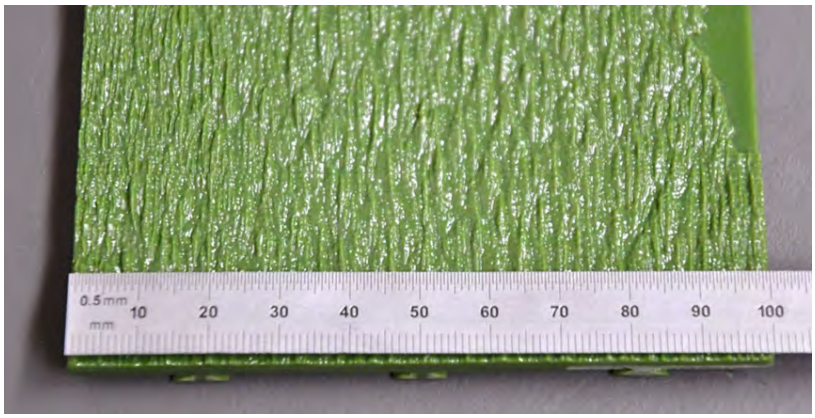

Figure 2.11: Pictured above is a portion of one 3D printed tile generated from laser scan data recorded during trials of a panel covered in live biofilm grown for ten weeks. Point cloud data from the scanner were meshed then printed using a Stratasys J750. As observed visually in the lab, the rigid replica geometry seen above appears to match the time-averaged, spatially filtered profile for the live biofilm (not shown) well.

It is notable that the early rigid replicas (5W3RRe, 10W2RR, 10W6RR) did not include scan data from the portion of the surface obscured by a 38 mm quartz window insert in the SF3 bottom window (which was installed to permit the PIV laser light sheet through). Instead, scan data from a 38 mm region just upstream of the window were substituted where these data were missing. Later rigid replicas generated using the MATLAB routines did include scan data in the region above the 38 mm quartz window. The impact of capturing the local topography accurately is shown clearly in the PIV results presented in Chapter Five.

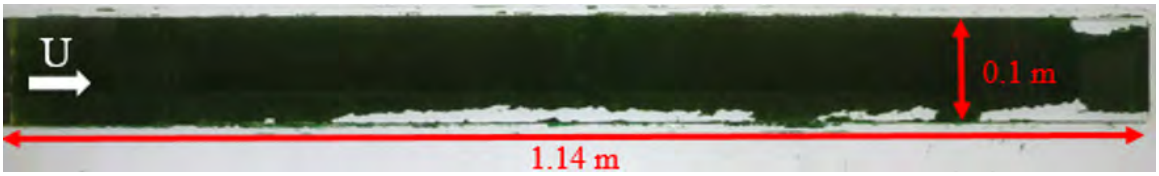

(a)

(b)

Figure 2.12: Overhead photos show (a) the extent of biofilm coverage on an acrylic test panel covered in biofilm grown for ten weeks after experimental trials as well as (b) a 3D printed copy of the surface in (a) generated from laser scan data.

Figure 2.12 shows overhead photos of a ten week biofilm (Trial 10W6) taken immediately after experimental trials and its 3D printed rigid replica (Trial 10W6RR). It appears that the rigid copy reproduces the live fouling coverage fairly well as areas where bulk sloughing occurred match. Comparisons can also be drawn between the topography for the two surfaces. Figure 2.13 displays MATLAB renderings derived from scans of the ten week biofilm layer and its rigid replica. The two show fairly good agreement with similar 'fin-like' protrusions that appear to align in the direction of the streamwise flow (upper left to lower right). These protrusions represent the time-averaged location of large streamers in the biofilm layer. It is likely that the rougher structure of the scan data for the live biofilm is a result of streamer flutter as the rigid replica rendering appears smoother. Steps made during mesh generation

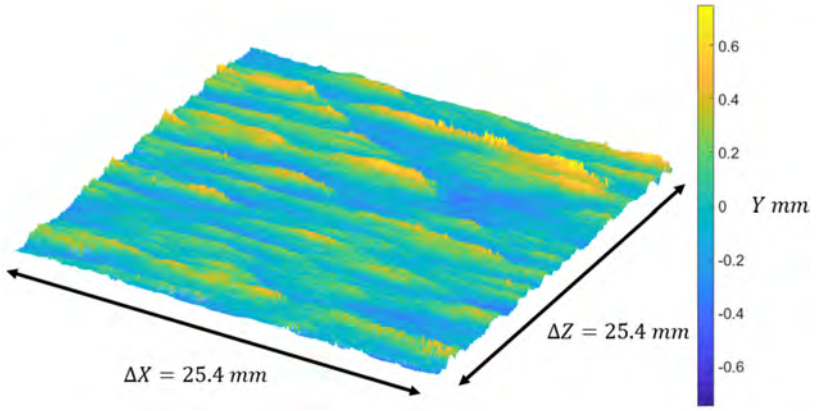

(a)

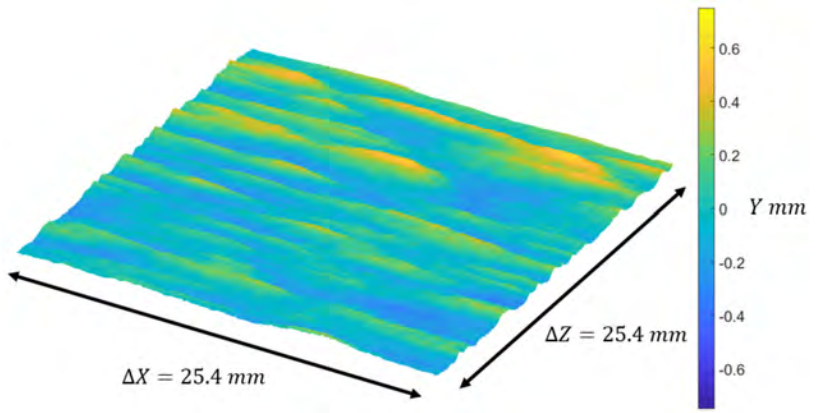

(b)

Figure 2.13: MATLAB renderings of laser scans collected for (a) a layer of ten week biofilm growth (Trial 10W6) and (b) its rigid replica (Trial 10W6RR). Note that scanner data were collected under similar flow conditions for both surfaces. Slight longitudinal and span shifts are observed in the renderings and are the result of an adjustment made to the laser scanning system location between trials.

and the process of printing may also filter some of this roughness. Aside from these small deviations, the live biofilm and rigid replica surface profiles appear to match within roughly 50–100 μm.

2.5 Measuring Resistance

The hydrodynamic performance of surfaces covered in soft biofilm was evaluated through experimental trials in the Skin-Friction Flow Facility (SF3) housed in the Marine Hydrodynamics Lab at the University of Michigan. This facility is a high-aspect ratio, closed-channel water tunnel with fully developed flow through its test section and is capable of reaching $Re_H \sim 150\ 000$. The SF3 channel gap height, H, is nominally 7 mm, its test section spans 101 mm, and has a downstream length of 1.14 m. The SF3 is seen in Figure 2.14 below (see [13] for further details).

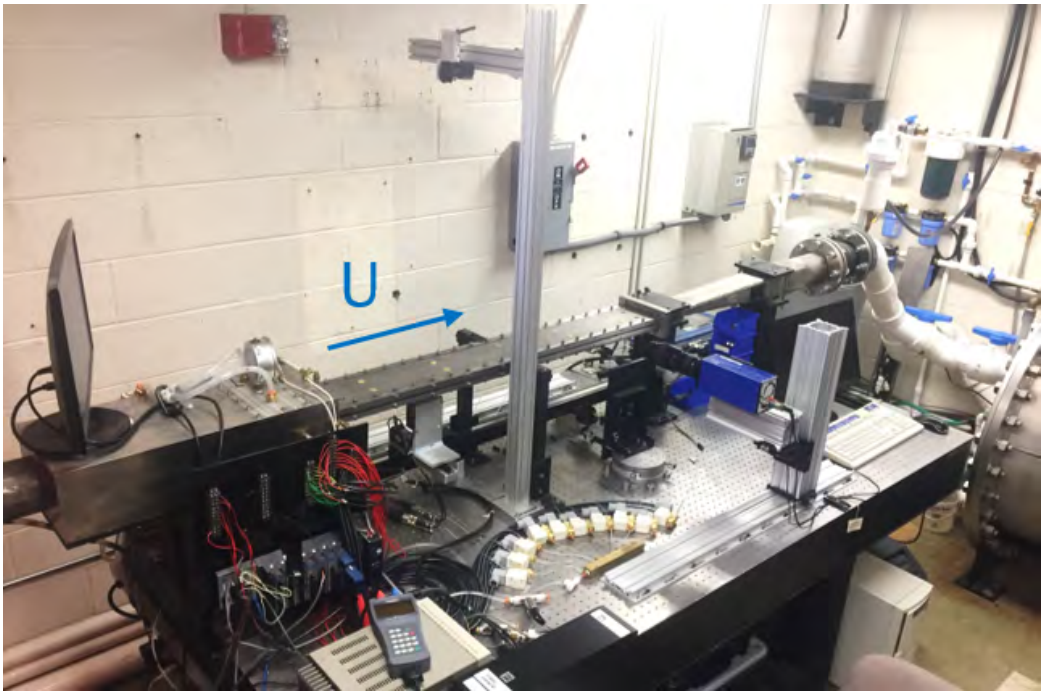

Figure 2.14: The Skin Friction Flow Facility (SF3) is a closed channel water tunnel with a high-aspect ratio that has been previously used to evaluate superhydrophobic surfaces (SHS) and was modified for evaluation of surfaces covered in soft, filamentous biofilm. The test section is roughly 1.14 meters long, spans just over 100 mm, and has a nominal gap height of 7 mm.

The resistance of six types of surfaces with varying roughness coverage was evaluated including: 1) a smooth baseline case, 2) a surface covered in 80 grit sandpaper, smooth surfaces covered by soft biofouling grown for 3) three, 4) five and 5) ten

week incubation times, and finally, 6) seven rigid replicas produced from scan data of the biofilm layers gathered while they were subject to flow during experimental trials. Before the start of a trial, the SF3 was filled to the test section and test panels (which also serve as the top window of the SF3) were installed. This insured that the biofilm layers were only exposed to air for a maximum time of one-to-two minutes so that they would remain wetted. Ten pressure ports machined at the centerline of the side windows of the SF3 test section provided measurements of the pressure drop along the streamwise direction of the test section (located at 20H, 30H, 50H, 70H, 84H, 98H, 112H, 126H, 140H, and 150H). Flow was tripped at the entrance to the SF3 test section using 50 grit sandpaper strips and only those ports located well downstream ($\geq$70H) of the trip were used to calculate the pressure drop, ensuring that measurements were taken in the fully developed portion of the test section. Note that the bottom window of the SF3 was hydrodynamically smooth and that—as a result—the mean velocity profile through the channel was asymmetric. Particle Image Velocimetry (PIV) was performed at each Reynolds number to measure the mean velocity profile of the flow (further discussion of the PIV measurements is provided in §2.6). A magnetic flow meter (Siemens Sitrans FM MAG5100 W; DN 50) provided readings of the volume flow rate through a known pipe diameter while the laser line scanner provided the channel gap height allowing bulk mean velocity to be estimated via conservation of mass. Estimates for the coefficient of friction for each test surface capture frictional performance and are given by Equations 1.1, 1.2, and 2.5.

A different procedure was followed when evaluating the surfaces covered in living biofilm than was used for the rigid surfaces. While it is reasonable to assume that the frictional performance of a rigid test surface does not depend on the previous flow conditions it experienced, the same cannot be said for a surface covered in biofilm, which will experience significant changes in surface profile due to sloughing (the loss of biofilm due to shear or drag in the flow). Data collection for trials of live biofilm began at Reynolds numbers below the nominal growth speed and after recording the pressure drop, $\frac{dp}{dx}$, channel gap height, H, volume flow rate, Q, fouled area A_b, mean flow field, $u(y)$, and time averaged biofilm surface profile, $Z_{biofilm}$ for a portion of the fouled surface, the flow speed through the loop was increased incrementally and the process of data collection repeated through the nominal growth speed until reaching a maximum value. Note that data collected during this first half of a trial are denoted as 'evolving' in the results below. When any further increase seemed likely to result in substantial loss of the biofilm layer due to bulk sloughing, the process of evaluating the surface was continued by incrementally decreasing the speed of the flow loop until

reaching the nominal pump speed first tested. Data acquired during the second half of the trial are termed 'stable' and little to no additional sloughing occurred during this period. As trials of the smooth baseline, 80 grit sandpaper, and rigid replica did not experience a changing roughness profile, data were collected only once at each speed. Results from the trials performed for the various surfaces are presented in Chapters 3-5.

2.6 Measuring the Flow Field

While the primary objective of this research was to evaluate the frictional performance of soft biofilms and rigid replicas having the same surface geometry, local flow field measurements were also collected along the surfaces and may provide insight into the complex relationship between roughness, compliance, and the interplay between a surface and the flow surrounding it. As noted in §2.7, measurements of the flow field through the entire channel were also used to account for the asymmetric boundary conditions which is necessary to accurately determine the shear stress experienced by the biofilm layers and rigid replicas.

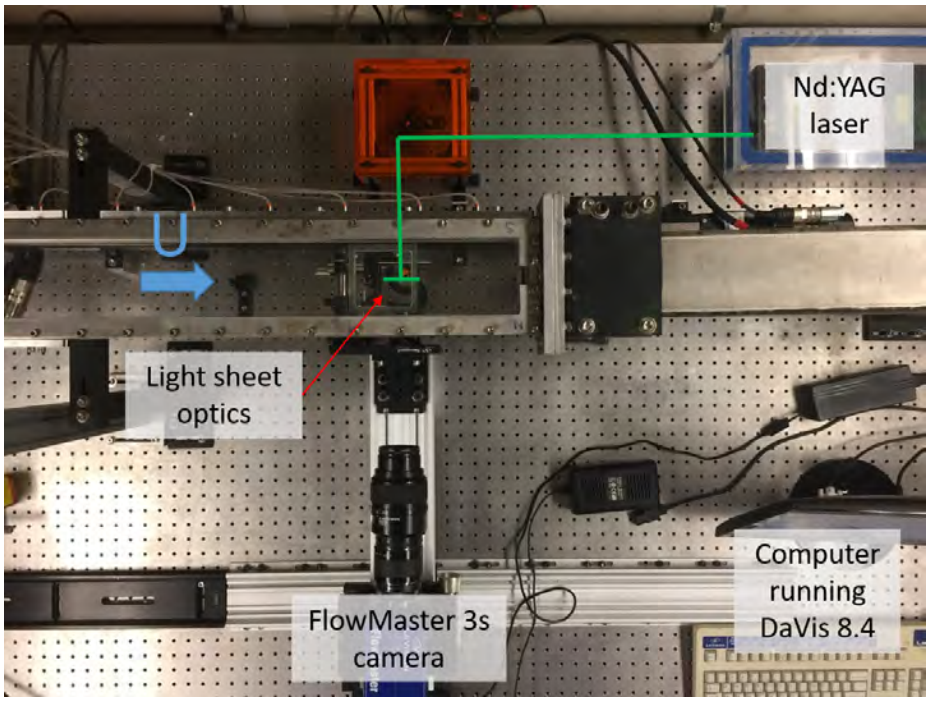

Figure 2.15: Two-dimensional, two component (2D2C), planar PIV measurements were collected using a dual-pulsed Nd:YAG laser, CCD camera, and computer running DaVis 8.4. Images were recorded at five locations in span but only those from the centerline are presented in this work.

Velocity data were collected using two-dimensional, two component Particle Image Velocimetry (2D2C PIV)—a well-established, whole-field technique capable of capturing intricate flow details in a region of interest. Figure 2.15 shows the setup used to collect images and calculate vector fields. The PIV setup consists of: a dual-cavity, pulsed power Nd:YAG laser (Quantel Evergreen 200), light sheet optics, and LaVision PIV system (including a CCD camera—the FlowMaster 3s, Programmable Timing Unit (PTU), and a computer running DaVis 8.4). The flow was seeded with TiO_2 particles having a median diameter of 300 nm (Ti-Pure R-706; donated by DuPont) to a particle density of roughly 0.03 particles per pixel. The typical particle diameter was around two pixels and the time step between images was optimized for a particle shift of three pixels (which is close to 1/4 of the final interrogation window size). Images were collected at five different locations across the SF3 span at roughly 950 mm (135H) downstream of the SF3 test section entrance. Recordings taken at the center of the span included 500 frame pairs while those taken at the other four span locations typically had 250 frame pairs. Figure 2.16 shows a typical image recorded at the center span location for a five week biofilm layer.

During image preprocessing, frame pairs were rotated and the minimum pixel intensity across the entire recording was subtracted for each pixel. Algorithmic and geometric masks were applied to reduce spurious vectors resulting from surface reflections and low seeding near the surface being examined. Steps in the algorithmic masking process included: 1) a sliding average with filter length of N = 9 pixels, 2) identifying pixels with an intensity above a threshold of 750 and setting their value to zero, 3) finding the local standard deviation over regions of N = 10 pixels, 4) finding the sliding maximum for a filter length of N = 7 pixels, and 5) setting pixel intensity to zero for pixels with intensities below 60. The shift between processed frame pairs was found first using a single pass of square interrogation windows 32 pixels wide with an overlap of 50%. Then the interrogation window size was reduced to 16 pixels and a round 1:1 Gaussian weighting function was implemented while making four passes with an overlap of 75%.

The resulting vector fields were post-processed to minimize spurious vectors (most of which occurred due to reflections off biofilm streamers or the rigid replica surface). Post processing steps included limiting the allowable vector ranges to four pixels in the streamwise direction and two pixels in the wall-normal direction, and then performing a median filter five times to remove and iteratively replace any remaining spurious vectors. Finally, vector statistics including the mean velocity profile and turbulent statistics were calculated across the full field of view (FOV) from the instantaneous

vector field data. Figure 2.17 shows the final (a) instantaneous and (b) time averaged vector fields corresponding to the frame and set shown in Figure 2.16.

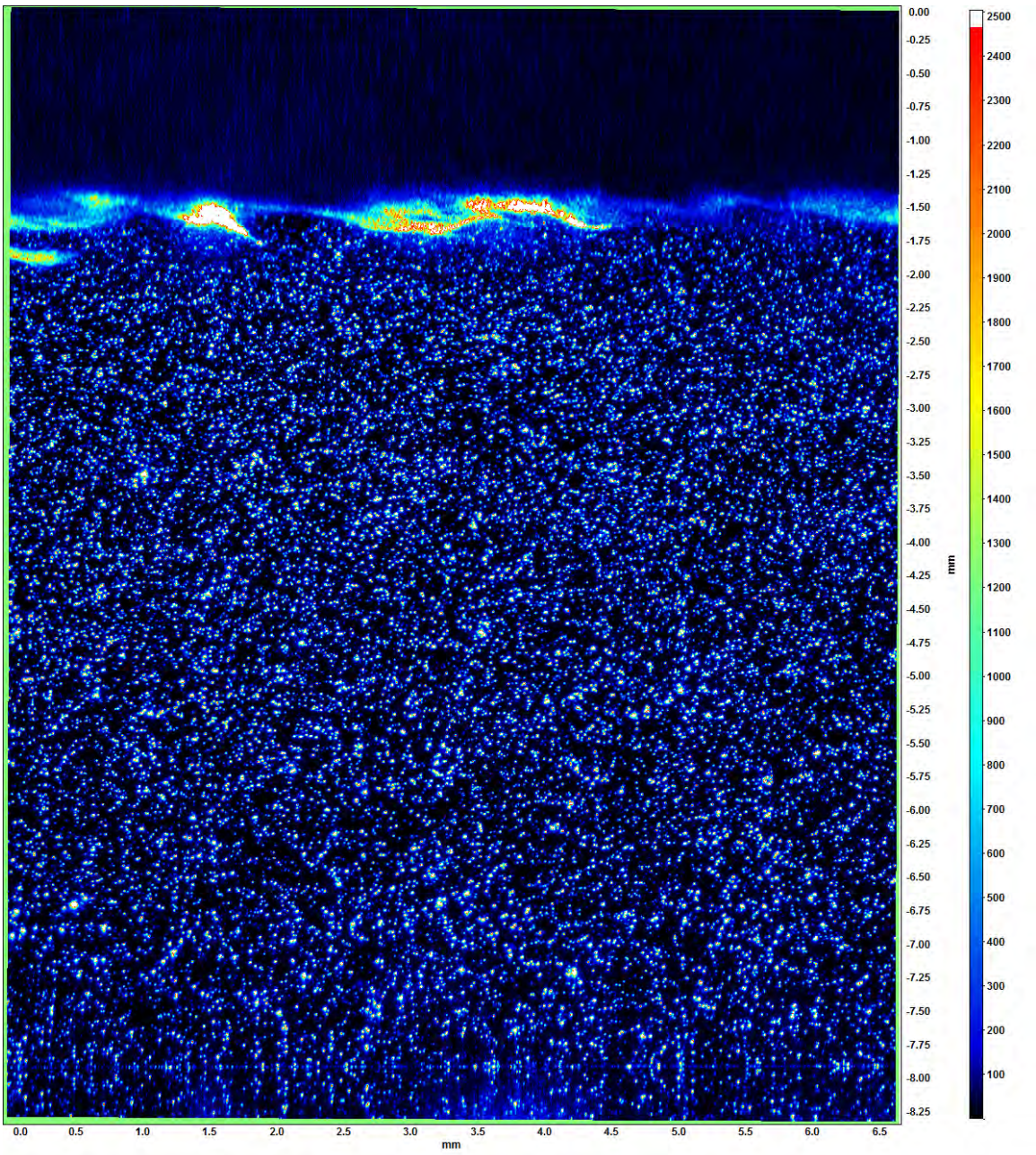

Figure 2.16: Images of the particle-laden flow field were recorded during experimental trials. The surface of a five week biofilm layer (and the strong reflections off it) is clearly visible in the above image. Pictures were collected at five spanwise locations and would later be used to perform planar, two component (2D2C) PIV. The image shown above is roughly 8.25 mm tall and 6.5 mm wide.

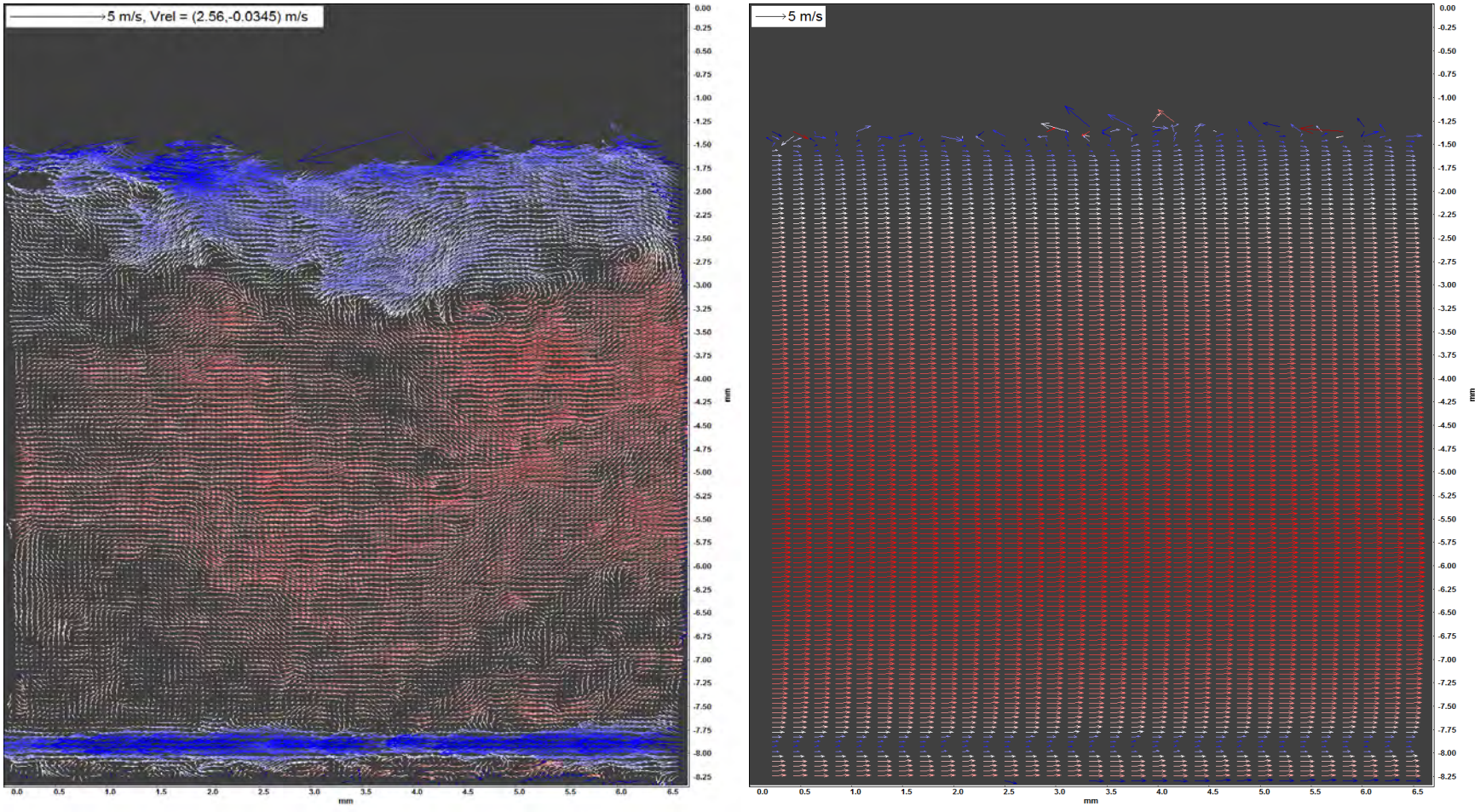

(a) (b)

Figure 2.17: Vector fields were produced from frame pairs in 2D2C PIV. Both (a) instantaneous and (b) time-averaged vector fields were calculated. Spurious vectors are seen near the top boundary of the flow which result from reflections off biofilm streamers. The particle reflections off the bottom smooth wall are captured allowing precise determination of its location. Vectors in (a) are shown relative to the mean flow field to visualize flow features such as vortical structures. Figure dimensions are the same as in Figure 2.16.

Analysis of the vector fields was performed using a custom written MATLAB routine. Firstly, the top and bottom surfaces needed to be located to determine the channel gap height across the image. The smooth bottom surface location (where $y = H$) was found from mirrored particles near the bottom of the PIV images. Biofilm surfaces—like all rough surfaces—do not have a clear origin (where $y = 0$) and reasonable candidate locations could be anywhere from the most outward extent of the streamers to the base of the layer. Typically, roughness studies assume $y = 0$ at one of the roughness extremities, then use the mean velocity profile to iteratively determine a wall offset, ϵ, which best reproduces the logarithmic layer (see [53] for further details).

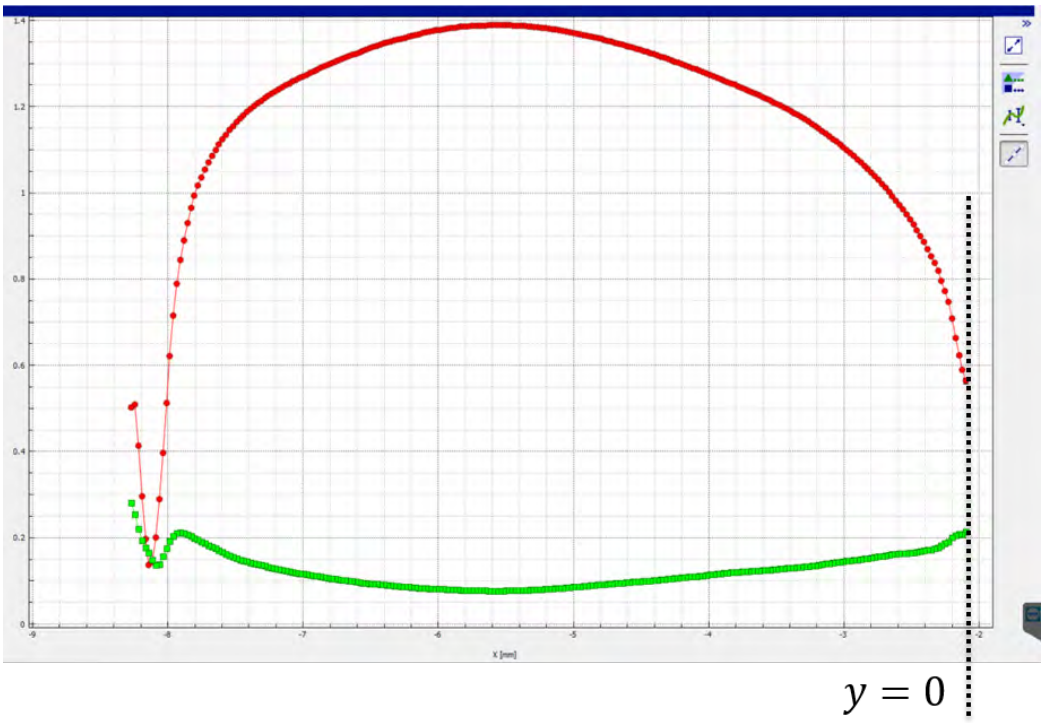

Figure 2.18: The mean velocity profile across the channel (red data points) was used to determine an initial guess for the location where $y = 0$. The origin was chosen either where the value of the velocity was zero, or where data began (if a null velocity was not measured). In the case shown, the offset between the PIV FOV origin and initial $y = 0$ is $\sim$2.1 mm.

This same goodness-of-fit procedure was performed by a subroutine in the MATLAB flow analysis program after: 1) first assuming that $y = 0$ where the velocity profile data reached a value of zero (or was terminated) and determining the bulk mean velocity, U_m, through the channel by integrating the full flow field from top to bottom and 2) calculating the friction velocity, u_τ, using the coefficient of friction,

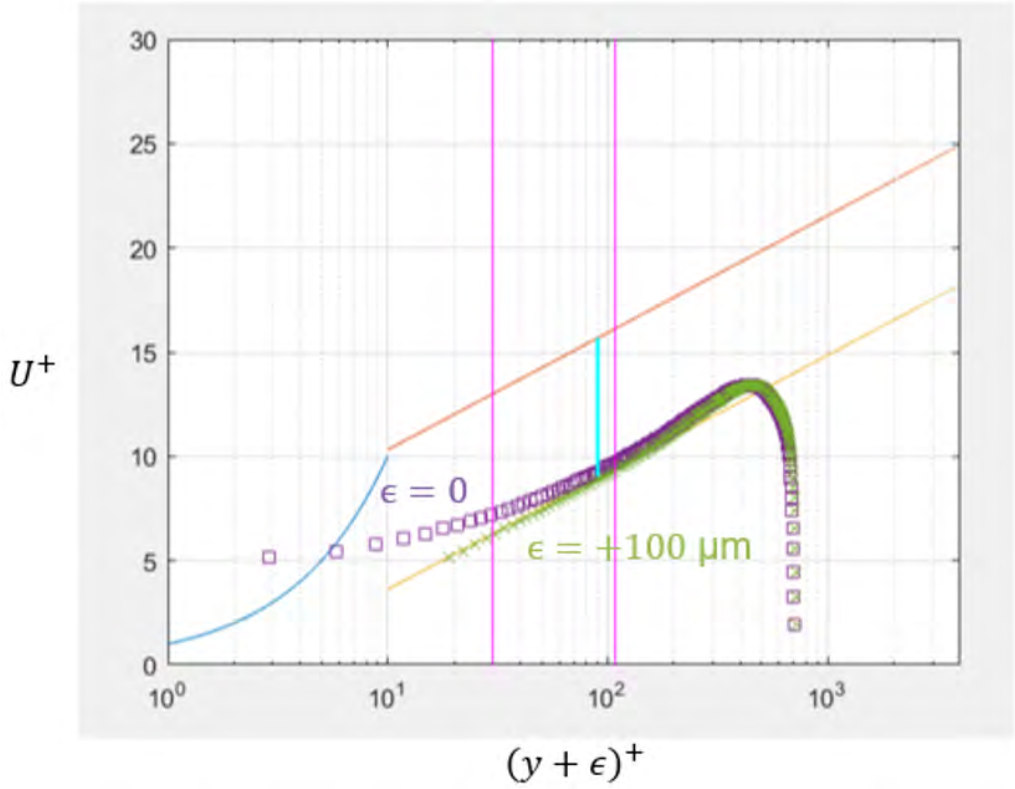

Figure 2.19: The effect of the wall offset, ϵ, on the velocity profile is seen in the figure above. A MATLAB routine found the line of best fit for inner-scaled velocity profile data in the log layer (the bounds are shown in purple and were assumed to be $y^+ = 30$ and $y/\delta = 0.3$ for this data set).

C_f, measured through frictional analysis. Figures 2.18 and 2.19 better illustrate the steps used to determine the wall offset and show how its value affects the resulting velocity profile data. Once ϵ was known, velocity profiles were produced using outer and inner layer scaling. The results are shown and discussed in detail in Chapter Five.

2.7 Measurement Challenges and Uncertainty Estimation

Studying the hydrodynamic performance of living biofilm introduces complexities not experienced during traditional hydrodynamic roughness experiments. Firstly, the surface of interest is compliant and appears to interact strongly with the flow via streamer fluttering and bulk biofilm layer vibrations. Secondly, the surface does not exhibit a stable condition as sloughing causes the biofilm layer to deteriorate over time. Furthermore, fundamental parameters—such as channel gap height–and

assumptions—such as symmetric boundaries—used in analysis of the frictional performance become ill-defined.

Accurate estimation of channel gap height, H, is critical in obtaining quality measurements of the coefficient of friction, C_f. While straightforward for smooth surfaces, it becomes particularly difficult to define H for a biofilm surface as a range of seemingly suitable values may be extracted from measures of the biofilm thickness. Initially, the channel gap height was determined using eight point measurements spaced along the SF3 test section at regular intervals. However, it was observed that this method did not account for 1) uneven growth of the biofilm layer due shading in the growth loop and 2) a slight rise in the SF3 test section along its downstream length. Scans of a smooth flat plate revealed these complications which were then accounted for by 1) subtracting the smooth, baseline elevation skew from the data and then 2) using samples taken from a continuous scan along the length of the SF3 to find the average biofilm layer thickness, k_b. Because C_f is derived from pressure data collected at taps located between 70H and 140H, the average channel gap height was calculated using scan data from this portion of the SF3 test section. Furthermore, bulk sloughing resulted in portions of the measurement volume which have $k_b = 0$ and were not included in the initial estimation of k_b and H. A correction was implemented which found the average channel gap height, across the SF3 measurement volume H_{AVG} by multiplying the average biofilm layer thickness, k_b, by the fouled area, A_b, and subtracting it from the smooth baseline channel gap height, H_o (see Equation 2.4). Note that the approximate measurement volume is shown boxed in red in Figure 2.6a.

$$H_{AVG} = H_o - k_b A_b \tag{2.4}$$

Another major complication which had to be addressed was the asymmetry between the biofouled and smooth walls bounding the flow. The control volume analysis referenced in Section §1.2 applies only to a channel with symmetric boundary conditions. Figure 2.20 shows a schematic of the channel flow as observed during trials—that is with asymmetric boundaries (before sloughing). A typical solution would be to install biofouled walls as both the top and bottom windows of the SF3 test section (thus returning to symmetric conditions). However, optical access to the biofilm was required for all laser scanner data necessitating the use of an optically clear, smooth bottom window. In order to address this impasse, the control volume analysis was modified for a channel with consistently asymmetric flow (i.e. the mean velocity profile at the measurement volume entrance matched that at its exit). Equation 2.5

shows the result:

$$\tau_{w,\,biofilm} = H_{AVG}\left|\frac{dp}{dx}\right| - \tau_{w,smooth} \tag{2.5}$$

While the modification required by asymmetric boundaries is simple, determining the shear stress on the bottom wall requires additional information that cannot be found without either direct measurement of the shear stress on the bottom wall or its derivation from the flow field above it. In this case, the smooth wall shear stress was determined using the Clauser chart method (described in [53]) from the mean velocity profiles given by PIV vector fields which were collected at every Reynolds number during the hydrodynamic trials. The above corrections for H_{AVG} and $\tau_{w,\,biofilm}$ provide the means to accurately determine the coefficient of friction for a biofilm covered surface according to Equation 2.6.

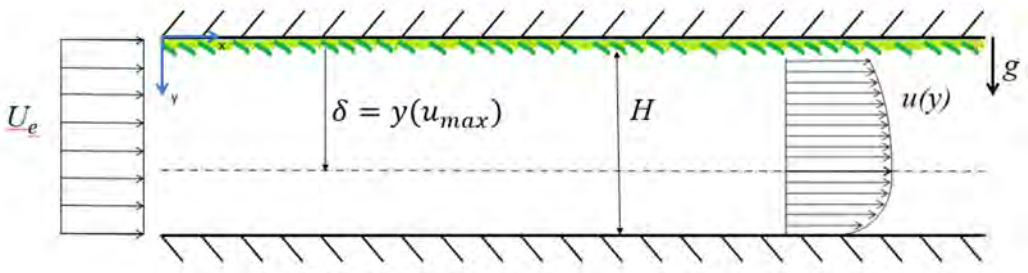

Figure 2.20: The schematic above shows the asymmetric boundaries in the SF3 and their affect on flow development. PIV data were used to determine the wall shear stress on the bottom (smooth) window via the Clauser chart method [53] which can then be used along with measurements of pressure drop and average channel gap height to determine the shear stress on the biofilm layer via Equation 2.5.

The channel asymmetry also affects determination of the relevant outer length scale, δ, which is normally considered to be the channel half-height ($H/2$) for symmetric boundaries. However, this is no longer the case for asymmetric flow and the relevant outer scale was assumed to be the distance from the average biofilm surface to the wall-normal location where the maximum average velocity occurred ($\delta = y(U_{max})$). While this procedure is relatively straightforward for uniform surface coverage, determination of the relevant outer scale is less than clear for moderate and severely sloughed panels. For these sloughed conditions, the channel half-height was assumed to represent δ.

$$C_{f,\,biofilm} = \frac{\tau_{w,\,biofilm}}{\frac{1}{2}\rho U_m^2} \tag{2.6}$$

A detailed uncertainty analysis was performed for the frictional results reported here following the procedure outlined by Moffat [32]. Sources of uncertainty considered included instrument accuracy, resolution, and repeatability values for the bulk mean velocity, U_m, average channel gap height, H_{AVG}, channel span, pressure drop $\frac{dp}{dx}$, smooth wall shear stress $\tau_{w,\,smooth}$ and temperature effects on water density, ρ, and viscosity, ν. Uncertainty bounds for the coefficient of friction ranged between ± 10 to $\pm 20\%$ for data collected at the lowest Reynolds numbers to $\pm 2\%$ through $\pm 4\%$ for the highest flow speeds. The largest sources of error were the estimation of bottom wall shear stress, $\tau_{w,\,smooth}$, and average channel gap height H_{AVG}. The uncertainty bounds on $C_{f,\,biofilm}$ are roughly twice what is reported by Schultz *et al.* [49] for low flow rates but are comparable at high Reynolds numbers. The difference is primarily due to the asymmetric boundaries and relatively small channel gap height (which is more sensitive to resolution uncertainty than would be the case for a larger channel).

2.8 Validation of Methodology for Smooth and Rough Surfaces

Figure 2.21 shows the resistance curve for a smooth acrylic panel as measured in the SF3 along with a correlation proposed by Zanoun *et al.* [58] relating the smooth wall coefficient of friction, $C_{f,\,smooth}$, for channel flow to Reynolds number, Re_H. While data in the plot are offset slightly below the expected curve, the values lie within the uncertainty bounds and generally show good agreement with the expected result.

Both Equation 1.1 (black squares) and 2.5 (purple diamonds) were used to find C_f resulting in slight differences across the range of Reynolds numbers. The added uncertainty associated with the asymmetric channel correction can be seen in the greater scatter of the purple data points shown in Figure 2.21. While the range of Re_H values investigated is relatively limited compared to the capability of the SF3 (up to $Re_H \approx 150\,000$), the baseline, smooth wall data span the range of flow speeds for all biofilm panels examined in this work.

A panel covered in sand grain roughness (Series ZK713X 80 grit, water resistant sanding belt) was also evaluated in the SF3 to verify the effect of channel asymmetry and gain experience with a type of roughness with better known hydrodynamic performance. The results are plotted in Figure 2.22. Data offset above the smooth baseline quantify the added drag (also known as the drag penalty) caused by the roughness. Equation 2.7 displays the relationship between added drag, ΔC_f, and the measured coefficient of friction, $C_{f,\,measured}$. Often there is a large effect in ΔC_f due

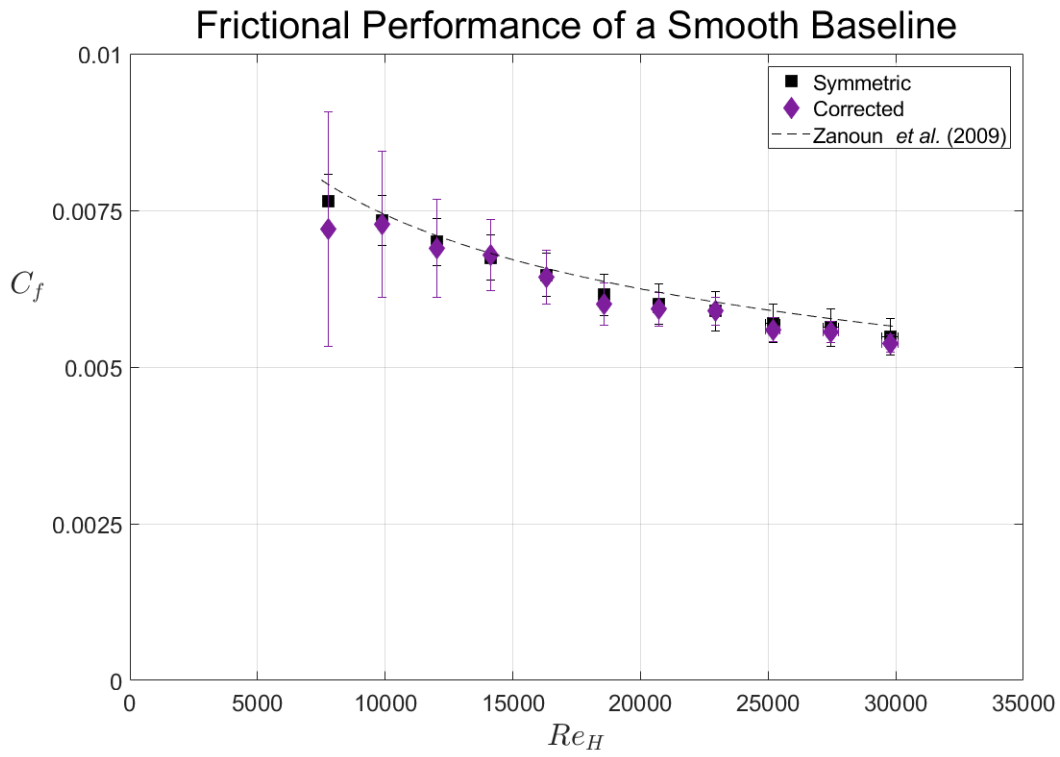

Figure 2.21: Measurements of a baseline smooth acrylic panel validate the method used to quantify frictional resistance of test surfaces and serve as a point of comparison for biofilm layers and rigid replicas. The correlation proposed by Zanoun *et al.* [58] (dashed line) is shown along with data calculated assuming symmetric walls (black squares) and corrected using PIV measurements (purple diamonds).

to channel asymmetry. In this case, the corrected data experience nearly twice the added drag compared with the result found when assuming symmetric channel walls (see §2.7 for details of the asymmetry correction).

$$\Delta C_f = \frac{C_{f,\,measured} - C_{f,\,smooth}}{C_{f,\,smooth}} \times 100\% \tag{2.7}$$

Figure 2.22 also reveals that the sand grain resistance curve displays Reynolds number dependence; although with a slighter decrease than is seen for the smooth baseline. The first two data points (below $Re_H = 12\ 000$) do not follow the trend seen for the rest of the data which appears to be a result of the asymmetry correction (data plotted assuming symmetric channel walls do not show this trend). Note that because uncertainty decreases with increasing C_f, the smaller uncertainty bounds for the corrected data in Figure 2.22 are contrary to what was observed for the smooth baseline data.

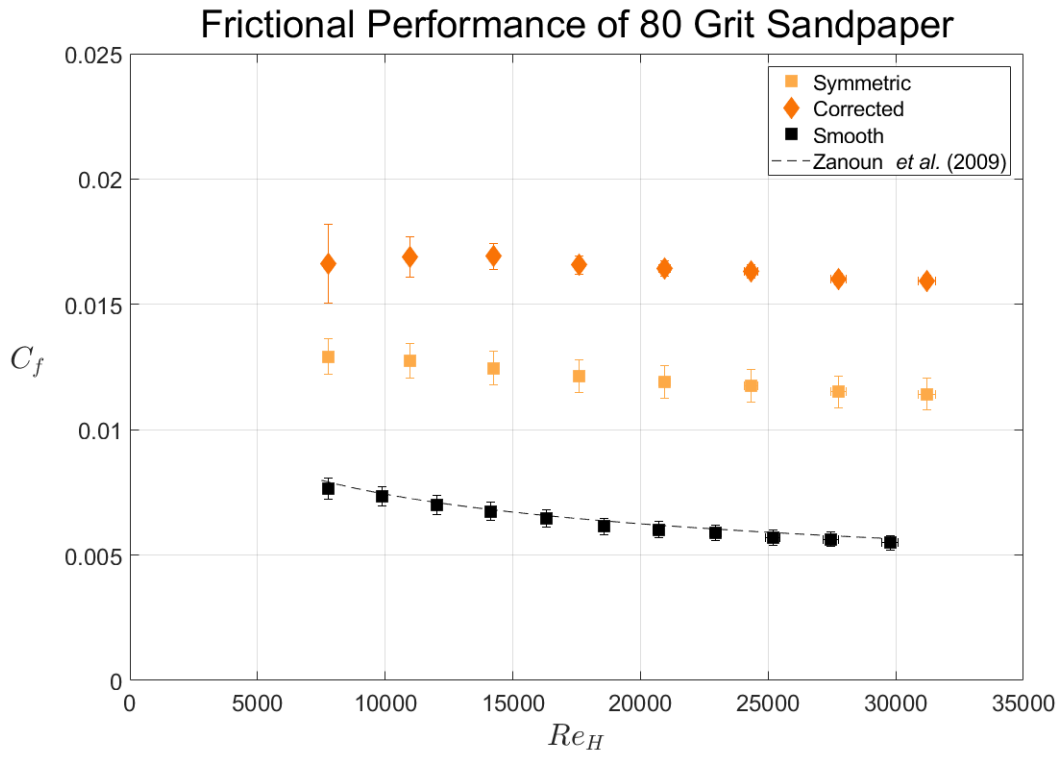

Figure 2.22: A panel covered in sand grain roughness shows a substantial (∼110–185%) increase in drag compared to the smooth baseline. Data corrected for the asymmetric channel walls (orange diamonds) show a significant increase in added drag ($\Delta C_f \approx 160\%$) as compared to results reported which assume symmetric boundaries (light orange squares, $\Delta C_f \approx 90\%$).

2.8.1 Mean Velocity Profiles Over Smooth Baseline and Sand Grain Roughness

Figure 2.23 shows the non-dimensional mean velocity profile using outer (Figure 2.23a) and inner (Figure 2.23b) scaling at a friction Reynolds number of $Re_\tau = 536$. Results from Direct Numerical Simulations (DNS) of turbulent channel flow at $Re_\tau = 550$ performed by Moser *et al.* [33] are shown alongside measured data in Figure 2.23a which confirm the PIV quality and demonstrate that flow through the SF3 is fully-developed and well conditioned. The same data are shown using inner layer scaling in 2.23b along with curves representing the viscous sublayer and logarithmic law of the wall. In this figure, the details of the near-wall region are clear and the measured mean velocity profile agrees with theory. A slight departure is present just prior to where the data begin to match the log layer. The cause of this irregularity is not clear, but the deviation appears to occur only in the high flow speed data and it does not limit the results reported comparing smooth flow behavior with that seen for flow

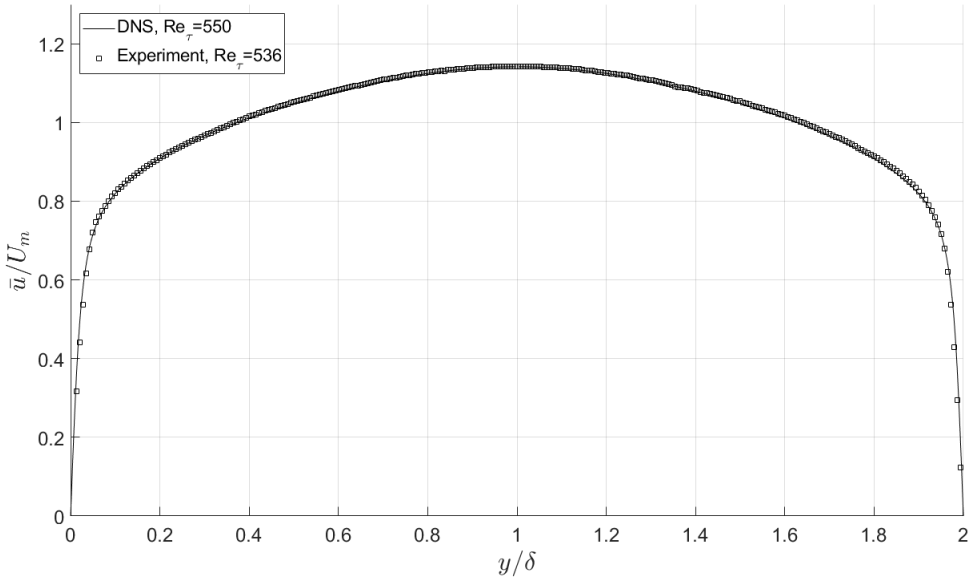

(a)

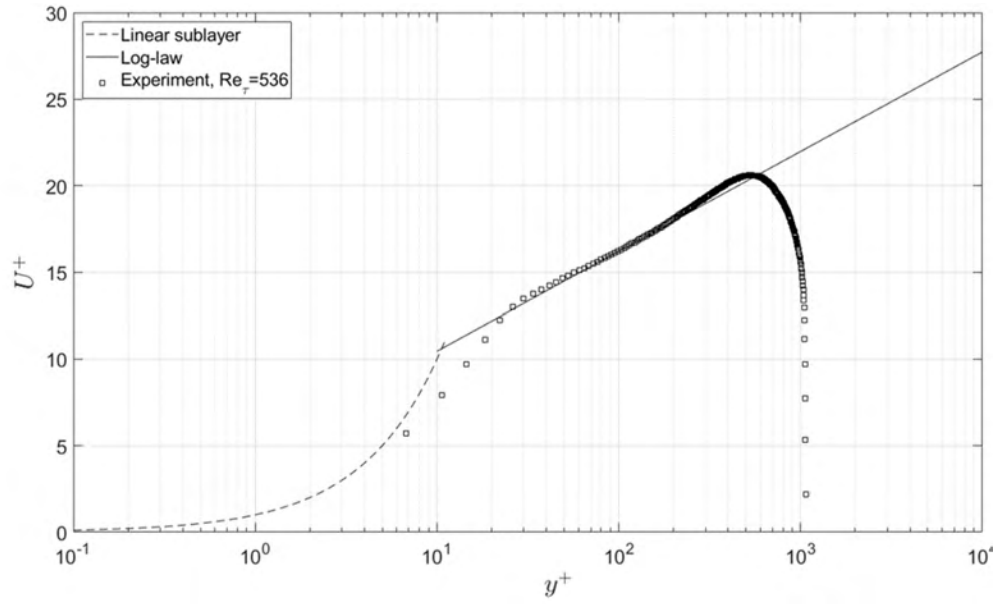

(b)

Figure 2.23: The mean velocity profile of flow through the SF3 test section is shown using (a) outer layer and (b) inner layer non-dimensionalizations. The results from PIV match those of DNS at a similar value of Re_τ [33].

over biofilm layers or rigid replicas. Note that it is also common to measure slight increases in mean velocity in the buffer layer.

While most of the PIV analysis relies only on results from the measured flow field, estimation of the wall shear stress was determined using pressure drop measurements.

In essence, the inner layer velocity profile data are scaled using the same values of C_f found from frictional analysis and therefore do not provide an entirely independent measure of the added drag. However, results from the PIV are used to independently estimate channel gap height and bulk mean velocity which are used when plotting velocity profile data.

Trials of a panel covered with 80 grit, water resistant sandpaper were performed to verify the measurements and analysis used to characterize roughness topography and mean velocity profiles. Figure 2.24 shows the results at $Re_\tau = 700$. Several differences are observed which hold for all of the rough-wall velocity profiles shown in this dissertation. Figure 2.24a displays the expected asymmetry in the mean velocity profile for the flow field over the sand grain roughness (SGR) which is due to the greater wall shear stress at the SGR surface (where $\frac{y+\epsilon}{\delta} = 0$). The increased resistance of the sandpaper is also manifested as a large shift in the roughness function, ΔU^+, in Figure 2.23b.

Shown in both graphs, highly resolved data characterize the development of the velocity profile beginning at the SGR surface and across the channel to the smooth bottom window. The data exhibit fully rough behavior in which high flow speeds lead to thinning of the near-wall sublayers relative to the sand grain roughness height. The result is a complete lack of viscous sublayer as shown in Figure 2.23b. Table 2.1 compares results of this study with the findings of Flack *et al.* [12] who measured a range of roughness types (including 80 grit sandpaper) in a variety of flow conditions.

Table 2.1: Comparison of 80 grit sandpaper roughness

	k_t [μm]	k_{rms} [μm]	s_k	k_u	k_s^+	k_s [μm]
Flack *et al.* [12]	546	67.9	0.497	4.49	36	529
Present study	671	72.8	0.663	3.67	105	657

Roughness values shown in Table 2.1 match well. The water-resistant sandpaper studied in this work had slightly greater trough-to-peak and root-mean-square roughness values than that studied by Flack *et al.* [12] which likely accounts for the difference in equivalent roughness height, k_s, but the offset may also occur because two different roughness flow regimes are shown. The results here are fully rough ($k_s^+ = 204$) while the findings of Flack *et al.* fall in the transitionally rough regime ($k_s^+ = 36$). Bearing in mind this distinction and acknowledging that measurements of the flow field over biofilm layers incur additional challenges—such as reflections off

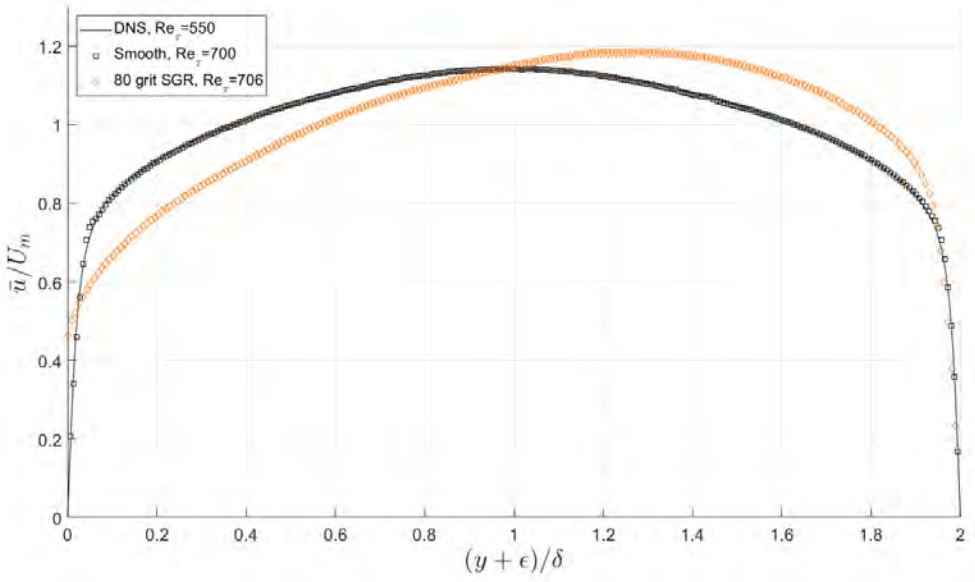

(a)

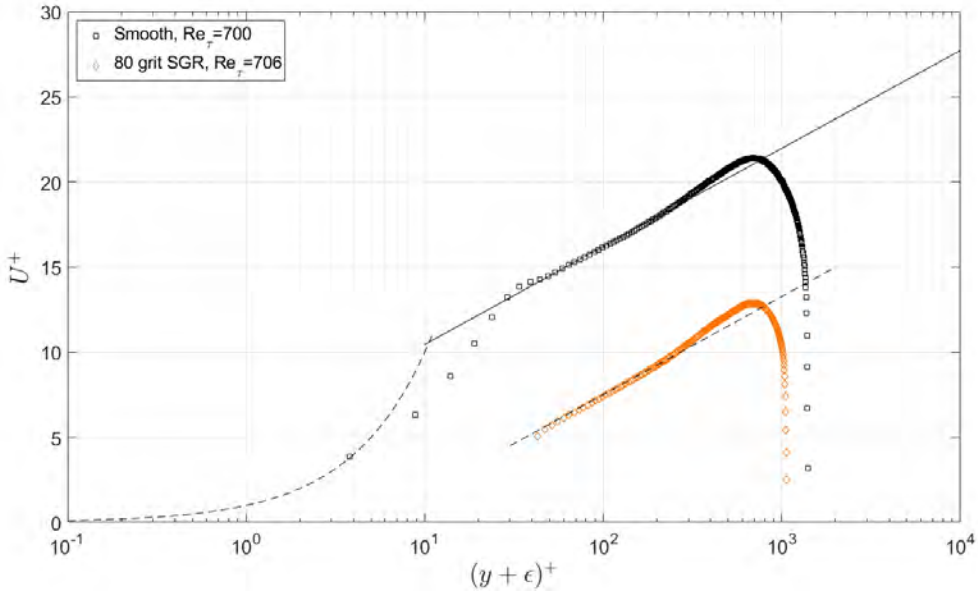

(b)

Figure 2.24: Turbulent flow over roughened surfaces (in this case 80 grit sandpaper, orange diamonds) experiences a drag increase which can be seen in (b) by a shift in the location of the log-layer data. This shift is the roughness function, ΔU^+. The asymmetric surface conditions of the top ($(y+\epsilon)/\delta = 0$) and bottom ($(y+\epsilon)/\delta = 2$) walls in the SF3 is evident by the shift in maximum velocity toward the smoother wall (shown in (a)).

streamers and local sloughing which can skew measurements taken for panels with little fouled area—the results shown above validate the PIV and flow field analysis performed in this dissertation.

CHAPTER III

Resistance of Biofilm Layers

3.1 Overview

The frictional performance of smooth panels covered in soft biofilm layers was investigated using a fully developed, high-aspect ratio water channel (the Skin Friction Flow Facility, SF3) at the University of Michigan's Marine Hydrodynamics Lab. Table 3.1 summarizes several key parameters of the experiments performed. As shown in this table, a total of 14 biofilm trials were conducted—five for biofilm layers grown between three and four weeks (termed three week biofilms), three consisting of biofilms grown four to five weeks (termed five week biofilms), and six trials were of biofilm layers grown for nine to ten weeks (termed ten week biofilms). These three nominal incubation times (IT) were chosen to investigate biofilm layers in various stages of development. The relatively sparse, non-uniform fouling of the three week biofilm layers complicated measurements, and analysis of their behavior was limited (as compared to the five and ten week trials). However, these less developed biofilms are of practical importance and of the three IT studied they appear most similar to the fouling observed on oceangoing vessels. Growing biofilms for four to five weeks produced relatively thin—yet fairly uniform—'adolescent' layers with short streamers. Biofilms grown for nine to ten weeks had dense coverage with longer, wider streamers which produced a textured look reminiscent of wet fur. Roughly two-thirds of the biofilm trials suffered from moderate or severe bulk sloughing which limited the range of flow speeds which could be explored. Despite the challenges of sparse coverage and sloughing, a range of flows over biofilm layers with various thicknesses and coverage were examined and the results presented here reveal insights into the nature of biofilm drag production.

Table 3.1: Matrix of biofilm experiments

Trial	**Surface**	**Flow Range,** Re_H	**Friction Velocity,** u_τ $[m/s]$	**Incubation Time** $[days]$	**Initial Thickness,** k_b $[\mu m]$	**Sloughing?**
FP	smooth	7800 – 29 800	0.064 – 0.208	–	–	–
SGR	sand grain—80 grit	7800 – 31 200	0.104 – 0.408	–	–	–
3W1	biofilm	8500 – 16 400	0.088 – 0.154	29	103	slight
3W2	biofilm	8000 – 25 900	0.079 – 0.198	28	200	severe
3W3	biofilm	9100 – 19 500	0.086 – 0.173	27	51	slight
3W4	biofilm	8200 – 21 400	0.095 – 0.208	26	198	moderate
3W5	biofilm	8400 – 21 100	0.095 – 0.205	25	195	moderate
5W1	biofilm	6500 – 19 500	0.093 – 0.218	32	1111	moderate
5W2	biofilm	7300 – 18 700	0.099 – 0.225	33	670	severe
5W3	biofilm	7200 – 20 400	0.104 – 0.282	35	761	slight
10W1	biofilm	5400 – 11 500	0.109 – 0.181	66	1900	moderate
10W2	biofilm	3900 – 13 800	0.116 – 0.287	67	2571	moderate
10W3	biofilm	5700 – 20 800	0.118 – 0.289	71	1725	moderate
10W4	biofilm	5900 – 13 900	0.114 – 0.209	66	1071	slight
10W5	biofilm	6100 – 24 700	0.084 – 0.219	67	1247	severe
10W6	biofilm	4200 – 29 800	0.08 – 0.473	71	1361	slight

3.2 Resistance of Biofilm Covered Surfaces

3.2.1 Three Week Biofilm Layers

Composed of living, adapting species and organic matter, a variety of biofilm layers were grown in this study that exhibited a range of structural characteristics and frictional performance. Biofilm layers grown on smooth acrylic panels for three weeks show a range of areal coverage similar to what can be observed on working vessels and study of their growth and frictional behavior is of practical importance. Table 3.2 summarizes the frictional performance of the three week biofilm trials and provides several parameters characterizing their structure. It is worth reminding the reader that the sparse, thin, and uneven coverage of the three week biofilm layers hampered accurate determination of the fouled area, A_b (and even challenged its definition). Despite the additional uncertainty in these measurements, comparisons can be made among the five trials and with the results found for the more developed biofilm layers presented in the following sections.

Table 3.2 summarizes data taken during both the evolving leg of the trial (during which panels may experience significant sloughing) and the stable portion (in which the areal coverage and roughness parameters typically do not vary greatly from their mean value). Measurements collected during the evolving leg of the three week biofilm trials reveal that four of the five fouled panels began with similar initial conditions. For these panels the initial average biofilm layer thickness, k_b, was between ∼100–200 μm, the beginning trough-to-peak roughness, k_t, around one millimeter, and about half of each surface was initially covered in measurable growth. Given these similarities it is not surprising that the added drag they experience (as defined in Equation 2.7) is also similar.

Results from the three week biofilm trials are summarized in Table 3.2 and shown visually in Figures 3.1—3.5. As accurate measurement of the fouled area could not be collected, the data have not been corrected to account for variations in biofilm thickness across the panel and—as a result—the effects of sloughing are magnified. Therefore, some caution should be taken when examining results for the evolving and stable biofilm layers.

Table 3.2: Results summary for three week biofilm trials

Trial	Re_H	Surface	ΔC_f [%]	A_b [%]	k_b [um]	k_{rms} [um]	k_t [um]
3W1	8500 – 16 420	Evolving	112–89	55–44	103–93	105–91	1077–900
		Stable	84	48	95	90	911
3W2	8040 – 25 870	Evolving	152–23	46–5	200–116	155–87	1216–693
		Stable	20	5	122	100	744
3W3	9110 – 19 540	Evolving	46–38	11–4	51–35	99–86	640–459
		Stable	30	6	40	97	605
3W4	8210 – 21 370	Evolving	119–61	50–13	198–128	102–61	1097–663
		Stable	60	11	110	64	679
3W5	8380 – 21 140	Evolving	130–64	63–40	195–134	133–100	1056–762
		Stable	65	37	143	114	846

The fouled panel investigated in Trial 3W3 showed significantly different behavior than was seen for the other trials. It had a particularly sparse biofilm layer with measurable fouling over only about a third of its surface (although a thin layer of streamers covering the entire panel was observed by eye). Initially, the average thickness of the biofilm layer was $k_b \approx 50$ μm and trough-to-peak roughness values were around $k_t \approx 600$ μm. These roughness values are about half of what was measured for the other three week biofilm trials and Trial 3W3 experienced about one-third the added drag. Note that while several measures characterizing the biofilm layers confirm Trial 3W3 as having a less developed biofilm layer, the initial root-mean-square surface roughness, k_{rms}, for all five biofilm layers appear to fall within a range of 120 $\pm$ 30 μm.

Data collected during the stable portion of the biofilm trials show significantly more variation among the panels. Measurements of the fouled area span ~50% to 5% and k_t values ranged from ~600–900 μm. The average added drag caused by the stable biofilm layers varied from 20% for Trial 3W2 to 84% for Trial 3W1. While uncertainty in measurements of the biofilm coverage increased substantially for the stable portions of the three week biofilm trials, visual inspection of the overhead images confirms the trend they reveal, as does examination of the trough-to-peak roughness values. However, it is notable that the average biofilm layer thickness, k_b, and root-mean-square, k_{rms}, values do not show the same deterioration—in fact, they appear to change little and values measured for the stable biofilm layer are similar to the average of what was measured while the surface was evolving.

The contradictory trends suggested between evolving and stable conditions may be explained by considering the measurement techniques used to estimate the fouled area, average biofilm thickness, and various roughness parameters. The values of the fouled area on a panel were derived from overhead camera images which are sensitive to color, saturation, and intensity. However, the biofilm thickness and roughness statistics are derived from representative laser scans taken along a strip covering the middle quarter of the entire length of a fouled panel, which—while somewhat sensitive to color—capture the surface topography better than the overhead photos. The laser scan data also seem to be relatively unbiased by the sloughed regions of the panel as only reflected light is measured.

Considering these measurement techniques and the values shown for stable biofilm in Table 3.2, it appears that regions of the panel covered in the thickest biofilm layer sloughed while regions with smaller features (e.g. smaller streamers) remained attached. Evidence in support of this claim includes the fact that darker portions

of fouling which can be measured by the overhead camera correspond to the thicker regions of fouling (where k_t is greatest). Furthermore, since k_t heights were derived from measurements taken at the same locations, a decrease in their value between different flow speeds could only occur by removal (or flattening) of the tallest portions of the biofilm.

Examination of the resistance curves for the three week biofilm trials confirms the proceeding findings. Figures 3.1—3.5 display the variation of C_f with flow rate as derived from pressure drop measurements alongside a series of overhead photos corresponding to the trial. These figures show the frictional behavior of the biofilm layer while evolving (right-pointing, light green triangles) and after reaching a stable state (left-pointing dark green triangles). All biofilm layers evaluated show signs of sloughing—both in the slightly steeper downward slope of the evolving data and the hysteresis between the evolving and stable curves.

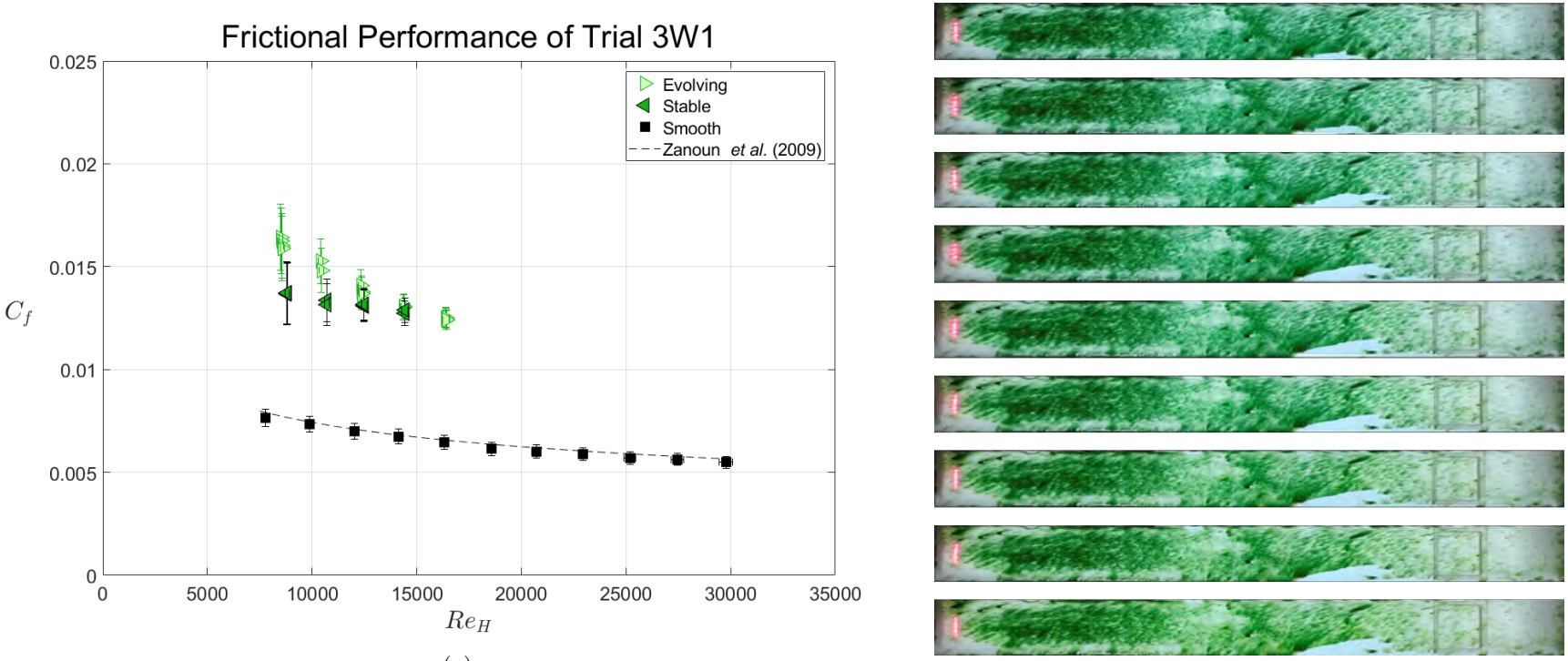

(a)

(b)

Figure 3.1: Trial 3W1 exhibited a very slight amount of sloughing. Resistance data in (a) show a drag increase of $\Delta C_f \approx$ 85–110% and only a moderate amount of hysteresis. Overhead pictures in (b) show the extent of fouling coverage. The top image in the series corresponds to the data at the beginning of the trial and the bottom images shows the fouling at the trial's end. The fifth image from the top was recorded at the maximum flow speed at the conclusion of the evolving leg of the trial (just before the stable portion began).

(a)

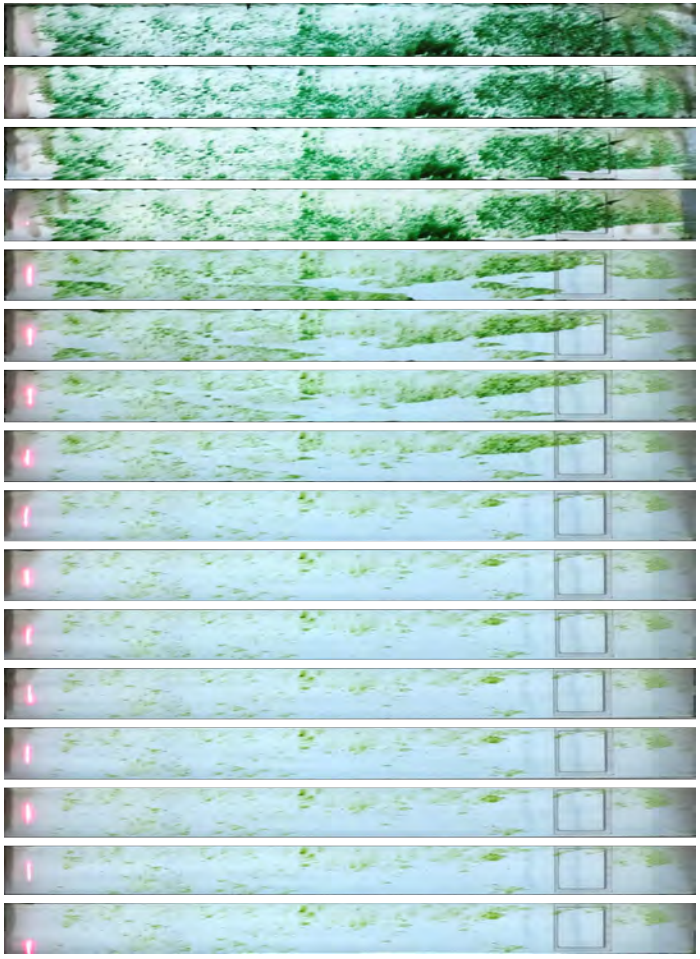

(b)

Figure 3.2: Trial 3W2 experienced severe sloughing. In (a) the drag increase begins at $\Delta C_f \approx 150\%$ but quickly drops to $\Delta C_f \approx 20\%$ then follows the trend seen for the smooth baseline. The maximum flow speed corresponds to the ninth image from the top in (b).

(a)

(b)

Figure 3.3: The panel with the least amount of fouling was evaluated in Trial 3W3. The added drag was roughly $\Delta C_f \approx 40\%$ as shown in (a). The panel experienced only a slight amount of sloughing as shown in (b). The peak flow speed was experienced in the sixth image from the top. Part of a clamp can be seen in the first two images which was later moved. Clamping is a precautionary measure used to keep the SF3 test section from expanding at elevated flow speeds.

(a)

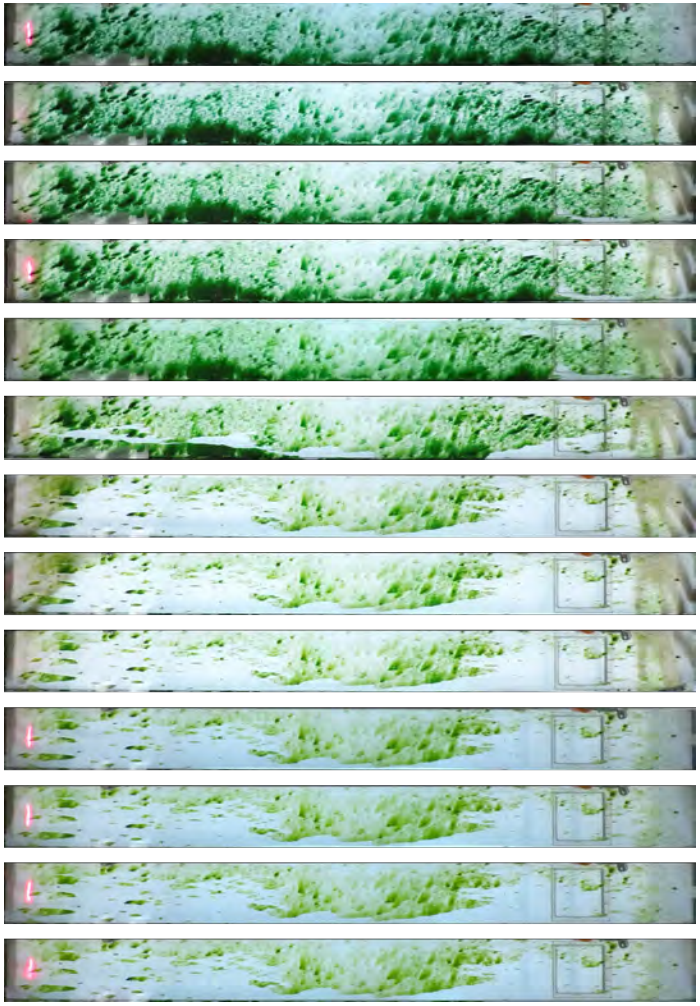

(b)

Figure 3.4: Resistance data for Trial 3W4 (a) show $\Delta C_f \approx 120\%$ initially which decreased to $\Delta C_f \approx 60\%$ after sloughing. The seventh image from the top in (b) was recorded at the maximum flow speed.

(a)

(b)

Figure 3.5: Resistance data for Trial 3W5 resemble those seen in Figure 3.4 with $\Delta C_f \approx 130\%$ initially and $\Delta C_f \approx 65\%$ after sloughing. The seventh image from the top in (b) was recorded at the maximum flow speed. Note that the reflection of overhead fluorescent lighting seen near the leading edge of the panel did not affect calculation of the fouled area.

The least amount of sloughing occurred during Trials 3W1 and 3W3, the most deterioration was experienced in Trial 3W2, and both Trials 3W4 and 3W5 showed moderate sloughing. Figure 3.1 reveals that C_f values for Trial 3W1 are roughly double what is seen for the baseline curve and the added drag values for this trial ranged between $\Delta C_f = 84$–112%. Reynolds number dependence is apparent for both the evolving and stable biofilm layers. As previously mentioned, the stronger link between flow speed and resistance for the evolving data is attributed to sloughing of biofilm from the panel surface. The Reynolds number dependence of the stable biofilm fouling appears to match the smooth baseline values—a trend that is often observed across the various panels and incubation times. Note that the similarity in slope between the smooth plate baseline and stable biofilm indicate that the added drag, ΔC_f, is relatively *independent* of Reynolds number which has important implications in the scaling analysis and prediction of C_f discussed at the end of this chapter.

Figure 3.3 shows that the biofouled panel examined in Trial 3W3 had similar frictional performance to Trial 3W1 but at a reduced magnitude. Here $\Delta C_f = 30$–46% and the values of C_f for the evolving surface are much closer to the baseline values than for any of the other trials. Overhead images in Figure 3.3b confirm that this panel has the least amount of fouling.

Figure 3.2 shows that Trial 3W2 had the strongest amount of sloughing. Initially, the coefficient of friction was about two and a half times that of the reference baseline corresponding to $\Delta C_f = 152\%$. However, the added drag drops sharply to 65% at $Re_H \approx 16\ 000$ which corresponds with the fifth overhead image in Figure 3.2b where it can be seen that significant portions of the biofilm layer were lost from the downstream half of the panel (where measurements of the pressure drop are collected). The surface continues to slough somewhat until the maximum flow speed is achieved. The resistance curve for the stable biofilm layer shows fairly good agreement with the baseline values at an offset $\Delta C_f = 20\%$. This is quite close to what was measured for the stable data in Trial 3W3 which also had a measured fouled area of $\sim$5%.

Results from Trials 3W4 and 3W5 appear to be quite similar with both fouled panels initially displaying $\Delta C_f \approx 120$–130% with significant drop-off after substantial sloughing occurs. The stable data for these two trials are also similar with Trial 3W4 having $\Delta C_f = 60\%$ and Trial 3W5 slightly higher with $\Delta C_f = 65\%$. Differences in the stable fouled area are substantial being 11% and 37% respectively. This is unexpected as most results show that the amount of added drag loosely corresponds to the fouled area. Poor estimation of the fouled area is likely the reason for the unexpected trend between ΔC_f and A_b for these trials.

3.2.2 Five Week Biofilm Layers

Unlike the sparse fouling observed for three week biofilms, the fuller growth of the five and ten week biofilm layers produced images from which the fouled area of a panel could be accurately determined. A record of pictures taken throughout the duration of each trial provided a history of the sloughing and was used to estimate the average channel gap height, H_{AVG} (details are provided in §2.7). This correction has been applied to all of the five and ten week results discussed in this dissertation. Note that while the effects of sloughing seen in the three week resistance curves are still observable in the C_f plots for the five and ten week growth, the data recorded after significant sloughing do not experience an 'out-sized' decrease in the magnitude of C_f and instead more faithfully reflect the drag experienced by each panel for its surface condition.

As mentioned previously, the biological nature of the roughness being studied leads to inconsistencies that must be taken in stride. Perhaps nowhere is this more evident than in the results shown below for biofilm layers grown for five weeks. All three panels tested with this incubation time were grown under the same flow rate and lighting conditions and at the same time; yet, the biofilm characteristics measured for the three trials show substantive differences and a wide range of proclivity toward sloughing. Table 3.3 summarizes the primary results from these trials. All three of the five week biofilm layers show significantly greater initial layer thickness and fouled area than was observed in the three week biofilm trials.

The roughness values of the five week biofilm layers are also larger than those measured for the three week trials; however, while the average initial biofilm thickness increased roughly five times for the five week IT, the corresponding increase in the initial roughness heights is only a factor of about one and a half. The added drag measured for the five week biofilms spanned from $\Delta C_f = 121$–191% before the surfaces experienced significant sloughing which ranged from severe (Trial 5W1) to moderate (Trial 5W2) to slight (Trial 5W3). While the initial average thickness of the five week biofilm layers shows a fairly wide variation, the roughness values appear to be similar with initial values of $k_t \approx 1500$ μm and $k_{rms} \approx 200 \pm 30$ μm. The slight elevation in measured roughness for Trial 5W2 may stem from the different growth pattern displayed for this panel (see Figure 3.7b) which appeared more as a collection of bulky streamer clumps than a contiguous layer. Measurements of streamer geometry are also included in Table 3.3. Streamer geometry was only measured for biofilm layers having $A_b \gtrsim 80\%$.

Table 3.3: Results summary for five week biofilm trials

Trial	Re_H	Surface	ΔC_f [%]	A_b [%]	k_b [μm]	k_{rms} [μm]	k_t [μm]	L_s [μm]	D_s [μm]	λ_z [μm]	λ_x [μm]
5W1	6540 – 19 550	Evolving	121–102	99–99	1111–927	174–158	1557–1362	5610	1520	2420	8840
		Stable	65	13	853	169	903	–	–	–	–
5W2	7350 – 18 700	Evolving	150–111	93–58	670–665	224–209	1826–1905	6020	1470	2480	9150
		Stable	104	41	705	220	1864	–	–	–	–
5W3	7240 – 20 410	Evolving	136–191	99–93	761–649	179–150	1476–1303	5910	1360	2490	9300
		Stable	168	92	642	165	1425	6570	1510	2580	11 120

Resistance curves and overhead images of the five week biofilm layers are presented in Figures 3.6—3.8. These figures show that the added drag initially experienced for the five week biofilm layers was about the same as was observed in the three week trials. This is surprising given the more uniform cover and greater layer thickness measured for longer incubation times. Although this could be a result of the fact that the five week data have been corrected for H_{AVG} while the three week trials have not, it may also indicate different frictional behavior for sparse biofilm layers. The stable data do not follow this trend with the stable five week biofilm data showing $\Delta C_f \approx 100\%$ where the stable three week biofilm layers had $\Delta C_f \approx 60\%$. The added drag measured for the stable portions of each five week trial vary significantly according to the level of sloughing that each experienced. Reynolds number similarity observed in the plots for five week biofilm layers resembles that seen for the three week trials and ΔC_f again appears to be independent of Reynolds number for all the stable biofilm layers and most of the evolving biofilms as well.

The added drag measured for Trial 5W1 ranged from $\Delta C_f = 121$–102% for the evolving portion of the curve and $\Delta C_f = 65\%$ on average for the stable biofilm layer. Severe sloughing is evident in Figure 3.6 and the overhead images shown in Figure 3.6b also reveal that the fouling was uneven in span which affects the assumption of two-dimensional flow across the channel; however, extreme sparseness of the fouling and narrowness of the channel help to maintain somewhat well-behaved flow.

Results in Figure 3.7 show that a moderate amount of sloughing occurred during Trial 5W2. Measurements taken at the maximum flow speed reveal that the rate of sloughing was relatively slow as several rounds of pressure drop measurements were collected before the panel reached a stable condition. This provides a nice capture of the transition from an evolving to stable surface. Added drag ranged from $\Delta C_f = 150$–111% for the evolving biofilm layer and an average of $\Delta C_f = 104\%$ was measured for the stable portion of the trial. Overhead images shown in Figure 3.7b also reveal a different fouling pattern than seen for most of the other developed biofilm layers (i.e. the five and ten week ITs). Rather than appearing as one continuous layer, a dense network of small biofilm patches is seen with portions of unfouled (or lightly fouled) panel between them. This growth pattern is particularly evident for the first half of the panel and it may explain why the roughness values shown in Table 3.3 are larger than those seen for the other five week trials while the average layer thickness is substantially less.

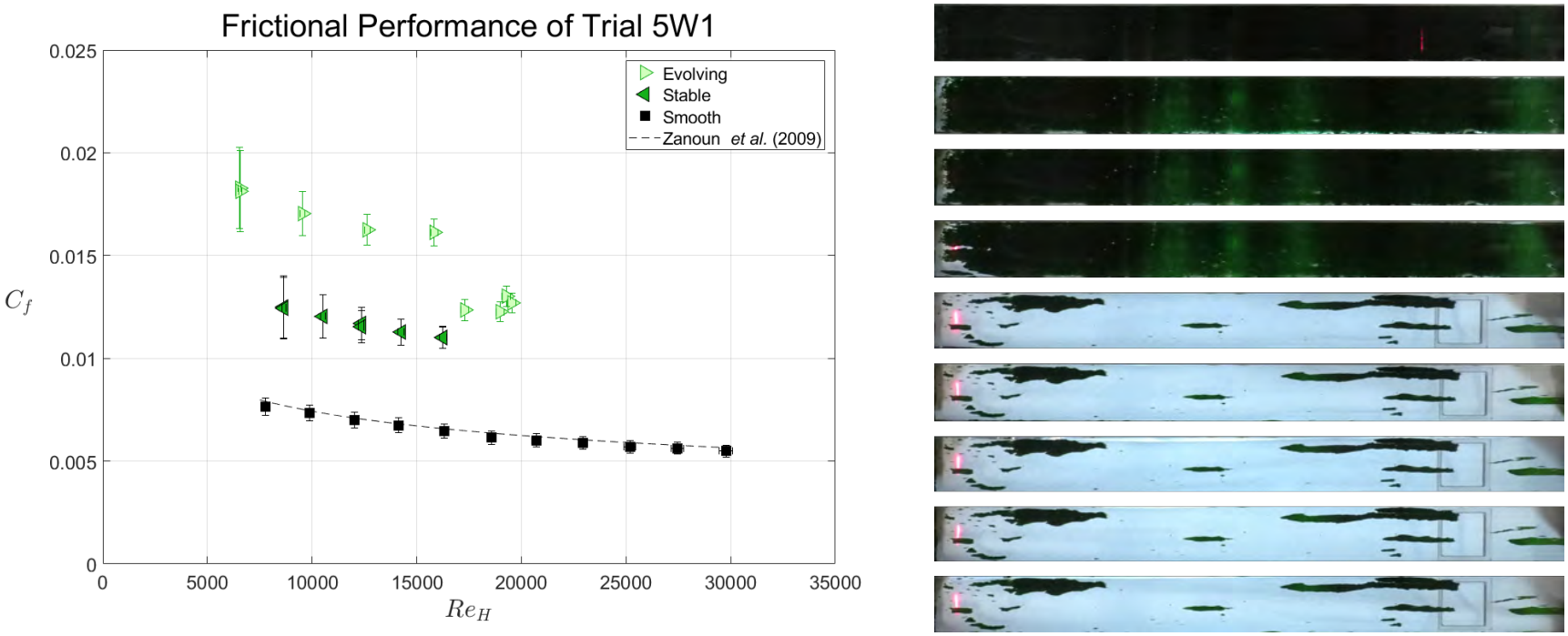

(a) (b)

Figure 3.6: Severe sloughing occurred in the evolving leg of Trial 5W1 as seen in the resistance data (a) and overhead images (b). The fifth image from the top in (b) was recorded during the maximum flow speed. Note that the heterogeneity in surface condition during the stable portion of the trial may violate the assumption that flow is two-dimensional through the SF3 test section.

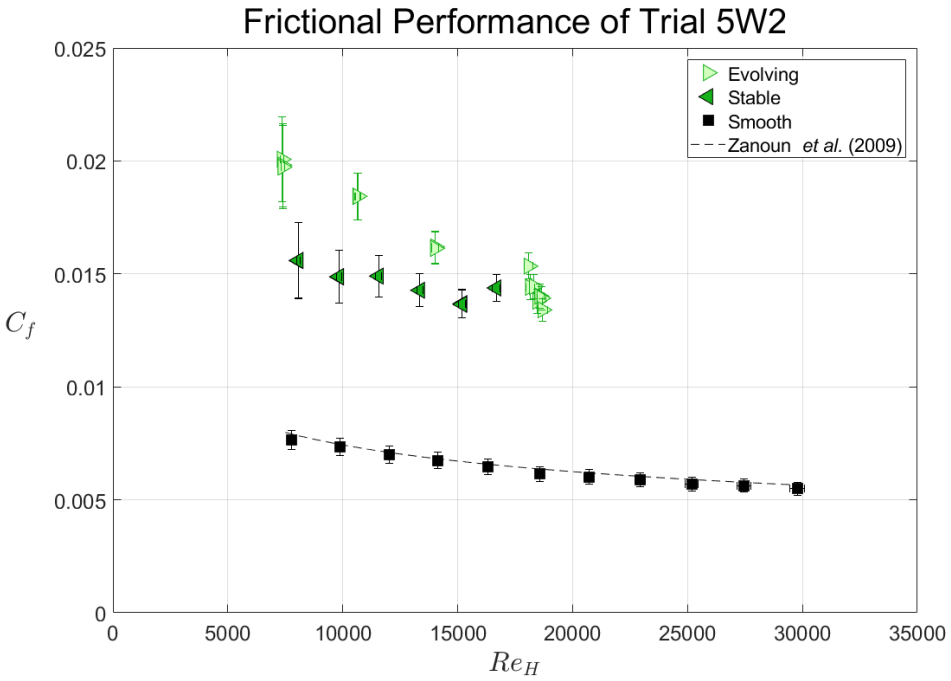

(a)

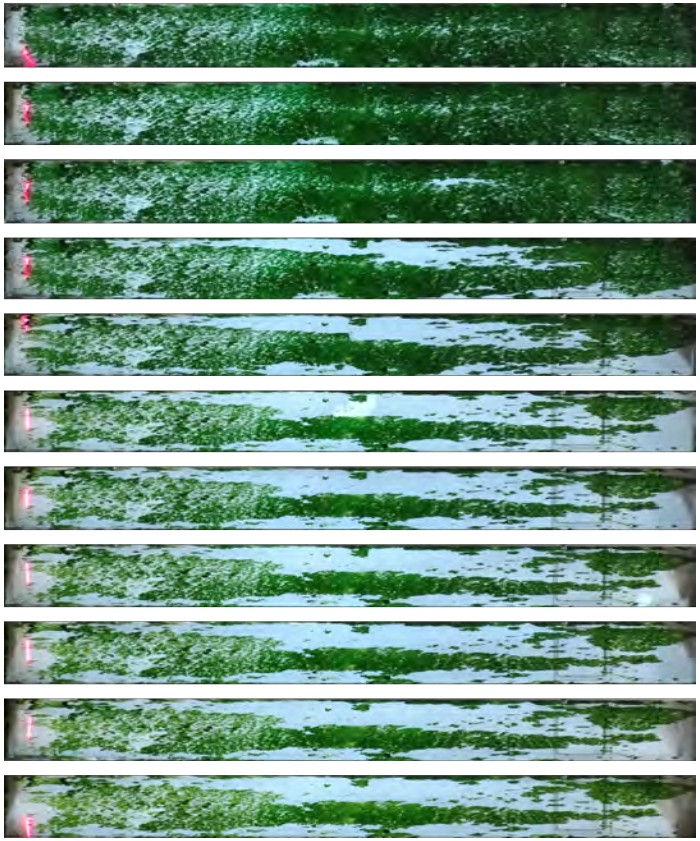

(b)

Figure 3.7: Only moderate sloughing occurred in Trial 5W2 which is reflected in a smaller hysteresis offset in the resistance data (a) between the evolving (right-pointing, light green triangles) and stable (left-pointing, dark green triangles) biofilm layers. The fourth images from the top in (b) was recorded during the maximum flow speed. Some sloughing continued after this as seen in the fifth image down (and also in the stable resistance data). Note that growth shown in (b) appears to be less uniform as compared to the other five week biofilm trials.

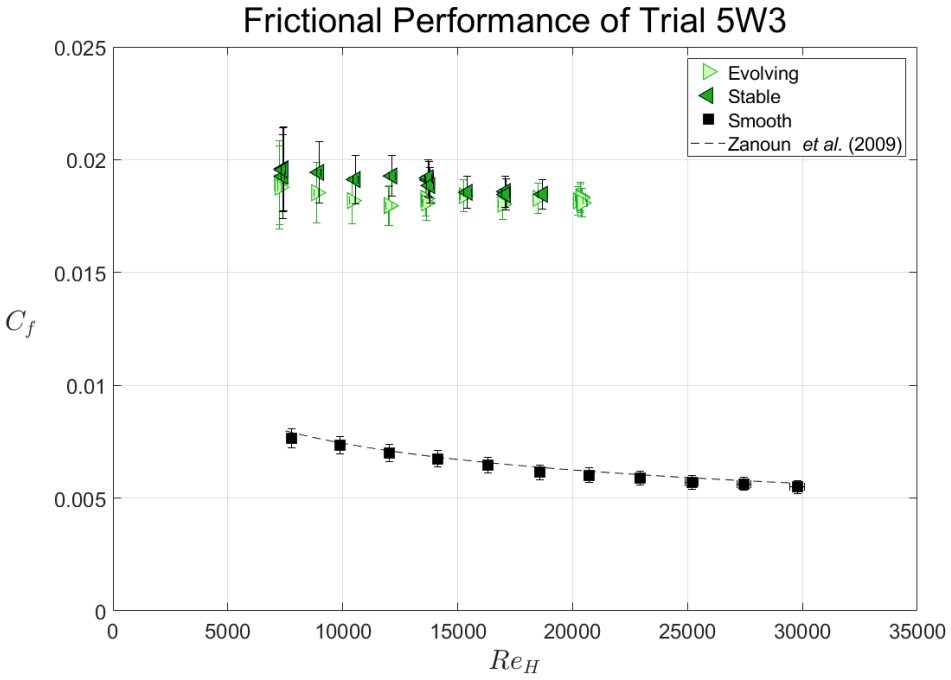

(a)

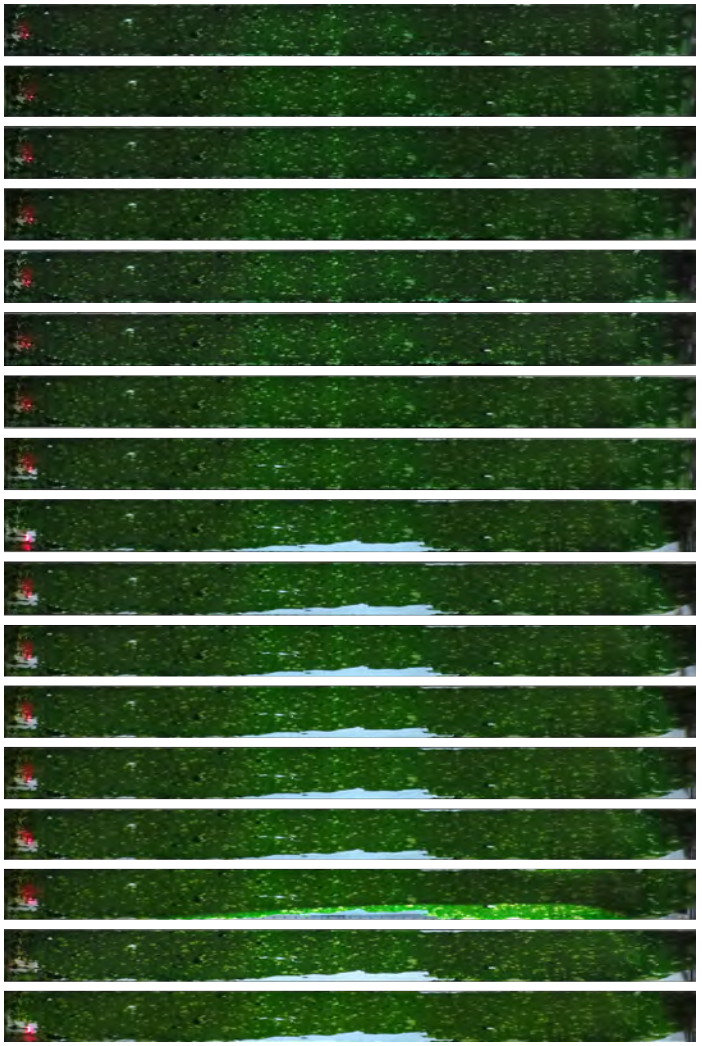

(b)

Figure 3.8: Very little sloughing was observed in Trial 5W1 and the resistance data (a) for the evolving and stable biofilm layers lie on top of one another. The picture series in (b) has been compressed for display purposes but the limit of sloughing can still be observed. The ninth image from the top shows the biofilm layer after the maximum flow speed was achieved.

The final five week biofilm trial shows consistent behavior between the evolving and stable portions of the trial which is due to a very slight amount of sloughing. The resiliency of this biofilm layer allowed a greater maximum flow speed to be achieved as seen in Figure 3.8. The resistance curves here appear to show slightly less Reynolds number dependence than was observed for most trials. Data points from the evolving and stable portions of the trial lie on top of one another within measurement uncertainty. The added drag for this biofilm layer ranged from $\Delta C_f =$ 136–191% with an average around 168%. These values align with those seen for the evolving legs of the other five week biofilm trials.

3.2.3 Ten Week Biofilm Layers

Six trials were performed which evaluated the structural geometry and frictional performance of biofilm layers grown on smooth acrylic panels for ten weeks. Several key results are summarized in Table 3.4. The added drag measured on these panels ranged from $\Delta C_f =$ 199–364% before sloughing occurred showing a substantial increase compared to the biofilm layers grown for shorter incubation times. The average layer thickness and roughness parameters were also significantly higher for the more mature biofilm and had a wider range with $k_b \approx$ 1100–2600 μm, $k_{rms} \approx$ 250–700 μm, and $k_t \approx$ 2400–3550 μm. As in the five week trials, biofilm layers grown for ten weeks covered nearly the entire exposed surface of the panels at the beginning of each trial and measurements of the channel gap height correct for sloughing effects using overhead images.

Results from the stable portion of the trials show that various amounts of sloughing were experienced by each panel with final fouled areas ranging from $A_b =$ 2–93%. The range of added drag measured for stable biofilm layers was correspondingly large with $\Delta C_f =$ 14–224%. Changes in the roughness values for the stable biofilm layers could be minimal or substantial and will be discussed in more detail below. Figures 3.9—3.14 present the resistance curves and overhead images for the ten week biofilm trials. Note that there are only two images shown for Trial 10W6 which is because the overhead camera was not installed above the SF3 test section at that time. Measurements of streamer geometry are also included for biofilm layers with $A_b \gtrsim 80\%$.

Table 3.4: Results summary for ten week biofilm trials

Trial	Re_H	Surface	ΔC_f [%]	A_b [%]	k_b [μm]	k_{rms} [μm]	k_t [μm]	L_s [μm]	D_s [μm]	λ_z [μm]	λ_x [μm]
10W1	5370 – 11 510	Evolving	210–219	96–42	1900–1775	248–387	2380–2946	7540	2450	3080	10 990
		Stable	211	42	1710	365	2660	–	–	–	–
10W2	3870 – 13 810	Evolving	364–333	98–68	2571–2049	277–219	2814–2128	8540	2030	3120	12 820
		Stable	224	67	1926	350	2556	–	–	–	–
10W3	5720 – 20 810	Evolving	297–173	85–44	1725–1513	694–512	3555–2959	9720	2880	5040	19 660
		Stable	162	41	1457	495	2544	–	–	–	–
10W4	5890 – 13 920	Evolving	272–186	100–85	1072–1003	332–287	2978–2187	8160	2100	3350	11 730
		Stable	159	76	1061	291	2176	–	–	–	–
10W5	6060 – 24 700	Evolving	230–17	100–2	1247–1077	280–487	2382–1993	6330	2040	3180	10 630
		Stable	14	2	392	293	1458	–	–	–	–
10W6	4180 – 29 770	Evolving	199–270	99–93	1361–1092	322–259	2712–1754	7340	1780	2930	10 390
		Stable	197	93	1060	197	1861	6490	1770	2680	9010

The resistance curves shown in Figure 3.9 span a significantly smaller range of Reynolds numbers than was observed for the three and five week biofilm layers. This is in part due to the reduced channel gap height caused by the increased thickness of the biofilm layer, and in part because sloughing generally seemed to occur at lower flow speeds for thicker biofilm layers and these trials were limited in flow speed to prevent complete loss of the biofilm layer. The data in this figure show a marked increase in resistance as compared to the three and five week biofilm trials which is similar to what is observed for most of the other ten week biofilm trials. Although a moderate amount of sloughing is observed in Figure 3.9b, no hysteresis is seen in the resistance data shown in Figure 3.9a.

Since the correction for H_{AVG} accounts for lost fouled area, the hysteresis typical of most resistance data should correspond with other changes in the biofilm layer—in particular 'trimming' of the streamers might be responsible for the hysteresis between most evolving and stable biofilm layers. Roughness measurements collected for Trial 10W1 show that k_b, k_{rms}, and k_t all remain similar between the evolving and stable portions of Trial 10W1 which would indicate that trimming does not occur. In fact, a substantial increase is seen in k_{rms} and k_t which likely corresponds to a portion (or multiple portions) of biofilm which have become detached from the panel but have not sloughed downstream (i.e. portions which 'flap' in the flow). Furthermore, if there are patches of biofilm that are 'flapping' in the flow, they may provide a drag increase which makes up for the decrease due to other changes in the layer (i.e. sloughing). While the behavior is slightly different than what is observed for most of the other biofilm layers that experience bulk sloughing, resistance data for Trial 10W1 do not show significant deviation from what was observed in the other biofilm trials.

The results of Trial 10W2 are shown in Figure 3.10. As shown in Table 3.4, the biofilm layer in this trial was by far the thickest and initially measured to be $k_b = 2571$ μm; yet a wide range of Reynolds numbers was achieved and the roughness of the panel is surprisingly muted with $k_{rms} \approx 250$ μm and $k_t \approx 2500$ μm for the evolving layer. The initial added drag was also the largest in this trial with $\Delta C_f = 364\%$. Sloughing is evident in Figure 3.10b and ranges over a large portion of the SF3 test section in which the pressure drop measurements were collected. The data largely follow the trends seen for most biofilm layers studied in this work although there is a slight 'hump' in the evolving resistance curve near the upper limit of the Reynolds number range. No explanation for this behavior is immediately evident but—within uncertainty bounds—it does not significantly alter the Reynolds number dependence observed for the evolving leg of a biofilm trial.

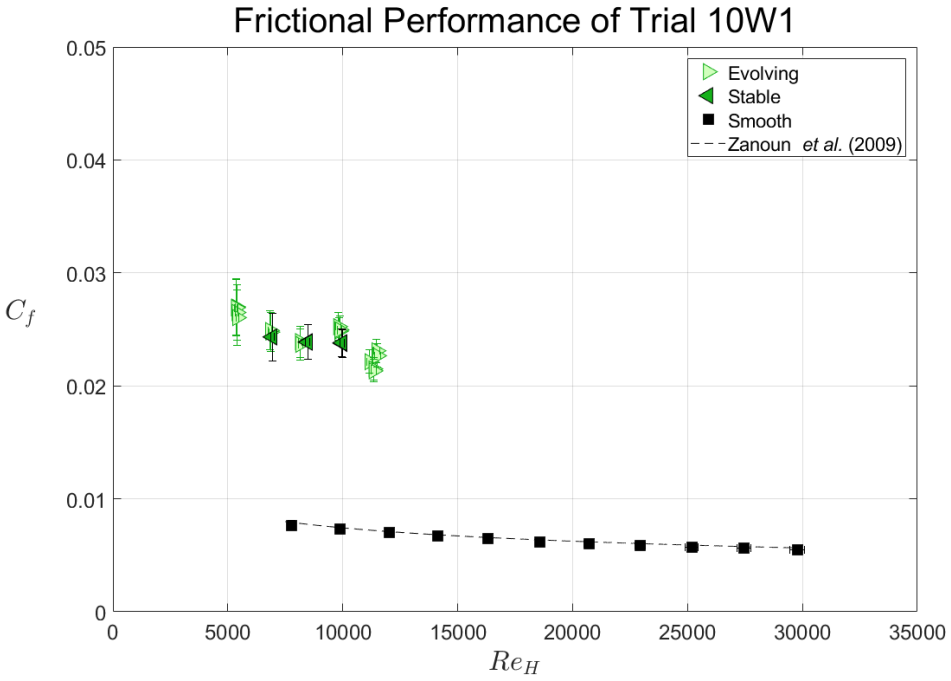

(a)

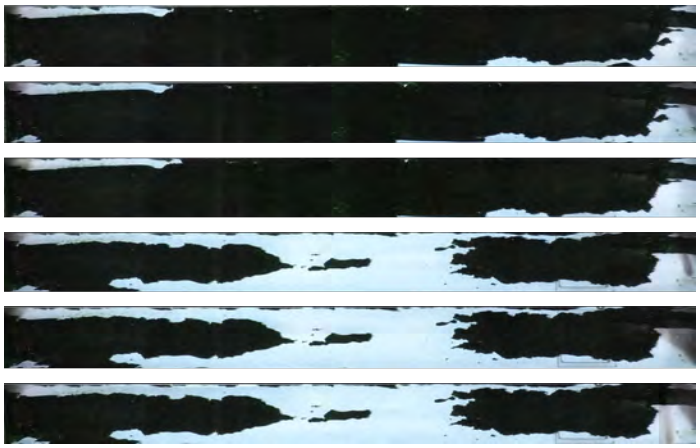

(b)

Figure 3.9: Resistance data (a) collected for Trial 10W1 do not show the hysteresis common in most other trials which also exhibited sloughing. Although the cause behind the lack of hysteresis is unknown it may related to the elevated values of k_{rms} and k_t seen in the stable portion of Trial 10W1. Overhead images in (b) show that the surface experiences a moderate amount of sloughing after the maximum flow speed was achieved (seen in the fourth image from the top in (b)).

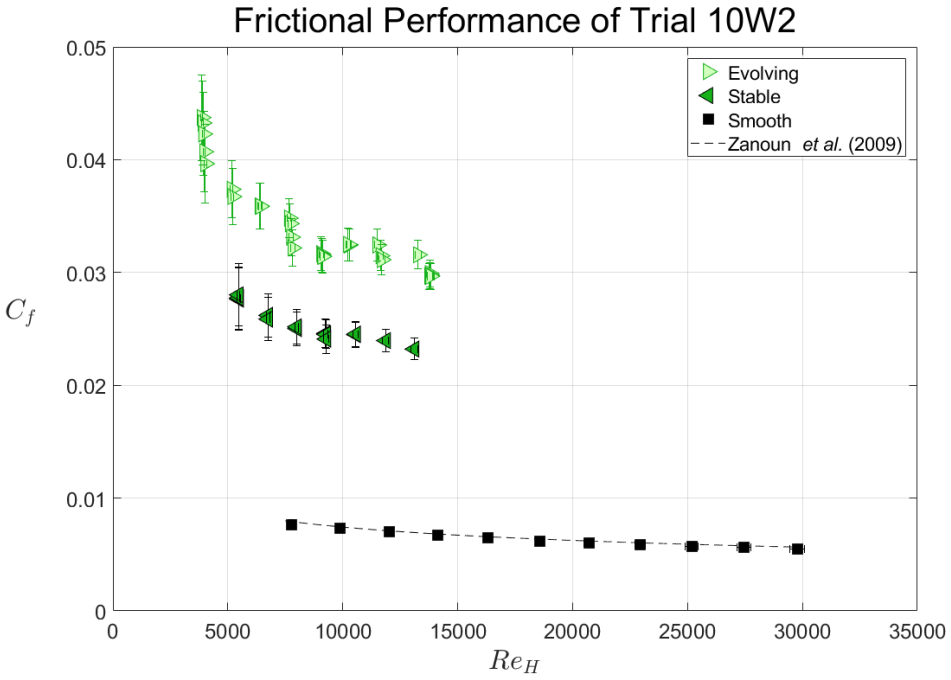

(a)

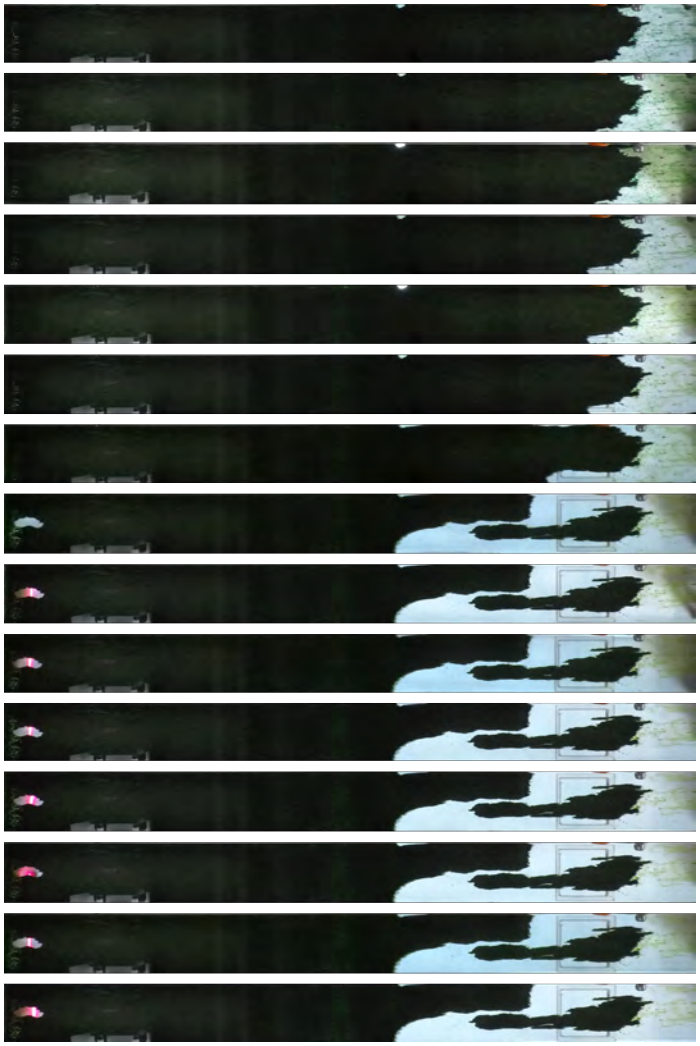

(b)

Figure 3.10: The biofilm layer was thickest in Trial 10W2 which also shows the greatest drag penalty, ΔC_f, as seen in (a). Overhead photos (b) show that sloughing was limited to the downstream half of the panel. The eighth panel from the top in (b) corresponds to the maximum achieved flow speed.

Figure 3.11 displays a much wider range of flow rates than seen for the prior two trials. Initially the added drag for this panel was $\Delta C_f = 297\%$; but, due to what appears as a relatively constant rate of sloughing, it eventually reduces to $\Delta C_f = 173\%$ by the end of the evolving leg of the trial. The resistance curve for the stable portion of the trial shows Reynolds number dependence matching what is seen for the baseline curve albeit at an average added drag of $\Delta C_f = 162\%$.

Overhead photos in Figure 3.11b reveal that growth of the biofilm layer on the panel investigated in Trial 10W3 was somewhat different than what was seen for the other ten week biofilm trials. While the other biofilm layers appear to grow almost as a single unit of uniform thickness or a collection of small biofilm patches having similar thickness and roughness topography, this panel appears to be covered in some portions that are substantially darker (and therefore thicker) than other areas. The average initial layer thickness for this trial was $k_b = 1725$ μm and it had substantially higher roughness values than the other ten week biofilm layers ranging from $k_{rms} =$ 694.4–511.8 μm and $k_t = 3555.1$–2959.3 μm for the evolving biofilm layer to an average $k_{rms} = 494.8$ μm and $k_t = 2544.2$ μm for the stable biofilm layer. Such results are not surprising given the appearance of the differing areas of biofilm growth observed in the overhead images. Despite these differences in biofilm layer structure, its frictional performance does not appear to fall outside of the behavior generally observed for a ten week biofilm layer—a somewhat surprising result.

Data in Figure 3.12 show that the panel examined in Trial 10W4 had an initial added drag of $\Delta C_f = 272\%$, modest Reynolds number range, and steep decline in C_f for the evolving biofilm layer. The stable portion of the trial shows similar Reynolds number dependence to the baseline curve with a drag penalty of $\Delta C_f = 159\%$. The difference in Reynolds number dependence between the evolving and stable halves of Trial 10W4 indicate that evolution of the biofilm layer was significant. Investigation of the roughness data shows that k_b and k_{rms} are not significantly altered but k_t does decrease substantially (by $\sim$800 μm).

(a)

(b)

Figure 3.11: The biofilm layer investigated in Trial 10W3 appears significantly different from most examined in this work as can be seen visually in (b). Despite the apparent differences in layer formation, the frictional behavior (a) appears quite similar to what was observed in other trials. Note that the eighth image from the top was captured while the panel was exposed to the maximum achieved flow speed.

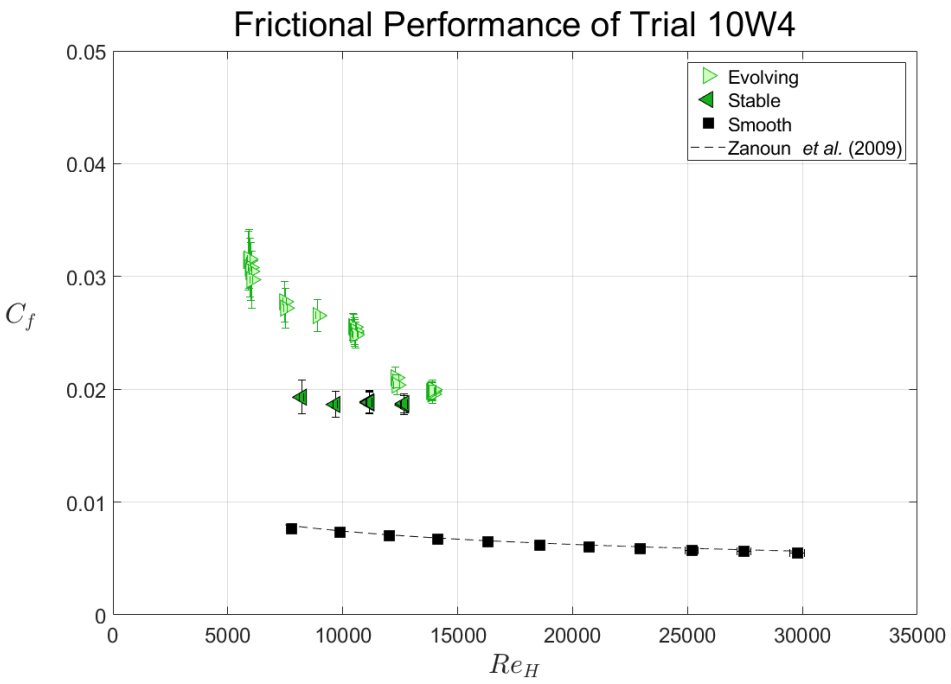

(a)

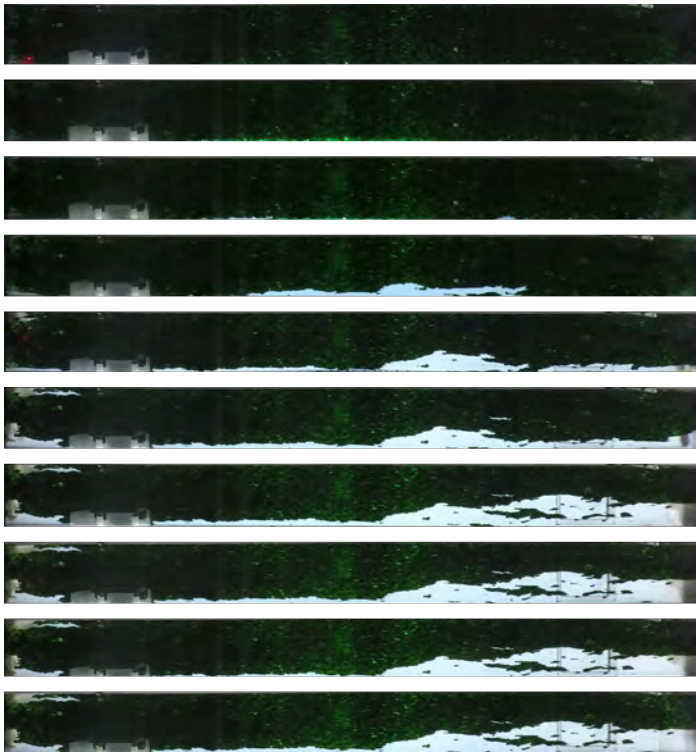

(b)

Figure 3.12: A modest Reynolds number range and relatively significant Reynolds number dependence were displayed in Trial 10W4 resistance data (a). Sloughing was relatively subdued as evidenced by the photo series in (b). Sloughing appeared to occur even after the maximum flow speed was recorded in the fifth image down as the seventh image down in (b) shows loss of the biofilm layer. Despite this, the stable resistance data appear unaffected.

Much like Trial 5W1, severe sloughing was observed for Trial 10W5 as evidenced by Figure 3.13. The first half of the evolving resistance curve shows good agreement with the other ten week biofilm trials but after $Re_H \approx 12\,500$ a sharp deterioration of the biofilm layer covering the panel is observed until the fouled area covers only 2% of the panel. The corresponding change in channel gap height is manifested as a sharp increase in Reynolds number and substantial decrease in the coefficient of friction which eventually settles just above the reference baseline curve with $\Delta C_f = 14\%$. This increase is minimal compared to what was initially experienced by the panel, but it is surprising that such a small amount of fouling can lead to a measurable increase in resistance.

Just as the severe sloughing observed in Trials 5W1 and 10W5 show similar outcomes in the frictional performance of the corresponding biofilm layers, the slight sloughing experienced in Trials 5W3 and 10W6 also show similar behavior. No discernible Reynolds number dependence is seen in Figure 3.14, and the added drag for both the evolving and stable surfaces is around $\Delta C_f = 200\%$ on average. Roughness measurements for the biofilm layer evaluated in Trial 10W6 appears to be similar with what was observed for most ten week biofilm layers ($k_b = 1361$ μm and $k_{rms} \approx$ 322.4–259.1 μm and $k_t \approx 2711.8$–1753.6 μm). Surprisingly, stable values for the layer thickness and root-mean-square roughness are measurably lower than those seen in the evolving leg of the trial with $k_b = 1060$ μm and $k_{rms} = 197.4$ μm. The average trough-to-peak roughness measured for the stable biofilm was essentially unchanged at $k_t = 1860.6$ μm.

Trial 10W6 had a slightly different setup than the other trials with the laser scanner set four millimeters higher (resulting in a slightly different calibration coefficient needed to account for changes in the index of refraction due to the acrylic bottom window and water flowing through the SF3). Because of this, the values for channel gap height and the roughness statistics may be slightly skewed compared with what is observed for the other biofilm trial data. However, this skew may be too small to account for a 100 μm difference in k_{rms} and another process may be responsible for the difference (e.g. 'trimming' of streamers by the flow). The discrepancy between values of C_f seen for the two data points at the lowest Reynolds numbers with the rest of the evolving biofilm layer curve might at first appear unsettling, but comparison with the other resistance curves for evolving ten week biofilm layers shows that the trend is typical. However, the resilience of the biofilm layer examined in Trial 10W6 is not typical. No convincing theory has been found which explains why Trials 5W3 and 10W6 show such resiliency and the difference has been assigned to natural

variation in the biological processes underlying biofilm formation.

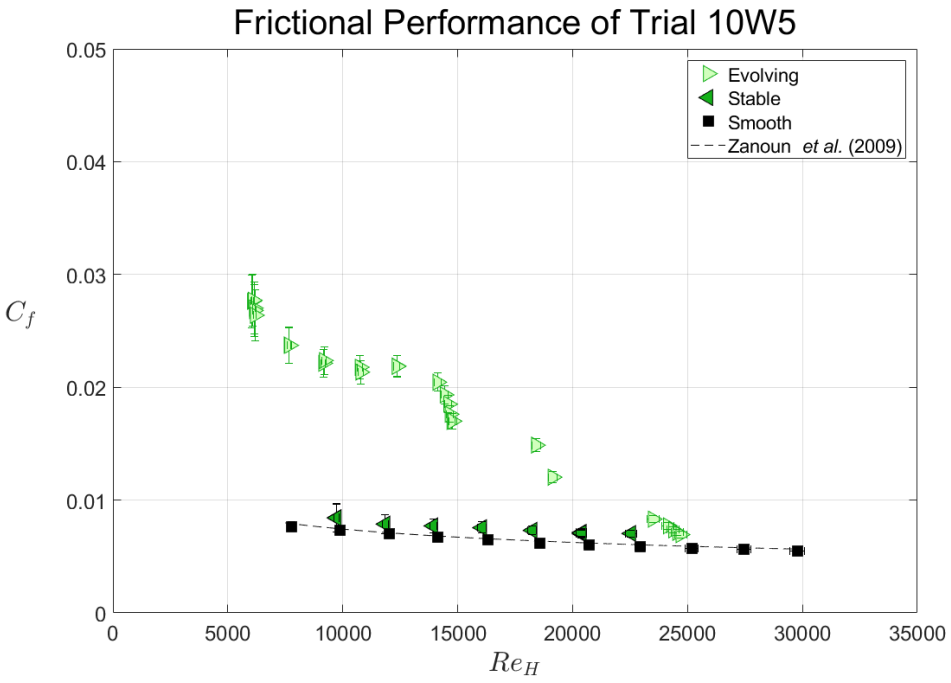

(a)

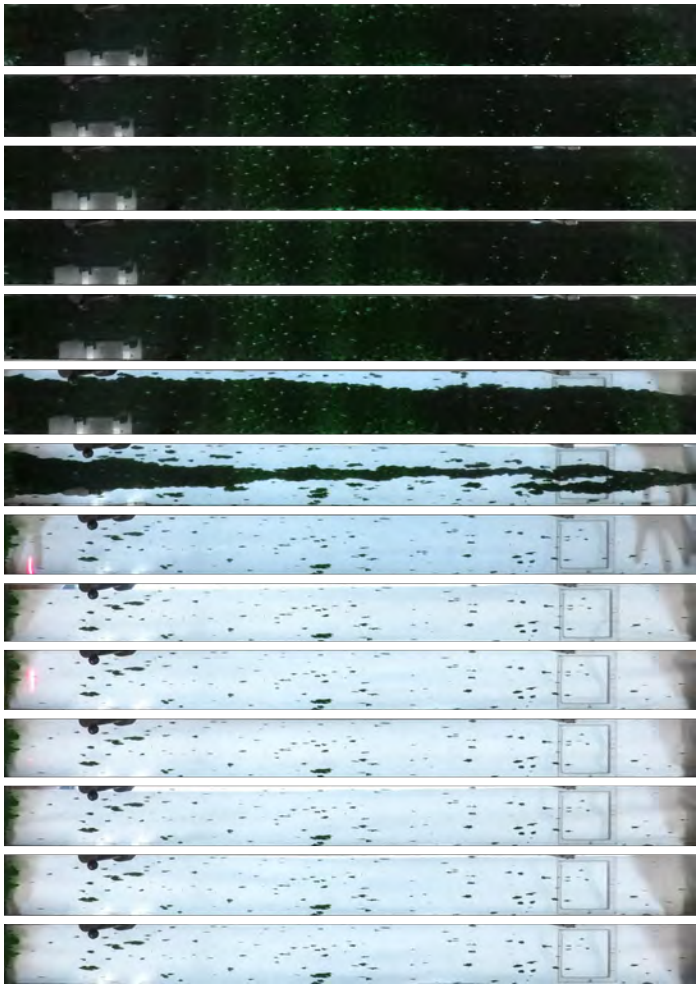

(b)

Figure 3.13: Nearly the entire biofilm layer was lost in Trial 10W5 as shown by the resistance data (a) and overhead photos (b). The rapid loss of biofilm results in a substantial increase in Re_H. The eighth photo from the top in (b) was recorded at the maximum flow rate. The portion of a support clamp which is visible (top, left) did not affect estimation of the fouled area since it was upstream of the measurement volume.

(a)

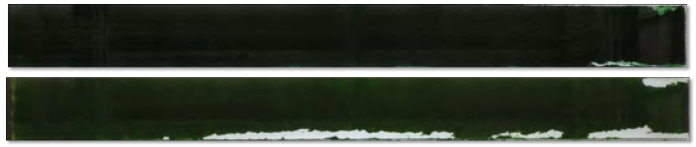

(b)

Figure 3.14: A very slight amount of bulk sloughing was observed in Trial 10W6 (similarly to Trial 5W1). The result is relatively steady, Reynolds number independent resistance data in (a). Trial 10W6 was performed prior to installation of an overhead camera in the SF3, but before and after photos (b) were taken which show the extent of sloughing (or lack thereof).

3.3 Scaling the Roughness Function for Biofilm Layers

The results presented above consistently demonstrate that biofilm layers attached to flow-bounding walls can cause substantial increases in resistance. The added drag caused by biofilm layers was quantified and listed along with several parameters characterizing geometric structure in Tables 3.2, 3.3, and 3.4. In this section, empirical relations linking the roughness function, ΔU^+, to features of the biofilm surfaces are explored. Data from the five and ten week biofilm trials are then examined to reveal some of the processes underlying filamentous biofilm drag production.

Researchers working at the University of Tasmania and the United States Naval Academy have proposed correlations which predict the roughness function of a biofilm layer from its trough-to-peak roughness and biofilm thickness [6, 49]. While the diversity of biofilms studied and differences in testing facilities will limit the applicability of empirical relations such as these, it is worthwhile to see how they apply to the biofilm layers evaluated in this dissertation.

Andrewartha [6] performed experimental trials of freshwater biofilms in external boundary layer flow and used the results to develop a scaling relationship which is given by Equation 3.1 below.

$$\Delta U^+_{Andrewartha} = \frac{1.185}{\kappa} \ln k^+ - 3.932 \tag{3.1}$$

Here $k^+ = k_t/l_\nu$ is the inner-scaled trough-to-peak roughness of the biofilm layers as measured immediately after testing via close-range photogrammetry (CRP). The biofilm layers were characterized outside of the testing facility—in air—with gravity acting against the biofilm layer which is contrary to the orientation during experimental trials. Despite these differences, Andrewartha found that Equation 3.1 provided relatively good collapse of the measured roughness function for all six of the fouled panels which were studied.

Schultz *et al.* [49] also proposed an effective roughness, k_{eff} (Equation 1.10), which was partially successful in collapsing the roughness function they measured for eight panels covered in biofilm. This relation relies on both the percent coverage of biofilm over the surface, A_b, and an estimate of the mean biofilm thickness, k_b. As in the work performed by Andrewartha, measurements characterizing the biofilm surface were performed in static conditions outside the experimental facility. Despite these different measurement conditions, the authors concluded that k_{eff} is a reliable scaling parameter for biofilm covered surfaces and showed that it collapsed the roughness function for eight trials into three distinct groupings. The authors postulated that

data did not collapse onto a single curve because the biofilm data fell into different roughness regimes. Most of the trials appeared to be transitionally rough and did not reach the fully rough flow regime.

Both the correlations proposed by Andrewartha and Schultz *et al.* were evaluated using the data collected in this work. The results are shown along with the proven correlations of Nikuradse (for uniform sand grain roughness) and Colebrook (for industrial pipe) in Figure 3.15 [8, 37].

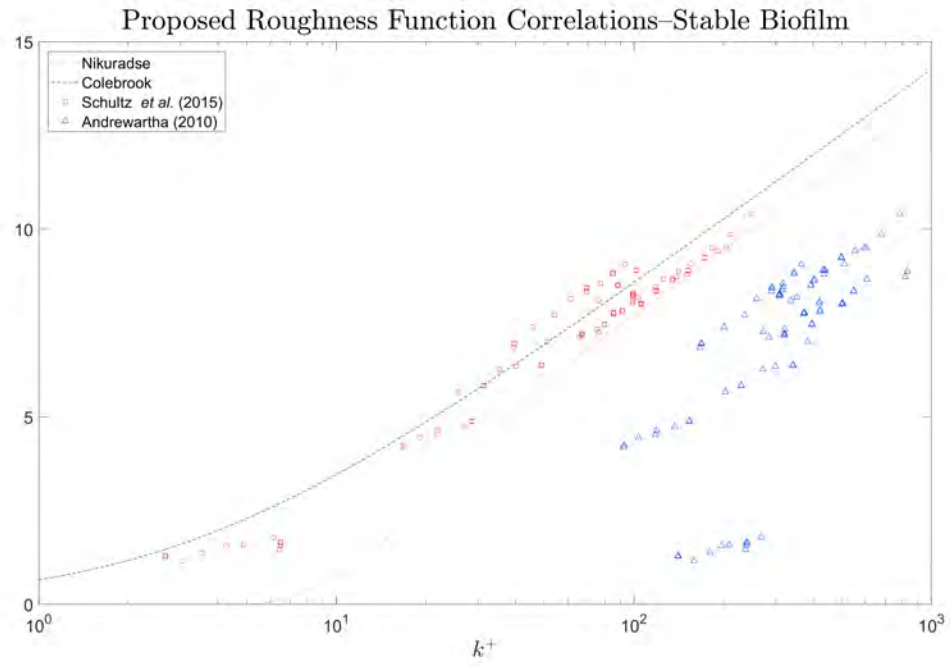

Figure 3.15: Several previously proposed correlations between roughness parameters and the roughness function, ΔU^+, were explored using the data collected in this dissertation. While it does not appear to completely collapse the data, the correlation proposed by Schultz *et al.* [49] provides reasonably good collapse.

As can be seen in Figure 3.15, neither correlation completely collapses the data onto a single relation curve and both lie off the traditional results of Nikuradse and Colebrook. However, closer inspection reveals that k_{eff} proposed by Schultz *et al.* [49] does demonstrate reasonably successful collapse of the current data. Furthermore, all that is needed to align the collapsed data with Colebrook's interpolation formula is a slight change in the constant included in k_{eff}. Doing so yields the adjusted Schultz correlation shown in Equation 3.2 which collapses the roughness function for the stable five and ten week biofilm layers as is shown in Figure 3.16. This slight change of multiplicative constant from 0.055 to 0.042 may be due to the fact that measurements of the biofilm surface are collected *in situ*.

$$k_{eff,\,adj} \;=\; 0.042 k_b A_b^{\frac{1}{2}} \tag{3.2}$$

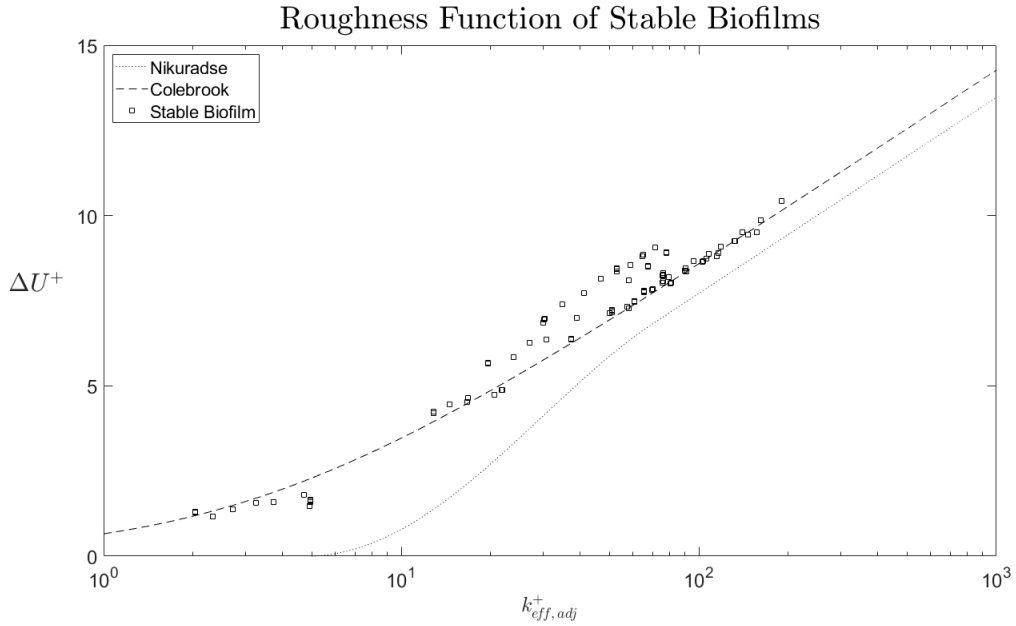

Figure 3.16: After a slight adjustment to the constant in k_{eff}, stable biofilm data appear to collapse relatively well and show Colebrook-type behavior. This is in contrast to many types of roughness which align better with the formula set forth by Nikuradse.

The success of $k_{eff,\,adj}$ in scaling the roughness function confirms that the average biofilm thickness, k_b, and portion of the surface covered in fouling, A_b, are important parameters in the drag production processes of the biofilm layers investigated in this work. Additional efforts were made to better collapse data points which lie above the Colebrook formula. Combinations investigated included k_t, k_{rms}, and other length scales pertaining to the streamer geometry, but no better collapse of the data was observed than is given by k_{eff}. As mentioned previously, the biofilm layers studied here were grown from the same species mix as used by Schultz *et al.* [49] and are investigated in fully developed, plane channel flow which may help explain the success of k_{eff} as a scaling parameter as compared to the correlation proposed by Andrewartha [6].

Some differences are seen when comparing results shown here with the findings of Schultz *et al.* [49]. For instance, the biofilm studied at the USNA exhibited behavior more in line with the uniform sand grain roughness results of Nikuradse than the Colebrook formula. The reasons for this behavior are unknown, but the results shown in this work suggest that the biofilm layers and industrial pipes studied

by Colebrook may share common geometric features which lead to a larger offset in ΔU^+ for transitionally rough surfaces. The limit behavior of the biofilms studied in this dissertation is also more in line with traditional theory than those investigated by Schultz *et al.* as all data appear to display a roughness function slope which tends toward κ^{-1} at large roughness Reynolds numbers ($k_{eff,\,adj} \gtrsim 10$).

The discrepancies in trends observed for ΔU^+ between this work and that of Schultz *et al.* [49] may be due to differences in the biofilm layer, facilities, or the type of panels tested. While the biofilm layers grown for this dissertation were developed using a sample collected from the USNA growth tank, the flows in which they were grown were fundamentally different. Biofilm layers grown for the USNA study experienced higher flow rates and flow was directed across the span of the test panels in an open tank whereas in this study internal flow was oriented in the same direction during growth and experimental trials. Furthermore, constant lighting conditions were provided in this work which might have led to a lower population of diatoms and greater concentration of filamentous green algae. Finally, the incubation times examined were significantly different. All of these effects could lead to fundamental differences in the biofilm layers produced.

Differences also exist between the materials and facilities used. In this study, only smooth acrylic panels served as the base substrate on which biofilm was grown, and while two of the eight surfaces used in the USNA effort were also smooth acrylic, the remaining six were covered in foul release coatings. Furthermore, the SF3 test section has a significantly smaller channel gap height ($\sim$7 mm) than the turbulent channel flow facility housed at the USNA ($\sim$25 mm). As the typical average layer thicknesses of the five and ten week biofilms were roughly two-to-three times those given in Schultz *et al.* [49], the ratio of average biofilm thickness to the outer length scale, k_b/δ, was roughly an order of magnitude larger for these data.

Given the significant differences in methods, materials, and facilities between this study and that performed at the USNA, it is not surprising that different behavior is observed for the biofilm layers studied. Despite this, the scaling parameter suggested by Schultz *et al.* [49] appears to extend to the biofilm layers investigated in this dissertation and future studies of soft biofouling should consider the merits of k_{eff} when evaluating the hydrodynamic performance of biofilm layers in turbulent flow.

3.4 Relating Added Drag to Biofilm Characteristics

The application of an adjusted k_{eff} formulation to successfully scale the stable biofilm layers provided evidence that biofilm thickness and areal coverage are important parameters in biofilm drag production. Therefore, predicting the added drag produced by a biofilm layer is based on these geometric characterization parameters. The Buckingham-Π theory was used to identify potential non-dimensional groups which might be combined to collapse frictional data (including parameters beside k_b and A_b). The added drag was assumed to be a power law function of the Π groups and a least squares, linear regression was performed to find the combination which best collapsed the data. The most successful Π grouping is shown in Equation 3.3:

$$\Pi = Re_H^{0.25} A_b^{0.52} \left(\frac{k_b}{H_o}\right)^{0.58} \tag{3.3}$$

and its linear relationship to ΔC_f is captured by Equation 3.4:

$$\Delta C_f = 0.63\,\Pi - 0.0738 \tag{3.4}$$

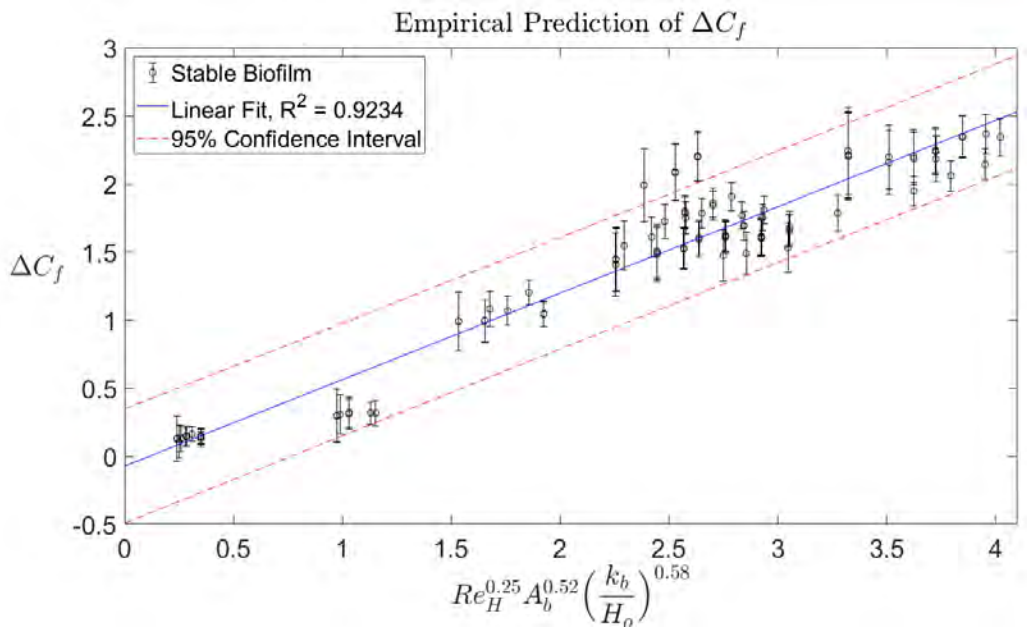

Figure 3.17: A least squares regression derived the optimal fit of stable biofilm data with a Π grouping (Equation 3.3) which contains the fouled area, A_b and non-dimensional mean biofilm thickness, k_b. Data for nearly all the stable biofilm layers fall within the 95% confidence interval for the suggested linear fit Equation 3.4. Note that H_o was used to non-dimensionalize k_b because the mean biofilm layer thickness is used to calculate the average channel gap height, H_{AVG}.

Figure 3.17 shows the result of this analysis including how well data from the five and ten week biofilm trials adhere to this trend. It is seen that—within the bounds of uncertainty—ΔC_f values predicted by Equation 3.4 generally apply well to those measured in this work. The analysis described above was performed using only data collected for stable biofilm layers; however, it is able to accurately predict the added drag, ΔC_f, and coefficient of friction, C_f, for several of the evolving biofilm layers as well. Table 3.5 shows the predicted and measured values of C_f for the trials and flow speeds used to generate rigid replicas. The results show that Equation 3.4 estimates the coefficient of friction for the stable biofilm layers within ±10%. Most of the C_f values for evolving layers also agree well but—for reasons not currently known—data shown from Trials 5W1 and 10W4 are not predicted as well.

Table 3.5: Comparison of predicted and measured biofilm resistance (for cases with rigid replica data)

Trial	Surface	Re_H	$C_{f,biofilm}$ measured	$C_{f,biofilm}$ predicted	% diff
5W1	Evolving	6547	0.01820	0.02362	-29.7
5W2	Evolving	7372	0.01987	0.01895	4.6
5W3	Evolving	13 609	0.01822	0.01792	1.7
5W3	Stable	13 755	0.01905	0.01757	7.8
10W2	Evolving	7737	0.03362	0.03115	7.3
10W4	Evolving	10 508	0.02521	0.02076	17.6
10W6	Stable	17 511	0.01903	0.02085	-9.6

The results above demonstrate that Equations 3.3 and 3.4 provide a reasonably accurate characterization of the added drag experienced by the biofilm layers in this work. The factor of $Re^{0.25}$ in the Π group of Equation 3.3 confirms what was seen visually in most of the resistance plots displayed in §3.2, namely that ΔC_f is Reynolds number independent for most biofilm layers. The power of the exponents on A_b and $\frac{k_b}{H_o}$ is similar, indicating that the areal coverage and layer thickness are about equally important.

3.5 Chapter Summary

The frictional resistance of smooth surfaces covered with soft biofilm layers was determined from hydrodynamic trials in a high-aspect ratio, closed-channel water tunnel at the University of Michigan. Biofilm layers were grown for nominal durations of three, five, and ten weeks on smooth acrylic test panels in a specially built flow

loop, and the extent of biofilm coverage was photographed before, during, and after trials using an overhead camera. Profiles of the surface topography were captured while the biofilm layers were subjected to flow using a laser line scanner. Roughness statistics were then derived using the point cloud data provided by the scanner.

Experiments were first performed on a smooth acrylic panel to establish a baseline resistance curve and to verify the measurement and analysis procedures. Additional corrections accounting for channel asymmetry are required to accurately capture the performance of rough panels. Therefore, a second validation experiment was performed of a panel covered in 80 grit sandpaper and the results were found to agree with the findings of Flack *et al.* [12] who also examined the frictional performance of 80 grit sandpaper.

Accurately characterizing the hydrodynamic performance of surfaces covered with soft biofouling is a complex and difficult undertaking. The compliance of the biofilm and sloughing of the surface complicate otherwise routine measurements and introduce confounding factors which defy simple incorporation in analysis procedures and uncertainty analysis. While these challenges were met and consistent trends were observed across the biofilm trials, investigators should be especially cautious when reporting and considering the findings of biofilm studies.

The results presented in this chapter demonstrate that the presence of even light biofilm layers can cause a substantial increase in flow resistance. Biofilm layers grown for three weeks resemble the low-form microfouling seen on in-service vessels with sparse and patchy coverage. The average thickness of these biofilm layers ranged from $k_b \approx 100$–200 μm and the fouled area measured spanned $A_b \approx 5$–50%; although it is difficult to determine—and even to define—what constitutes fouling for these developing biofilms. Roughness statistics were derived from scanned profiles of the biofilm topography showing $k_{rms} \approx 100$–150 μm and $k_t \approx 600$–1200 μm. A range of flow speeds were investigated spanning $Re_H \approx 8\,000$ – $25\,900$ and the drag increase caused by the three week biofilm layers ranged from $\Delta C_f \approx 20$–150%.

Results for trials of biofilm layers grown for five weeks showed that the fouling was more developed. The average layer thickness was $k_b \approx 650$–1100 μm and while all three panels examined for this incubation time began with more than 90% of their surface fouled, significantly different levels of sloughing were observed for each with final fouled areas being $A_b = 13\%$, 41%, and 92%. The measured trough-to-peak roughness heights ranged from $k_t \approx 900$–1900 μm which is significantly larger than those of the three week layers; but, the values of the root-mean-squared roughness were only slightly larger with $k_{rms} \approx 150$–200 μm. The added drag measured was

generally about twice that of the three week layers but the range covered ($\Delta C_f \approx$ 65–150%) and the initial drag penalty (i.e. before sloughing) was similar for the three and five week ITs. This is quite surprising given the stark differences in average layer thickness and fouled area for the two ITs; it may suggest that different physical processes drive drag production for sparse or developing biofilm layers. Unfortunately, the complications caused by the condition of the three week layers prevented accurate scaling analysis, and data for the three week ITs were not included in scaling attempts or empirical characterization of frictional behavior.

The results for six trials of biofilm layers grown for ten weeks were also presented and showed the widest range of variation. Typically, the average biofilm layer thickness was about one to two millimeters but values from $k_b \approx$ 400–2600 μm were measured. Initially, most panels were completely covered in biofilm but a range of sloughing occurred across the trials. Stable biofilms typically had fouled areas of 40–70%, but one panel exhibited almost complete sloughing with $A_b = 2\%$ and another experienced almost no loss of its fouling with $A_b = 93\%$. In general, measured roughness heights were $k_{rms} \approx$ 300–400 μm and $k_t \approx$ 2000 μm; however, the full range of roughness spanned $k_{rms} \approx$ 200–700 μm and $k_t \approx$ 1500–3600 μm. The drag increase experienced by the ten week biofilm layers ranged widely depending on the thickness, fouled area, roughness, and level of sloughing. Measurements spanned $\Delta C_f \approx$ 14–364% but most values of the added drag were around $\Delta C_f \approx 200\%$.

The findings shown in this chapter reveal several suggestive trends between the biofilm characterization parameters and measured resistance. As the incubation time of a biofilm layer is increased, the added drag it experiences also grows. Since only three nominal ITs were considered in this work, it is difficult to determine if the added drag of a biofouled surface will scale with incubation time. In these data, the relationship appears to be roughly linear for stable biofilm layers as on average, the three week fouling showed $\Delta C_f \approx$ 60–100%, the five week biofilms generally showed $\Delta C_f \approx$ 130–160%, and the ten week layers typically experienced $\Delta C_f \approx$ 200–250%. However, the results for evolving biofilm layers in the three and five week trials suggest that added drag may not increase linearly with growth duration for large areas of developing and/or sparse soft fouling. It may be that thin, sparse layers generate out-sized drag penalties.

Rather than attempting to correlate the added drag caused by soft biofouling with growth time, the frictional performance of a biofilm layer should be linked to its surface condition. Scaling correlations connecting the roughness function, ΔU^+, to average biofilm layer thickness, k_b, areal coverage, A_b, and roughness statistics,

k_{rms}, k_t, were proposed by Andrewartha [6] and Schultz *et al.* [49] and have been evaluated using data collected in this dissertation. The effective roughness height, k_{eff} proposed by Schultz *et al.* was found to collapse the biofilm data reasonably well (after slight modification of an included multiplicative constant) and although several other combinations of the various biofilm characterization parameters were explored (failed attempts were not shown in this dissertation), none showed better success in predicting the roughness function.

While k_{eff} provides the means to estimate ΔU^+ which can provide C_f via Granville's method, an iterative process is required since the viscous length scale, l_ν, is used to non-dimensionalize k_{eff}, and l_ν depends implicitly on C_f. Therefore, a least squares regression was performed assuming that ΔC_f could be empirically determined by the product of the Reynolds number, Re_H, fouled area, A_b, and dimensionless average layer thickness, $\frac{k_b}{H_o}$. The resulting equations were applied to the biofilm data and demonstrated that the frictional performance of stable biofilm layers could be characterized within $\pm 10\%$. The scaling relations and equations used to determine added drag were developed using only data collected for the stable biofilm; yet, the results still hold for several of the evolving biofilm layers. Note that the results presented in this dissertation only pertain to the biofilm layers and facilities used in this work and therefore cannot be said to apply in general. In particular, the extension of these findings for soft fouling on ships is problematic as the trials were performed in a channel flow facility and the length scales associated with the inner and outer layers of the flow are likely significantly different. Furthermore, biofilm development (i.e. streamer length) may have been limited by the growth setup and soft fouling of in-service vessels may be significantly different in structure (e.g. comprised of long streamers having narrower aspect ratios). Measurements of fouling grown and evaluated in an external boundary layer (such as that in a large water tunnel or on towed panels) would be required to better replicate the scales seen for in-services vessels.

Trials of biofilm layers grown for three, five, and ten weeks provided data which were used to characterize their frictional performance, successfully evaluate a scaling correlation ($k_{eff,\,adj}$) for the roughness function, and perform a regression analysis to empirically relate the added drag caused by the biofilm layers to their surface geometry (Equations 3.3 and 3.4). While the findings presented in this chapter apply to biofilm layers grown and evaluated in channel flows, the insights gained relating frictional behavior to surface features can inform future efforts and may provide useful tools to engineers and designers of systems with a range of flow conditions which are susceptible to soft biofouling.

CHAPTER IV

Resistance of Rigid Replicas

4.1 Overview

Previous studies [3, 34] suggest that increased resistance due to biofilm layers results not only from drag production mechanisms associated with a rough surface, but also through interactions between biofilm and flow (i.e. streamer flutter and vibrations of the underlying 'mat'). Previous attempts to quantify the role of compliance in drag production have been limited to the study of biofilm streamer motion and the behavior of artificial biofilms such as nylon strings and wool strands. While informative, these efforts seek to replicate compliance characteristics of biofilms and neglect the role of drag production mechanisms associated with the rough geometry of the fouling. In this chapter, the frictional behavior of rigid replicas having the same time-averaged, spatially filtered surface geometry is presented and discussed.

In total, seven rigid replicas were manufactured which represent six unique biofilm trials. Table 4.1 summarizes the frictional performance and roughness parameters of the rigid replicas and the biofilm layers which they replicate. Three correspond to ten week trials and four were generated using full scans of the five week trials. One of the five week biofilm trials (Trial 5W3) experienced slight sloughing and two rigid replicas were printed of full scans recorded on both the evolving leg and stable portion of the trial to investigate repeatability and consistency in the rigid replica printing process and experimental trials.

Table 4.1: Results summary for rigid replicas and the biofilm layers to which they correspond

Trial	Re_H	Surface	ΔC_f [%]	k_b [μm]	k_{rms} [μm]	k_t [μm]	L_s [μm]	D_s [μm]	λ_z [μm]	λ_x [μm]
5W1	6550	Biofilm–Evolving	120	1110.5	174.4	1556.9	5610	1520	2420	8840
5W1RR		Rigid Replica	57	1056.6	161.8	1488.5	5900	1720	2500	8550
5W2	7370	Biofilm–Evolving	148	670.1	223.7	1826.4	6020	1470	2480	9150
5W2RR		Rigid Replica	84	622.5	201	1618.1	6170	1770	2890	10 270
5W3	13 610	Biofilm–Evolving	165	707.9	155.5	1287.4	5910	1360	2490	9300
5W3RRe		Rigid Replica	101	613.8	142.4	1262.3	6770	1550	2740	10 460
5W3	13 760	Biofilm–Stable	178	635.7	160.3	1408.8	6570	1510	2580	11 120
5W3RRs		Rigid Replica	89	199	127	1282.3	7140	1540	3070	14 300
10W2	7740	Biofilm–Evolving	324	2240.8	237.7	2170.9	8540	2030	3120	12 820
10W2RR		Rigid Replica	193	1886.5	218.7	2133.9	10 610	2070	3870	19 280
10W4	10 510	Biofilm–Evolving	243	991.9	296.4	2148.9	8160	2100	3350	11 730
10W4RR		Rigid Replica	129	865	282.7	2064.6	8310	2080	3400	12 260
10W6	17 510	Biofilm–Stable	195	1040	191.6	1809.4	6490	1770	2680	9010
10W6RR		Rigid Replica	124	1647	195	1839.1	7580	1790	2890	10 120

Table 4.2: Differences between biofilm and rigid replica frictional behavior and surface features

Surface Pair	$\Delta C_{f,soft}$ [%]	Δk_b [μm]	Δk_{rms} [μm]	Δk_t [μm]	ΔL_s[μm]	ΔD_s [μm]	$\Delta \lambda_z$ [μm]	$\Delta \lambda_x$ [μm]
5W1/5W1RR	52.5	53.9	12.6	68.4	-290	-200	-80	290
5W2/5W2RR	43.2	47.6	22.7	208.3	-150	-300	-410	-1120
5W3/5W3RRe	38.8	94.1	13.1	25.1	-860	-190	-250	-1160
5W3/5W3RRs	50.0	436.7	33.1	184.1	-570	-30	-490	-3180
10W2/10W2RR	40.4	354.3	19	-440.4	-2070	-40	-750	-6460
10W4/10W4RR	46.9	126.9	13.7	68.9	-150	20	-50	-530
10W6/10W6RR	36.4	-607	-3.4	-29.7	-1090	-20	-210	-1110

Rigid replicas were generated only for surfaces exhibiting a small amount of sloughing and are therefore typically derived from the evolving legs of biofilm trials. Efforts to manufacture replicas of panels covered in sparse coverage (i.e. the three week trials and sloughed biofilm layers) failed; however, two of the replicas were generated using data collected for stable biofilm layers which had only slight sloughing. Section §2.4 details the procedure used to manufacture the rigid replicas and includes comparisons of laser scan data for the final prints with the original biofilm scans. Table 4.2 shows the differences between the various rigid replicas and the biofilm layers to which they correspond.

The results shown in Tables 4.1 and 4.2 demonstrate that, in general, the roughness of the rigid replicas match measured values for the living biofilm well. Deviations in k_{rms} are within 35 μm and often below 15 μm indicating that the 'average' biofilm and rigid replica surface have the same texture. Comparisons of k_t show a wider range with differences from a little as 25 μm to as large as 440.4 μm which is not surprising given the small sample size and sensitivity of measurements used to determine k_t.

Large differences between the biofilm layers and rigid replicas are primarily confined to measurements of the average thicknesses which shows deviations as small as 48 μm and as large as 608 μm. This wide range is likely attributable to two causes. Firstly, improvements in the printing procedure occurred part of the way through this work and three of the panels were printed prior to the enhancement (Trials 10W6RR, 10W2RR, and 5W3RRs) while the remaining four (Trials 5W1RR, 5W2RR, 5W3RRe, 10W4RR) followed a more robust manufacturing process. The first three panels were printed from .stl files requiring a user-set 'zero' point (i.e. the location of the smooth acrylic surface) which was estimated from point measurements and had a greater uncertainty than the final four panels which were generated using a suite of expressly written MATLAB routines. The accuracy and precision of the 'zero' point (or origin) of the panel was more robust in the MATLAB routines since full scan data were used. The offset in the assumed acrylic panel position did not affect the surface characteristics during the printing process but it did affect the measured channel gap height (which leads to different blockage in the SF3 test section).

Secondly, to ensure a tight fit between rigid replicas and the base panel used to install them in the SF3, printed tiles were slightly too thick and the back dovetail grooves which slide into the base panel needed to be lightly sanded prior to installation of a rigid replica. Sanding was only performed on the back of the tiles and the textured 'biofilm' sides were not modified. Although unknown, variations in the rigid replica thickness due to sanding are likely less than $\sim$100 μm. The change in manufacturing

procedure for rigid replicas and—to a lesser extent—the effect of sanding, likely led to the differences in the thickness of the rigid replicas and their biofilm layers. This change in thickness does not affect the texture or roughness of the surfaces but will change flow through the SF3 by introducing variable blockage between trials of live biofilm and their rigid replicas. As the effect of blockage is accounted for by the channel gap height, the discrepancy in thickness between a rigid replica and the biofilm layer it replicates should not affect calculations of $C_{f,\,measured}$.

The results above demonstrate that pairing an accurate laser scanning system with state-of-the-art 3D printers has enabled detailed, spatially filtered, and accurate rigid replicas to be manufactured from time-averaged, laser scan data of living biofilm surfaces. The frictional performance of these rigid replicas was evaluated through hydrodynamic trials performed in the SF3. Comparisons of the results for rigid replicas and the biofilm layers they represent is provided in the following section and the findings are then used to separate the added drag caused by roughness and compliance effects (discussed in §4.5).

4.2 Comparing the Resistance of Biofilms to Their Rigid Replicas

Along with the quantification of differences between the rigid replicas and biofilm geometry, Table 4.2 provides added drag measurements for the surfaces at the same Reynolds number (Re_H). As the rigid replicas appear to represent the time-averaged biofilm layers well, this difference is attributed to effects of compliance such as streamer flutter and mat vibrations. The values shown in Table 4.2 indicate that roughly half of the added drag produced by biofilms is attributable to compliance effects. This 'compliance' drag is defined in Equation 4.1.

$$\Delta C_{f,\,soft} = \frac{C_{f,\,biofilm} - C_{f,\,replica}}{C_{f,\,smooth}} \times 100\% \tag{4.1}$$

While direct comparison must be limited to matching values of Re_H, Figures 4.1—4.12 display the differences in resistance between the rigid replicas and biofilm layers across a range of Reynolds numbers.

4.2.1 Five Week Biofilms and Rigid Replicas

Figure 4.1 shows the frictional behavior of Trial 5W1 along with that of a rigid replica developed from laser scans of the full surface collected at the beginning of the

trial (Trial 5W1RR, scanned at $Re_H \approx 6500$). The compliance drag is estimated to be $\Delta C_{f,\,soft} = 53\%$ although the large uncertainty bounds show that its true value lies in a wide range. Even with the large range of potential $\Delta C_{f,\,soft}$ values, it is clear that a significant portion of the added drag is due to the effects of compliance.

The rigid replica evaluated in Trial 5W2RR was also manufactured from scan data collected at a relatively low flow speed ($Re_H = 7400$) and while results shown in Figure 4.3 display an increased value of C_f for the biofilm layer, a corresponding shift is seen for the rigid replica data and $\Delta C_{f,\,soft} = 43.2\%$ which is similar to what was measured for Trial 5W1RR. While the magnitude of compliance drag is 10% less in this case, the difference is relatively slight given the uncertainty bounds on the data. It is also interesting to note that the Reynolds number dependence of the biofilm layer does not follow the trend seen for the rigid replica, indicating that sloughing effects may have been significant in Trial 5W2. This is contrary to what is seen in Figure 4.1 where the biofilm and rigid replica data appear to display similar trends with increasing flow (at least until substantial bulk sloughing occurs).

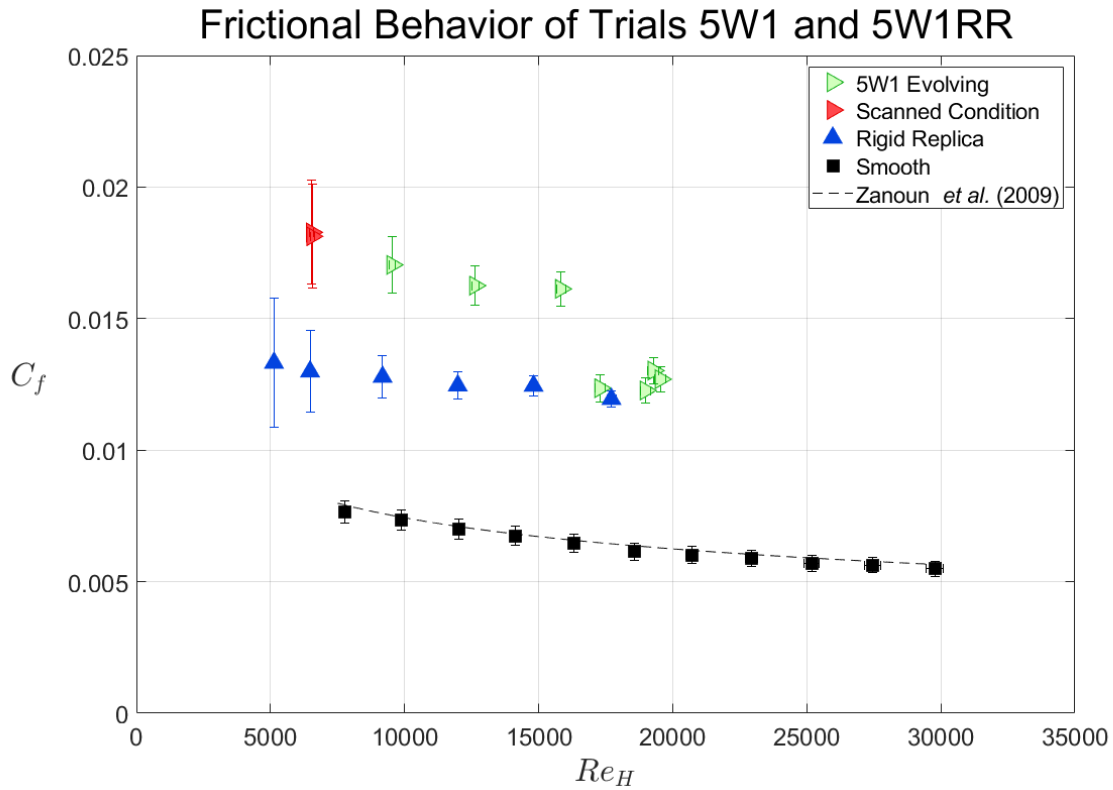

(a)

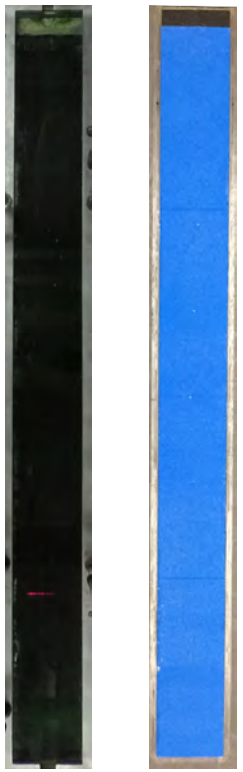

(b) (c)

Figure 4.1: Resistance data for the evolving biofilm in Trial 5W1 (right-pointing triangles; overhead picture shown in (b)) are compared with data for a rigid replica (upward-pointing blue triangles; shown in (c)) of the surface scanned at $Re_H \approx 6500$ (shown in solid red). The data show substantial differences in the magnitude of C_f indicating that both roughness and compliance effects are important in drag production.

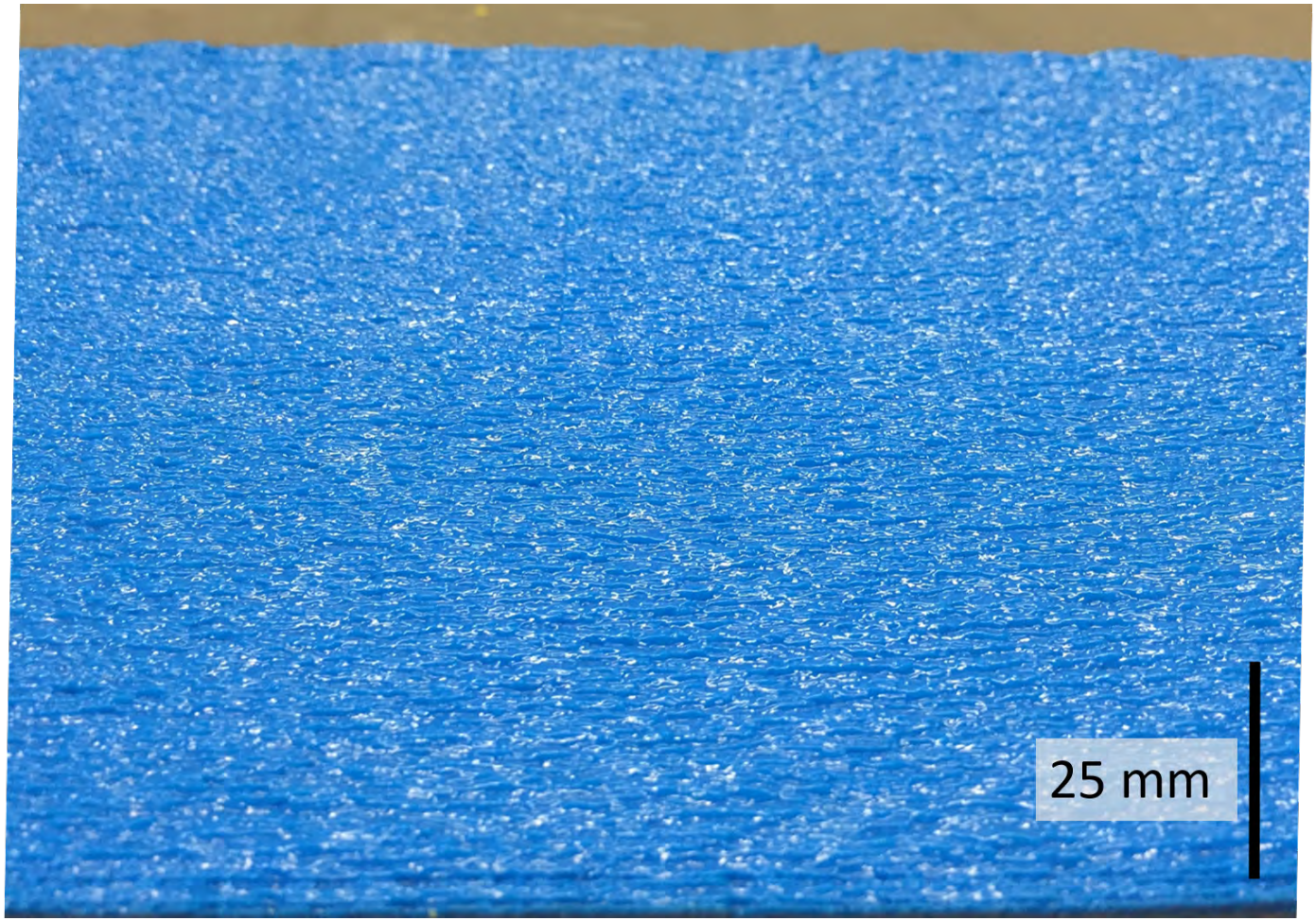

Figure 4.2: A closeup shows the texture of the rigid replica evaluated in Trial 5W1RR. A dense patchwork of small streamers can be observed. Note that the image shown here was taken at an angle to show better contrast between streamers which was not accounted for by the shown scale bar.

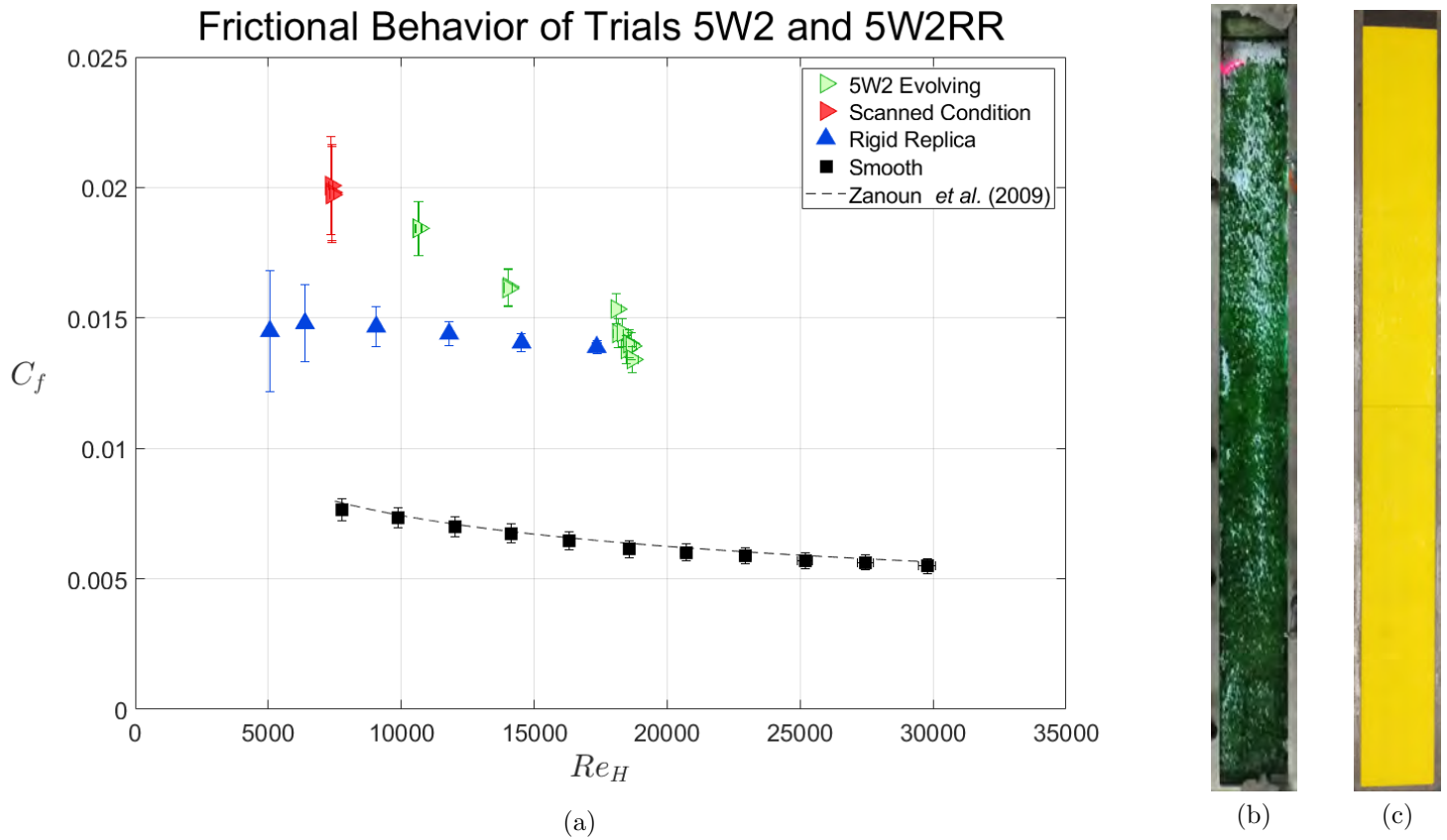

(a) (b) (c)

Figure 4.3: The frictional behavior of Trials 5W2 and 5W2RR shows similar offsets between biofilm and rigid replica data with $\Delta C_{f,soft} = 43.2\%$. The large uncertainty bounds make it difficult to determine if the slight decrease in added drag due to compliance is the result of differences in the biofilm layer. The biofilm shown in (b) and rigid replica in (c) had good agreement in surface coverage which is difficult to visualize from the yellow coloring of the rigid replica.

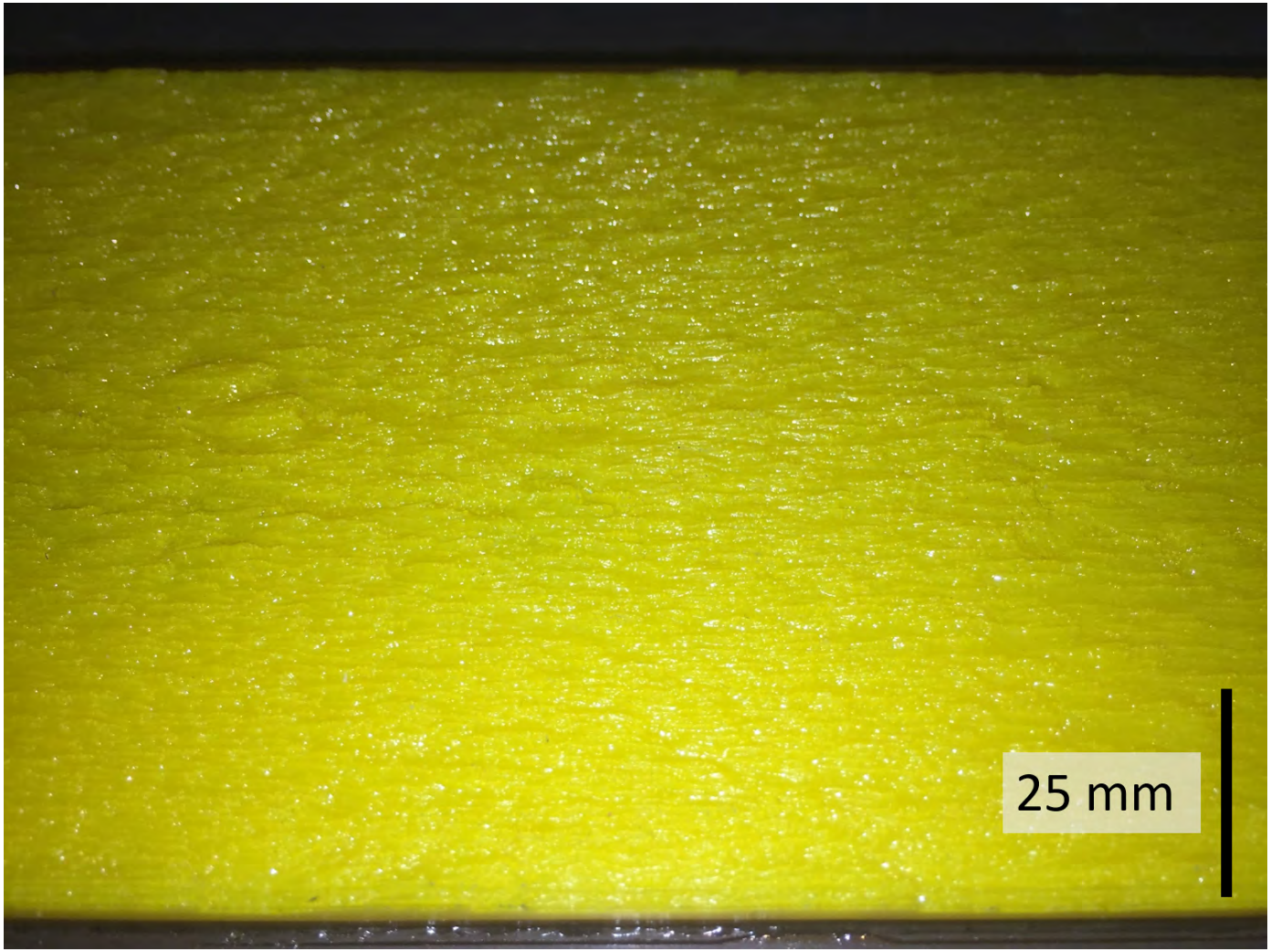

Figure 4.4: A closeup shows the texture of the rigid replica evaluated in Trial 5W2RR. A flash camera was used to better illuminate surface texture since the yellow color causes 'flat' lighting conditions. Note that the image shown here was taken at an angle to show better contrast between streamers which was not accounted for by the shown scale bar.

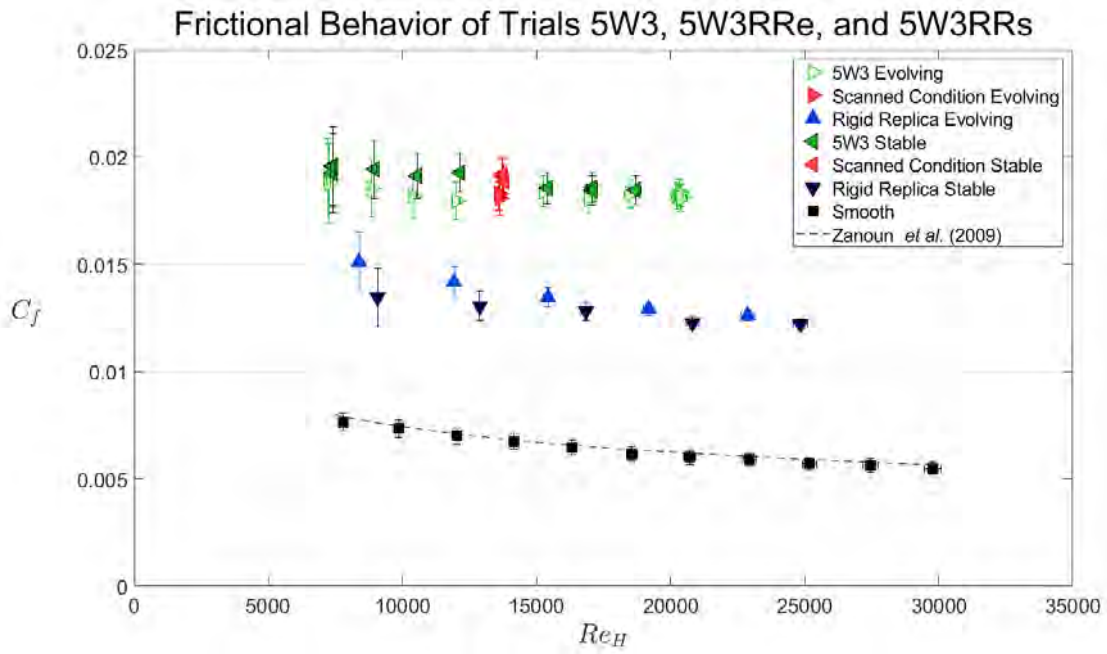

(a)

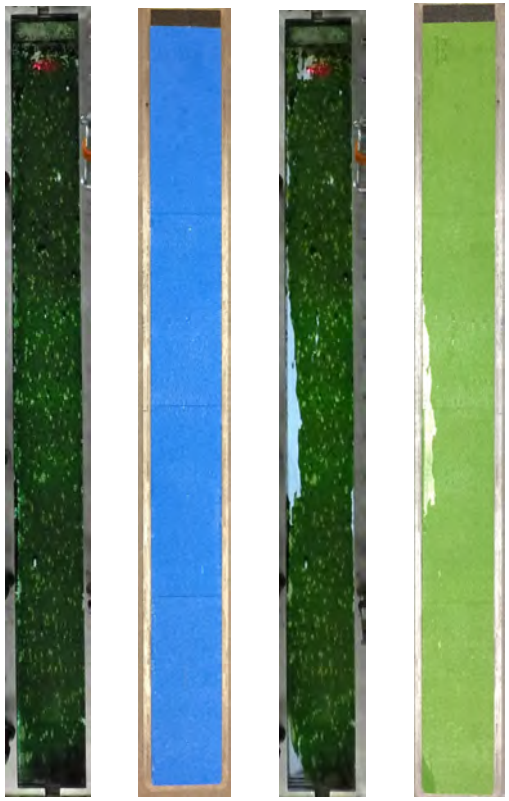

(b) (c) (d) (e)

Figure 4.5: Two rigid replicas were produced from data collected in Trial 5W3. As shown here, biofilm resistance data (left-, right-pointing triangles) and data from corresponding rigid replicas (upward-, downward-pointing blue triangles) show consistent behavior in $\Delta C_{f,soft}$ and Reynolds number dependence. Although some deviation is seen at low Reynolds numbers between Trial 5W3RRe (upward-pointing blue triangles) and Trial 5W3RRs (downward-pointing dark blue triangles), the data agree well near the scanned flow speed ($Re_H \approx 13\ 700$). Overhead images in (b)–(e) show the sloughing which occurred over Trial 5W3 and also demonstrate that the rigid replicas accurately capture areal coverage.

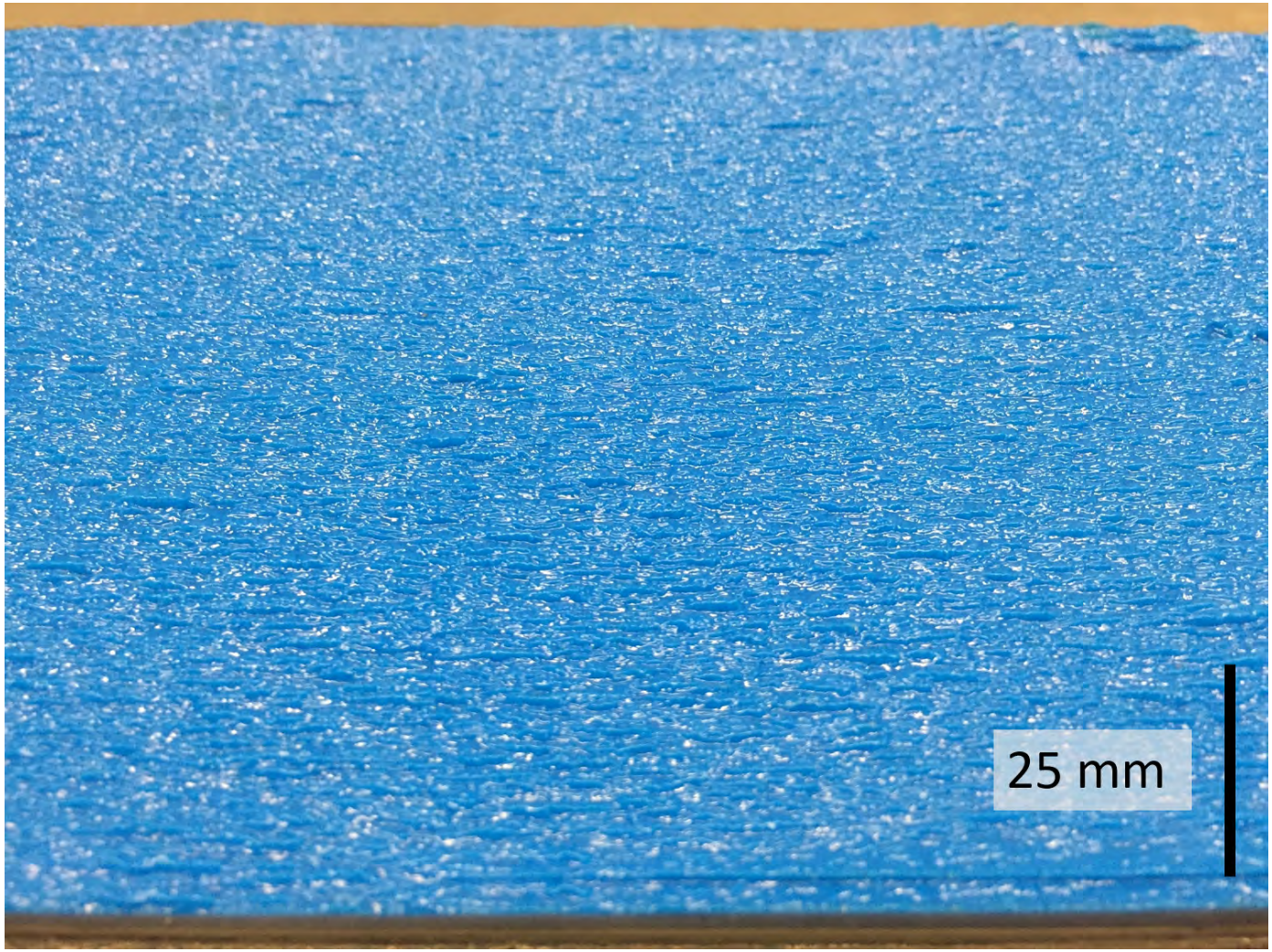

Figure 4.6: A close-up shows the texture of the rigid replica evaluated in Trial 5W3RRe. A dense patchwork of small streamers similar to those of Trial 5W1RR can be observed. Note that the image shown here was taken at an angle to show better contrast between streamers which was not accounted for by the shown scale bar.

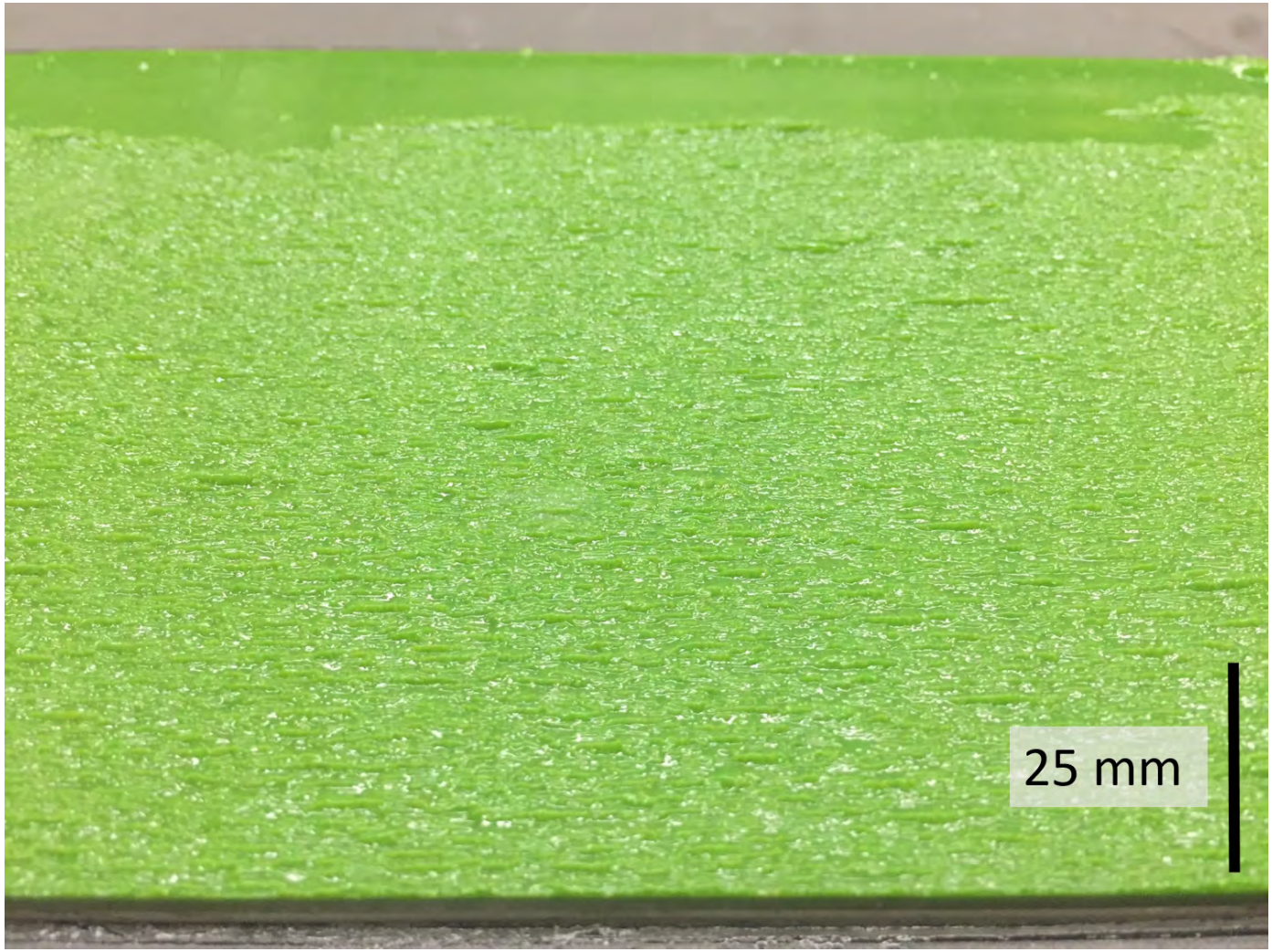

Figure 4.7: A portion of the rigid replica evaluated in Trial 5W3RRs. Since the picture was taken near the same location as in Figure 4.6, specific streamers can be found which are duplicated between the two trials . Note that the image shown here was taken at an angle to show better contrast between streamers which was not accounted for by the shown scale bar.

The results from three different trials are shown in Figure 4.5. As previously mentioned, two rigid replicas were manufactured from full scans collected during Trial 5W3 which covered both the evolving leg and stable portion of the trial. The resulting resistance curves show good agreement in the region of Reynolds numbers near the scanned flow speed ($Re_H \approx 13\ 700$) as data for both rigid replicas show similar C_f values and a matching shift below the biofilm data curves. Despite this consistent behavior, there is a measurable difference in the average compliance drag with $\Delta C_{f,\,soft} = 38.8\%$ for the evolving data and $\Delta C_{f,\,soft} = 50\%$ for the stable results. Note that this difference can be accounted for by the uncertainty estimates.

It is tempting to relate differences between measured thickness and roughness values to the variation in $\Delta C_{f,\,soft}$ for the five week trials and their rigid replicas; however, given the relative level of noise seen in the data, it is likely that the deviations stem from minor variations in the measurements and analysis. Sources of uncertainty in the corrections made for asymmetric boundaries and H_{AVG} alone can account for the differences in $\Delta C_{f,\,soft}$ between trials. Further evidence that the deviations in $\Delta C_{f,\,soft}$ are due to slight variations in the measurements and analysis is provided from comparison of the difference in compliance drag penalty for the two rigid replicas which were fabricated using laser scan data of the same panel at roughly equal Reynolds numbers. The difference in the values of $\Delta C_{f,\,soft}$ across this one biofilm trial (Trials 5W3RRe and 5W3RRs, $\sim$11%) correspond well to those observed for replicas of different panels at similar Reynolds numbers (Trials 5W1RR and 5W2RR, $\sim$9%). Although a 14% uncertainty in $\Delta C_{f,\,soft}$ across all five week trials is greater than desirable, it is a reasonable value given difficulties associated with measurement and analysis.

4.2.2 Ten Week Biofilms and Rigid Replicas

Figures 4.8–4.12 compare the frictional performance of three ten week biofilm trials and their corresponding rigid replicas. Two of the rigid replicas (10W2RR and 10W4RR) were manufactured from full scans of evolving biofilm layers while a stable biofilm which experienced only slight sloughing served as the source for a final replica. Values for $\Delta C_{f,\,soft}$ shown in Table 4.2 corresponding to the ten week biofilm trials are similar to what is seen for the five week trials, although the magnitude of the compliance drag is slightly lower on average for the ten week trials (average $\Delta C_{f,\,soft} = 46\%$ and 41%, respectively).

Figure 4.8 displays the relationship between Trial 10W2 and a rigid replica manufactured from data collected at $Re_H \approx 7700$. The compliance drag penalty was

measured to be $\Delta C_{f,\,soft} = 40.4\%$. Here, it may be important to note that this value was derived using the average value of $C_{f,\,biofilm}$ at a given flow speed as there is a noticeable spread between data collected at the beginning of this flow speed and at the end (just before flow through the SF3 was increased). Figure 4.8 shows a relatively large difference in the Reynold number dependence between the data for the live biofilm and rigid replica which appears to be greater than what was typically observed in the figures comparing five week biofilm layers with their corresponding rigid replicas.

Figure 4.10 shows a similar disparity in Reynolds number dependence between biofilm and rigid replica data. Since this is not the case for Figures 4.5 and 4.12, it is likely due to the sloughing which occurs during the evolving leg of the biofilm trials. The steeper slope generally observed for the evolving ten week biofilm layers likely reflects a higher rate of sloughing which could be due to the greater constriction of the channel and/or structural differences between biofilms grown for different incubation times.

Data in Figure 4.10 show the greatest amount of compliance drag of any ten week biofilm/rigid replica pairings with $\Delta C_{f,\,soft} = 46.9\%$. This is 10% greater than the compliance drag penalty derived from the resistance curves shown in Figure 4.12 which displays the stable portion of Trial 10W6 along with its corresponding rigid replica. The trends seen in Figure 4.12 show essentially no Reynolds number dependence which—while more in line with what is observed for slightly sloughing, stable biofilm layers—is a departure from what has been observed for the other resistance curves shown in this chapter.

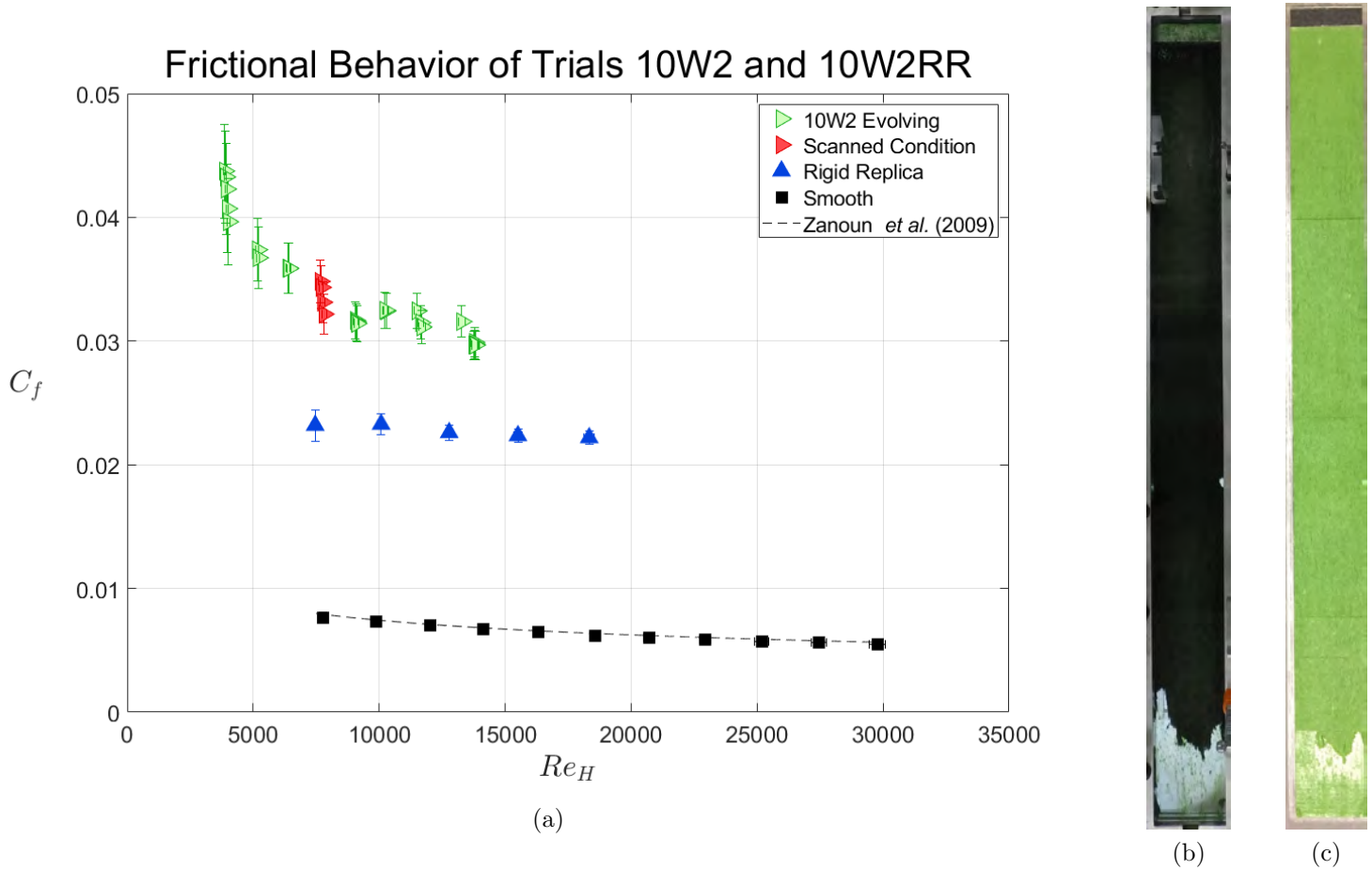

(a) (b) (c)

Figure 4.8: Trials 10W2 and 10W2RR show a compliance drag penalty of $\Delta C_{f,soft} = 40.4\%$. Rigid replica data (shown as upward-pointing blue triangles) show little Reynolds number dependence which is contrary to data collected for the evolving biofilm layer (right-pointing green triangles). Comparison of $\Delta C_{f,soft}$ is made at the scanned condition (solid red right-pointing triangles).

Figure 4.9: A portion of the rigid replica evaluated in Trial 10W2RR. Streamers were particularly elongated for this thickest of the biofilm layers. Note that the image shown here was taken at an angle to show better contrast between streamers which was not accounted for by the shown scale bar.

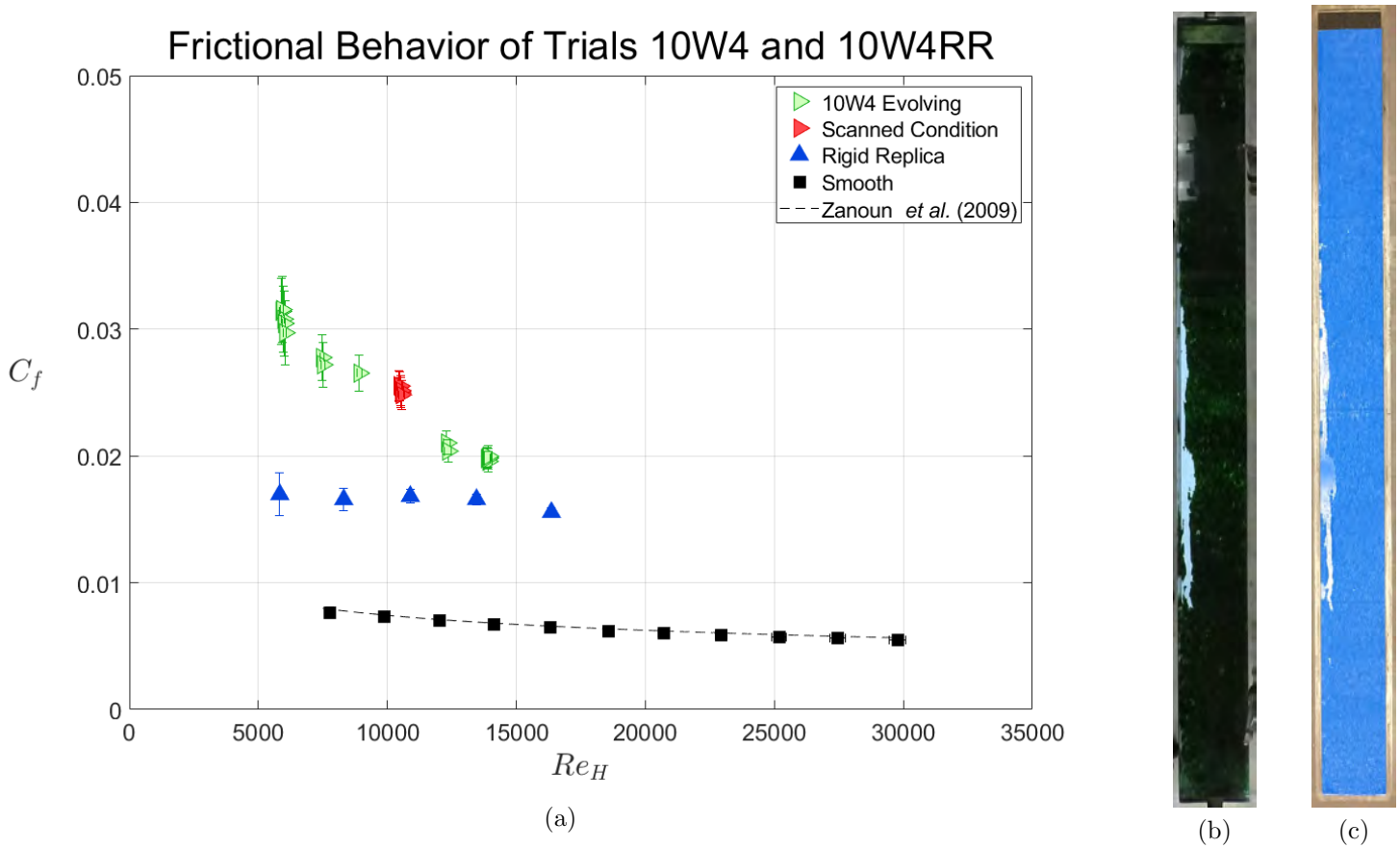

Figure 4.10: Resistance data are shown for Trials 10W4 (right-pointing light green triangles) and 10W4RR (upward-pointing blue triangles). The compliance drag penalty at the scanned condition (right-pointing red triangles) was $\Delta C_{f,\,soft} = 46.9\%$ which was the highest of any ten week trials.

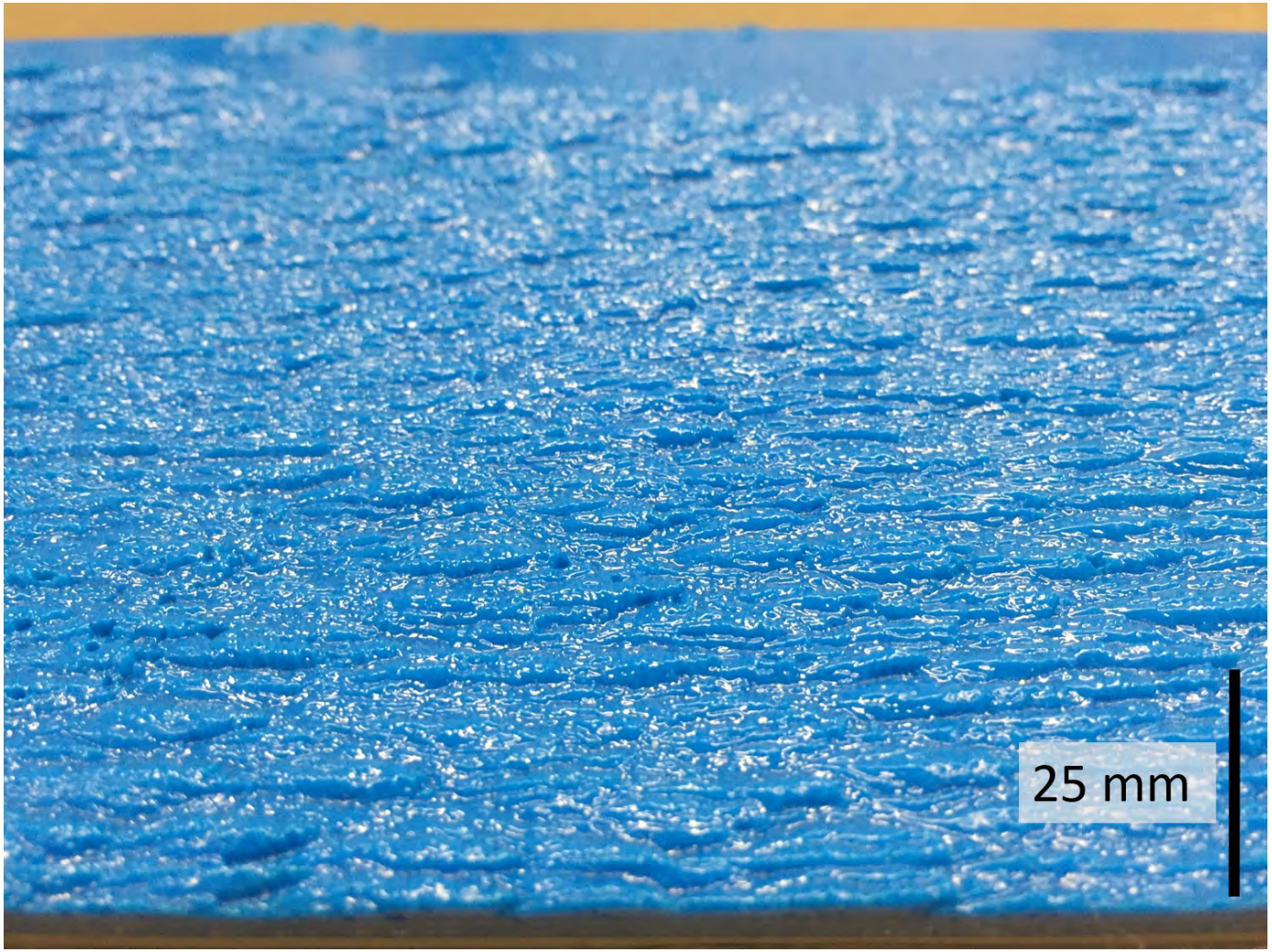

Figure 4.11: A portion of the rigid replica evaluated in Trial 10W4RR. The surface shows particularly sharp contrast between large streamers and the surrounding biofilm unlike what was observed for the rigid replica evaluated in Trial 10W2RR. Note that the image shown here was taken at an angle to show better contrast between streamers which was not accounted for by the shown scale bar.

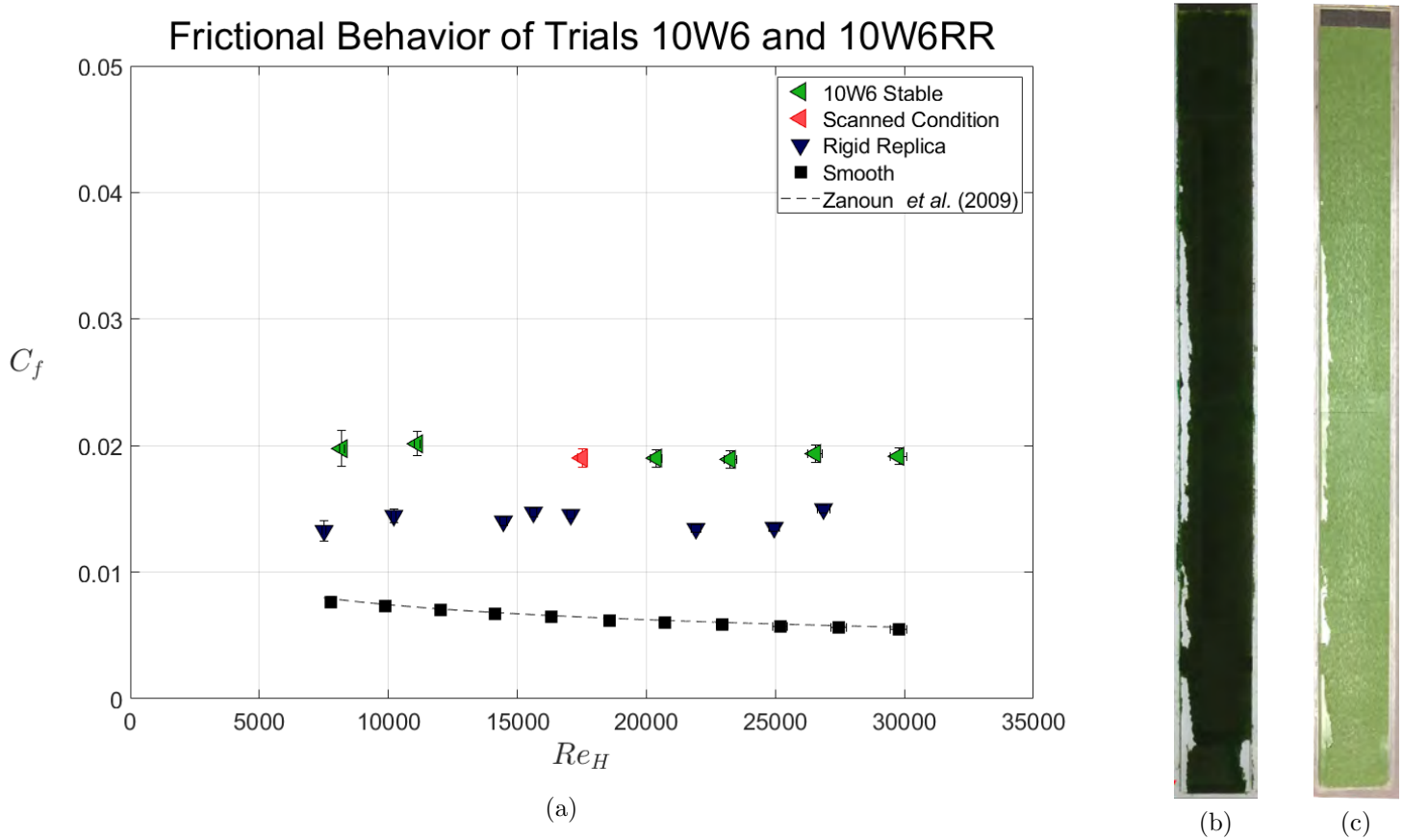

(a) (b) (c)

Figure 4.12: Resistance data for a stable biofilm layer (left-pointing green triangles) and its rigid replica (downward-pointing dark blue triangles) are shown above. Despite the fact that the data correspond to a stable surface condition, and that different methods were used to find the bulk mean velocity, U_m, the compliance drag penalty was similar to what was measured for the other ten week trials ($\Delta C_{f,soft} = 36.4\%$).

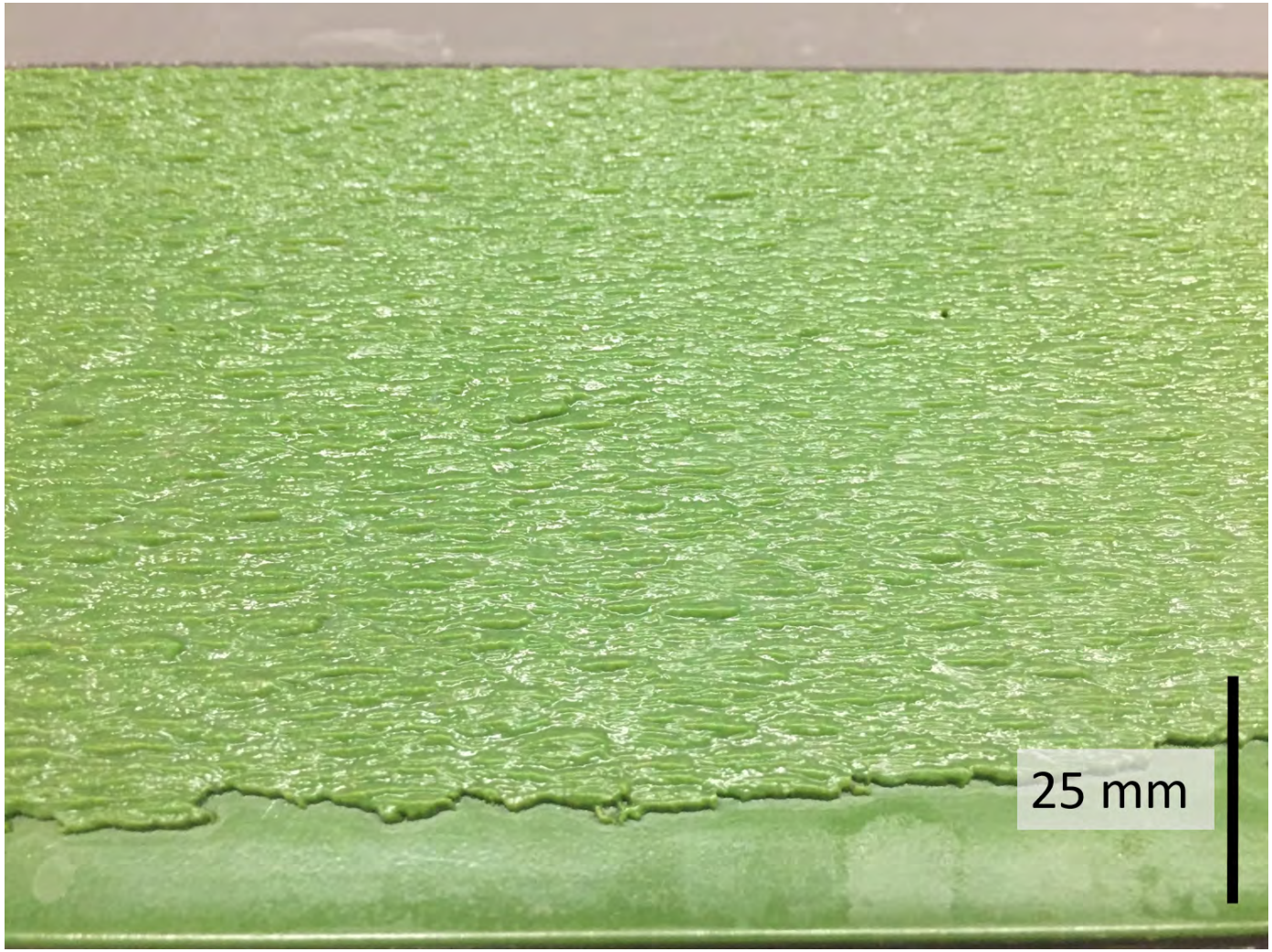

Figure 4.13: A portion of the rigid replica evaluated in Trial 10W6RR. Sloughing shows the thickness of the biofilm layer and surface streamers are partiularly well visualized by this slightly darker green color. Note that the image shown here was taken at an angle to show better contrast between streamers which was not accounted for by the shown scale bar.

Trial 10W6 and 10W6RR were performed before installation of the overhead camera and are not corrected for changes in channel gap height due to sloughing. However, the total level of sloughing was slight with only ∼5% of the surface being lost, meaning that the effect of the correction would also be minimal. Data shown in Figure 4.12 relied on PIV measurements to determine the bulk mean velocity, U_m, through the channel as the magnetic flow meter had not yet been installed. However, the bulk mean velocity calculated from PIV measurements generally agrees to within 5% of that measured by the magnetic flow meter so it is reasonable to assume that resistance data shown in 4.12 are of similar character to those measured in the other ten week trials. Note that the magnitude of C_f is somewhat less than what is observed in Figures 4.10 and 4.8 which might be due to differences in the measurement methodology but is more likely a result of the fact that data are shown for a stable biofilm layer.

While these differences in setup may be responsible for the lack of Reynolds number dependence seen for Trial 10W6 and 10W6RR, it is also possible–and perhaps more likely—that the surface exhibited different behavior because fewer measurements were taken which span a substantially larger range of Reynolds numbers or because a biofilm layer with somewhat different hydrodynamic behavior was developed through natural variation of the species comprising it. Regardless of the discrepancy in Reynolds number dependence, the magnitude of the compliance drag penalty aligns well with what was observed for the other biofilm/rigid replica pairs.

4.3 Scaling the Roughness Function for Rigid Replicas

Empirical relationships between the roughness function and added drag and roughness parameters of the rigid replicas have been derived using the same methods as described in §3.3 and §3.4. This analysis resulted in an equivalent roughness length scale which does not appear to neatly collapse measurements of ΔU^+ for the rigid replicas. However, the length scale shown in Equation 4.2 best predicted ΔU^+ for the rigid replicas. Figure 4.14 shows the results.

$$k_{RR} \;=\; 0.05(k_t \lambda_x)^{\frac{1}{2}} \tag{4.2}$$

Using the non-dimensional form of the suggested roughness height, k^+_{RR}, as a scaling parameter does not result in a complete collapse of the data onto a single curve which may be the result of relatively large levels of uncertainty in the measurements. It is also possible that a key aspect of the rigid replica geometry is

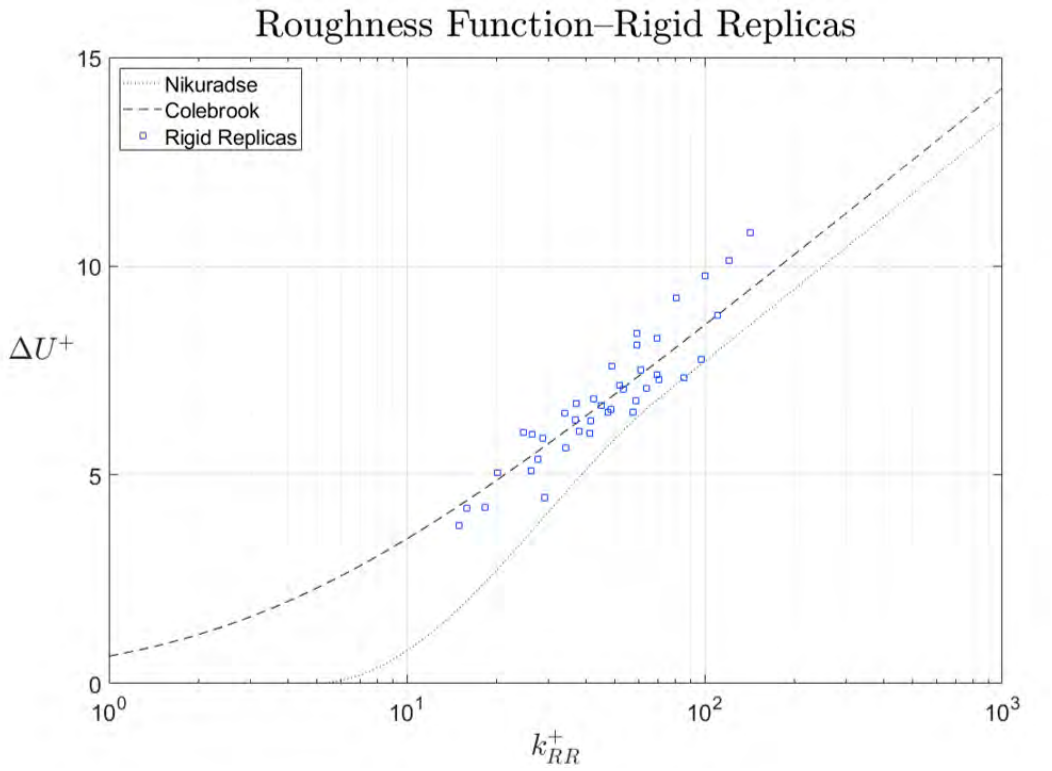

Figure 4.14: An equivalent roughness length scale, k_{RR}, provides a partial collapse of ΔU^+ for the rigid replica data. It is difficult to tell if the scatter remaining is due to uncertainty in the estimates of k_t and λ_x or if a key roughness parameter in drag production remains missing.

missing which would better collapse the data. While a wide array of roughness parameters were investigated and various combinations of length scales including $A_b^{\frac{1}{2}}$, $k_b, k_{rms}, L_s, D_s, \lambda_x, \lambda_z$ were explored, none produced complete collapse. The effective roughness height proposed by Schultz *et al.* [49] was also considered, and it is noteworthy that k_{eff} produced relatively poor collapse of the rigid replica data. Given the obvious differences between the live biofilm and rigid replicas this is not a surprising result.

While k^+_{RR} does not appear to fully collapse the data plotted in Figure 4.14, it does show that the rigid replicas exhibit fully rough behavior with slopes corresponding to κ^{-1}. Furthermore, the partial collapse provides a reasonable estimate of ΔU^+ which may be used to roughly estimate the hydrodynamic performance of the rigid replicas. The formulation of k_{RR} also provides insight into which surface features produce the most drag and gives a direction when attempting to predict their added drag, ΔC_f.

4.4 Characterizing the Added Drag of Rigid Replicas

To characterize the added drag of the rigid replicas, a Buckingham-Π analysis and the regression procedure summarized in §3.4 were performed for the rigid replica trial data. The results are shown in Equations 4.3 and 4.4 and Figure 4.15.

$$\Delta C_{f,\,RR} = 0.3\,\Pi_{RR} - 0.56 \tag{4.3}$$

where

$$\Pi_{RR} = Re_H^{0.25} A_b \left(\frac{k_t}{H}\right)^{0.81} \left(\frac{\lambda_x}{L_s}\right)^{1.03} \tag{4.4}$$

Within uncertainty, all of the added drag values are captured in the 95% confidence interval of Equation 4.3 and a tighter fit is seen than was observed for the biofilm data. This is not surprising given the more complex interaction between the biofilm layer and surrounding flow field. It also suggests that the scatter seen in Figure 4.14 might be due to relatively poor estimation of k_t and/or λ_x since $\Delta C_{f,\,RR}$ is reasonably well predicted by the combination of just these two parameters, the Reynolds number, Re_H, and fouled area, A_b.

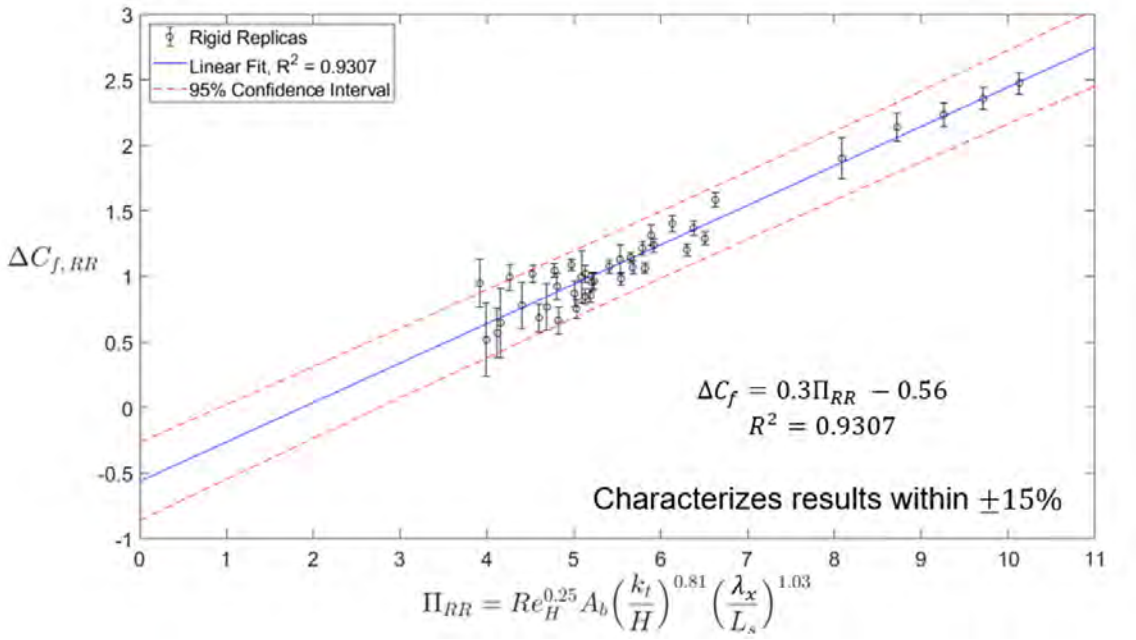

Figure 4.15: The empirical relationship defined in Equation 4.4 consistently captures the drag penalty for rigid replicas, $\Delta C_{f,\,RR}$. Within uncertainty, all measured data correspond with the 95% confidence interval for Equation 4.3.

Note that because sloughed panels are difficult to manufacture, rigid replicas were only generated for trials and flow speeds with significantly fouled area, $A_b \gtrsim 80\%$. As a result, it is difficult to distinguish the role played by A_b which was assumed to scale linearly with $\Delta C_{f,\,RR}$. Evidence of the better fit between rigid replica data and the least squares regression provided by Equations 4.3 and 4.4 is also seen in Table 4.3.

The measured and predicted values of $C_{f,\,replica}$ presented in Table 4.3 verify that the equations given above predict the drag on a rigid replica within roughly $\pm 15\%$ of the measured value. Data from Trials 5W1RR and 5W3RRe show the poorest estimation and it is not clear if this is the result of the particular nature of these panels or random variability. The exponents in Equation 4.4 provide the relative contribution of the various non-dimensional groupings to ΔC_f. As the added drag produced by the rigid replicas is generally Reynolds number independent, the contribution from Re_H simply accounts for the normalization of $C_{f,\,replica} - C_{f,\,smooth}$ by $C_{f,\,smooth}$. Furthermore, because the fouled area of most rigid replicas was near unity, the contribution from A_b is relatively minor and most of the drag increase can be accounted for by the highest roughness features (as captured by k_t) and the spacing between streamers, λ_x.

Table 4.3: Comparison of predicted and measured biofilm resistance (for cases with rigid replica data)

Trial	Surface condition	Re_H	$C_{f,\,replica}$ measured	$C_{f,\,replica}$ predicted	% diff
5W1RR	Evolving	6547	0.01411	0.01298	-8.7
5W2RR	Evolving	7372	0.01475	0.01452	1.6
5W3RRe	Evolving	13 609	0.01383	0.01208	12.7
5W3RRs	Stable	13 755	0.013	0.01327	-2.0
10W2RR	Evolving	7737	0.02361	0.02292	2.9
10W4RR	Evolving	10 508	0.01679	0.01615	3.8
10W6RR	Stable	17 511	0.01444	0.01439	0.4

One explanation suggested by these relationships may be that the drag experienced by the rigid replicas is primarily from shedding of the largest 'streamers' and that replicas having larger spacing between streamers do not benefit from a 'sheltering' effect as those with closely spaced streamers might. However, this explanation derives solely from empirical formulations and no direct evidence has been presented to confirm it. Nevertheless, the results shown in Table 4.3 confirm that the frictional performance of the rigid replicas can be inferred from knowledge of just the fluid

properties, flow speed, channel gap height, fouled area, trough-to-peak roughness, and average streamer length and spacing.

4.5 Roughness and Compliance Contributions to Added Drag

The results of hydrodynamic trials, scaling, and regression analysis for the biofilm layers and their rigid replicas have revealed key insight into which parameters play a role in drag production for these two different types of roughness. Furthermore, the empirical equations relating the roughness geometry of a surface to its coefficient of friction allow estimation of drag produced by roughness and compliance effects. Figure 4.16 shows the application of results from measurements of stable biofilm to the empirical formulation proposed for rigid replicas. While the data appear to collapse somewhat (although not as well as in Figure 3.17), the characterization curve for the $\Delta C_{f,RR}$ (shown by the blue line) under-predicts the drag penalty for biofilm layers. This is consistent with the resistance curves shown throughout Chapter Four and confirms that the effects of compliance are substantial in drag production.

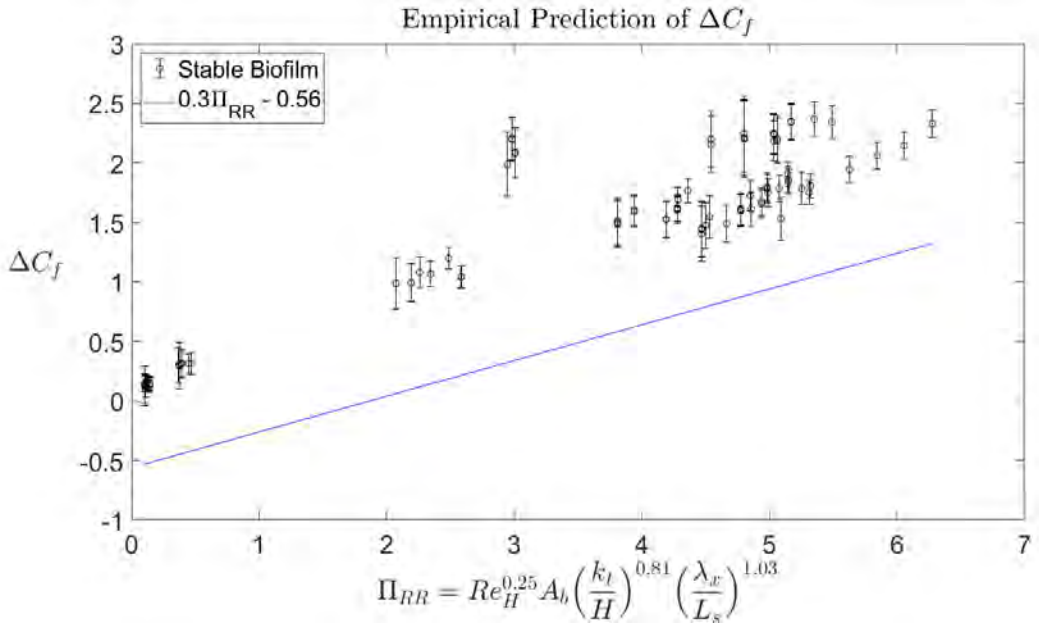

Figure 4.16: Applying the empirical formulas which characterize the rigid replica drag penalty shows that compliance effects are important in drag production of biofilm layers.

Disassociating the contributions of roughness and compliance to the drag penalty can be performed using a simple model as shown in Equation 4.5. Note that although this model provides a simple and practical way to understand biofilm drag production,

the flow physics underlying the drag increase for biofilm layers and rigid replicas are complex and not easy to determine.

$$\Delta C_{f,\,biofilm} \;=\; \Delta C_{f,\,rough} + \Delta C_{f,\,soft} \tag{4.5}$$

and

$$C_{f,\,biofilm} \;=\; \Delta C_{f,\,biofilm} + C_{f,\,smooth} \tag{4.6}$$

Table 4.4: Measured and predicted added drag contributions due to softness and roughness

	Trial	Surface	Re_H	$C_{f,\,smooth}$	$C_{f,\,biofilm}$	$\frac{\Delta C_{f,\,rough}}{\Delta C_{f,\,biofilm}}$ [%]	$\frac{\Delta C_{f,\,soft}}{\Delta C_{f,\,biofilm}}$ [%]
Measured	5W1	Evolving	6547	0.00826	0.0182	47.5	52.5
	5W2	Evolving	7372	0.00802	0.01987	56.8	43.2
	5W3	Evolving	13 609	0.00688	0.01822	61.3	38.7
	5W3	Stable	13 755	0.00686	0.01905	50.3	49.7
	10W2	Evolving	7737	0.00792	0.03362	61.1	38.9
	10W4	Evolving	10 508	0.00734	0.02521	52.9	47.1
	10W6	Stable	17 511	0.00646	0.01903	63.5	36.5
Predicted	5W1	Evolving	6547	0.00826	0.02345	38.5	61.5
	5W1	Evolving	7372	0.00802	0.01858	61.5	38.5
	5W3	Evolving	13 609	0.00688	0.01753	48.8	51.2
	5W3	Stable	13 755	0.00686	0.01722	61.8	38.2
	10W2	Evolving	7737	0.00792	0.03172	63	37
	10W4	Evolving	10 508	0.00734	0.02055	66.7	33.3
	10W6	Stable	17 511	0.00646	0.02073	55.6	44.4

Using the above equations and the results from the hydrodynamic trials, the added drag due to roughness, $\Delta C_{f,\,rough}$, and compliance, $\Delta C_{f,\,soft}$, were calculated. Because Equations 4.5 and 4.6 must be calculated at the same Reynolds number (Re_H), values for $\Delta C_{f,\,rough}$ were found via interpolation. Table 4.4 shows the measured contributions of roughness and compliance to the overall biofilm drag penalty ($\frac{\Delta C_{f,\,rough}}{\Delta C_{f,\,biofilm}}$ and $\frac{\Delta C_{f,\,soft}}{\Delta C_{f,\,biofilm}}$, respectively). The proportion of measured added drag due to the effects of compliance ranged from 36.5%–52.5% which is somewhat narrower than the predicted range of 33.3%–61.5%. Characterization of the percent compliance drag which contributes to the overall added resistance of the biofilm layers were within ±15% of the measured values. While these findings are encouraging, the proposed empirical

relations may not apply to soft fouling investigated in other studies or observed in the field.

4.6 Chapter Summary

Rigid replicas of several five and ten week biofilm layers were manufactured and evaluated in the SF3 to establish the contributions of roughness and compliance effects in biofilm drag production. Measurements of surface topography demonstrate that the rigid replicas matched the time-averaged, spatially filtered geometry of the biofilm layers which they replicate. Three panels showed significant deviation in assumed wall-zero location; however, this discrepancy does not affect the measured surface profile and is accounted for through the use of an appropriate channel gap height. Results for all of the rigid replicas may be confidently compared to the biofilm layers which they represent.

Frictional behavior of the rigid replicas was determined from hydrodynamic trials in the SF3 which showed that the added drag they experienced was less than that observed for the biofilm layers. Because C_f for rigid replicas demonstrated a different trend in Reynolds number dependence than that measured for the biofilm layers, direct comparison of the drag was limited to the range of Re_H values near the scanned condition. Results show that both roughness and compliance effects contribute to the total increase in resistance with each supplying roughly half of the overall added drag for a biofilm layer.

Since the results may be specific to the biofilm layers and facilities used in this work, attempts were made to scale the roughness function and predict the added drag based on the structural characteristics of the biofilm layers and rigid replicas. Although complete collapse of the roughness function measured for rigid replicas was not found, a scaling parameter, k_{RR}—based on the average trough-to-peak roughness height, k_t and streamwise spacing between the biofilm streamers, λ_x—was proposed which was partially successful in collapsing the roughness function measurements. Also, empirical equations relating $\Delta C_{f,RR}$ to k_t and λ_x were presented which typically characterized the coefficient of friction within 5% of measured values (although differences as large as 12.7% were seen).

A simple model was proposed in which the drag penalty of a biofilm layer, $\Delta C_{f,biofilm}$, was decomposed into contributions from roughness and compliance effects, $\Delta C_{f,rough}$ and $\Delta C_{f,soft}$, respectively. Once the drag penalty of the biofilm layer is known, determining $C_{f,biofilm}$ from $\Delta C_{f,biofilm}$ is straightforward. The flow physics of the

biofilm layers are complex and resist this simple description but coarse understanding of phenomena underlying the increase in resistance are provided by the model and predictions of $\Delta C_{f,\,soft}$ matched within $\pm 15\%$ of the measured results.

CHAPTER V

Flow over Biofilms and Their Rigid Replicas

5.1 Overview

The primary objective of this dissertation is to investigate the role of rough and compliant drag production mechanisms of biofilm layers which cover walls bounding turbulent flow. The results and conclusions laid forth in earlier chapters are derived from measurements of the biofilm surface and flow resistance through the Skin-Friction Flow Facility (SF3) but no description of the flow structure has been provided. In this chapter, measurements of the average local flow field over biofilm layers and their corresponding rigid replicas are presented and discussed. Then, comparisons are made between the local details revealed by the flow field with global parameters inferred from the frictional results.

Flow across the entire channel was captured using Particle Image Velocimetry (details provided in §2.6) at high resolution and the resulting vector fields provided a detailed mapping of the mean velocity profiles over the various biofilm layers. Measurements collected near the bottom (smooth) wall were also used to correct for channel asymmetry, and integration of the velocity profile from wall-to-wall provided a concomitant measure of the bulk mean velocity through the channel—a vital backup in the case of Trials 10W6 and 10W6RR which were performed before installation of a high-accuracy magnetic flow meter in the SF3.

Measurements of the flow field were collected at multiple spanwise locations for every surface and Reynolds number discussed in this dissertation. However, due to the significant amount of time required to perform highly resolved PIV analysis, results presented in the following sections were from a single spanwise location (typically at the centerline of the SF3) and are limited to 16 different surfaces: the smooth baseline, 80 grit sandpaper, the seven rigid replicas and their corresponding biofilm layers. Findings presented here are also limited to the mean flow field and higher order

turbulent statistics are not discussed. While Reynolds stresses were calculated, study of the resulting profiles indicate that the inability of the PIV software to account for reflections from the biofilm layer, and the relatively low number of frame pairs collected may have prevented the determination of accurate, converged statistics. Although the scope of the results presented below is limited, a reliable description of the flow field is provided. Both common features and particularities of flow over biofilm layers and their rigid replicas are discussed.

5.2 Mean Velocity Profiles

5.2.1 Five Week Biofilms and Rigid Replicas

Figures 5.1—5.13 present the mean velocity profiles for each rigid replica and the biofilm layer to which it corresponds at approximately the same friction Reynolds number, Re_τ (which is usually also the closest Re_H value). Plots are given in both outer (a) and inner layer (b) scaling providing a visual description of the average flow field across the entire channel and also details of the near-wall region. Velocity defect plots are also provided which demonstrate how well outer layer similarity holds for flow above the smooth baseline, rigid replicas, and biofilm covered surfaces. Velocity data collected from trials of the rigid replicas are shown as blue triangles while those data pertaining to the original biofilm layer are plotted as green circles. Baseline (smooth) data collected at the closest friction Reynolds number are also presented in each figure (shown as black squares).

Data for Trials 5W1 and 5W1RR are shown in Figures 5.1 and 5.2. The outer layer velocity profile immediately reveals a large difference in the level of asymmetry across the flow field between the rigid replica and soft biofilm. As the data are non-dimensionalized by the channel gap height, it is not obvious if the difference is due to variations in the level of wall shear stress or the effect of blockage. Consulting Table 4.2 shows the thickness of the two layers is within $\sim$55 μm so it appears that the bulk of the difference in asymmetry is due to the wall shear stress which conditions the velocity profile throughout the channel.

While it can be seen that the rough surfaces experience an increase in drag from Figure 5.1a, it is more clearly displayed by the roughness function, ΔU^+, shown in the inner layer plot (Figure 5.1b). A few further observations can be made regarding Figure 5.1b. Firstly, although the rigid replica curve displays fully rough behavior with no apparent viscous sublayer, biofilm data appear to exhibit a nearly linear drop in velocity when approaching the origin of the biofilm layer. It is difficult to verify

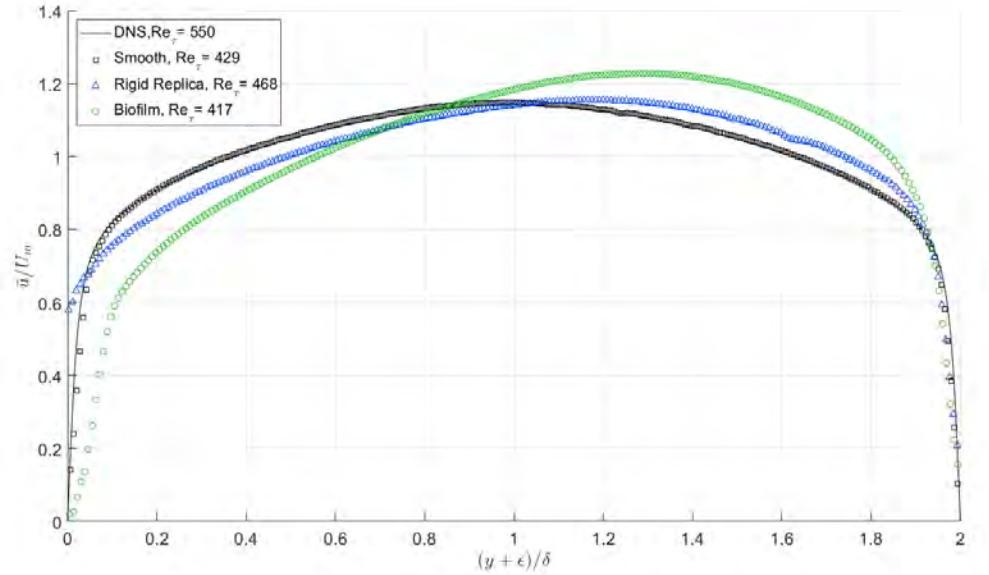

(a)

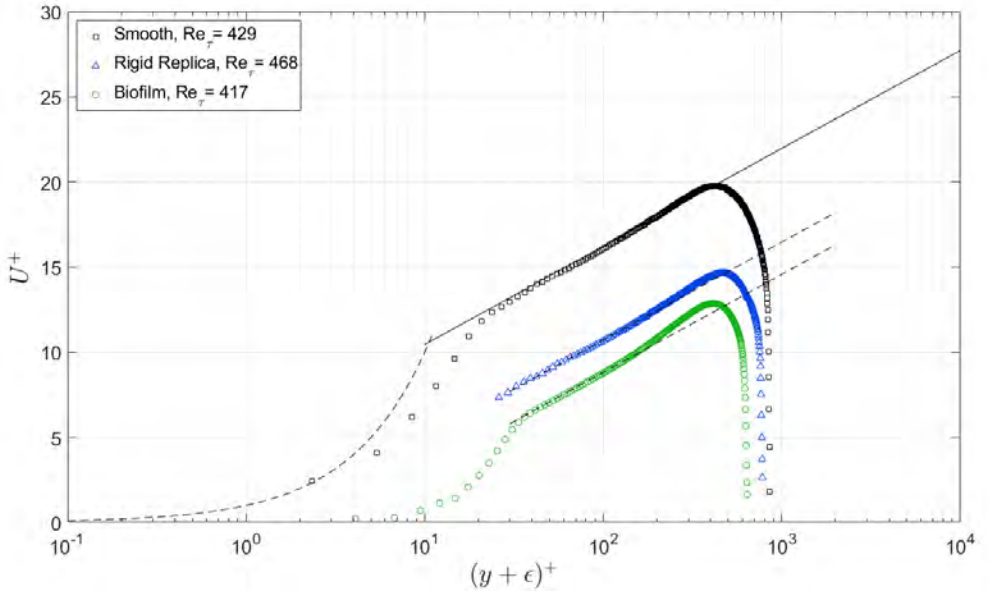

(b)

Figure 5.1: Mean velocity profiles for Trials 5W1 and 5W1RR show that the biofilm layer experiences a greater drag increase. The biofilm data (green circles) also appear to display 'near-viscous' behavior in the region of flow immediately adjacent to the wall while data for the rigid replica (blue triangles) exhibit fully rough behavior. Biofilm flow data also appear to show an increased 'wake' region in the outer layer flow.

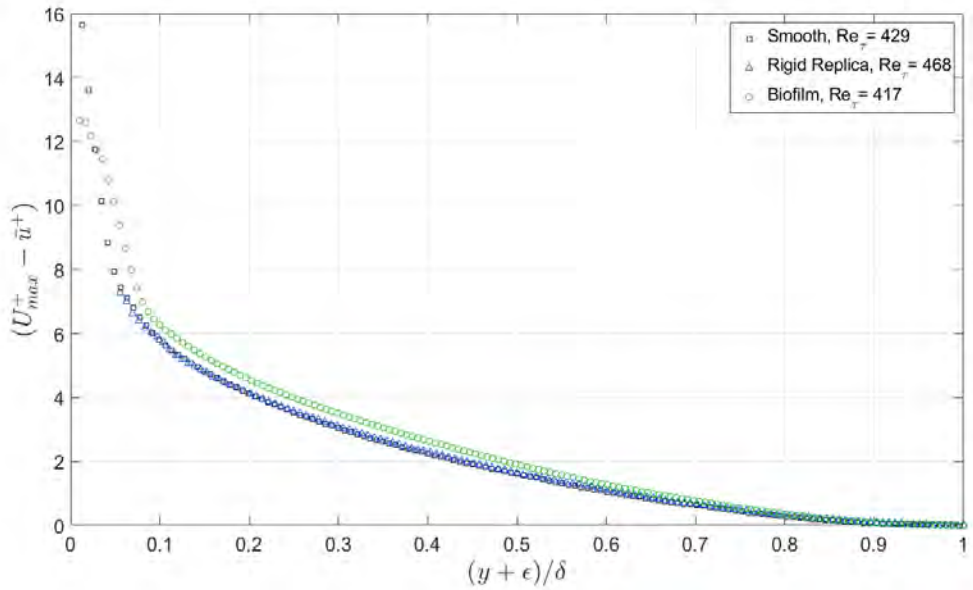

Figure 5.2: Velocity defect profiles for Trials 5W1 and 5W1RR show that outer layer flow over the biofilm surface deviates somewhat from those measured for the smooth baseline and rigid replica.

this finding given the very thin region of the flow to which these data belong (in this case ∼300 μm), but it is possible that the mean flow increases linearly as it passes from the base of the biofilm layer through an ever-decreasing density of streamers until reaching the log layer.

Secondly, the behavior of the live biofilm mean velocity profile shows a sharper increase in flow speed for a 'wake-like' region which occurs before the flow reaches its maximum velocity. This is in contrast with the profiles belonging to the smooth and rigid replica data in which almost no 'wake-like' behavior is seen. This second effect may be Reynolds number dependent as trials at higher Re_τ flows do show a 'wake' region for the smooth data and rigid replicas. The presence of a wake-like region of flow is confirmed by Figure 5.2 which shows how well the velocity profiles above the three surfaces match one another when presented in velocity defect form.

Figure 3.7 compares the flow fields for Trials 5W2 and 5W2RR. As the rigid replicas examined in Trial 5W1RR and 5W2RR were produced using scan data recorded at similar Reynolds numbers, it is not surprising that many common features are seen in Figures 3.6 and 3.7. For instance, similar disparity in channel asymmetry for the rigid replicas and biofilm layers is seen in the two figures produced using outer layer scaling. Also, the offset in ΔU^+ values appears to be repeated in the inner layer plots and, again, the biofilm data appear to show a sort of linear sublayer in the near-wall

region. Differences in the flow structure of the outer layer are seen as Trial 5W2RR does appear to display a pronounced wake region where Trial 5W1RR did not. The

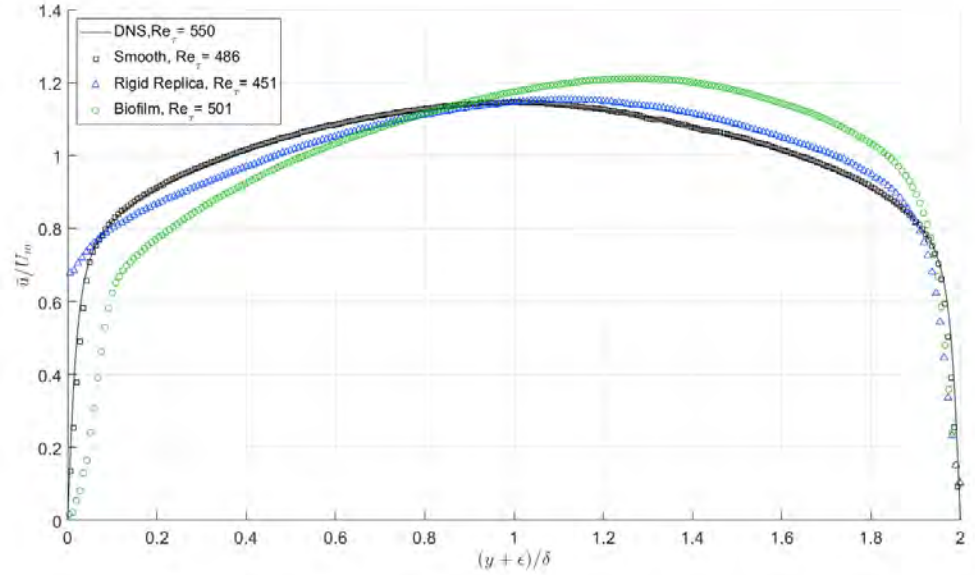

(a)

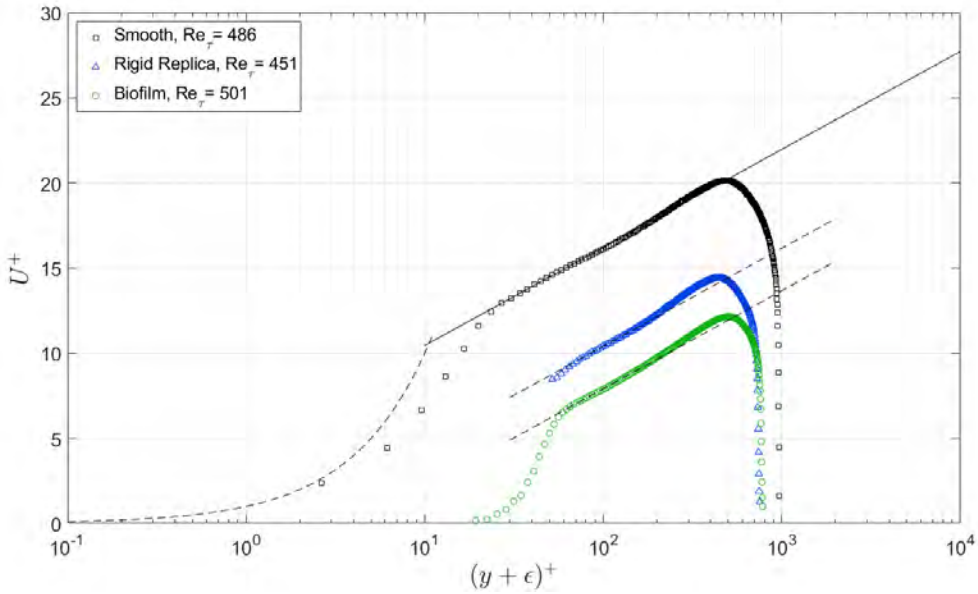

(b)

Figure 5.3: Mean velocity profiles derived from PIV data collected during Trials 5W2 and 5W2RR show similar behavior with what can be observed in Figure 5.1. Note that one difference is the slight, wake region of flow observed in the rigid replica data shown in (a). The inner-scaled mean velocity profiles between rigid replica and soft biofilm exhibit strikingly similar behavior in the log-layer and beyond.

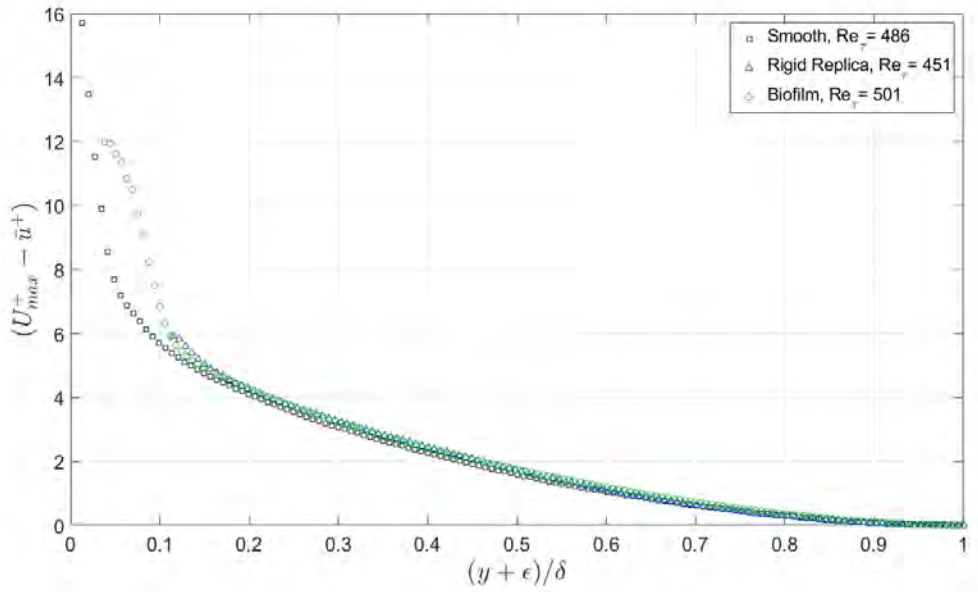

Figure 5.4: Outer layer similarity is observed for the flow the surfaces evaluated in Trials 5W2 and 5W2RR. This is in contrast to what was observed for Trials 5W1 and 5W1RR. The reason for the difference is not known but may be due to the specific features of the local topography above the PIV field of view.

reason for this is unknown, but it may be associated with differences in local topography between the two cases. Another difference is the relative location of the peak velocity seen for the curves. The better alignment seen in Figure 5.3b results from the closer proximity in Re_τ for Trials 5W2 and 5W2RR which is confirmed by the tight grouping of the drop-off in flow data after the peak flow speed. Note that good agreement in outer layer similarity shown in Figure 5.4 confirms the assertion that velocity profiles recorded for Trials 5W2 and 5W2RR match better than Trials 5W1 and 5W1RR.

Flow fields measured in Trials 5W3, 5W3RRe, and 5W3RRs are shown in Figures 5.5—5.8. The rigid replicas studied in these trials were collected at the same flow speed but during the evolving and stable portions of Trial 5W3 (Re_τ = 871 and 895, respectively) and only differ by the value of u_τ used to non-dimensionalize the plots, in the amount of sloughing experienced by the panel (which was slight), and in the rigid replica production process. Trial 5W3RRs was produced prior to implementation of the MATLAB routines which enabled scan data of the biofilm surface above the 38 mm quartz insert to be included in the manufacturing process. Therefore, Trial 5W3RRs does not have the same local topography for the rigid replica and biofilm surfaces. Since the rigid replica produced for Trial 5W3RRe did include this enhancement, it

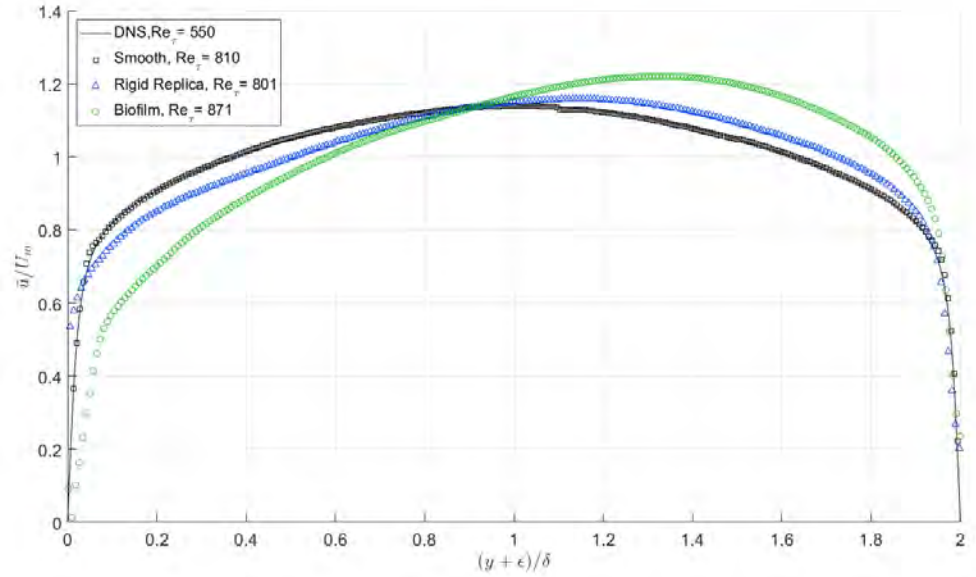

(a)

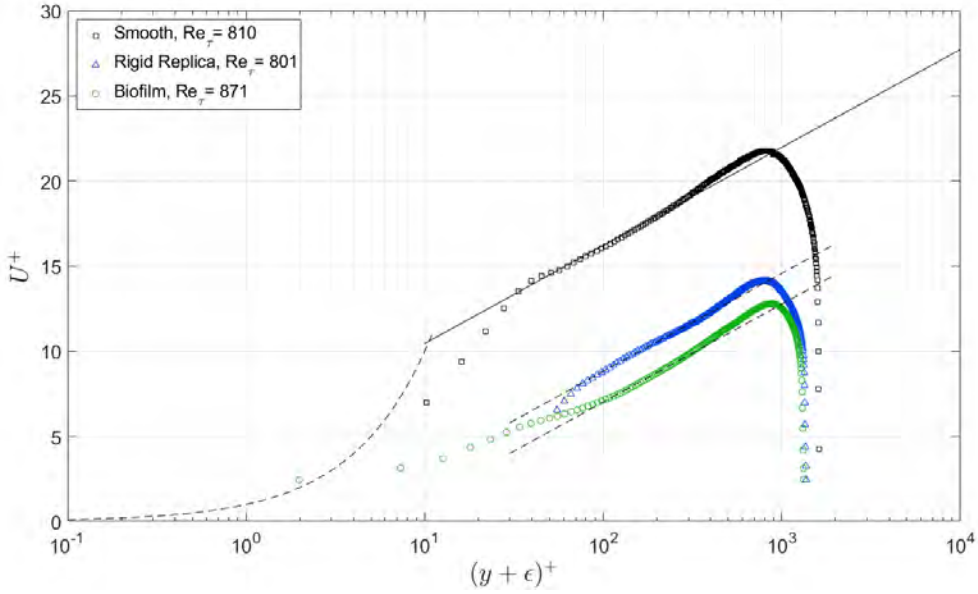

(b)

Figure 5.5: Flow over the biofilm layer in Trial 5W3 shows somewhat different near-wall behavior than was observed for the other trials with a slow increase in ΔU^+ until the log-layer is reached. Rigid replica data for Trial 5W3RRe also have slightly different behavior but the reasons behind the difference are unknown.

has the same time-averaged local topography. This may explain why the velocity profiles display a closer match for data collected in Trials 5W3e and 5W3RRe than

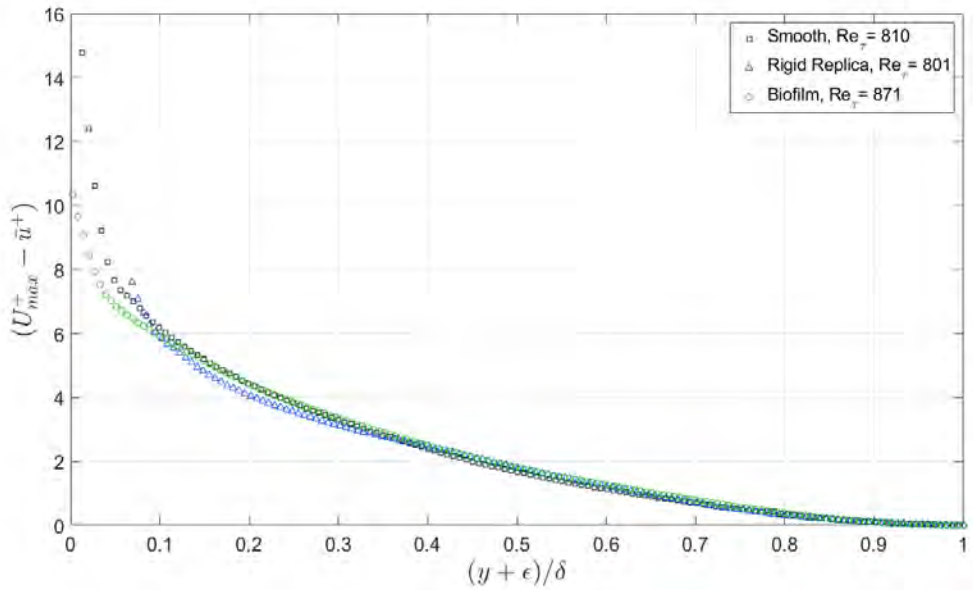

Figure 5.6: Outer layer similarity appears to hold for the smooth baseline, rigid replica, and biofilm surfaces in Trials 5W3e and Trial 5W3RRe. The data begin to diverge around $(y+\epsilon)/\delta = 0.3$.

Trials 5W3s and 5W3RRs.

Beside slight differences in the level of asymmetry observed for the two rigid replicas (likely due to the difference in channel blockage), the outer layer plots displayed in Figures 5.5a and 5.7a show velocity profiles in relatively good agreement. Data for both rigid replicas and biofilm layers have a slightly lower velocity gradient than the smooth panel data in the near-wall region ($(y+\epsilon)/\delta \lesssim 0.2$); however, while flow over the rigid replicas continues to increase smoothly, there appears to be a slight inflection point for the biofilm layers around $(y+\epsilon)/\delta \approx 0.1$. This peculiar inflection point is also evident in the inner layer plots displayed in Figures 5.5b and 5.7b where it appears as a slight hump in the velocity profiles around ($y^+ = 50$). The persistence of this feature across both the evolving and stable biofilm layers suggests that it may be linked to the unique biofilm topography bounding the flow measurement region. In these figures, the velocity profiles over the biofilm layer do not show the same near-wall behavior as was seen for Trials 5W1 and 5W2. Instead, flow increases in a more logarithmic manner. However, similarities are seen in the outer flow region with all biofilm layers displaying velocity profiles which appear to contain a strong wake region after a somewhat abbreviated log layer.

Flow over both rigid replicas of Trial 5W3 exhibit fully rough behavior in the near-wall region but some differences in the outer region far from the surface (which are

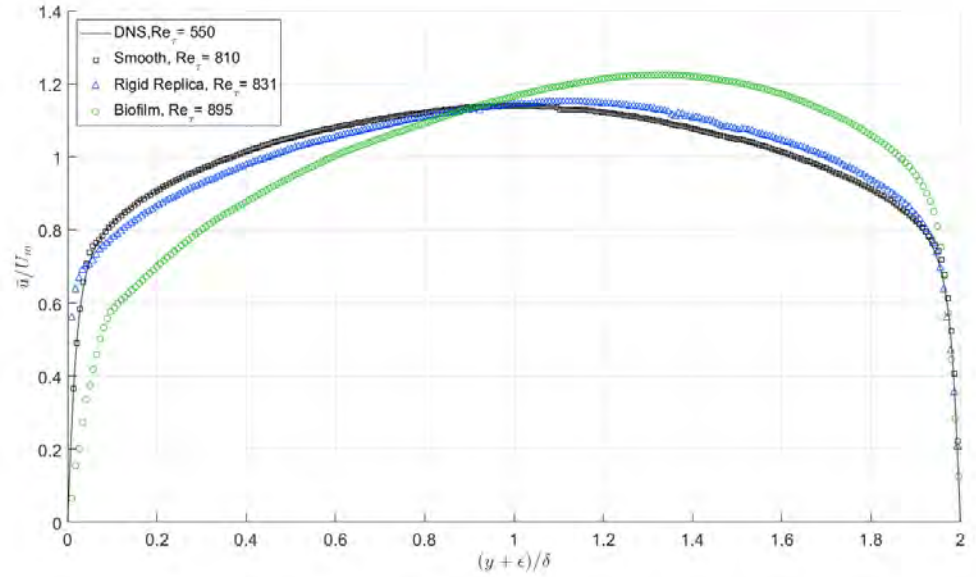

(a)

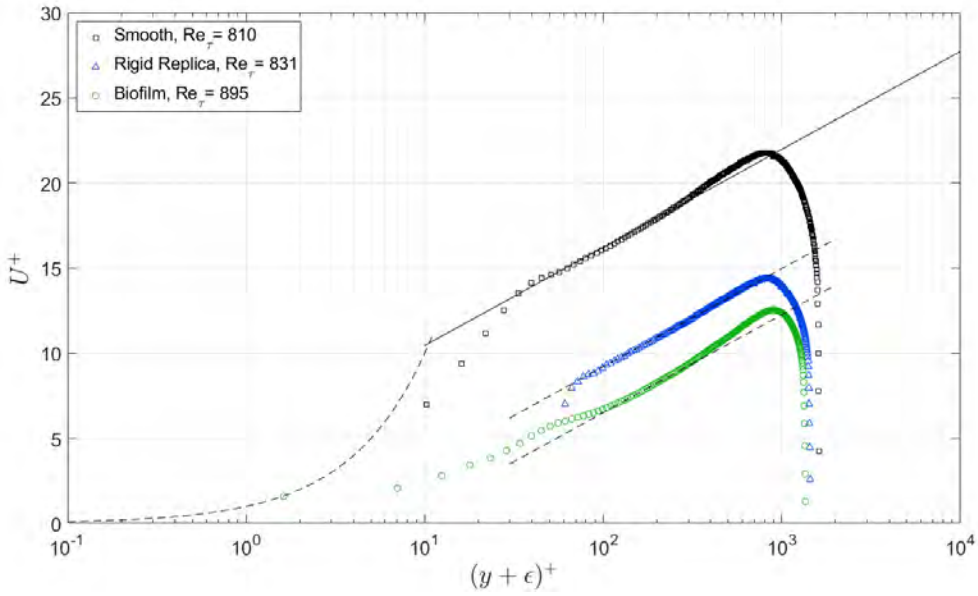

(b)

Figure 5.7: Mean velocity profiles captured during Trials 5W3 and 5W3RRs are shown above using outer (a) and inner (b) scaling. Flow over the rigid replica examined in Trial 5W3RRs appears to be somewhat different than that for Trial 5W3RRe (Figure 5.5) despite replicating the same panel (but for evolving and stable conditions). The asymmetry shown in (a) for the stable rigid replica appears to be slighter than was seen for the evolving replica and the stable replica also does not show a wake-like flow region although the evolving replica did.

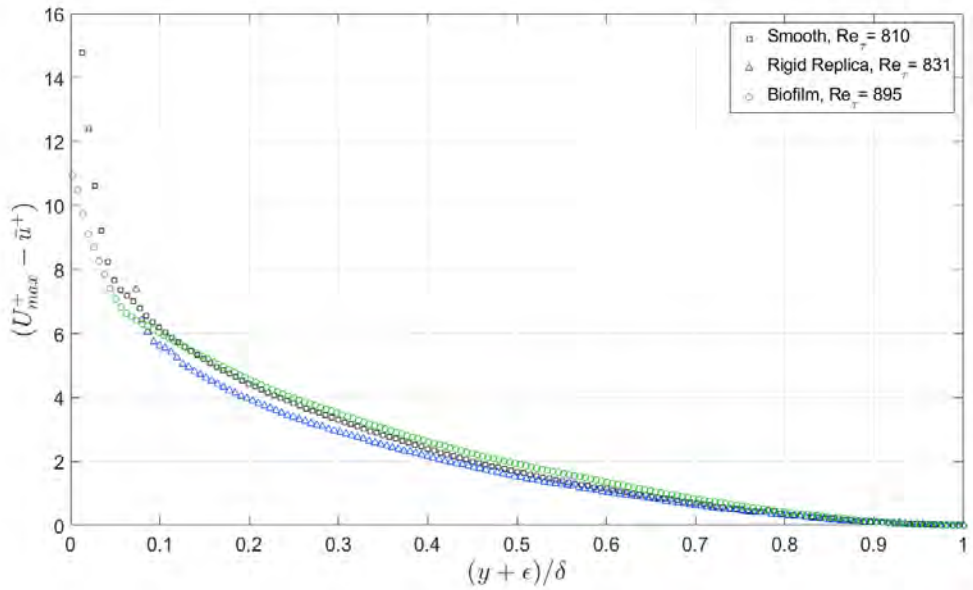

Figure 5.8: In contrast to what was observed for the evolving data, the velocity defect profiles in Trials 5W3s and 5W3sRR do not appear to exhibit particularly similar outer layer flow. As the flow over the biofilm layers in Trials 5W3e and 5W3s appears to collapse tolerably well with the smooth baseline data, this is likely due to differences in the manufacturing process used between the Trials 5W3RRe and 5W3RRs.

likely due to differences in the manufacturing process described above). The velocity profile shown for Trial 5W3RRe appears to have a wake region but that shown for Trial 5W3RRs does not. Furthermore, a noticeable difference exists in the separation between rigid replica/biofilm curves for the evolving and stable trials. Figures 5.6 and 5.8 further support the theory that differences in the outer layer stem from local topography. This is not entirely surprising given the large scale of the rigid replica roughness to the outer length scale of the channel flow.

5.2.2 Ten Week Biofilms and Rigid Replicas

As shown in Figures 5.9—5.14, greater variation is observed in the velocity profiles over biofilm layers grown for ten weeks and their rigid replicas than for the five week trials. For instance, examination of the outer layer plots reveals that while the flow field over the biofilm layers all exhibit fairly strong departure from the symmetric, smooth wall velocity profile, the rigid replicas show various degrees of asymmetry. Also, a wide range of separation is seen in the roughness function offset between the rigid replicas and biofilm layers. Finally, velocity defect profiles show that some biofilm/rigid replica pairs display strong outer layer similarity while others do not. These results are presented and discussed in greater detail below.

The mean velocity profiles presented in Figure 5.9 show similar behavior to the results of Trial 5W3 with a sharp inflection in the velocity gradient over the biofilm layer at $(y+\epsilon)/\delta \approx 0.15$. Interference caused by strong reflections off the rigid replica in Trial 10W2RR confound the flow data, but it appears that this behavior is also seen for the rigid replica and might be the result of flow around a large streamer. While the inner layer plot shows less agreement between the flow fields over the biofilm layer and rigid replica, the inflection point is present as a hump in near-wall flow profile which occurs just before the onset of the log layer.

While the velocity profiles over the rigid and compliant roughness share this feature in the near-wall region, their behavior in the outer flow appears to deviate with flow over the biofilm exhibiting a strong wake where the rigid replica appears to have none. This is seen clearly in Figure 5.10 which shows that flow is relatively dissimilar for the biofilm layer across almost the entire flow field. Although the rigid replica evaluated in Trial 10W2RR shows better agreement with the smooth baseline velocity defect profile, it also deviates in the outer layer (beginning at $(y+\epsilon)/\delta \approx 0.45$). As the biofilm layer evaluated in Trial 10W2 was the thickest of all those studied, it is not surprising that the flow over this surface fails to display outer layer similarity. It is also notable that the rigid replica evaluated in Trial 10W2RR was manufactured before implementation of the MATLAB code which allowed the topography above the quartz insert to be replicated and a portion of scan data was substituted which does not match the local biofilm topography. Both the thickness of the biofilm layer and differences in local topography likely conspire to prevent outer layer similarity.

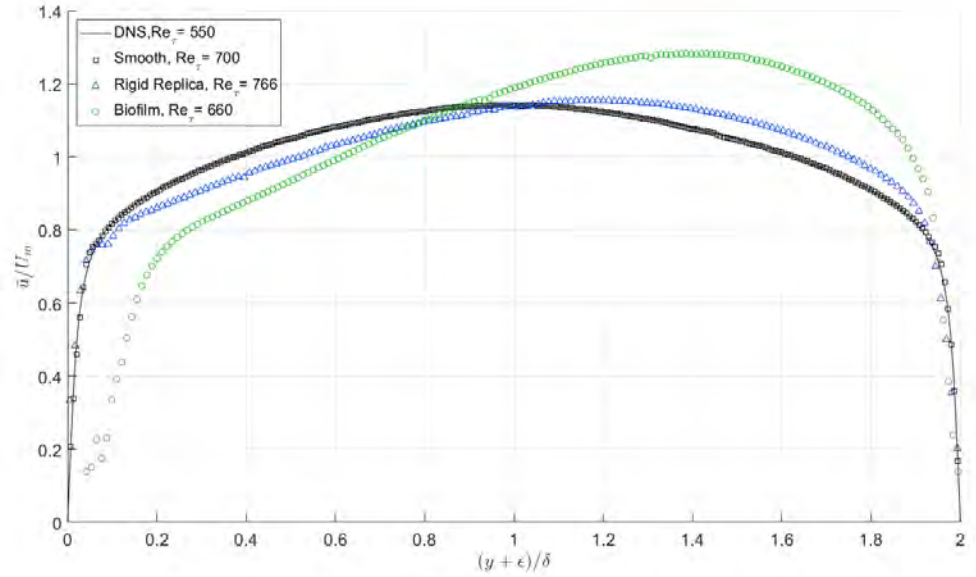

(a)

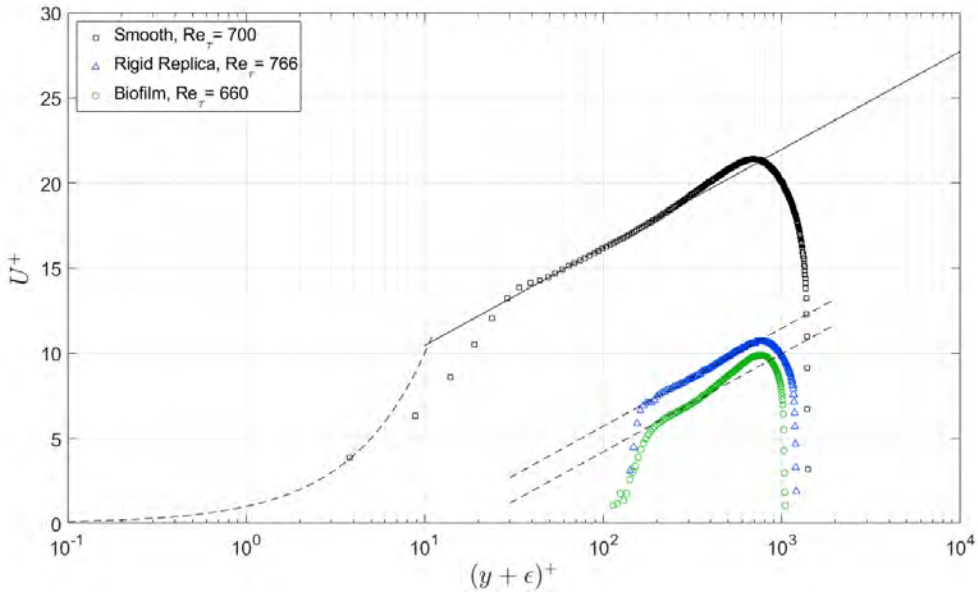

(b)

Figure 5.9: Flow data collected during Trial 10W2 and 10W2RR show peculiar features in the near-wall region as an inflection point can be seen which is not generally observed for flow data from the other ten week trials. Significant differences in flow structure can be seen between the biofilm layer and its rigid replica in the outer layer of flow as well. These are likely due to differences in local topography and the relatively small separation in surface roughness and outer flow length scales.

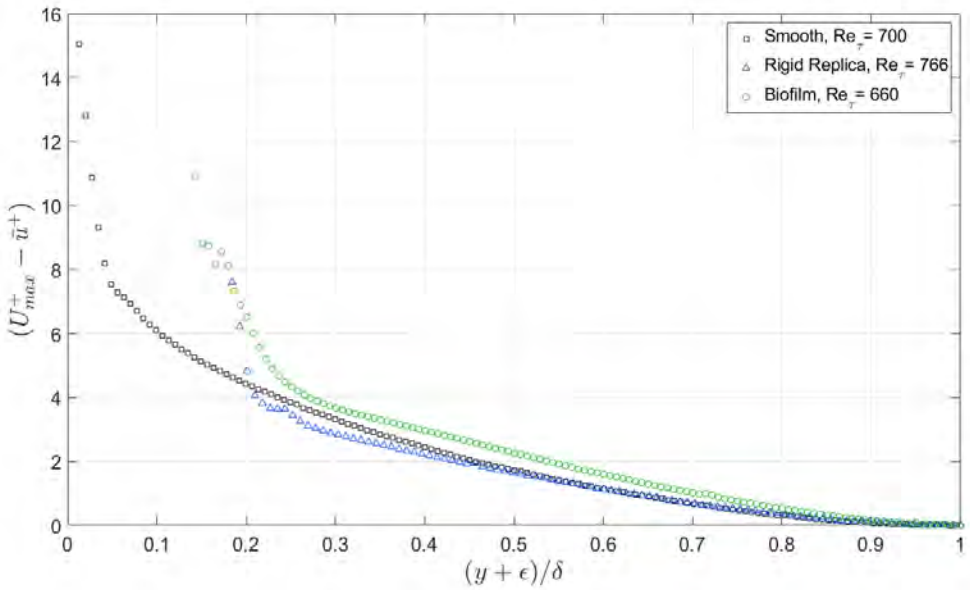

Figure 5.10: Velocity profiles from Trials 10W2 and 10W2RR show significant differences with one another and the smooth baseline. This is likely due to differing local topography and the small separation in surface roughness and outer length scales.

Figures 5.11 and 5.12 detail the flow field measured in Trials 10W4 and 10W4RR. Here, good agreement between the rigid replica and biofilm layer is observed in both the outer and inner layer plots and velocity defect plot which may be due to the matching local topography (the rigid replica in Trial 10W4RR was produced using scan data above the quartz insert). Both velocity profiles show similar levels of asymmetry, and behavior in the outer region of the flow agrees with both surfaces showing wake-like flow. The only difference between the two velocity profiles is the existence of a near-wall flow region which is captured by the biofilm data where none exists for the rigid replica. This is a consistent finding for the rigid replica/biofilm pairs. Noisy flow measurements taken during Trial 10W4 were caused by occasional obstruction of the camera FOV by a partially sloughed portion of biofilm between the camera lens and light sheet plane.

Flow data shown in Figures 5.13 and 5.14 typically behave well for the biofilm layer but the trends observed for the rigid replica appear particularly peculiar. As

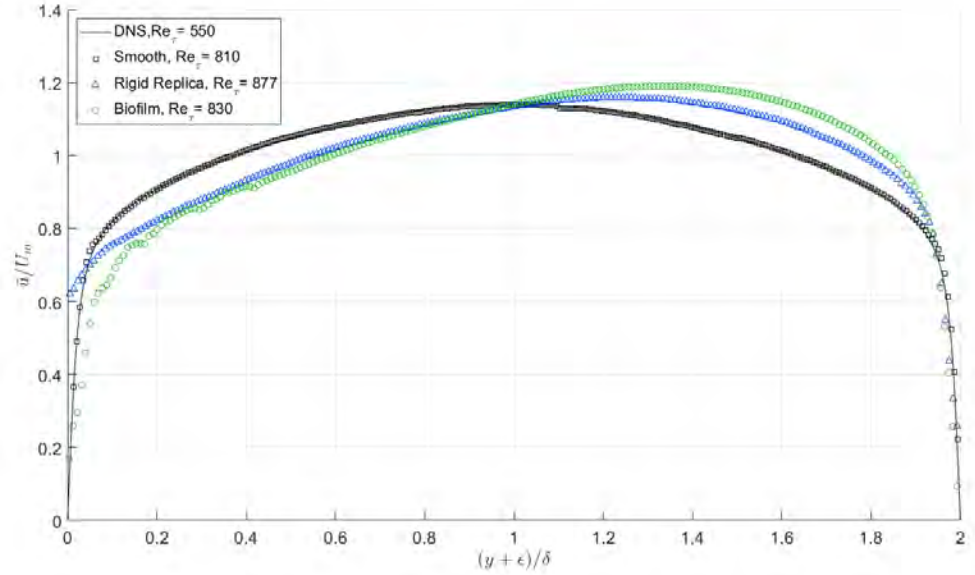

(a)

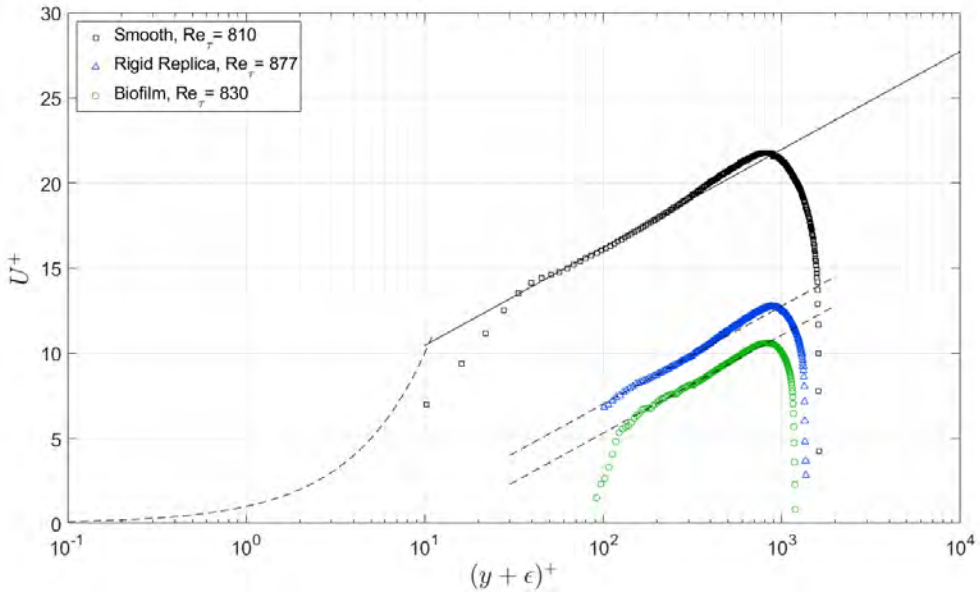

(b)

Figure 5.11: The mean velocity profiles for Trials 5W4 and 5W4RR show similar behavior in both (a) and (b). A surprisingly similar level of asymmetry is seen in (a) while the behavior of the flow over the rigid replica closely mimics that for the biofilm layer, albeit at a lesser offset in ΔU^+. Note that the near-wall behavior between the two surfaces does not agree which is typical.

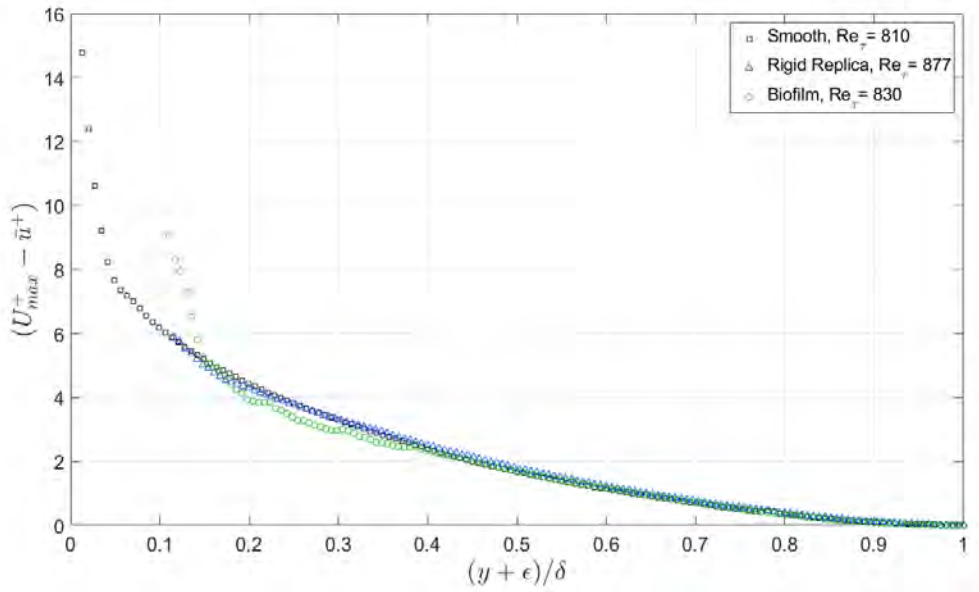

Figure 5.12: The relatively good collapse of velocity defect profile data in Trials 10W4 and 10W4RR stands in contrast to what was observed for Trials 10W2 and 10W2RR. It is difficult to know whether the difference is due to the scale separation between surface roughness and outer flow length scale or differences in manufacturing for the two rigid replicas.

previously mentioned, Trials 10W6 and 10W6RR were performed roughly half a year prior to the rest of data collection and a different analysis process was followed during the PIV procedure which may affect the observed results. For instance, the lack of flow data in the near-wall region of the velocity profile over the biofilm layer results from the use of a geometric mask which prevented flow analysis in this region.

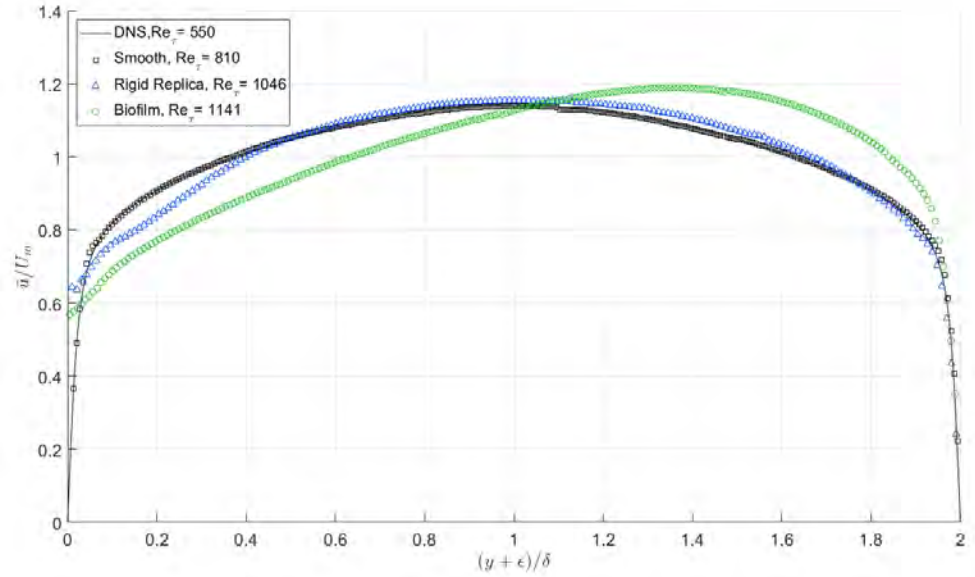

(a)

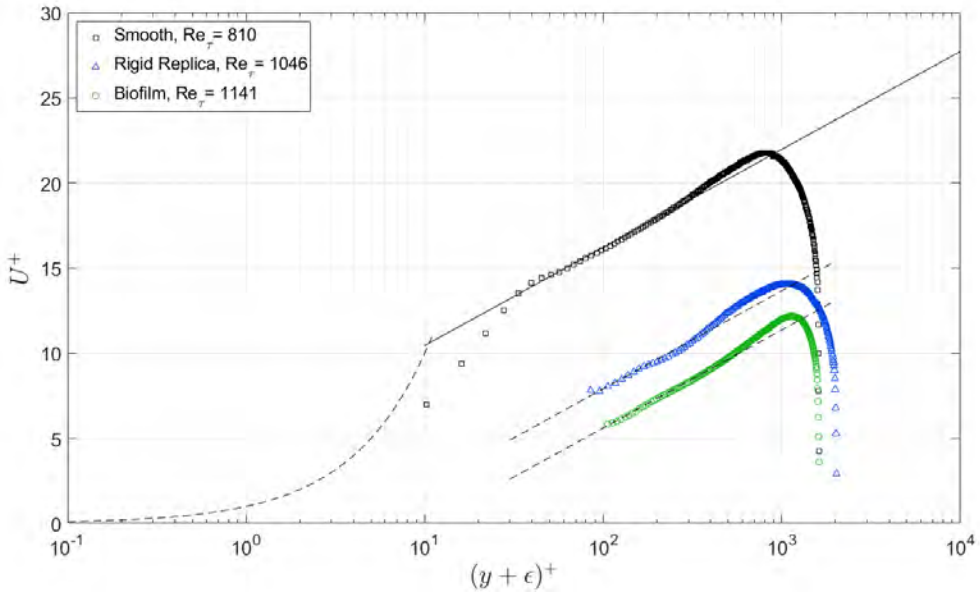

(b)

Figure 5.13: Flow data for Trials 10W6 and 10W6RR show fairly strong differences as compared to the other trials. The lack of 'viscous sublayer-like' flow in the region just above the biofilm layer is likely due to the use of a geometric mask in PIV analysis which was not used for the other trials. Strong reflections off the rigid replica's surface are likely the cause of the peculiar flow in the near-wall region above it.

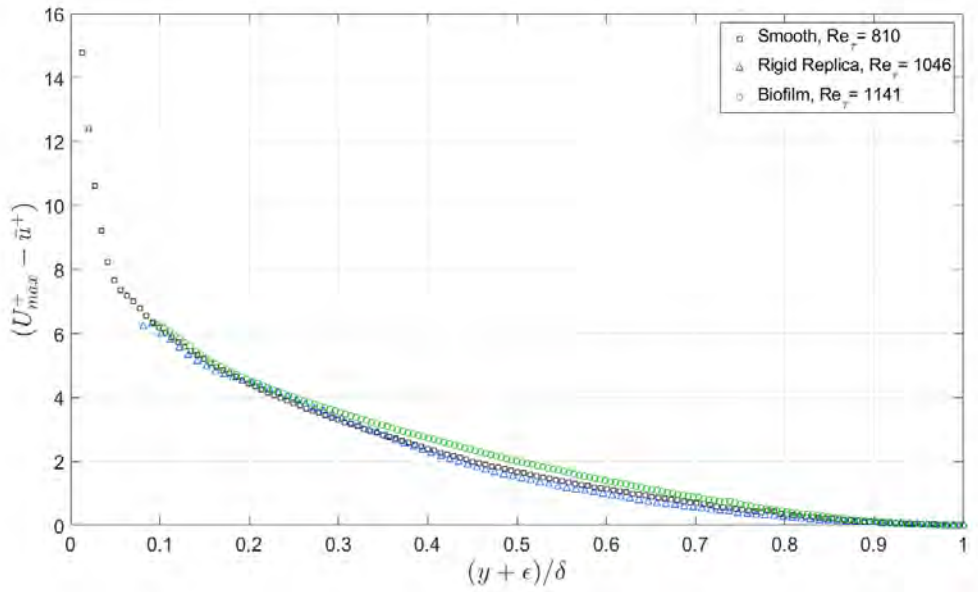

Figure 5.14: Collapse of the velocity data for Trials 10W6 and 10W6RR is relatively good considering the large separation in Re_τ values among the flow over the three surfaces. The departure seen between the biofilm and rigid replica flow data in the middle of the curves may be an artifact of the procedure used to find the wall offset, ϵ.

5.3 Comparing Results from Flow and Friction

Not only does knowledge of flow field behavior above biofilm layers and their rigid replicas complement the frictional data presented in earlier chapters, it also provides the opportunity to observe consistent trends and findings. Table 5.1 summarizes several key results derived from PIV measurements and analysis alongside those determined from frictional data using Granville's method [14]. Note that although values of both the roughness function, ΔU^+, and equivalent sand grain roughness height, k_s, are provided here, k_s may be derived from ΔU^+ in the fully rough regime using Equation 5.1.

$$\Delta U^+ = \frac{1}{\kappa} \ln k_s^+ - B + 8.5 \tag{5.1}$$

The results summarized in Table 5.1 show a consistent, relatively small offset of 3–12% in the two estimates of ΔU^+ and roughly 7–35% difference for values of k_s. It is important to recall that both Granville's method and the values of ΔU^+_{PIV} implicitly rely on measurements of the pressure drop to determine wall shear stress, τ_w, and are therefore not completely independent. Furthermore, in Granville's method, outer

layer similarity is assumed to hold when comparing results for rough and smooth surfaces. Therefore, it might be expected that the surfaces which display the poorest outer layer similarity may not agree between the two methods. However, this effect appears to be slight as results for Trials 5W1 and 10W2 (which appeared to display the least degree of outer layer similarity) do not appear to deviate significantly in Table 5.1. Instead the disparity must stem from differences in parameters which are independently measured—namely the mean velocity profile, $u(y)$, bulk mean velocity, U_m, and channel gap height, H. The ratio between equivalent sand grain roughness height, $k_{s,\,Granville}$ and average layer thickness, k_b is also given. The ratios shown here are roughly three times smaller than that given by Murphy *et al.* [35] which may be due to the difference in flow conditions (ZPG TBL versus fully developed channel flow) or the ratio of biofilm roughness heights to outer length scales which were significantly different between the two studies.

Measurements of the bulk mean velocity were recorded using a high-accuracy magnetic flow meter and typically agree within 5% of values estimated using PIV data. For the frictional results, the average channel gap height was determined using laser scan data taken during a representative scan of the biofilm layer and overhead photos of the extent of biofilm coverage. For the PIV analysis, the channel gap height was estimated by comparing the locations where measurements of the mean velocity profile stopped (or reached a value equal to zero) at either the top ($(y+\epsilon)/\delta = 0$) or bottom ($(y+\epsilon)/\delta = 2$) wall. Measurements of H taken using these different methods also typically agree within 5%. While these differences are in themselves relatively minor, they become amplified through the calculations performed in Granville's method (and through the use of Equation 5.1) which explains the shift observed in Table 5.1. Note that the outer scale used to determine $\Delta U^+_{Granville}$ was that described in §2.7.

Table 5.1: Results summary for rigid replicas and the biofilm layers to which they correspond

Trial	Re_H	$Re_{\tau,Granville}$	$Re_{\tau,PIV}$	$\Delta U^+_{Granville}$	ΔU^+_{PIV}	% diff	$k_{s,\,Granville}$ [μm]	$k_{s,\,PIV}$ [μm]	% diff	$k_{s,\,Granville}/k_b$	k_b^+
5W1	6550	419	417	6.9	7.4	6	701	848	17.3	0.64	116
5W1RR		453	468	5.1	5.5	7	289	340	14.9	–	–
5W2	7370	481	501	7.7	8.3	7	887	1115	20.4	1.3	76
5W2RR		445	451	5.9	5.8	-1	405	354	-3.4	–	–
5W3	13 610	858	871	8.8	9.2	4	788	893	11.8	1.1	144
5W3RRe		761	801	6.8	7.4	8	358	452	20.8	–	–
5W3	13 760	882	895	9.2	9.7	5	872	1074	18.8	1.37	131
5W3RRs		774	831	6.6	7.0	6	323	385	16.1	–	–
10W2	7740	646	660	10.8	12.0	10	1713	2728	37.2	0.76	456
10W2RR		634	766	9.2	10.5	12	880	1462	39.8	–	–
10W4	10 510	791	830	10.2	10.9	6	1419	1872	24.2	1.43	190
10W4RR		788	877	8.1	9.2	12	601	924	35	–	–
10W6	17 510	1257	1141	10.2	10.6	4	965	1126	14.3	0.93	293
10W6RR		795	795	7.4	8.2	10	331	455	27.3	–	–

It is also important to distinguish that the primary difference between the frictional measurements and those found from PIV lies in the region to which they apply. Measurements used in the frictional analysis take into account a more global view of each surface being investigated while PIV velocity fields pertain only to the thin measurement plane captured by the camera's field of view. Therefore, the results provided by PIV will not hold if the local surface condition varies significantly from the rest of the panel as is the case once substantial sloughing begins. While not shown here, estimates of the roughness function and equivalent sand grain roughness height can vary widely between the two methods depending on the type and location of sloughing. The particular susceptibility of results derived from PIV measurements prohibits comparison with the frictional results outside of uniformly covered surfaces, and the more reliable, global measurements used in the frictional analysis are considered to be a better representation of the 'true' value of a given parameter.

5.4 Chapter Summary

The mean flow field above biofilm layers and their rigid replicas was determined using Particle Image Velocimetry. Highly resolved velocity vectors provide the flow details from the surface of interest and across the full channel but only in a narrow location at the centerline of the SF3 span. Therefore, the results presented in this chapter only correspond to biofilm trials which did not experience significant sloughing. Trials of a baseline smooth acrylic panel and sand grain roughness were performed to validate the methods used to collect and analyze measurements. Comparison with theory and prior results showed good agreement for the validation data.

Examination of the mean velocity profiles over biofilm layers show consistent findings. Somewhat surprisingly, flow in the immediate vicinity of the biofilm layer developed in a manner similar to a viscous sublayer despite the significant roughness of the biofilm layers. The log layer of flow over biofilm surfaces demonstrated a slope with κ^{-1} which is expected. The outer region of flow over biofilm layers often shows a wake-like behavior which may be the result of streamer flutter or bulk biofilm vibration. Unique features were sometimes observed for specific biofilm layers which may be the result of topography specific to each layer (as PIV data are local, they are more susceptible to local variations of the biofilm layer).

Flow over rigid replicas demonstrated less consistent behavior. While all rigid replicas displayed fully rough behavior (i.e. no viscous sublayer) and the expected behavior in the log-layer, the structure of the outer flow varied. Roughly half of

the rigid replica trials had mean velocity profiles which mimic the biofilm layers by displaying wake-like behavior while the other half appeared to demonstrate a profile which followed the log-law from the rigid replica surface to the maximum flow velocity. Velocity defect plots showed that outer layer similarity between the smooth baseline, rigid replicas, and biofilm layers agreed well for some trials but deviated somewhat for others. Trials of rigid replicas produced using the advanced MATLAB algorithms (which better replicated local topography at the location where PIV data was collected) were more likely to agree with smooth (baseline) and biofilm data. The reasons driving the presence of a wake region in the flow away from some of the rigid replicas is not known but may relate to specific, local flow features such as the presence of a particularly large streamer upstream of the measurement FOV.

Finally, the roughness function and equivalent sand grain roughness height determined using data from both the frictional and flow measurements were compared. Although ΔU^+ and k_s rely on C_f which was determined only from pressure drop data, differences in the two different data sets were observed in measurements of the estimated velocity profile, bulk mean velocity, and channel gap height which were made independently for the two methods. The differences were only $\sim$5% for U_m and H, but propagation of the uncertainty through Granville's method and Equation 5.1 resulted in an offset in the roughness function of roughly -1–12% and in the equivalent sand grain roughness heights of about -3.4–39.8%.

CHAPTER VI

Conclusions and Recommendations

The primary objective of this dissertation was to disassociate the added drag produced by filamentous biofilm layers into contributions from roughness and compliance effects. This effort began with the design and construction of a growth loop in which smooth acrylic panels were installed and exposed to a mix of diatomaceous and filamentous biofouling organisms. Once fouling had developed on test surfaces for three, five, and ten week intervals, their hydrodynamic performance was evaluated. Experimental trials were performed in a high-aspect ratio, fully developed channel flow facility for speeds ranging from $Re_H \approx 5\ 000 - 30\ 000$. Measurements of the pressure drop along the channel's length captured the frictional performance of the biofilm covered surfaces while data recorded by an overhead camera and custom built laser scanning system allowed calculation of biofilm characterization parameters including the average biofilm layer thickness, fouled area, and roughness statistics. Seven rigid replicas of six different fouled panels were manufactured from scans of the time-averaged, spatially filtered surface profile over the entire span of the facility. The frictional performance of these rigid replicas was determined for the same flow conditions as the biofilm layers they replicate. Details of the mean flow field located above the biofilm layers and rigid replicas were provided by planar (2D2C) Particle Image Velocimetry.

6.1 Conclusions

6.1.1 Frictional Performance of Biofilm Layers

Experimental trials of fourteen different biofilm covered panels were conducted for three nominal growth incubation times. The main conclusions were:

- Smooth acrylic panels covered in filamentous biofilm layers experienced a wide range of added drag;
- Biofilm layers grown for three weeks displayed sparse, uneven coverage with average layer thicknesses of k_b = 40–200 μm and drag penalties ranging from ΔC_f = 20–152%;
- Five week biofilm layers experienced a similar range of added drag—ΔC_f = 65–191%—despite having significantly larger average layer thicknesses of k_b = 642–1111 μm and a wider range of percentage fouled area; and
- Surfaces exposed for ten weeks experienced the greatest variation in growth with initial layer thicknesses averaging from k_b = 1072–2571 μm and also the widest deterioration due to sloughing with fouled areas which ranged from A_b = 2–100%. It is not surprising that these biofilm layers also exhibited the widest range of added drag with ΔC_f = 14–364%.

6.1.2 Scaling and Predicting Biofilm Resistance

Assuming biofilm layers exhibit outer layer similarity, the findings from lab scale studies can be extended to fouled systems of engineering interest such as pipelines, waterways, and ships. A previously proposed scaling correlation was evaluated in Chapter Three using data collected for the biofilm covered surfaces examined in this dissertation. The main conclusions were:

- The roughness functions, ΔU^+, measured for five and ten week biofilm layers were successfully collapsed by $k_{eff,\,adj} = 0.042 k_b A_b^{\frac{1}{2}}$ which is a slight adjustment to the effective biofilm roughness height proposed by Schultz *et al.* [49]; and
- Drag penalties for stable five and ten week biofilm layers depended primarily on Reynolds number, Re_H, the average thickness of the biofilm layer, k_b, and the percentage of the surface covered in fouling, A_b. An empirical formula was presented which characterizes the added drag of stable five and ten week biofilm layers within ±10%.

6.1.3 Frictional Performance of Rigid Replicas

Rigid replicas were manufactured from laser scan data of biofilm layers and accurately capture their time-averaged, spatially filtered surface profile. Chapter Four presented the frictional performance of the rigid replicas and compared the results

directly with measurements for the corresponding biofilm surfaces. The main conclusions were:

- Rigid replicas of five week biofilm layers had drag penalties ranging from $\Delta C_f =$ 57–101% which is roughly half of what was measured for the live biofilm layers which they replicate; and
- The drag penalty of ten week biofilm layer rigid replicas was $\Delta C_f = 124$–193% which was also roughly half of what was measured for the live biofilm layers to which they correspond.

6.1.4 Scaling and Predicting Rigid Replica Resistance

Efforts were made to find a characteristic roughness height which would scale the roughness function for rigid replicas. As shown in Chapter Four, the result was partially successful and helped inform the analysis to derive an empirical relationship between rigid replica geometry and added drag. The main conclusions were:

- Partial collapse of the measured roughness function for rigid replicas using a characteristic effective roughness height, $k_{RR} = 0.05(k_t\lambda_x)^{\frac{1}{2}}$; and
- An empirical relationship was determined which relates the added drag experienced by the rigid replicas to the Reynolds number, Re_H, their trough-to-peak roughness height, k_t, and the average streamwise distance between large streamers, λ_x. Predicted values of ΔC_f matched measurements within $\pm 15\%$.

6.1.5 Roughness and Compliance Contributions to Added Drag

The contributions of rough and compliant effects to added drag was estimated in Chapter Four using a simple model and frictional results from trials of biofilm layers and rigid replicas. The main conclusion was:

- Both roughness and the effects of compliance contribute to the biofilm drag penalty with each contributing roughly half of the added drag experienced by the five and ten week biofilm layers bounding turbulent flow. Values predicted by the empirical relationships presented in Chapters Three and Four agreed within $\pm 15\%$ of the measured results.

6.1.6 Mean Flow Structure Over Biofilm Layers and Their Rigid Replicas

Highly resolved planar PIV measurements of the mean flow field over biofilm layers and their rigid replicas was presented in Chapter Five. The main conclusions were:

- Although velocity data pertaining to some trials showed poor outer layer similiarity, the mean velocity profiles over biofilm layers and rigid replicas typically match well in the outer region of the flow indicating that drag production mechanisms are generally confined to the near-wall region; and
- The mean velocity profile along biofilm layers appeared to show varying behavior prior to the beginning of the log layer. Occasionally, flow data appeared to follow a trend similar to the linear sublayer observed over smooth surfaces; this is surprising given the ratio of biofilm thickness and roughness to the outer length scale and may indicate that flow in the space between streamers increases gradually from the base of the biofilm layer.

6.1.7 Contributions

The original work presented in this dissertation expanded on previous findings examining biofilm flow behavior and drag production mechanisms. Prior research studies have shown that the presence of soft biofouling on surfaces bounding turbulent flow can lead to significant drag increases, have proposed scaling correlations linking biofilm geometry with the roughness function, and theorized that compliance mechanisms play a role in drag production. The original contributions of this work were:

- Collection of highly resolved *in situ* measurements of biofilm surfaces; and
- Determination of the frictional performance of a single filamentous biofilm species mix across a range of fouling conditions; and
- Confirmation of a previously proposed scaling correlation linking a biofilm layer's thickness and percentage fouled area to its roughness function. The results were then used to empirically characterize the added drag produced by a biofilm layer; and
- Manufacture of rigid replicas which accurately represent living biofilm layers grown for five and ten weeks and evaluation of their frictional performance to disassociate the contributions from rough and compliance effects to overall

added drag determining that roughly half of the added drag produced by these biofilm layers was due to rough effects; and

- Proposal of a scaling correlation and empirical formula linking the rigid replicas' average trough-to-peak roughness heights and downstream spacing between large streamers to the roughness function; and
- Characterization of the mean flow field above biofilm layers and their rigid replicas, providing basic insight into features of the velocity profile.

6.2 Limitations and Recommendations for Future Research

Several limitations exist pertaining to the findings of this dissertation. Firstly, it should be noted that the biofilm layers studied were grown from only one species mix and—although they varied naturally—the findings may not apply to the wide range of diverse biofilm fouling observed in the field. In particular, biofilms without streamers may exhibit significantly different behavior than was seen for the filamentous ones studied here. Furthermore, biofilm layers were grown and evaluated in fully developed channel flow facilities with a narrow channel gap height. This may have limited streamer geometry and also resulted in a relatively low ratio between biofilm roughness heights and outer length scale ($k/\delta \approx 0.03$–0.5). This ratio may be significantly different for external boundary layer flows or flows through larger channels or pipes and could result in different dynamics.

Additionally, sloughing of the biofilm layer from test panels complicated measurements and limited the range of Reynolds numbers which could be achieved. Sloughing introduced greater uncertainty in the results from experimental trials and several correction techniques had to be developed to account for the changes brought on by the unsteady surface condition (see §2.7). The sparse coverage of the three week biofilm layers also limited the analysis which could be performed on data corresponding to their frictional behavior and prevented the manufacture of rigid replicas for these trials. Furthermore, the relatively large drag penalties for these low-form biofilm layers may indicate that the effects of compliance are more important than roughness for sparse, or developing biofilm layers.

Open questions regarding the mechanisms and consequences of biofilm drag production still exist and further study is needed. Future efforts might follow two paths: 1) academic pursuits linking parameters characterizing different aspects of biofilm roughness and compliance to frictional behavior and flow features and/or 2) evalu-

ation of the practical consequences of biofilm fouling including the effect of surface chemistry and roughness on drag production and sloughing.

Researchers pursuing greater understanding of the physical aspects of roughness and compliance drag production mechanisms could make use of emerging technologies (such as 3D printing of finely featured, compliant surfaces) to develop and study drag on and flow over surfaces with tailored compliance and geometry. Investigating a range of streamer geometries and rheological properties could link processes like streamer flutter and mat vibrations to frictional performance and flow structure. Furthermore, biofilms of varying morphology and development should be investigated in a variety of flow conditions to determine if the findings of this study can be applied to external boundary layers or for biofilm layers with small thickness compared to the largest flow scales.

Investigators interested in the practical consequences of biofilm drag production might examine the effects of surface curvature and underlying roughness on biofilm sloughing. A range of biofilm morphologies could be grown on smooth and rough control surfaces as well as commercial antifouling and foul release coatings. While research of this nature has been performed, the continual development of new coatings and strategies to produce non-fouling surfaces necessitates sustained investigation.

6.3 Concluding Remarks

Studying the drag production and turbulent flow over biofilm layers is a challenging undertaking. It is hoped that the methodology and findings presented in this dissertation will inform future researchers of the difficulties which need to be considered during the growth, testing, and analysis stages of lab-scale biofilm studies. The author welcomes the inquires of any future researchers and is happy to provide greater detail of the project to the interested reader. He may be contacted via email at: jdharte@umich.edu.

BIBLIOGRAPHY

BIBLIOGRAPHY

[1] Abbott, A., Abel, P.D., Arnold, D.W., Milne, A.: Cost-benefit analysis of the use of TBT: the case for a treatment approach. Science of the Total Environment **258**(1-2), 5–19 (2000). DOI 10.1016/S0048-9697(00)00505-2

[2] Alzieu, C.: Environmental impact of TBT: the French experience. Science of the Total Environment **258**(1-2), 99–102 (2000). DOI 10.1016/S0048-9697(00)00510-6

[3] Andrewartha, J., Perkins, K., Sargison, J., Osborn, J., Walker, G., Henderson, A., Hallegraeff, G.: Drag force and surface roughness measurements on freshwater biofouled surfaces. Biofouling **26**(4), 487–496 (2010). DOI 10.1080/08927014.2010.482208

[4] Andrewartha, J., Sargison, J.: Turbulence and mean-velocity structure of flows over filamentous biofilms. IAHR Congress (July), 2225–2232 (2011). URL `http://ecite.utas.edu.au/76555/1/2011AndrewarthaandSargisonIAHR.pdf`

[5] Andrewartha, J., Sargison, J., Henderson, A., Perkins, K., Walker, G.: The effect of freshwater biofilms on skin friction drag. In: 16th IAHR-APD Congress and 3rd Symposium of IAHR-ISHS (2008)

[6] Andrewartha, J.M.: The effect of fresh water biofilms on turbulent boundary layers and the implications for hydropower canals. Ph.D. thesis, University of Tasmania (2010)

[7] Carpenter, P.W.: Current status of the use of wall compliance for laminar- flow control. Experimental Thermal and Fluid Science **16**, 133–140 (1998)

[8] Colebrook, C.F.: Turbulent flow in pipes, with particular reference to the transition region between the smooth and rough pipe laws. Journal of the Institute of Civil Engineering **11**(February), 133–156 (1939)

[9] Durr, S., Thomason, J.C.: Biofouling. John Wiley & Sons (2009)

[10] Flack, K.A., Schultz, M.P.: Review of hydraulic roughness scales in the fully rough regime. Journal of Fluids Engineering **132**(4), 041,203 (2010). DOI 10.1115/1.4001492

[11] Flack, K.A., Schultz, M.P.: Roughness effects on wall-bounded turbulent flows. Physics of Fluids **26**(10) (2014). DOI 10.1063/1.4896280. URL http://dx.doi.org/10.1063/1.4896280

[12] Flack, K.A., Schultz, M.P., Connelly, J.S.: Examination of a critical roughness height for outer layer similarity. Physics of Fluids **19**(9) (2007). DOI 10.1063/1.2757708. URL https://doi.org/10.1063/1.2757708

[13] Gose, J.W., Golovin, K., Boban, M., Mabry, J.M., Tuteja, A., Perlin, M., Ceccio, S.L.: Characterization of superhydrophobic surfaces for drag reduction in turbulent flow. Journal of Fluid Mechanics **845**, 560–580 (2018). DOI 10.1017/jfm.2018.210

[14] Granville, P.S.: Modified law of the wake for turbulent shear layers. Journal of Fluids Engineering **98**(3), 578–580 (1976). DOI 10.1115/1.3448405

[15] Grigson, C.: Drag losses of new ships caused by hull finish. Journal of Ship Research **36**(2), 182–196 (1992)

[16] Gad-el hak, M.: Compliant coatings: the simpler alternative. Experimental Thermal and Fluid Science **16**, 141–156 (1998)

[17] Haslbeck, E.G., Bohlander, G.S.: Microbial biofilm effects on drag-lab and field. In: SNAME Symposium (1992)

[18] Hondzo, M., Wang, H.: Effects of turbulence on growth and metabolism of periphyton in a laboratory flume. Water Resources Research **38**(12), 13–1–13–9 (2002). DOI 10.1029/2002WR001409. URL http://doi.wiley.com/10.1029/2002WR001409

[19] Hunsucker, J.T., Hunsucker, K.Z., Gardner, H., Swain, G.: Influence of hydrodynamic stress on the frictional drag of biofouling communities. Biofouling **32**(10), 1–13 (2016). DOI 10.1080/08927014.2016.1242724. URL http://dx.doi.org/10.1080/08927014.2016.1242724

[20] Jimenez, J.: Turbulent flows over rough walls. Annual Review of Fluid Mechanics **36**(1), 173–196 (2004). DOI 10.1146/annurev.fluid.36.050802.122103

[21] von Karman, T.: Mechanische ahnlichkeit und turbulenz. In: Proceedings of the Third International Congress of Applied Mathematics (1930)

[22] Kim, J., Moin, P., Moser, R.: Turbulence statistics in fully developed channel flow at low Reynolds number. Journal of Fluid Mechanics **177**, 133–166 (1987)

[23] Kramer, M.O.: Boundary-layer stabilization by distributed damping. Journal of Aerospace Sciences **27**(1), 69–69 (1960)

[24] Kreplin, H.P., Eckelmann, H.: Behavior of the three fluctuating velocity components in the wall region of a turbulent channel flow. Physics of Fluids **22**(7), 1233–1239 (1979). DOI 10.1063/1.862737

[25] Kundu, P.K., Cohen, I.M., Dowling, D.: Fluid mechanics, 5 edn. Academic Press, Waltham, MA (2012)

[26] Lee, B.T., Fisher, M., Schwarz, W.H.: Investigation of the stable interaction of a passive compliant surface with a turbulent boundary layer. Journal of Fluid Mechanics **257**(373-401) (1993)

[27] Lewandoski, Z., Stoodley, P.: Flow induced vibrations, drag force, and pressure drop in conduits covered with biofilm. Water Science Technology **32**(8) (1995)

[28] Lewkowicz, A., Das, D.: Turbulent boundary layers on rough surfaces with and without a pliable overlayer: a simulation of marine fouling. International Shipbuilding Progress, Marine Technology Monthly (32), 174–186 (1985)

[29] Lewthwiate, J.C., Phil, M., Molland, A.F., Thomas, K.W.: An investigation into the variation of ship skin frictional resistance with fouling. Royal Institution of Naval Architects **127** (1985). DOI 10.1093/jpids/pix105/4823046

[30] Ligrani, P.M.: Structure of transitionally rough and fully rough turbulent boundary layers. Journal of Fluid Mechanics **162**, 69–98 (1986)

[31] Marusic, I., Adrian, R.: The eddies and scales of wall turbulence. In: P.A. Davidson, Y. Kaneda, K.R. Sreenivasan (eds.) Ten Chapters in Turbulence, chap. 5, pp. 176–220 (2013). DOI 10.1017/CBO9781139032810. URL `http://dx.doi.org/10.1017/CBO9781139032810`

[32] Moffat, R.J.: Describing the uncertainties in experimental results. Experimental Thermal and Fluid Science pp. 3–17 (1988)

[33] Moser, R.D., Kim, J.: Direct numerical simulation of turbulent channel flow up to Re = 590. Physics of Fluids **11**(4), 1999–2001 (2001)

[34] Murphy, E., Barros, J., Schultz, M., Flack, K., Steppe, C., Reidenbach, M.: The turbulent boundary layer structure over diatomaceous slime fouling. 10th International Symposium on Turbulence and Shear Flow Phenomena, TSFP 2017 **1**, 1–7 (2017)

[35] Murphy, E.A.K., Barros, J.M., Schutlz, M.P., Flack, K.A., Steppe, C.N., Reidenbach, M.A.: Roughness effects of diatomaceous slime fouling on turbulent boundary layer hydrodynamics. Biofouling (2019). DOI 10.1080/08927014.2018.1517867

[36] Ng, S.K., Walker, J.M.: Measuring turbulence characteristics of artificial biofilms using LDV and high speed photography. In: 18th Australian Fluid Mechanics Conference, December (2012)

[37] Nikuradse, J.: Laws of flow in rough pipes. NACA Technical Memorandum (192) (1933)

[38] Oweis, G.F., Winkel, E.S., Cutbrith, J.M., Ceccio, S.L., Perlin, M., Dowling, D.R.: The mean velocity profile of a smooth-flat-plate turbulent boundary layer at high Reynolds number. Journal of Fluid Mechanics **665**, 357–381 (2010). DOI 10.1017/S0022112010003952

[39] Perlin, M., Dowling, D.R., Ceccio, S.L.: Freeman scholar review: passive and active skin-friction drag reduction in turbulent boundary layers. Journal of Fluids Engineering **138**(9), 091,104 (2016). DOI 10.1115/1.4033295. URL `http://fluidsengineering.asmedigitalcollection.asme.org/article.aspx?doi=10.1115/1.4033295`

[40] Pope, S.B.: Turbulent flows, 1st edn. Cambridge University Press, Cambridge, UK (2001)

[41] Prandtl, L.: Attaining a steady air stream in wind tunnels. Technical Memorandum National Advisory Committee For Aeronautics (1933)

[42] Renslow, R., Lewandowski, Z., Beyenal, H.: Biofilm image reconstruction for assessing structural parameters. Biotechnology and Bioengineering **108**(6), 1383–1394 (2011). DOI 10.1002/bit.23060

[43] Schultz, M.P.: Turbulent boundary layers on surfaces covered with filamentous algae. Journal of Fluids Engineering **122**(2), 357 (2000). DOI 10.1115/1.483265

[44] Schultz, M.P.: Frictional resistance of antifouling coating systems. Journal of Fluids Engineering **126**(6), 1039–1047 (2004). DOI 10.1115/1.1845552

[45] Schultz, M.P., Bendick, J.A., Holm, E.R., Hertel, W.M.: Economic impact of biofouling on a naval surface ship. Biofouling **27**(1), 87–98 (2011). DOI 10.1080/08927014.2010.542809

[46] Schultz, M.P., Flack, K.A.: The rough-wall turbulent boundary layer from the hydraulically smooth to the fully rough regime. Journal of Fluid Mechanics **580**, 381 (2007). DOI 10.1017/S0022112007005502

[47] Schultz, M.P., Flack, K.A.: Reynolds-number scaling of turbulent channel flow. Physics of Fluids **25**(2), 1–13 (2013). DOI 10.1063/1.4791606

[48] Schultz, M.P., Swain, G.W.: The effect of biofilms on turbulent boundary layers. Journal of Fluids Engineering **121**(3) (1999). DOI 10.1115/1.3240989

[49] Schultz, M.P., Walker, J.M., Steppe, C.N., Flack, K.A.: Impact of diatomaceous biofilms on the frictional drag of fouling-release coatings. Biofouling **31**(9-10), 759–773 (2015). DOI 10.1080/08927014.2015.1108407

[50] Smits, A.J., McKeon, B.J., Marusic, I.: High Reynolds number wall turbulence. Annual Review of Fluid Mechanics **43**(1), 353–375 (2011). DOI 10.1146/annurev-fluid-122109-160753. URL `http://www.annualreviews.org/doi/10.1146/annurev-fluid-122109-160753`

[51] Squire, D.T., Morrill-Winter, C., Hutchins, N., Schultz, M.P., Klewicki, J.C., Marusic, I.: Comparison of turbulent boundary layers over smooth and rough surfaces up to high Reynolds numbers. Journal of Fluid Mechanics **795**, 210–240 (2016). DOI 10.1017/jfm.2016.196

[52] Townsin, R.L.: The ship hull fouling penalty. Biofouling **19**, 9–15 (2003). DOI 10.1080/0892701031000088535

[53] Walker, J.M.: The application of wall similarity techniques to determine wall shear velocity in smooth and rough wall turbulent boundary layers. Journal of Fluids Engineering **136**(5), 051,204 (2014). DOI 10.1115/1.4026512. URL `http://fluidsengineering.asmedigitalcollection.asme.org/article.aspx?doi=10.1115/1.4026512`

[54] Walker, J.M., Sargison, J.E., Henderson, A.D.: Turbulent boundary-layer structure of flows over freshwater biofilms. Experiments in Fluids **54**(12) (2013). DOI 10.1007/s00348-013-1628-x

[55] White, F.M.: Fluid mechanics, 5th edn. McGraw-Hill, Boston (2003)

[56] White, F.M.: Viscous fluid flow, 3rd edn. McGraw-Hill, Singapore (2006)

[57] Yeginbayeva, I., Atlar, M., Kidd, B., Finnie, A.A.: Investigating the impact of surface condition on the frictional resistance of fouling control coating technologies. In: 31st Symposium on Naval Hydrodynamics, September 2016, pp. 11–16 (2016)

[58] Zanoun, E.S., Nagib, H., Durst, F.: Refined cf relation for turbulent channels and consequences for high-Re experiments. Fluid Dynamics Research **15**(10), 3079–3089 (2009). DOI 10.1088/0169-5983/41/2/021405